Modification of Heme Proteins for Reactivity and Mechanistic Studies

by

Victor Sosa Alfaro

A dissertation submitted in partial fulfillment
of the requirements for the degree of
Doctor of Philosophy
(Chemistry)
in the University of Michigan
2023

Doctoral Committee:

Professor Nicolai Lehnert, Chair
Professor Jennifer Bridwell-Rabb
Professor Vincent L. Pecoraro
Professor Emily Scott

Victor Sosa Alfaro

sosavic@umich.edu

ORCID iD: 0000-0001-8149-5137

To my family. I could not have done it without you.

To the future generations of Latin American scientist.

¡Si se puede!

Acknowledgements

First, I want to thank my advisor Prof. Nicolai Lehnert, for your guidance and support through my time at the University of Michigan, it meant a lot to me. Thank you for always being so positive and believing in me. Right from the start you made me feel welcomed. Your knowledge and mentorship have made me a better scientist and person.

I want to thank my committee members Professor Vincent L. Pecoraro, Professor Jennifer Bridwell-Rabb, and Professor Emily Scott for your guidance, advice, and always taking the time to assist my scientific journey.

Lehnert Group colleagues and friends, thank you for all your support and help over the years; Abby, Allie, Andrew, Bloom, Brad, Corey, Esmee, Garrett, Hai, Hannah, Jill, Lizzie, Luis, Manon, Matt, Michael, Molly, and Virginia. You've always been there to talk about research, brighten my day, and laugh. Jill and Elvin, I will always be grateful for our friendship that started right from the beginning. Matt, thank you for your mentorship, for all that you taught me, and always making me laugh with your silly personality. Hannah, thank you for all your hard work and your dedication to research, I am excited for your bright future. Andrew and Corey, you guys made graduate school a lot more fun. Jill, Virginia, and Garrett, it was great doing all those fun activities together.

I would like to give a special thanks to Professor Vincent L. Pecoraro for all his help, advice throughout the years and always going above and beyond as a mentor. To the Pecoraro lab, April, Audrey, Berni, Elvin, Jake, Karl, Tyler, and Winston thank you for being great and always treating me as a part of your lab. I would like to give a distinct thanks to Karl and Audrey for being my mentors during my rotation, you two taught me a lot about *de novo* design and kinetics.

I have several collaborators to thank and acknowledge: To Dr. Eric Hegg, Dr. Julius Campeciño, and Krystina Hird for our NrfA discussions, dedication to expressing protein, and being a part of a collaboration that became a large part of my thesis. Dr. Sean Elliott and Matthew Tracy thank you for all you help with electrochemistry. To Dr. Martin Weissenborn and Anja Knorrscheidt for our YfeX collaboration. To Dr. Christo Christov, and Sodiq Waheed for all your computational chemistry help. Dr. Jennifer Bridwell-Rabb and David Boggs, thank you for being patient with me and teaching me about Stopped-flow.

The Chemistry department staff, I appreciate all your assistance with instrumentation, fixing equipment, and your help with all the problems I ran into over the years. Jim Windak, you have been the hero for always knowing how to trouble shoot the instruments. The Rackham Merit Fellowship (RMF) staff, thank you for all your guidance and financial support throughout the years.

I would like to thank Professor Jon M. Fukuto, for your mentorship and for inspiring me to continue a chemistry career.

I would like to thank my parents and family for their unconditional love, support, and always pushing me to continue my education. Siempre disfruto los momentos de felizidad, y estoy entusiasmado de tener muchos más.

Celia, your love and encouragement has meant a lot to me. I am so lucky and happy to have you in my life, I don't think I would have made it through without you. Espero que nuestro amor sea inmarcesible, y que siempre seamos felices juntos.

Table of Contents

List of Tables

List of Figures

Abstract

In the past decade, carbene transfer biocatalysis has evolved from basic scientific research to an area with vast potential for the development of new industrial processes in the pharmaceutical industry. In this work YfeX, naturally a peroxidase, is shown to have a great potential for the development of new carbene transferases. Intrinsic reactivity of wild-type (WT) YfeX is in many cases on par with the best Mb variants available, and this protein shows high stability against organic co-solvents, thereby enabling us to solubilize hydrophobic substrates to improve turnover. In the cyclopropanation of styrene, WT YfeX naturally generates the *trans* product with 87% selectivity for the (R,R) enantiomer. WT YfeX also catalyzes N-H insertion with aliphatic amines (benzylamine) in high yield. Most excitingly, YfeX can catalyze the Si—H insertion of dimethylphenylsilane with 11% yield, which is the highest yield for any WT protein observed so far, and QM/MM calculations reveal further details of the mechanism of the unusual Si—H insertion reaction.

To explore the steric and electrostatic effects of the second coordination sphere near the active site of YfeX, utilizing rational design, four YfeX variants (I230A, D143A, R232A, and S234A) were investigated for enhanced carbene transferase reactivity. It was shown that R232A (with 75% yield) and I230A (with 92% yield) variants have increased N-H insertion reactivity and are a good starting point to further improve YfeX reactivity. These studies demonstrate that YfeX and variants are great biocatalysts and motivate the development of novel YfeX carbene transferases.

The second part of my thesis focuses on the investigation of the electron storage and distribution properties within the pentaheme scaffold of *Geobacter lovleyi* cytochrome c nitrite reductase (NrfA or ccNiR), a newly discovered subclass of cytochrome c nitrite reductases. NrfA from *G. lovleyi*, has emerged as a model representative of bacteria that have an important role in the global nitrogen cycle via the dissimilatory nitrate reduction to ammonium (DNRA) pathway. Initially, a chemical reduction method was established to sequentially add electrons to the fully oxidized protein, which was then studied using UV-Vis and electron paramagnetic resonance (EPR) spectroscopy. Based on quantitative analysis and simulation of the EPR data, we demonstrate that Hemes 1, 3, and 4 are exchange coupled, and the EPR signals of all five hemes in fully oxidized NrfA could be identified for the first time. EPR-spectral simulations were used to elucidate the sequence of heme reduction and reveal that Hemes 5 and 4 are reduced first (before the active site Heme 1) and can serve the purpose of an electron storage unit within the protein, instead of merely serving as a wire to pass electrons into Heme 1. Additionally, to probe the role of the central Heme 3, a H108M NrfA variant was generated with a positively shifted reduction potential, making it the first heme to be reduced. This H108M variant has a significant impact on the distribution of electrons within the pentaheme scaffold and decreases the catalytic activity of the enzyme to 3% compared to WT NrfA.

These studies demonstrate that the four bis-His hemes of NrfA are much more than just a wire that allows for electron transfer to the active site Heme 1. Furthermore, this work elucidates fundamental information about the complicated mechanism of electron storage within Hemes 4 and 5 and the overall electron distribution in NrfA.

Chapter 1 Introduction

1.1 Biocatalysts

Enzymes are important macromolecules that have evolved to catalyze a variety of specific biochemical reactions with high efficiency under various environmental conditions. Additionally, they can catalyze a variety of organic transformations with high activity and selectivity for a specific product, utilizing a variety of cofactors and highly organized active sites that are tailored for precise product stereoselectivity.[1-2] Ultimately enzymes are a part of diverse functions that are essential for living organisms including but not limited to photosynthesis, synthesis of building blocks (such as DNA, RNA, and amino acids), and nitrogen fixation. By contrast, human-developed catalysts use a diversity of transition metals and perform numerous types of reactions, including many that are unknown in nature. Several examples of these transition metal catalysts are implemented in the chemical industry, including Wilkinson's catalyst, which effectively hydrogenates olefins and alkenes,[3] Grubb's catalyst, which facilitates olefin metathesis,[4] and several catalysts such as the rhodium catalyst are available for hydroformylation, an important process to produce aldehydes.[5] There are a variety of organometallic reactions not observed in nature that are crucial for forming new C-C, C-H, C-N, C-Si, and C-S bonds, and ultimately important for the development of new products in the chemical industry. Although efficient, these man-made catalysts have a negative impact on the environment once they are scaled up in industry due to the need for expensive rare metals, and the usage of organic solvents during catalysis, which generates large amounts of waste.[4-11]

One of the main goals in industry is to catalyze organic reactions in water with high control of product stereoselectivity, turnover number (TON), turnover frequency (TOF), and long lifetime of the catalyst.[12-14] The implementation of biocatalysts is an attractive avenue due to the ability of metalloenzymes to operate under environmentally friendly conditions (often at physiological pH, pressure, and temperature), at high rates and with high stereo- and enantioselectivity, and they usually utilize earth-abundant metals to do these reactions (**Figure 1.1)**.[2, 15] These biological catalysts lead to a significant reduction in waste and cost in industrial-scale synthesis compared to stoichiometric syntheses and other catalytic processes.[16-17] Metalloenzymes are of particular interest in the fields of biochemistry and catalysis since these proteins catalyze interesting natural reactions such as oxo-atom transfer to inactivated C-H bonds,[18] water oxidation to dioxygen,[19] and the formation of methane[20] among many others. In addition to the high activity of metalloenzymes, many enzymes are promiscuous towards non-natural substrates and reactions, although protein modifications are usually required to enhance abiological activity.[21] Due to the potential of biocatalysis, in the last 20 years numerous companies have implemented selective enzymes to manufacture chemicals, active compounds, or generate novel materials.[11, 15]

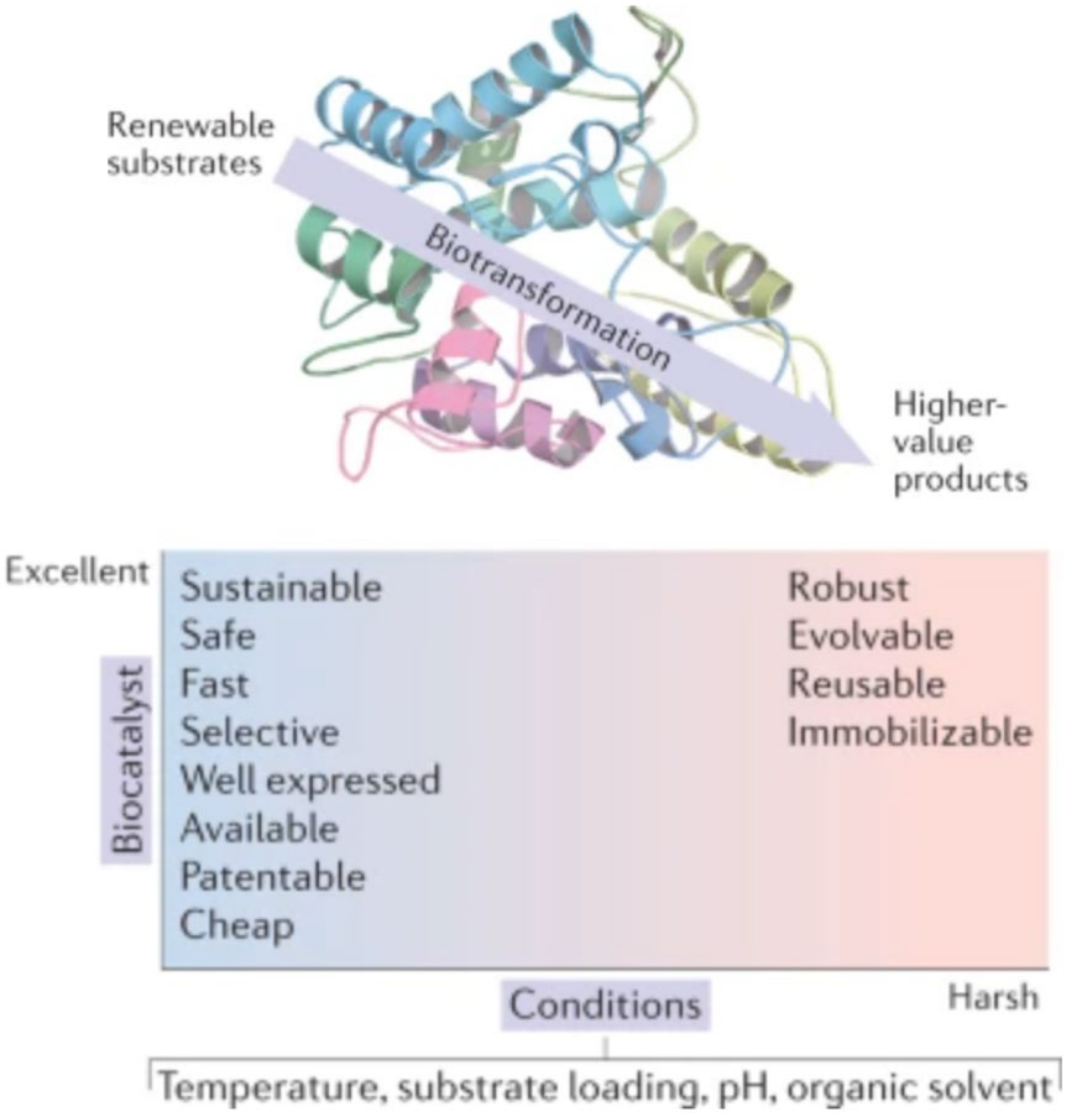

Figure 1.1 Representation of the ideal industrial biocatalysts that can efficiently convert renewable raw materials into higher-value molecules (Top). Their favorable characteristics are indicated in the plot (Bottom). Adopted from ref.[11]

To catalyze organometallic reactions with high product stereoselectivity, metalloproteins and enzymes must be designed and modified to tolerate different unnatural substrates, reagents, and reaction conditions. Utilizing inspiration from synthetic chemistry, novel biocatalysts have been developed including artificial enzymes that can activate C–H bonds, via carbene transferases.[22-26] Researchers can access a variety of different catalysts from the same or similar

protein scaffolds in order to catalyze a variety of organometallic reactions or to produce specific product isomers. In recent years, multiple groups have sought to modify heme proteins (containing Fe porphyrin cofactors) to produce new types of stereoselective and water-soluble biocatalyst, including carbene transferases.[22-26] Generating an effective biocatalyst with abiological reactivity has been a key step in the field. Protein modification can be implemented using various methods to bioengineer the desired traits to achieve enhanced abiological reactivity, discussed further in the next section.

1.2 Approaches to Bioengineering a Novel Biocatalyst

Enzymes with potential synthetic utility should be used as a starting point for engineering biocatalysts with broad substrate scope, high catalytic efficiency, and good site- and stereoselectivity. In addition, enzyme reactions take place under mild conditions and do not require toxic solvents with negative effect on the environment.[16, 25, 27-28] Protein engineering tools such as directed evolution,[29] *de novo* design,[30] and rational design[31] aid to further improve/tune the enzymatic activity for a desired transformation and enhance abiological reactivity. These three methods target specific amino acids within the active site and beyond to help increase desired traits for specific reactivity.

In the directed evolution strategy, a native enzyme or protein undergoes multiple rounds of random mutagenesis to structurally modify the protein scaffold to have the desired activity (**Figure 1.2**). During the process new protein variants are tested via high-throughput screening for desired qualities and once any improved trait is found this process is repeated until the predicted protein variant has optimal enhanced properties. Usual modifications through directed evolution target the secondary coordination sphere (SCS) or the tertiary protein structure and can be implemented to

enhance abiological reactivity. Initial efforts in the field were focused on cytochrome (Cyt) P450s,[32] a superfamily of heme-containing monooxygenases, and it has been shown by Arnold and coworkers that they can be engineered to do carbene transfer reactions with high activity via directed evolution.[29, 33-36] In their initial work they showed that a single mutation on Cyt $P450_{BM3}$, the T268A mutation on the distal face of the heme, increased cyclopropanation yields from 1% to 65% with 98% *d.e.* for the *trans*-cyclopropane product.[36] Furthermore, they were able to switch Cyt $P450_{BM3}$ stereoselectivity, from *trans* to *cis*, through 13 rounds of directed evolution, with mutations that targeted amino acids above the active site, and generated an active catalyst with 59% yield for cyclopropanation with 84% *d.e.* for the *cis*-cyclopropane.[36] From their initial work, directed evolution has now been implemented on various hemoproteins and has been used to expand novel enzyme activity not known in the biological world (as highlighted by the 2018 Nobel Prize for Chemistry for Frances Arnold).[37] Recently, directed evolution has been applied to various enzymes to have biocatalytic reactivity towards carbon-silicon bond formation,[38-39] and carbon-boron bond formation.[40]

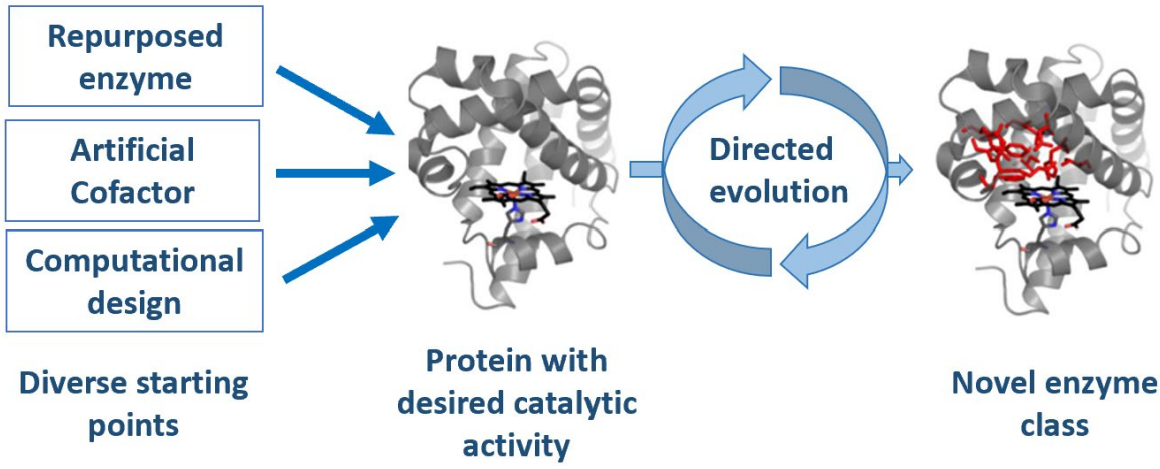

Figure 1.2 Representation of the directed evolution approach. Novel enzymes are developed with specific function through consecutive rounds of mutation and selection, starting from a parent protein with a related function active site. Adopted from ref.[29]

In the *de novo* design approach, efforts focus on generating novel protein scaffolds from scratch utilizing pre-existing scaffolds found naturally in the biosphere, such as α-helical coiled-coils or helical bundles, that implement specific metal binding or active sites within the protein structure.[41] This method allows researchers to investigate and manipulate the primary and secondary coordination sphere readily, since the scaffold design is dictated by the researchers. Utilizing *de novo* design, various groups have been able to mimic natural enzymes such as carbonic anhydrase,[42] peroxidases,[43] and copper nitrite reductase,[30] to name a few. Furthermore, *de novo* design can be also implemented and optimized for abiological reactivity, such as carbene transferase activity. Using C45, a *de novo* designed cytochrome c heme motif with peroxidase activity, Stenner and coworkers showed that a carbene-iron porphyrin intermediate could be generated under typical carbene transfer reactivity conditions with EDA.[44] They found that this carbene intermediate is stable up to 20 minutes without degradation, and most importantly reactive with styrene substrates for cyclopropanation reactivity. Interestingly, C45's flexible scaffold enables the incorporation of bulky substrates such as benzyl-diazoacetate and *tert*-butyl-diazoacetate carbene precursors. Overall, *de novo* design is a valuable strategy for bioengineering and has been an important method in designing novel enzymes with abiological reactivity.

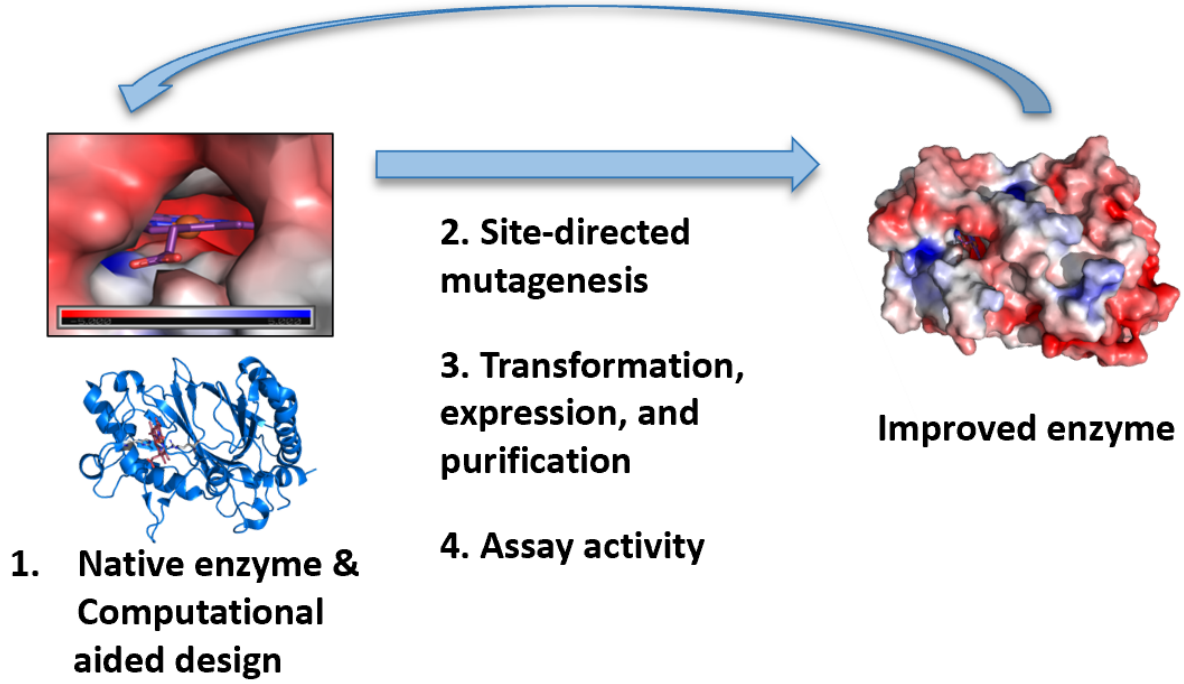

Figure 1.3 Representation of the rational design approach. Improved enzymes are developed with specific function through multiple rounds of site-directed mutagenesis guided by computational research, starting from a parent protein with a related function.

In the rational design strategy, a natural protein or enzyme is modified by site-directed mutagenesis on targeted key primary or secondary amino acids near the active site, this usually guided by computational analysis (see **Figure 1.3**).[45-46] The novel protein scaffold is then assayed for enhanced desired traits, such as improving carbene insertion reactivity, and additional rounds site-directed mutagenesis can be done to generate an optimized novel protein scaffold. As an example, Lu and co-workers designed a Cytochrome c oxidase (CcO) mimetic using Mb by incorporating a Cu_B center near the natural heme site.[45-47] To design this Cu_B center, specific SCS residues in the distal pocket of Mb were mutated to incorporate the CcO His_3Tyr Cu coordination site, generating F33Y-CuB Mb (see **Figure 1.4**).[45-47] They showed that their F33Y-CuB Mb model enhances oxygen reduction reactivity rates via electrochemically, with an overall rate of ($1.98 \cdot 10^7$

$M^{-1\ s-1}$), which is two orders of magnitude greater than that of synthetic models of CcO.[47] Rational design is a powerful tool that allows you to bioengineer new active sites or modify preexisting active sites to promote new reactivity or enhance existing activity.

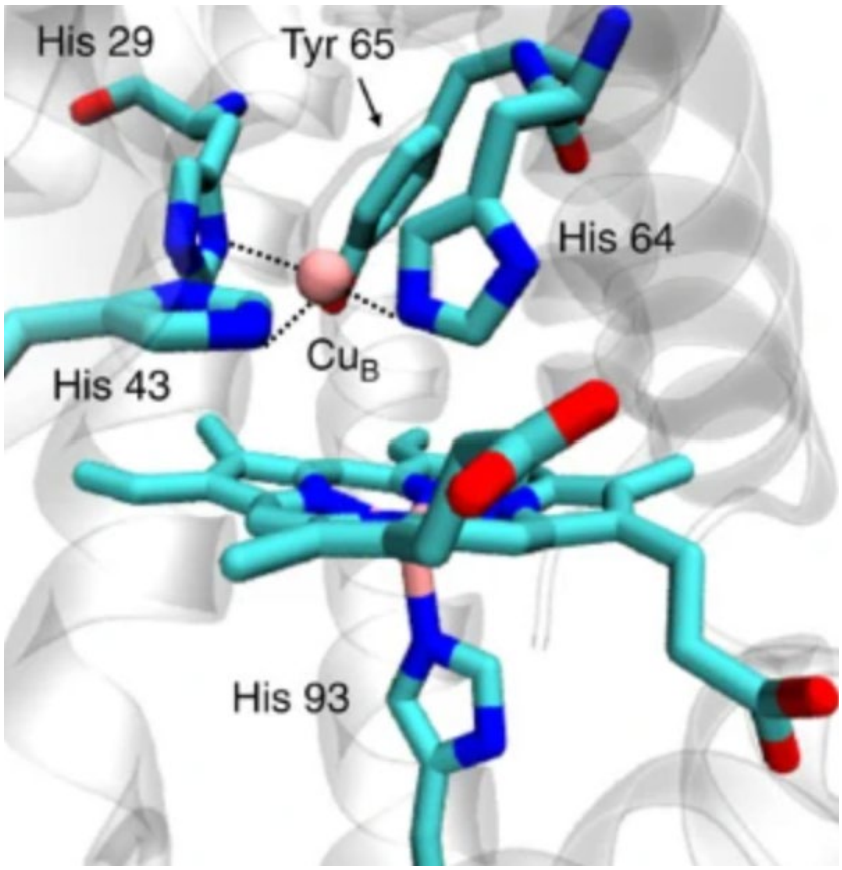

Figure 1.4 Crystal structure of the active site of a Mb-based biosynthetic model of CcO, F33Y-Cu_BMb (pdb: 4FWY). Adopted from ref.[47]

Rational design can also be used to modify the primary coordination sphere in a metalloprotein scaffold by changing the metal center, metal cofactor, or amino acids within the active site.[48-49] This approach sets rational design apart from directed evolution, since it cannot be readily implemented with directed evolution. Incorporating non-native metal complexes into protein scaffolds can help with both the active site chirality and substrate binding sites within

proteins scaffold by positioning substrate towards the metal center and promote product stereoselectivity. To incorporate a new metal complex, initially native metal cofactor removal can be done utilizing Teale's method.[50] The resulting apo-protein can be reconstituted with a new metal cofactor through several different methods.[51-52] Previous work from our group, Wolf *et al.,* showed that free Ru-mesoporphyrin IX (RuMpIX) is also an active catalyst that exhibits high activity for both the carbene transfer into N-H bonds of aromatic amines and cyclopropanation of styrene derivatives compared to free heme.[53] Upon substitution of the native heme in myoglobin with the RuMpIX cofactor, the reconstituted Mb protein and Mb variants gave astonishingly low to moderate yields for carbene transfer. The decrease in productive catalysis was shown to be due to high intrinsic reactivity of the Ru-carbene intermediate, which can undergo internal carbene transfer within the protein matrix and even within the RuMpIX cofactor itself. Notably, mutation of the H64 residue on the distal face of the cofactor, creating a larger and more hydrophobic cavity, did improve activity. Similarly, Hartwig and coworkers, using protoporphyrin IX (PpIX) bound to a series of transition metals, reconstituted them into Mb for the investigation of enhanced biocatalytic carbene transfer reactivity.[54] In this influential work, they showed that the incorporation of Ir(Me)(PpIX) displays the highest activity for carbene transfer in their metal activity assay, compared to native heme Mb.[54] Overall, rational design has been shown to be a promising method for heme protein engineering and it is the main strategy used herein with YfeX.

1.3 Carbene Transfer Reactivity with Biocatalysts

Carbene transfer reactions are an important route in organic synthesis since they generate hard to synthesize carbon-carbon or carbon-heteroatom bonds, and, importantly, these methods can be used in late-stage functionalization of larger molecules.[6, 29, 33-36, 55] Synthetic chemists have

developed powerful methods for direct C=C and C–H functionalization based on transition metal–catalyzed carbenoid and nitrenoid transfers, reactions that are widely used to synthesize natural product intermediates and pharmaceuticals. Different methods for carbene transfer reactions have previously been developed utilizing transition-metal complexes of Rh(II), Ir(III), Au(I) and Pd(II) that catalyze the decomposition of diazo reagents to form an electrophilic metal−carbene unit, which is subsequently attacked by a nucleophilic reagent such as an olefin (for cyclopropanation) or an amine (for N−H insertion), and others.[56-58] They are of particular interest in the quickly developing field of organometallic biocatalysts. Utilizing nature as an inspiration, our laboratory and others have developed carbene transfer biocatalysts based on porphyrin-containing enzymes.[53, 59-67]

The development of biocatalysts with carbene transfer reactivity has been inspired by heme-dependent Cyt P450 monooxygenase enzymes, which are metalloporphyrin catalysts that play a key role in fundamental biological chemical transformations.[68-69] Cyt P450s contain an Fe-porphyrin cofactor, which can utilize O_2 or H_2O_2 to generate a highly active $FeIV{=}O^{\cdot+}$ heme intermediate (known as Compound I). This high-valent metal-oxo intermediate selectively and efficiently activates C-H bonds of aliphatic substrates to generate alcohols.[70-71] Various model metalloporphyrin complexes have since been used for their O-atom transfer capability in C-H bond activation and epoxidation reactions.[68-69, 72] An influential paper by Coelho and coworkers demonstrated that Cyt $P450_{BM3}$ and other heme-containing proteins can catalyze the cyclopropanation of styrene using ethyl diazoacetate (EDA) as a carbene precursor (further discussion in section 1.2).[36] Their work paved the way to a novel approach in the field of biocatalysis.

In addition, metalloporphyrins are also pertinent and attractive catalysts for group-transfer transformations such as carbene or nitrene transfer to generate C-C or C-N bonds, respectively. **Figure 1.5.** shows the general mechanism of carbene transfer reactions, starting from a diazo compound, here EDA, which reacts with the heme, generating a metal-carbenoid intermediate while releasing dinitrogen, shown at the bottom of the scheme. In iron-porphyrin catalyzed cyclopropanation reactions, the mechanism of carbene transfer is concerted with the rate-determining step being the activation of a diazo substrate to generate the metallo-carbenoid intermediate.[58] Next, substrate binds within the heme pocket, in this case styrene, and reacts with the carbenoid intermediate generating a cyclopropane ethyl acetate product and regenerating the heme in its active state. Further engineering strategies can then be used to facilitate carbene insertion reactions, optimize selectivity, and broaden the substrate scope of the reactions to generate high value products.

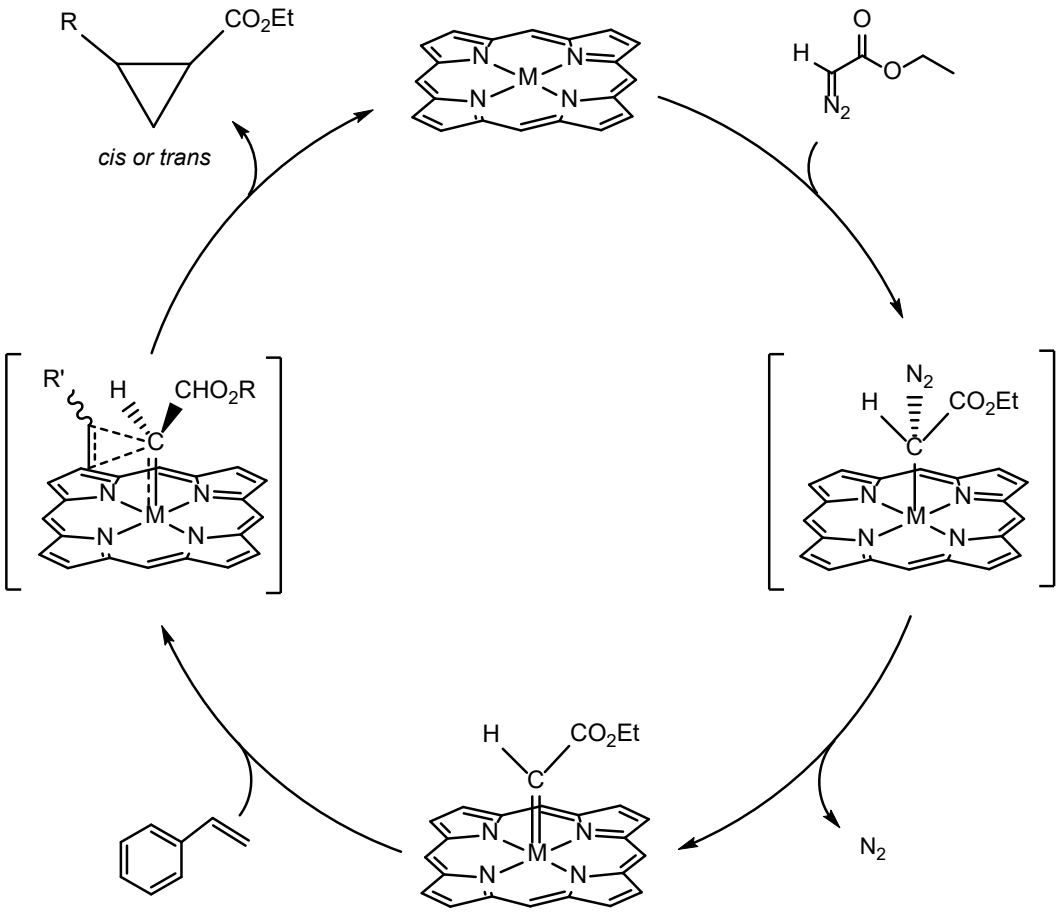

Figure 1.5 Scheme of cyclopropanation mechanism of heme enzymes via carbene insertion.[58]

1.4 YfeX - a Biocatalysts for Carbene Transfer

As discussed above, besides Cyt P450s, another heme protein that has extensively been used for biocatalyst development is myoglobin (Mb).[53, 59, 62-63] In this case, however, the choice of utilizing Mb was guided by the protein stability and ease of access to this protein heme site. Unlike Cyt P450s that have a proper active site, Mb does not and can potentially limit its biocatalyst development. Other heme-His type proteins might provide a much better platform for biocatalyst development. Recently, our focus has shifted to the use of YfeX, a novel heme protein found to have native peroxidase like activity in *E. Coli* (**Figure 1.6**).[73-74] YfeX contains a buried heme in a

large active site that is connected to the protein surface via a tunnel, which, in the native peroxidase reaction of YfeX, is proposed to guide hydrogen peroxide to the active site. The heme active site is ligated by a proximal histidine and an arginine flanks the distal side (**Figure 1.6**). Overall, YfeX is has an ideal protein scaffold and active site that allows for site directed mutagenesis studies for enhance carbene transferase activity.

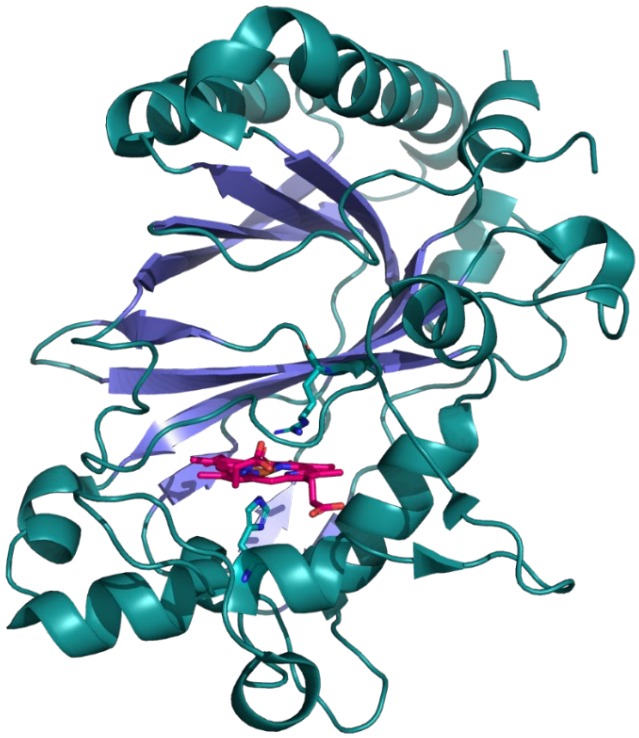

Figure 1.6 PyMol representation of the tertiary structure of YfeX. The cartoon shows α-helix (dark green), β-sheets (blue), and the heme active site (red) (PDB code: 2IIZ).

YfeX, a typical dye peroxidase type heme-containing peroxidase (DyP), is found in the extracellular matrix of *E. coli*. DyPs are a superfamily of peroxidases that contain sequence similarities with one another and are usually comprised of two-domains, an α and β ferredoxin-like fold motif, that are distinct from other peroxidase superfamilies α-helical fold. The first DyP,

identified relatively recently in the fungus *Geotrichum candidum*, was characterized with respect to its ability to catalyze the degradation of anthraquinone-based industrial dyes, hence termed decolorization peroxidase.[75] These DyP enzymes are now known to be present in fungi and bacterial organisms, but do not appear to occur in plants or animals.[76-77] They are involved in a variety of physiological processes, although in many cases their overall roles remain unknown.[76] Previously, initial work done by Weissenborn and coworkers showed that WT YfeX can catalyze carbonyl olefination reactions with turnover numbers (TON) up to 16 under optimized conditions.[78] DyPs have a considerable biotechnological potential, and as shown here, YfeX has great potential as a carbene transferase biocatalyst.

1.5 Scope of Thesis

In this work, we investigated the catalytic abilities of YfeX as a carbene transferase, using olefins, amines, and silanes as substrates. Chapter 2 focuses on the investigation of substrate scope, co-solvents, and reaction kinetics. Moreover, we modified the active site by incorporating Ru-mesoporphyrin IX (RuMpIX) and Co-protoporphyrin IX (CoPpIX) into apo YfeX to determine whether catalytic activity can be further improved using unnatural cofactors. This work establishes YfeX as a superior platform for biocatalyst development compared to Mb, with an intrinsically much higher reactivity, especially for N-H and Si-H insertion reactions. Furthermore, utilizing both molecular dynamics (MD) simulations and combined Quantum Mechanics/Molecular Mechanics (QM/MM) calculations, we analyzed the atomistic and electronic structure factors that contribute to the stability of the metal-carbenoid complex and then explored the reaction mechanism of Si—H insertion by YfeX. The study offers general insight into the role of the SCS in YfeX for carbene transfer reactions, and in this way, identifies targets for future mutagenesis

studies to further improve catalysis with YfeX, especially selectivity, which is further discussed in chapter 3. This chapter has been reproduced in part from a manuscript published in Chem. Eur. J. (**Victor Sosa Alfaro**, Sodiq Waheed, Hannah Palomino, Anja Knorrscheidt, Martin Weissenborn, Christo Christov, Nicolai Lehnert., **2022**.)[79]

The second aim focuses on generating YfeX mutants to further enhance carbene transfer reactivity. YfeX styrene cyclopropanation and Si-H insertion reactions have moderate product yields and, in the case of the former, a low diastereomer selectivity. The active site of YfeX has an overall hydrophilic pocket due to three prominent amino acids, D143, R232, and S234. The substrate, styrene, is a non-polar substrate with low water solubility, requiring hydrophobic interactions. One of the important steps in reactivity is substrate binding in the active site. Low cyclopropanation and Si-H insertion yields could be due to lack of substrate binding inside the active site. If the active site would become more hydrophobic, this may help to improve substate binding and retention. The three key amino acids within the active site, D143, R232, and/or S234, play an important role in keeping the active site hydrophilic. Therefore, the approach is to mutate each of these three amino acids to an alanine, a small hydrophobic amino acid, generating three distinct mutants, D143A, R232A, and S234A, and then study their reactivity. Lastly, amino acid I230, found in the entrance channel, is also mutated to further open the active site channel, and help bind substrate into the active site. These mutations are investigated for their potential to increase reactivity.

The final aim of this thesis focuses on the storage and distribution of electrons within the *G. lovleyi* Cytochrome *c* nitrite reductases (C*c*NIR or NrfA) pentaheme scaffold.[80] NrfA has an important role in reversing nitrification and conserving the usable nitrogen in the environment, via **the** dissimilatory nitrate reduction to ammonium (DNRA) pathway.[81] Dissimilatory nitrate

reduction is a two-step process,[82-83] where nitrate is first reduced to nitrite by nitrate reductases then followed by the reduction of nitrite to ammonium by NrfA in one multi-step reaction. NrfA's proposed catalytic mechanism for nitrite reduction, mostly based on crystallographic and computational analysis,[84-87] is still under investigation and this work helps further understand the complicated mechanism of electron transport, storage, and distribution in NrfA. First, I established a chemical method to sequentially add electrons to the fully oxidized protein, one equivalent at a time, and then followed the reduction of the hemes using UV-Vis and EPR spectroscopy. Based on detailed EPR simulations, we identified the signals of all five hemes in the EPR spectra, and we demonstrated that the first electron goes to Heme 5, providing strong evidence that Hemes 4 and 5 serve as an electron storage unit. Based on its location in the electron transfer chain, Heme 3 plays a central role (as a branching point) in distributing electrons either to the active site Heme 1, or Hemes 4 and 5. In addition, our simulations show that Hemes 1-3-4 are exchange coupled, which explains the unusual EPR spectra of fully oxidized enzyme. In this way, we were able to completely assign the EPR spectra of oxidized NrfA for the first time. These results are corroborated using cyanide-bound enzyme, where Heme 1 becomes low-spin, and a Heme 3 His-to-Met mutant, which dramatically changes the redox potential of this heme. Finally, we measured the redox potentials of all five hemes, and we assigned them to individual hemes based on the EPR titration results. Comparison of these results to those obtained for *S. oneidensis* NrfA is further made in this thesis. This chapter has been reproduced in part from a manuscript published in *Biochemistry* (**Victor Sosa Alfaro**, Julius Campeciño, Matthew Tracy, Sean J. Elliott, Eric L. Hegg, Nicolai Lehnert. *Biochemistry* **2021**, *60*, 1853-1867).[88]

Chapter 2 YfeX: A Biocatalytic Carbene Transferase

In this chapter, the basic catalytic abilities of YfeX as a carbene transferase, using olefins, primary and secondary aromatic and aliphatic amines, and silanes as substrates are investigated via reactivity and computational studies. The following work was done in collaboration with Professor Martin Weissenborn and student Anja Knorrscheidt from Martin-Luther-University Halle-Wittenberg, who provided protein plasmids, and with Professor Christo Z. Christov and student Sodiq O. Waheed from Michigan Technological University, who conducted the computational studies. Undergraduate student Hannah Palomino also contributed with reactivity studies presented herein. The following manuscript was published for this chapter: **Victor Sosa Alfaro**, Sodiq Waheed, Hannah Palomino, Anja Knorrscheidt, Martin Weissenborn, Christo Christov, Nicolai Lehnert. "YfeX – A New Platform for Carbene Transferase Development with High Intrinsic Reactivity", *Chem. Eur. J.* **2022,** e202201474.[79]

2.1 Introduction

Carbene transfer biocatalysis has evolved from basic scientific research to an area with vast potential for the development of new industrial processes in the pharmaceutical industry. Despite the growing significance of "carbene transferases", it is surprising that their development has been limited to a narrow range of proteins; mostly Cyt. P450s and myoglobin (Mb). However, there is a broad scope of protein scaffolds that have the potential for enhancing carbene transferase activity. Initial work by some of our collaborators (Weissenborn and coworkers) showed that WT YfeX

can catalyze carbonyl olefination reactions with turnover numbers TON up to 16 under optimized conditions.[78] YfeX contains a buried heme in a large active site that contains positively charged amino acids in the second coordination sphere (SCS), including a key distal arginine residue (**Figure 2.1**). The active site is connected to the protein surface via a tunnel, which, in the native peroxidase reaction of YfeX, is proposed to guide hydrogen peroxide to the active site.[74] This tunnel is important, as the substrates for abiological carbene transfer catalysis with YfeX also must enter the active site via this tunnel. These distinct features of Mb versus YfeX contribute to the different reactivity profiles of these proteins, as discussed in detail in this chapter.

Here, we focused on the investigation of substrate scope, reaction kinetics, and the pH dependence of the observed carbene transfer reactivity utilizing YfeX. Moreover, we modified the active site by incorporating Ru-mesoporphyrin IX (RuMpIX) and Co-protoporphyrin IX (CoPpIX) into apo YfeX to determine whether catalytic activity can be further improved by use of unnatural cofactors. In addition, the protein shows high stability against organic solvents, thereby enabling the use of organic co-solvents whenever necessary to solubilize substrates in order to improve turnover. This work establishes WT YfeX as an excellent platform for biocatalyst development compared to WT Mb, with a high intrinsic reactivity, especially for N-H and Si-H insertion reactions. Furthermore, utilizing both molecular dynamics (MD) simulations and combined Quantum Mechanics/Molecular Mechanics (QM/MM) calculations, we analyzed the atomistic and electronic structure factors that contribute to the stability of the metal-carbenoid complex and then explored the reaction mechanism of Si—H insertion by YfeX. Finally, the rather large active site of YfeX promises exciting applications of this protein in the synthesis of pharmaceuticals, allowing for the processing of rather large substrates. YfeX is an exciting new target for the development of improved carbene transferases. This chapter has been reproduced in part from a

manuscript published in *Chem. Eur. J.* (**Victor Sosa Alfaro**, Sodiq Waheed, Hannah Palomino, Anja Knorrscheidt, Martin Weissenborn, Christo Christov, Nicolai Lehnert., **2022**, e202201474.)[79]

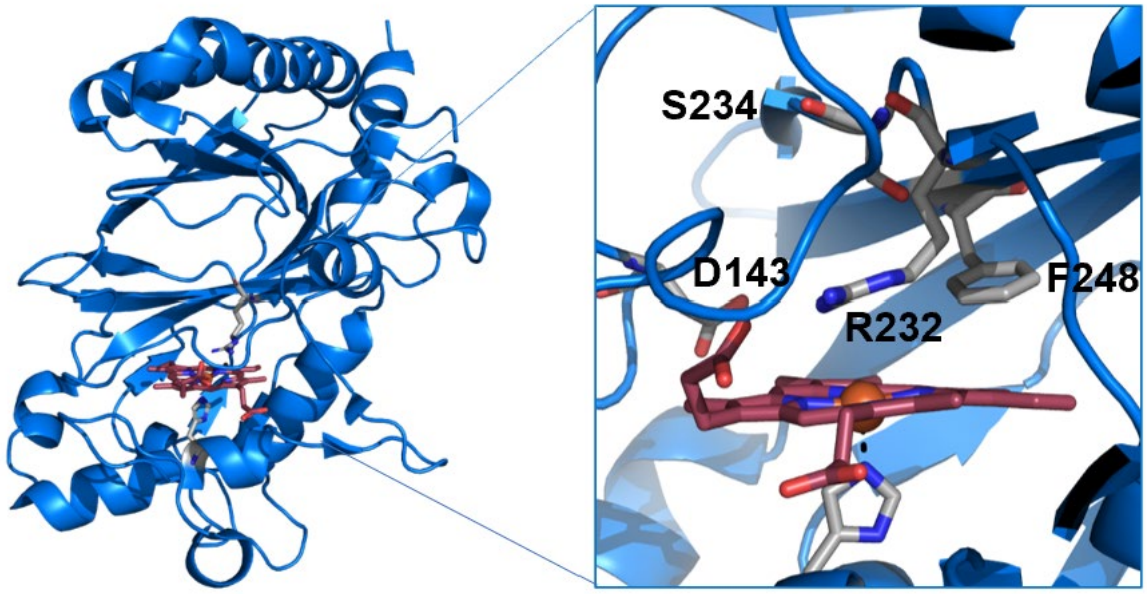

Figure 2.1 PyMol representation of the crystal structure of YfeX (left), and of the active site with important SCS amino acids highlighted (PDB code: 2IIZ).

2.2 Wild-type YfeX Carbene Insertion Reactivity

Initial work focused on the carbene transfer reactivity of wild-type (WT) YfeX using two different carbene transfer reactions: N−H insertion and cyclopropanation. As shown in **Table 1**, the N−H insertion activity of YfeX with aniline as the substrate is higher (72% yield) compared to [Fe^{II}PpIX] (27% yield) and sperm whale (SW) WT FeMb (21% yield).[89] We achieved the highest Turnover Number (TON) of 6274 for this reaction using 0.001% catalyst loading over 20 hours. Additionally, at higher YfeX loading aniline can produce the mono- (usual product) and di-insertion product (diethyl 2,2-(phenylimino) diacetate) with EDA (see header of **Table 2.1**). At 0.1% catalyst loading, 30% of the disubstitution product is obtained, but as the catalyst loading is

reduced (or, in other words, the excess of aniline is increased), the disubstitution reaction is suppressed. In fact, at 0.01% catalyst loading, the di-insertion product only contributes 1% to the total yield. This result directly shows that after the first N−H insertion, the monosubstituted product is released from the YfeX active site, and then reacts again (enters the active site again) to generate the disubstituted product. If the monosubstituted product would remain in the YfeX active site and react again to yield the disubstituted product, the yield of the disubstituted product would not decrease substantially upon an increase in substrate concentration (= decrease in catalyst loading). On the other hand, if the monosubstituted product is released from the active site, then a large excess of aniline would statistically decrease the likelihood of monosubstituted product to become disubstituted, and this is what we observe experimentally. In this way, the ratio of mono- to di-insertion product can be directly controlled in YfeX catalysis.

Table 2.1 Results for the N-H insertion reaction of aniline with WT YfeX.

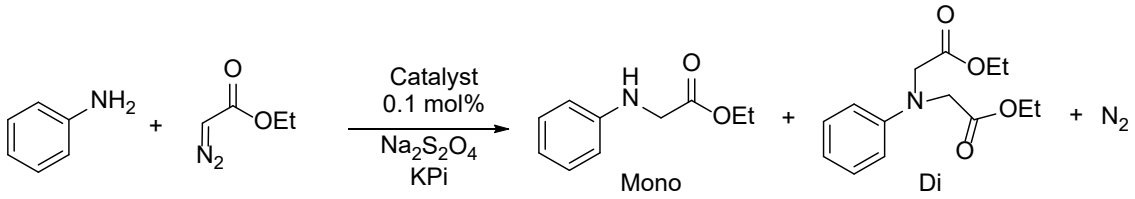

Catalyst	Total Yield [a] (%)	TON	Mono:Di
[Fe^{II}PpIX]	27	271 ± 38	
WT Mb [b]	21	210	
YfeX (0.1 mol%)	72	724 ± 32	70:30
YfeX (0.01 mol%)	27	2658± 274	99:1
YfeX (0.001 mol%)	3	3026± 573	100:0
YfeX (0.001 mol%)[c]	6	6274± 226	100:0

[a] Reaction conditions: 20-0.2 μM YfeX (0.1-0.001 mol%), 20 mM aniline, 40 mM EDA, 10 mM dithionite, 1 hour reaction time in 50 mM phosphate buffer (pH 7.4). Yields are based on GC/MS analysis. [*b*] Based on studies by Sreenilayam et al.[89] The yield was determined after 16 hours reaction time. [*c*] The yield was determined after 20 hours reaction time.

Recently, Fasan and coworkers have shown that WT Mb and variants can also generate the di-insertion product, but only with benzylamine as the substrate (at 1:13 mono:di product ratio), and they further engineered Mb to have higher reactivity and, by lowering the catalyst loading, the mono-insertion product can again be produced as the main product.[90] It was further shown that when more sterically demanding amino acids where introduced into the Mb active site, for example via the double mutant Mb(H64G, V68A), the amount of disubstituted benzylamine product was not affected. The disubstitution in this case could only be suppressed by reducing catalyst loading.[90] Similarly, our results show that YfeX's relative larger active site can also promote the disubstitution of aniline, with increased mono-substitution when catalyst loading is reduced. Here, the mono- to disubstitution ratio can be controlled by modifying the substrate loading. At low EDA

concentration (1:4 EDA:aniline) 99% mono-substitution is observed. Conversely, at high EDA concentration (4:1 EDA:aniline), 51% disubstituted product is obtained. Furthermore, time course kinetic measurements were conducted for the N−H insertion reaction of aniline by monitoring the yield of monosubstituted product via GC/MS. It was found that YfeX has a $k_{obs} = 0.210\ min^{-1}$, as shown in **Figure 2.2**.

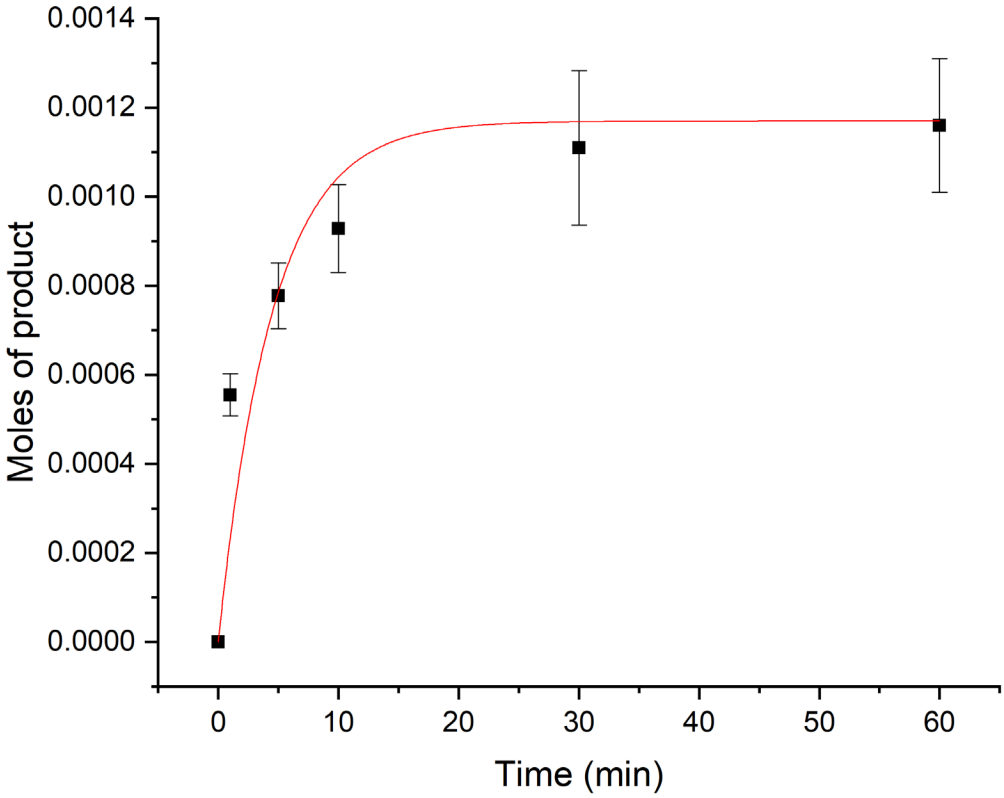

Figure 2.2 Time course of the N−H insertion reaction of aniline catalyzed by YfeX. The catalyst was prepared at 20 μM concentration and reduced with 500 equivalents of $Na_2S_2O_4$ before addition of 1000 equivalents of aniline and 2000 equivalents of EDA to a final volume of 500 μL. The organic products were extracted with 3 mL of ethyl acetate after the following time points: 2, 5, 10, 30, and 60 minutes. Finally, the product was quantified by GC/MS. Exponential fit of the data gives a kobs = $0.210\ min^{-1}$.

In contrast to the outstanding N−H insertion activity of YfeX, the cyclopropanation reaction with this protein generates a 27% yield with a TON of 268, which is comparable to that of WT Mb (36% yield, with a TON of 180).[24] Further analysis of the styrene cyclopropane product shows a *cis* to *trans* ratio of the product of 11 to 89 (see **Table 2.2**), again comparable to WT Mb (9:91) and [Fe^{II}PpIX] (13:87), indicating that the protein matrix of YfeX is not interfering with the natural *cis:trans* selectivity of iron-porphyrins. In addition, YfeX forms the trans product with 87% selectivity for the (R,R) enantiomer, which is different from WT Mb, which produces 47% (R,R) enantiomer.[24] This difference in enantioselectivity is surprising, and indicates that either the orientation of the carbene ligand in the YfeX active site is more restricted, or that the styrene substrate predominantly enters the active site of YfeX in a predefined orientation. The fact that the N−H insertion reactivity of YfeX is much more robust than its cyclopropanation reactivity further indicates that the relatively low yield of cyclopropanes is not related to problems with the generation of the carbene intermediate or its reactivity, but rather with substrate (styrene) access to the YfeX active site via the enzyme's substrate channel.

Table 2.2 Results for the cyclopropanation reaction of styrene with WT YfeX.

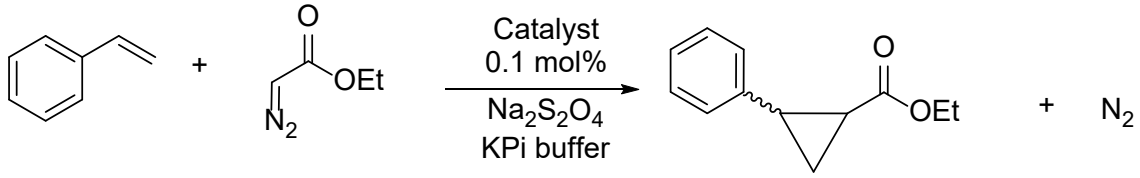

Catalyst	Total Yield [a] (%)	TON	Cis: Trans [b]	(R,R) Trans [b]
[Fe^{II}PpIX]	16	158 ± 64	13:87	
WT Mb	36[c]	180 ± 28	7:93	47%
YfeX	27	268 ± 72	11:89	87%

YfeX [d]	47	474 ± 15	9:91	87%
YfeX [e]	59	593 ± 81	9:91	88%

[*a*] Reaction conditions: 20 μM YfeX (0.1 mol%), 20 mM styrene, 40 mM EDA, 10 mM dithionite, 1 hour reaction time in 50mM phosphate buffer (pH 7.4). [*b*] Values determined by GC/MS or supercritical fluid chromatography. [*c*] Based on studies by Bajaj et al.[24] Reaction conditions: : 20 μM Mb (0.1 mol%), 10 mM styrene, 20 mM EDA, 10 mM dithionite, 16 hours reaction time. [*d*] Reaction performed in 30% methanol. [*e*] Reaction performed in 30% DMSO.

The stability of YfeX was further investigated under catalytic conditions by UV−vis spectroscopy. Our results show that WT YfeX is as stable as WT Mb:[53] after addition of EDA to a reduced sample of YfeX, the Soret band of the heme shifts to 430 nm (similar to what is seen with WT Mb and Rma TDE),[53, 91] and this carbenoid species is stable for 60+ minutes (Figure S1). The small decrease of the Soret band at 430 nm after 20 minutes is indicative of a small amount of the YfeX decomposing (**Figure 2.3**). One of the important steps in the cyclopropanation reaction is substrate access to the active site. Styrene, a non-polar substrate with low water solubility, requires hydrophobic interactions to go into and stably bind in the active site of a protein. However, the active site of YfeX, shown in **Figure 2.1**, is overall hydrophilic due to three prominent amino acids, D143, S234, and R232 (discussed below). The low solubility of styrene in buffer combined with the high polarity of the substrate channel and active site of YfeX could be responsible for the low cyclopropanation yields. Kinetic measurements were conducted by monitoring the styrene cyclopropanation yields via GC/MS over time. It was found that YfeX has a $k_{obs} = 0.096\ min^{-1}$ for cyclopropanation (see **Figure 2.4**), which is distinctively smaller than the rate constant obtained for the N−H insertion reaction, in agreement with the higher yield of the latter reaction in 1 hour.

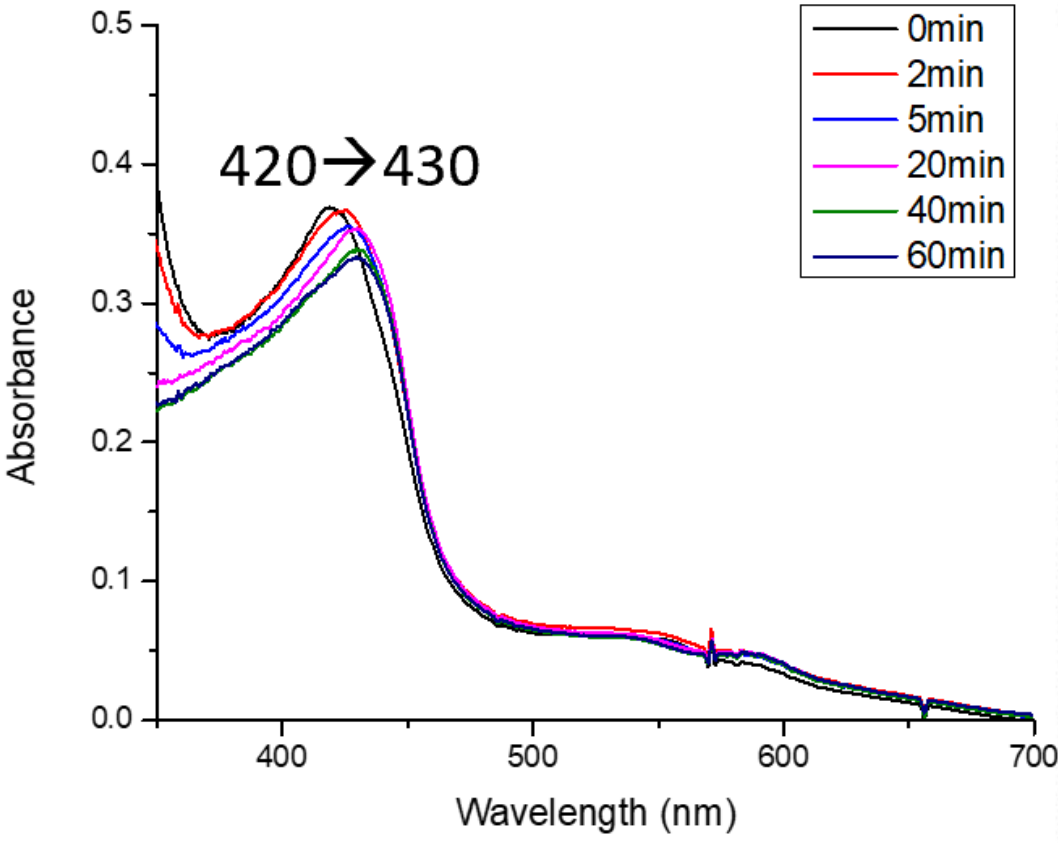

Figure 2.3 Stability of the wild type (WT) YfeX [10 μM] carbene intermediate under catalytic conditions after the addition of dithionite [20 mM] and EDA [10 mM], followed by UV-vis spectroscopy in [100 mM] potassium phosphate buffer.

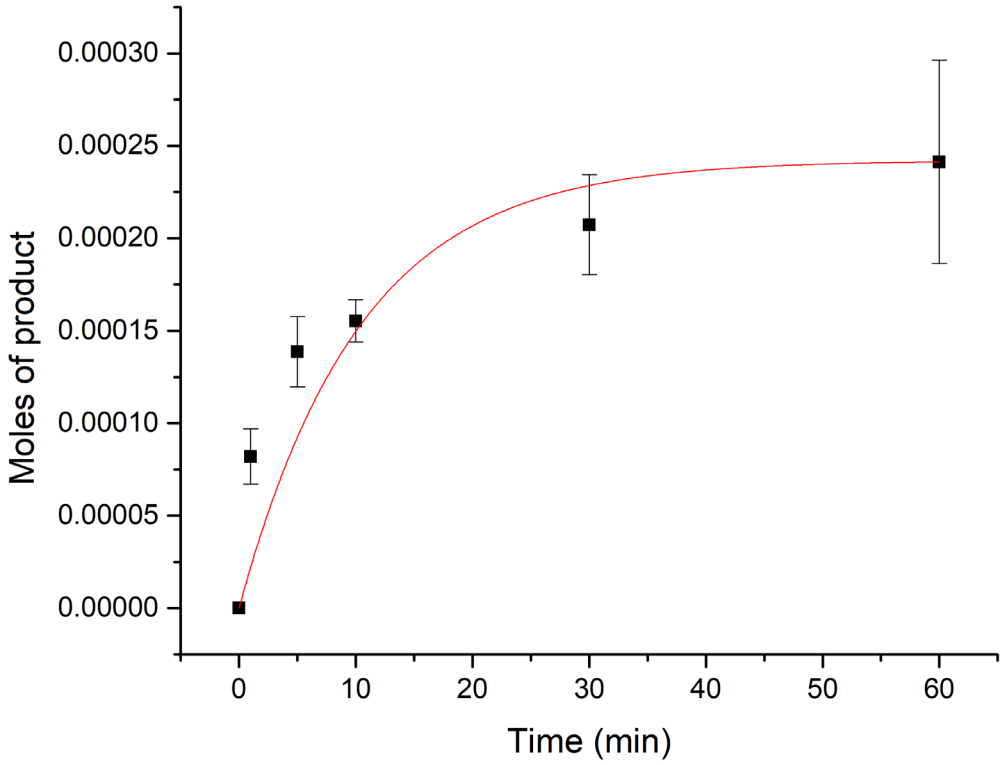

Figure 2.4 Time course of the cyclopropanation reaction of styrene catalyzed by YfeX. The catalyst was prepared at 20 μM concentration and reduced with 500 equivalents of $Na_2S_2O_4$ before addition of 1000 equivalents of styrene and 2000 equivalents of EDA at final volume of 500 μL. The organic products were extracted with 3 mL of ethyl acetate after the following time points: 2, 5, 10, 30, and 60 minutes. Finally, the product was quantified by GC/MS. Exponential fit of the data gives a kobs = 0.096 min^{-1}.

2.3 Substrate Scope of the Carbene Transfer Reactions

Since YfeX is an outstanding catalyst for the N−H insertion reaction, we further investigated its substrate scope. The N−H insertion reaction of secondary amines was investigated using *N*-methyl aniline as a substrate, giving a 62% yield with a TON of 620 (see **Table 3**). This result further confirms that di-insertion of aniline with EDA is due to the inherent reactivity of WT YfeX towards primary and secondary N−H bonds. Further substrate scope studies for the N−H

insertion reaction used anilines with electron-withdrawing (4-bromoaniline, 4-trifluoromethylaniline) and electron-donating (4-methylthioaniline, 4-methoxyl-6-methylaniline, *p*-toluidine) substituents. The electron-rich substrates give 52 - 57% yield, indicating a preference for electron-rich substrates, whereas the electron-poor substrates give 40 - 51% yield. Here, the electron-withdrawing −Br and $-CF_3$ groups are expected to decrease the nucleophilicity of the aniline NH_2 group and thus exhibit less reactivity with the electrophilic Fe-carbene intermediate. Furthermore, the steric effects within the active site pocket were analyzed utilizing *ortho-, meta-* and *para*-toluidine as the substrates. As the methyl group moves closer to the reactive amine group, from *-para* to *-meta* to *-ortho* substitution, the N−H insertion yields decrease accordingly, from 57% to 37% to 23% (see **Table 2.3**).

Table 2.3 Results for the N−H insertion reaction of aniline derivatives with WT YfeX.

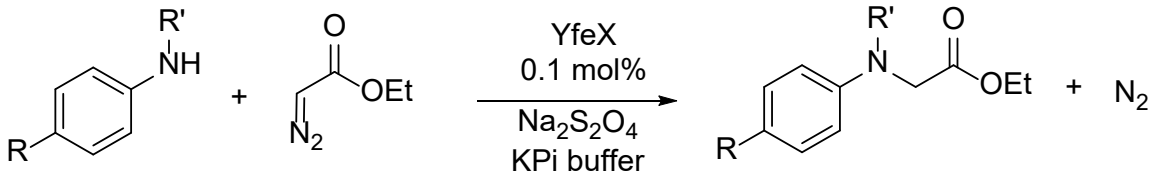

R= -H, -Br,-CF_3, -S-Me, -O-Me
R'= -H, -Me

Substrate	**Total Yield [a] (%)**	**TON**	**Mono: Di**
N-methyl aniline	62	623 ± 36	100:0
4-bromoaniline	40	404 ± 62	100:0
4-trifluormethylaniline	51	510 ± 25	100:0
4-methylthiolaniline	57	568 ± 48	100:0
4-methoxy-6-methyl aniline	52	515 ± 49	43:57

p-toluidine	57	571 ± 19	49:50
o-toluidine	28	279 ± 30	64:36
m-toluidine	37	374 ± 19	43:57
benzylamine[b]	56	558 ± 28	0:100
4-nitroaniline[b]	25	248 ± 23	100:0

[*a*] Reaction conditions: 20 μM YfeX (0.1 mol%), 20 mM aniline derivative, 40 mM EDA, 10 mM dithionite, 1 hour reaction time in 50 mM phosphate buffer (pH 7.4). Yields are based on GC/MS analysis. [*b*] Reactions were run in 30% methanol.

The substrate scope for the cyclopropanation reaction was also investigated using WT YfeX. Various para-substituted styrene derivatives were examined for cyclopropanation activity, with the functional groups analogous to the aniline derivatives discussed above (see **Table 2.4**). 4-methylstyrene shows the highest yield with 48% compared to styrene and other derivatives. Vinylanisole, 4-chlorostyrene, and 4-trifluorormethylstyrene show a moderate conversion to the cyclopropane products with similar yields (30%, 23% and 29%, respectively). Lower yields are expected for the substrates with the electron-withdrawing -Cl and -CF_3 groups, but not for vinylanisole with an electron-donating -OMe group. In the latter case, the lower yield might therefore be due to steric reasons. All the substrates exhibit similar diastereoselectivity, yielding 80 - 90% of the *trans* isomer.

Table 2.4 Results for the cyclopropanation reaction of styrene derivatives with WT YfeX.

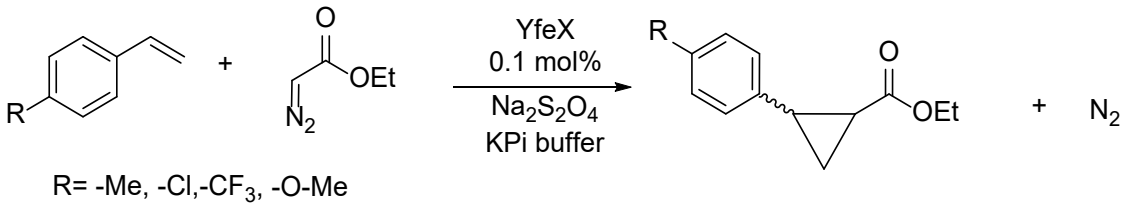

Substrate	Total Yield [a] (%)	TON	Cis:Trans
4-methylstyrene	48	484 ± 30	23:77
vinylanisole	30	297 ± 84	14:86
4-chlorostyrene	23	230 ± 33	13:87
4-trifluoromethylstyrene	29	293 ± 30	10:90

[*a*] Reaction conditions: 20 μM YfeX (0.1 mol%), 20 mM styrene derivative, 40 mM EDA, 10 mM dithionite, 1 hour reaction time in 50 mM phosphate buffer (pH 7.4). Yields are based on GC/MS analysis.

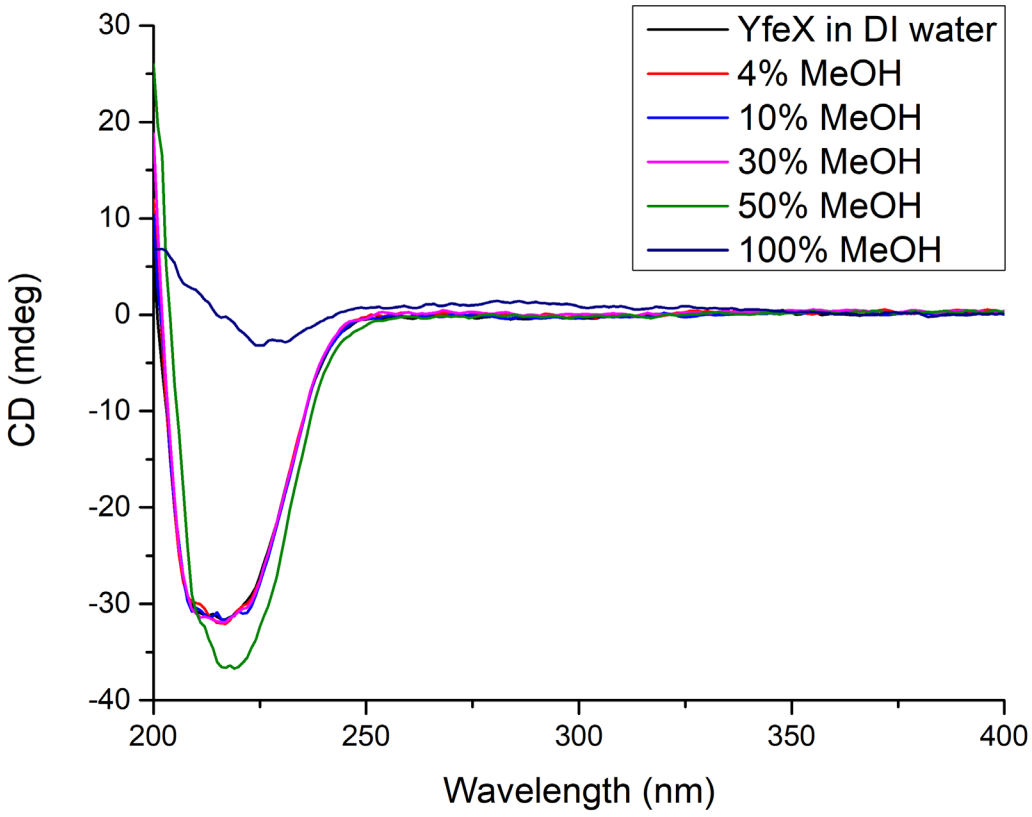

Figure 2.5 Circular dichroism spectra of WT YfeX [30μM] at various buffer/methanol mixtures. The data show that at 50% methanol concentration structural changes to the protein occur.

As discussed above, the N-H insertion with YfeX is greatly favored over the cyclopropanation reaction, which could be caused by the low solubility of styrene in the reaction medium. We sought to probe this hypothesis by improving substrate solubility, which can be accomplished by increasing the amount of the methanol co-solvent in the reaction mixtures (see **Table 5**). As the methanol concentration is increased to 10%, the yields for both aniline and styrene reactions remain unchanged. At a 30% methanol co-solvent concentration, the yield for the aniline-based product remains similar, but, importantly, *a doubling of the yield for the styrene substrate is observed* (47% yield). At 50% methanol co-solvent concentration, a decrease in product yield is observed in both reactions. Further characterization via circular dichroism spectroscopy (CD) shows that at 50% methanol co-solvent concentration, YfeX begins to unfold or aggregate, which is likely the reason for the decreased yields under these conditions (see **Figure 2.5**). We further show that 30% DMSO as a co-solvent further improves the cyclopropanation yield, with an increase to 59% (see **Tables 2.2** and **2.5**). Furthermore, two additional substrates with very low aqueous solubility were screened, 4-nitroaniline (25% yield) and benzylamine (double insertion, 56% yield) using 30% MeOH co-solvent (see **Table 2.3**). *Overall, our result show that as the concentration of the methanol co-solvent increases, the solubility of styrene and other substrates increases accordingly, leading to greatly enhanced product yields*. The optimal methanol concentration is ~30%.

Table 2.5 Carbene transfer reactivity of WT YfeX in the presence of methanol and DMSO co-solvent.

[% Methanol]	Aniline (% yield)	Styrene (% yield)	Cis:Trans	Trans (R,R)
0	72 ± 32	27 ± 7.2	11:89	87%
10	50.9 ± 4.3	-----		
30	51.0 ± 3.8	47.4 ± 1.5	9:91	87%

50	40.2 ± 2.6	39.2 ± 2.9

[% DMSO]	Aniline (% yield)	Styrene (% yield)	Cis:Trans	Trans (R,R)
30	71± 51	59 ± 8.1	9:91	88%

Furthermore, utilizing dimethylphenylsilane as a substrate, we explored whether YfeX can catalyze the carbene insertion into silicon-hydrogen (Si−H) bonds. This reaction has so far only been observed in few examples. This includes WT Mb (turnover number (TON) = 175 after 12 hours using 0.2 mol% catalyst loading), horseradish peroxidase (HRP; TON = 5 after 12 hours at 0.2 mol% catalyst loading), WT *Rhodothermus marinus* Cyt. *c* (*Rma* Cyt. *c*; total turnover number (TTN) = 44± 27) and others.[38, 92] Arnold and coworkers used directed evolution to further optimize *Rma* Cyt. *c* for this reaction, resulting in a triple mutant (V75T, M100D, M103E) that catalyzes Si−H insertion with TTN = 1518 ± 51 with a diazopropanoate.[38] Excitingly, WT YfeX is able to catalyze the carbene transfer to dimethylphenylsilane, generating ethyl[dimethyl(phenyl)silyl] acetate in 11% yield with a TON of 108 at 0.1 mole percent of catalyst *after just one hour* (see **Table 2.6**), *without any optimization*. This finding emphasizes the potential of YfeX for further development into a highly versatile carbene transferase. Recently, the Arnold and Houk groups used conformational dynamics and mutagenesis experiments to further optimize catalysis with *Rma* Cyt. *c*. Based on their computational predictions; they were able to control the chemoselectivity of *Rma* Cyt. *c* for either N−H or Si−H insertion.[39]

Table 2.6 Catalytic activity of YfeX for the Si−H insertion reaction.

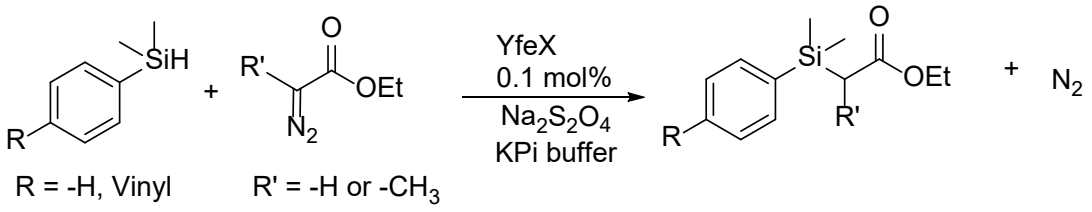

R = -H, Vinyl R' = -H or -CH_3

Substrate	Catalyst	Total Yield (%)	Turnover	Ref.
dimethylphenylsilane	YfeX[a]	11	108 ± 33 [TON]	This work
dimethylphenylsilane	Rma Cyt. C[b]	---	44 ± 27 [TTN]	38
dimethylphenylsilane	Mb[c]	35	175 [TON]	92
4-(dimethylsilyl) styrene	HRP[c]	1	5 [TON]	92

[*a*] Reaction conditions: 20 μM YfeX (0.1 mol%), 20 mM dimethylphenylsilane, 40 mM EDA, 10mM dithionite, 1 hour reaction time. Yields are based on GC/MS analysis. [*b*] Yields based on 0.1 mol% catalyst loading for 1.5 hrs with Me-EDA. [c] Yields based on 0.2 mol% catalyst loading for 12 hrs with EDA.

2.4 RuMpIX and CoPpIX Reconstituted YfeX

RuMpIX was prepared as previously described by Wolf et al. and reconstituted into YfeX.[53] The Soret band of free $[RuMpIX]^+$ at 389 nm shifts by 15 nm to lower energy after incorporation into the YfeX protein (**Figure 2.6**). Upon reduction of Ru(III)YfeX with $Na_2S_2O_4$, the Soret band sharpens, and Q-bands appear at 495 and 520 nm, which is similar to Ru(II)Mb (**Figure 2.6**). The stability of both WT YfeX and RuYfeX under catalytic conditions was investigated by UV−vis spectroscopy. Most notably, after the addition of reductant and EDA to RuYfeX, a rapid decrease in the Soret band at 396 nm and the Q band at 521 nm occurs (**Figure 2.7**). The decrease of the Soret band indicates that the porphyrin cofactor is modified over time, likely via intramolecular carbene transfer, as previously reported for RuMb.[53] This likely leads to

a rather fast decay of the reactivity of RuYfeX. Similarly, the Soret band of RuMb at 396 nm, corresponding to the carbene intermediate, decays over 1 hour, with an initial decay of about half of the Soret band intensity over the first 20 minutes of the reaction with EDA.[53]

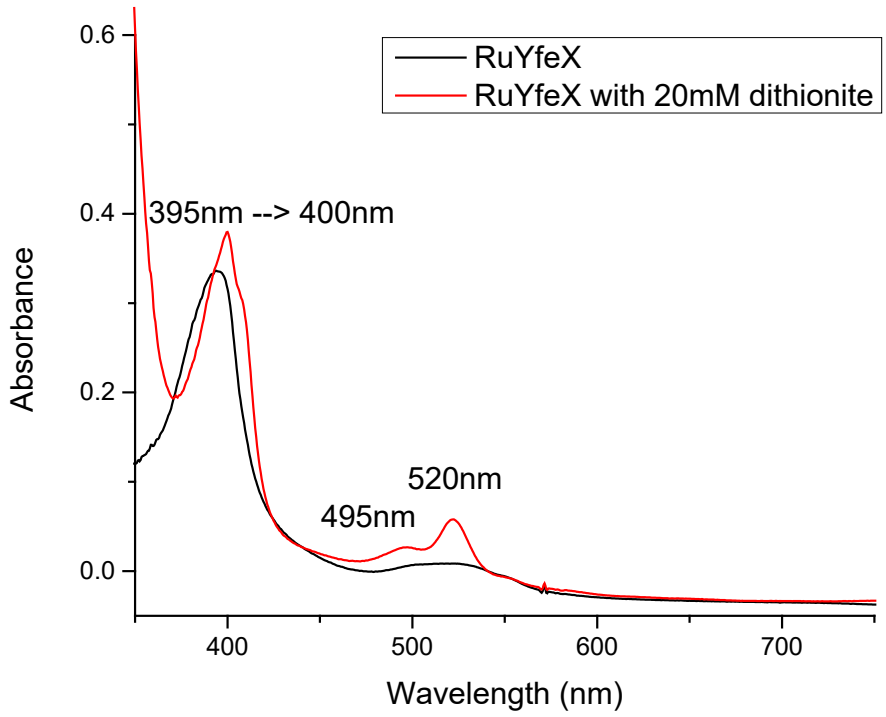

Figure 2.6 Reduction of RuYfeX, which corresponds to apo-YfeX reconstituted with Ruthenium-mesoporphyrin IX, followed by UV-vis spectroscopy.

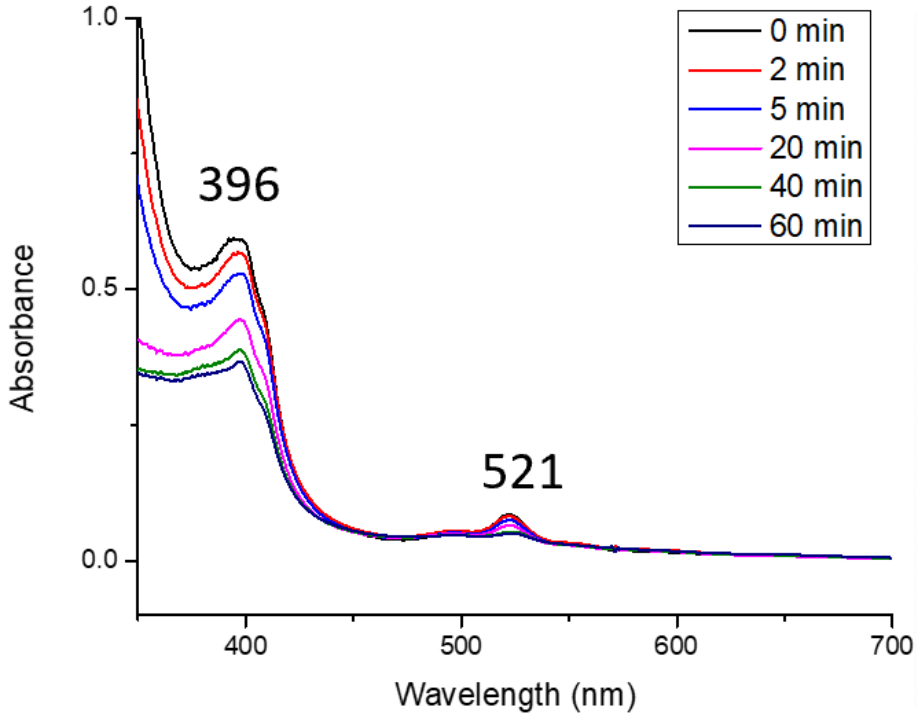

Figure 2.7 Stability of the carbene intermediate of RuYfeX [20 μM] under catalytic conditions, generated by addition of EDA [20 mM] to Ru(II)YfeX, followed by UV-vis spectroscopy in pH 7.4 [100 mM] potassium phosphate buffer.

The ability of RuYfeX to mediate carbene transfer reactions, N−H insertion and cyclopropanation, in buffer was further investigated as shown in **Table 2.7**. Activity toward the N−H insertion of aniline is similar between free [Ru^{II}MpIX], RuMb and variants,[53] WT Mb and variants, and RuYfeX, with the latter achieving a 43% yield (TON of 433) at pH 7. The N−H insertion of a secondary amine, *N*-methyl aniline, gave a somewhat lower yield of 39% compared to aniline. Nevertheless, these numbers all pale in comparison to the N-H insertion activity of WT YfeX. Similar to Mb, the TONs decrease for the cyclopropanation of styrene upon RuMpIX substitution into YfeX, giving a yield of 20% for RuYfeX at pH 7, which is comparable to free [Ru^{II}MpIX] and WT Mb and variants. Notably though, the cyclopropanation activity of RuYfeX

is greatly superior to RuMb.[53] Styrene cyclopropanation with RuYfeX delivers a *cis* to *trans* ratio of 15 to 85, showing a higher trans selectivity compared to free [Ru^{II}MpIX], which yields a *cis* to *trans* ratio of 38 to 62.

Similarly, CoPpIX-reconstituted YfeX was characterized by UV-vis spectroscopy to show incorporation of the Co-porphyrin cofactor into YfeX. Co(III)YfeX shows the Soret band at 417 nm, with a shift to higher energy after reduction to the Co(II) form with dithionite to 398 nm (**Figure 2.8**). A CoYfeX carbene intermediate is generated upon addition of EDA to a solution of the protein, as shown by UV-vis spectroscopy, evident from a broadening and a concomitant shift of the Soret band to 393 nm. CoYfeX can facilitate carbene transfer reactivity at pH 7 in buffer for the N−H insertion of aniline, albeit only with 29% yield (with a TON of 292), and for the cyclopropanation of styrene, the latter with a very small TON of only 49 (see **Table 2.8**). Previously, the Fasan group used the CoPpIX-reconstituted Mb(H64V, V68A) mutant to analyze carbene transfer reactivity.[51] Their results show that CoMb(H64V, V68A) has a lower reactivity for the N−H insertion than CoYfeX, with 13 % yield (and a TON of 129), but similar styrene cyclopropanation activity with 4 % yield.[51] The catalytic activity of CoYfeX is relatively low compared to both WT YfeX and RuYfeX, and was therefore not further pursued.

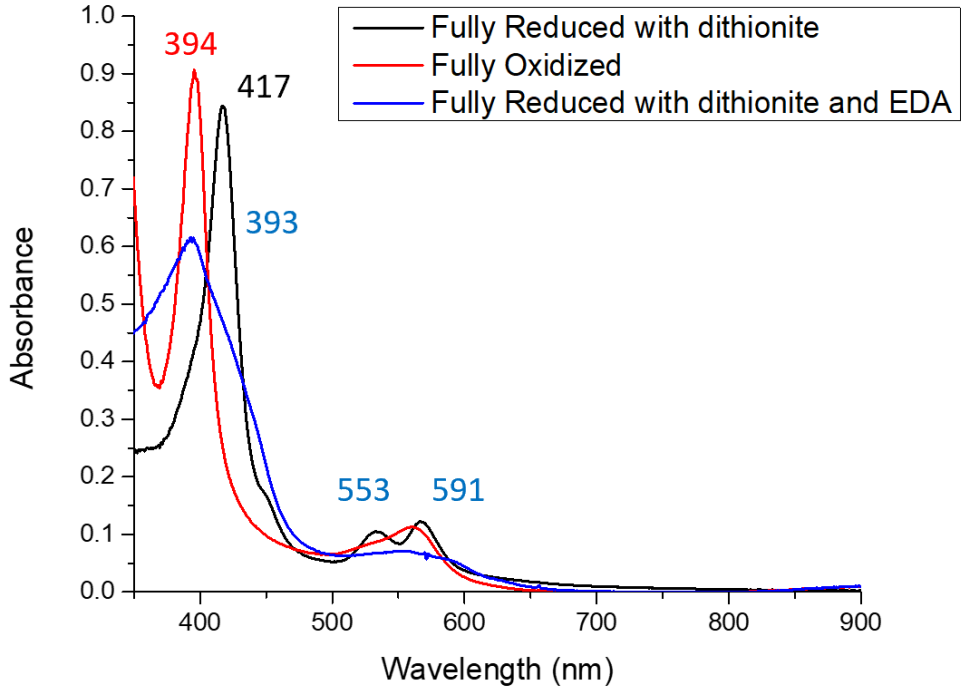

Figure 2.8 UV-vis spectra of CoYfeX [10 μM], which corresponds to apo-YfeX reconstituted with Cobalt-protoporphyrin IX, in the oxidized form (red line), after reduction with sodium dithionite [20 mM] (black line), and after generation of the carbene intermediate via addition of dithionite [20 mM] and EDA [10 mM] (blue line).

Table 2.7 Carbene transfer reactivity of RuYfeX and CoYfeX.

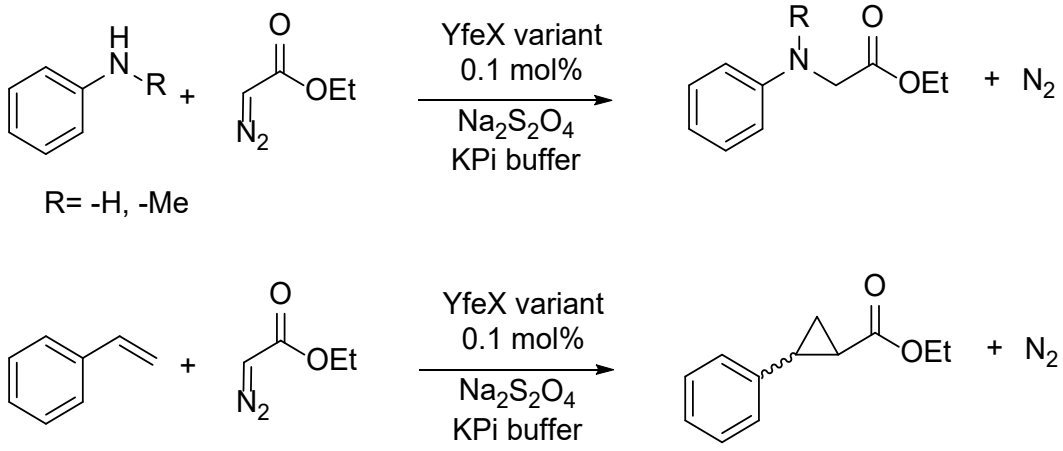

Substrate	Catalyst	Yield [a] (%)	TON	Cis:Trans
aniline	RuMpIX	48	482 ± 11	
aniline	SW RuMb	36	360 ± 37	
aniline	RuYfeX	43	433 ± 21	
N-methyl aniline	RuYfeX	39	385 ± 60	
aniline	CoYfeX	29	292 ± 11	
N-methyl aniline	CoYfeX	5	49 ± 10	
aniline	CoMb(H64V, V68A)[b]	13	129	
styrene	RuMpIX	26	263 ± 121	38:62
styrene	SW RuMb	3	32 ± 12	20:80
styrene	RuYfeX	20	203 ± 56	15:85
styrene	CoYfeX	5	49 ± 16	15:85
styrene	CoMb(H64V, V68A)[b]	4	not reported	

[*a*] Reaction conditions: 20 μM YfeX derivative (0.1 mol%), 20 mM substrate, 40 mM EDA, 10 mM dithionite, 1 hour reaction time. Yields are based on GC/MS analysis. [*b*] Based on studies by Sreenilayam et al.[51]

2.5 MD and QM/MM Studies on the Si—H Insertion Reaction of YfeX

MD and QM/MM studies were performed by our collaborators, the Christov group from Michigan Technological University. Since the Si—H insertion reaction is unusual and not fully

understood, we undertook further computational studies to gain detailed insight into the energetics and the mechanism of this reaction, in the YfeX active site. To evaluate effects of the protein matrix as well, molecular dynamics and QM/MM studies were undertaken.

Conformational Flexibility of the YfeX-IPC Intermediate in the Presence of the Dimethylphenylsilane Substrate. Heme-protein catalyzed carbene insertion reactions have been reported to occur through a catalytic iron-porphyrin carbene (IPC) intermediate,[39, 61, 91, 93-95] which has been recently crystalized in the active site of *Rhodothermus marinus* (*Rma*) Cytochrome *c* by Arnold and co-workers.[91] Since enzymes experience a broad range of internal motions that might be crucial for catalysis,[96-98] we performed MD simulations of the reactive IPC intermediate in the presence of the substrate, dimethylphenylsilane, in the active site (**Figure 2.9a**) to gain insight into its dynamical behavior and especially, the important interactions in the YFeX active site that might enhance the stability of the carbene intermediate and influence the orientation of the dimethylphenylsilane substrate. The protein complex is stable with an average root-mean-square deviation (RMSD) of 1.51 Å (**Figure 2.9b**), implying that the YfeX enzyme does not undergo huge conformational changes in the presence of the coordinated carbene group and the dimethylphenylsilane substrate, which are not naturally present in the enzyme's active site. The average distance between the carbene carbon atom and the Si atom of the substrate is 3.68 Å (**Figure 9c**), which is favorable for catalysis. The average N4-Fe-C1-C2 dihedral angle is found to be -95.2°, and this orientation of the carbene unit (relative to the heme) is stable (**Figure 2.9d**). This orientation of the carbene in the IPC with an N4-Fe-C1-C2 dihedral angle value of -90° has been reported in the captured IPC intermediate by Arnold and co-workers,[91] which is consistent with our results with just a slight deviation due to the specific active site environment in YfeX.

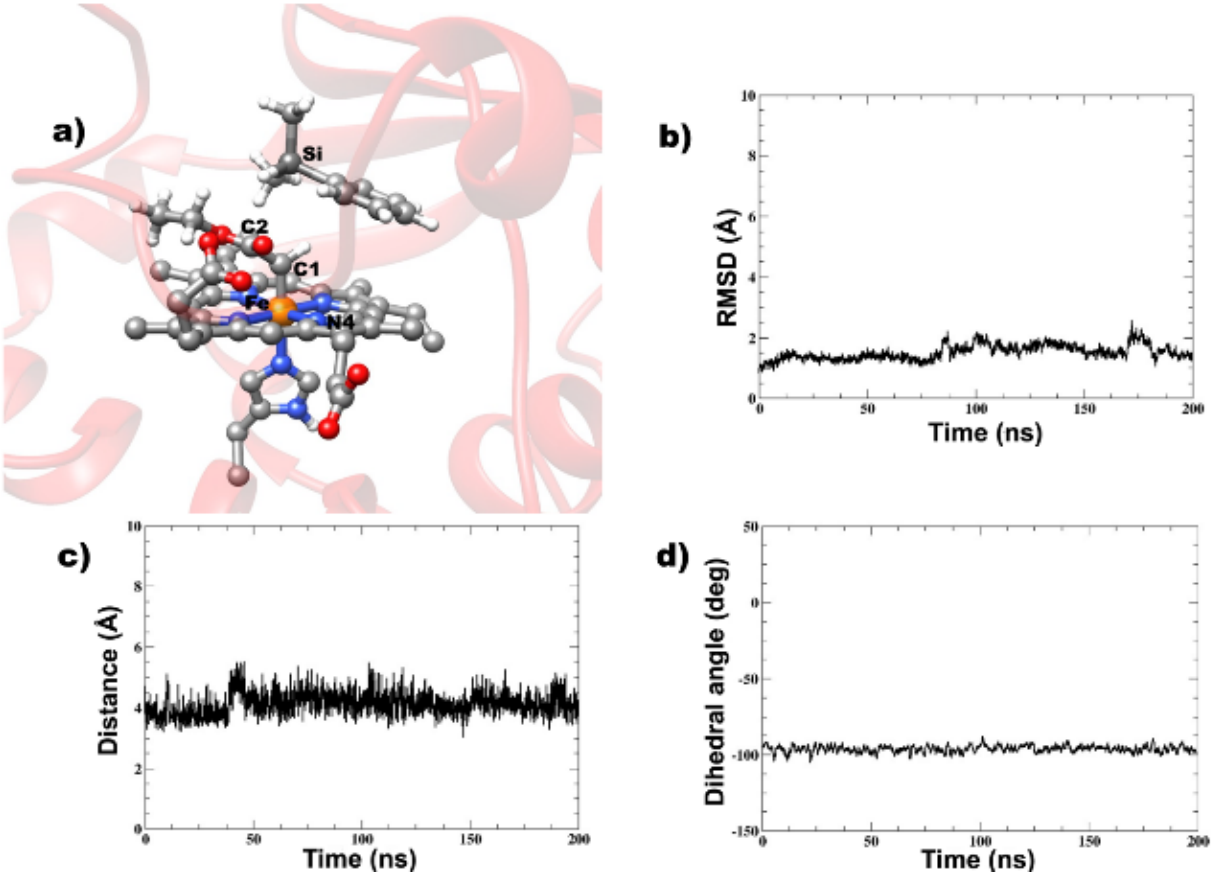

Figure 2.9 (a) Iron-porphyrin carbene (IPC) complex of YfeX with the substrate dimethylphenylsilane present in the active site. (b) Plot of RMSD for the YfeX IPC bound to dimethylphenylsilane substrate; (c) plot of the distance between the carbene carbon (C1) and the substrate silicon (Si); and (d) plot of the N4—Fe—C1—C2 dihedral angle (see panel a) during the course of the simulation.

The phenyl ring of the substrate orients parallel to one of the pyrrole rings of the heme in a manner favoring its stability by π-stacking (**Figure 2.10A**), which is a key interaction that stabilizes the substrate orientation in the IPC complex. Several SCS residues further stabilize both the substrate and the IPC in the active site. For example, the orientation of the substrate is further stabilized via both π-stacking and cation-π stacking interactions of its phenyl ring with the aromatic ring of Phe248 and with the guanidinium group of Arg232 (**Figure 2.10B**), respectively. The salt-bridge interaction between Arg232 and one of the heme carboxylates enhances its favorable interactions with the substrate (**Figure 2.10B**). Furthermore, the methyl groups of the

substrate are stabilized by hydrophobic interactions with the methylene group of the Ser234 side chain and the ethyl group of the IPC carbene unit (**Figure 2.10A**). Finally, the Asp143 side chain orients in such a way that its methylene group is locked in by hydrophobic interactions with the ethyl group of the IPC carbene unit (**Figure 2.10A**) Networks of hydrogen bonding interactions between the axially ligating His215 and residues Asp274, Ser214, and Leu216, which are present in 69%, 39% and 31% of the MD trajectories, respectively, likely contribute to the stability of the complex. All these interactions play crucial roles in the stabilization of both the substrate and the IPC carbene unit and the proper orientation of the overall reactant complex. In particular, the IPC unit is firmly locked into this conformation, whereas the substrate shows some movement in the different trajectories.

(A)

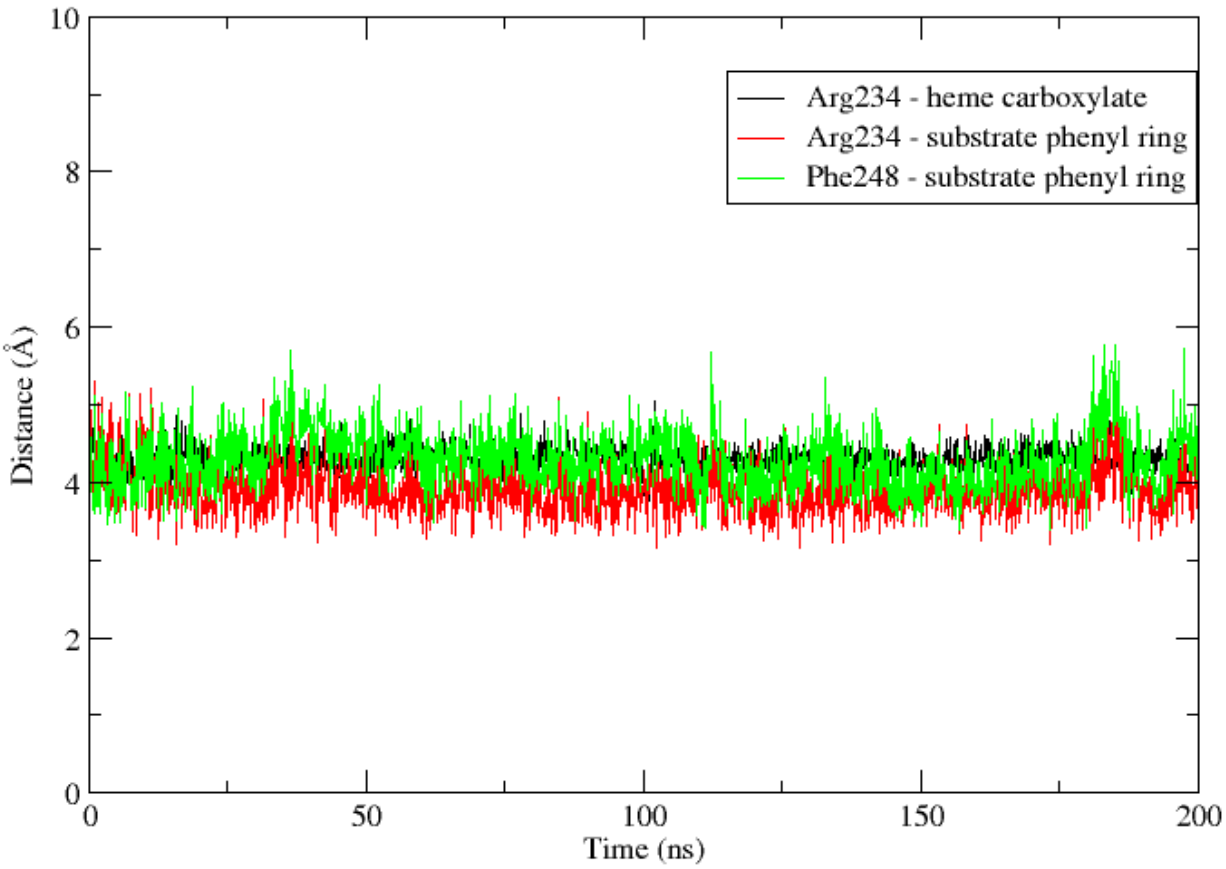
Arg234 - heme carboxylate
Arg234 - substrate phenyl ring
Phe248 - substrate phenyl ring
Distance (Å)
Time (ns)
0
2
4
6
8
10
0
50
100
150
200

(B)

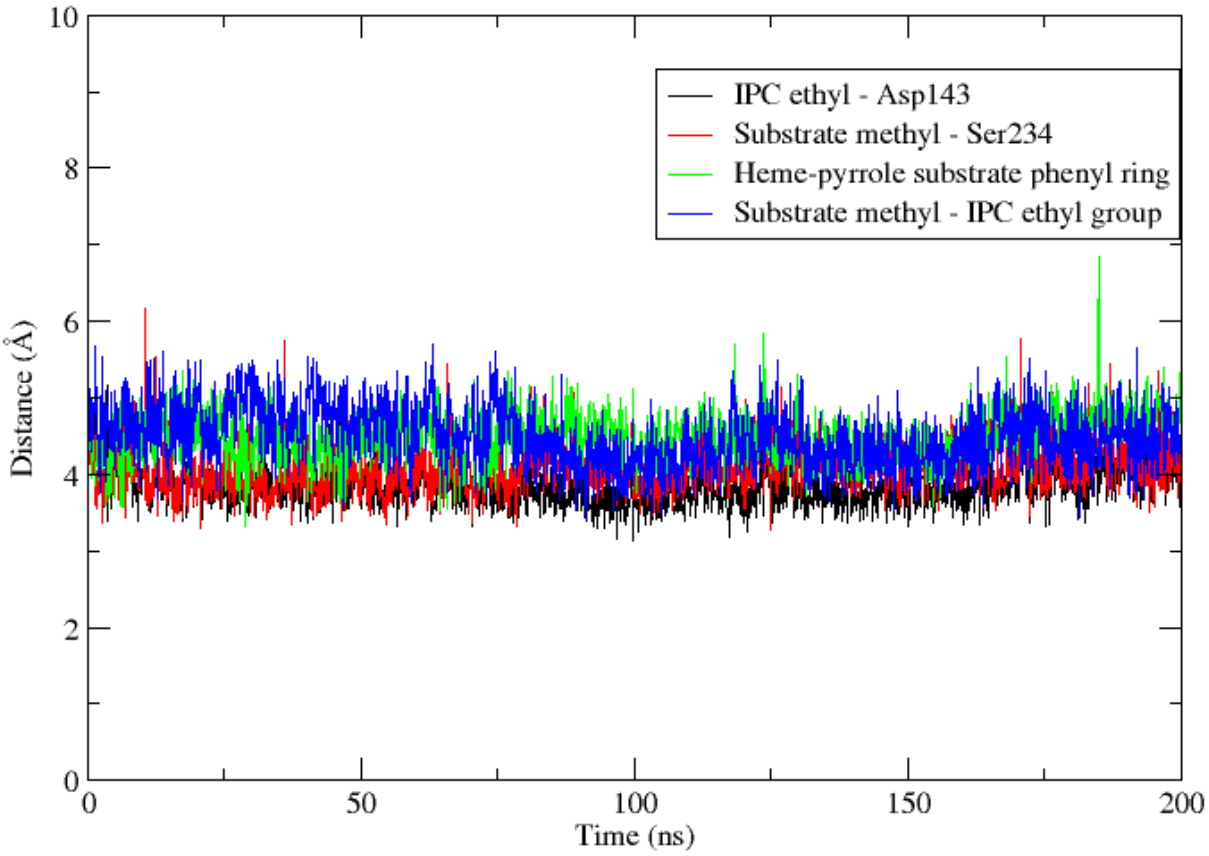

Figure 2.10 (A) Dynamics of the hydrophobic interactions between the ethyl group of IPC, the substrate methyl group, and the methylene groups of the Asp143 and Ser234 side chains, and of the π-stacking interaction between one of the heme pyrroles with the phenyl ring of the substrate. (B) Dynamics of the π-π stacking and cation-π stacking interactions of the Phe248 and Arg232 side chains with the phenyl ring of the substrate, and of the salt bridge between the guanidinium group of Arg232 and one of the heme carboxylates.

QM/MM Calculations of the Reaction Mechanism of Si—H Insertion. In the carbene transfer reactions by iron porphyrin systems, the IPC intermediate has been reported to adopt three different spin states, namely the open-shell singlet (OSS), closed-shell singlet (CSS), and triplet state.[39, 91, 93, 99] To characterize the mechanism of carbene insertion into the Si-H bond of the substrate dimethylphenylsilane, we used combined QM/MM calculations using Turbomole[100] and DL_POLY[101] for QM and MM, respectively, as implemented in the ChemShell package.[102]

Interestingly, the QM/MM optimized IPC intermediates in the three spin states gave the triplet state as the lowest energy, 2.1 and 4.6 kcal/mol more stable than the OSS and CSS, respectively. In the optimized structures, the Fe-C1 bond distance in the triplet and OSS state are 1.92 and 1.86 Å, respectively, while a shorter bond distance of 1.79 Å is obtained in CSS. These structural parameters agree with earlier computational results; however, the question of the correct spin state of the IPC intermediate is still unclear.[39, 91, 93, 99, 103] Computational studies that favor each one of these spin states as the ground state have been reported.[39, 62, 93, 95, 103-104] However, the majority of studies have reported the OSS to be the lowest energy state.[91, 93, 99, 103] Furthermore, although this is still an open question, the protein environment might not affect the spin state energy order: a recent study, using both a QM cluster model and the QM/MM method, concluded that the spin state energy order is preserved in both cases for the studied system, independent of whether the protein environment is included or not.[99] The process of Si—H insertion, involving partial hydride transfer from the silane to the carbene carbon and then the formation of a C-Si bond, passes through transition states **TS$_{OSS}$**, **TS$_{CSS}$**, and **TS$_{triplet}$** for the OSS, CSS, and triplet spin states, respectively, with reaction barriers of 16.4, 22.8 and 27.6 kcal/mol, respectively. Hence, even though the triplet IPC has the lowest energy, our calculations reveal that the reaction coordinate requires a spin state crossing and that the reaction passing through **TS$_{OSS}$** is faster than the reactions through the other two transition states. **TS$_{OSS}$** is more favorable as it has the lowest barrier when compared to those observed for the other two spin states; therefore, **TS$_{OSS}$** is preferred over **TS$_{CSS}$** and **TS$_{triplet}$**. The computational results therefore point to a favorable OSS electronic spin state, in agreement with some previously reported computational findings.[91, 93, 99, 103] However, as discussed above, the nature of the most probable electronic ground state of the IPC intermediate is still a matter of discussion.

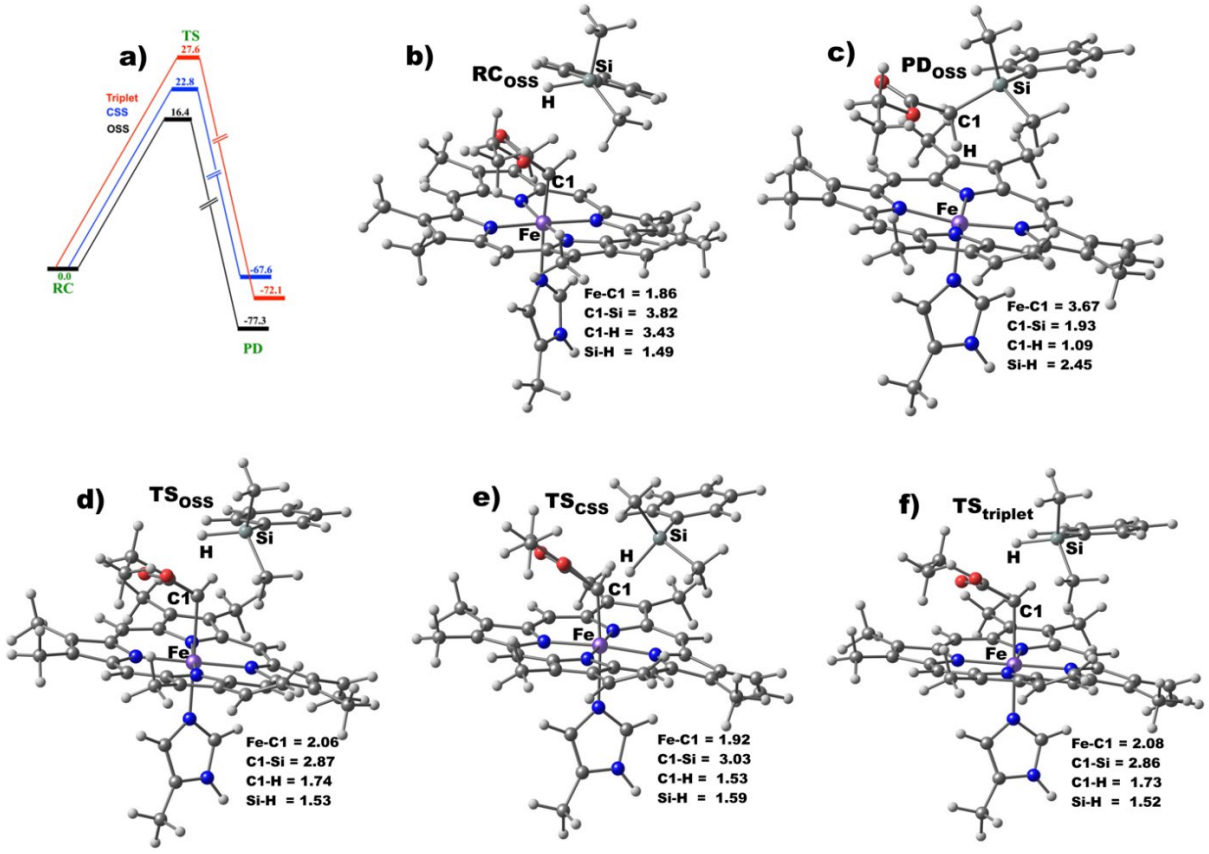

Figure 2.11 (a) QM/MM potential energy profile for Si—H insertion catalyzed by YfeX-IPC, calculated at the BS2 + ZPE level of theory, (b-c) geometries of the reactant and product complexes for the OSS state, and (d-f) geometries of the transition states in the OSS, CSS and triplet spin states. The relative energies in (a) are in kcal/mol while the distances in (b-f) are in Å.

At the **TS**$_{OSS}$, the Fe-C1 and Si-H bonds elongate to 2.06 Å and 1.53 Å from 1.86 Å and 1.49 Å, respectively, while both the C1-Si and C1-H bonds shorten in readiness to form a new product involving the C1-Si bond, in agreement with previous computations.[39, 94-95] These bond distances are shorter for **TS**$_{CSS}$, as presented in **Figure 2.11**, than those obtained for the OSS and triplet spin states. Importantly, the transition state geometries are stabilized by several SCS residues. In **TS**$_{OSS}$, the guanidinium group of R232 forms a salt bridge with one of the heme carboxylates. Further, the phenyl ring of the substrate is stabilized by both π stacking and cation-π stacking interactions with the phenyl ring of F248 and the guanidinium group of R232,

respectively. These interactions are also conserved in the MD simulation. A network of hydrophobic interactions around the substrate and the carbene unit enhance the stabilization of the transition states. The methylene backbones of D137, D143 and F141 form hydrophobic interactions with the ethyl group of the carbene. The phenyl ring of F141 orients in a perpendicular manner to the heme ring and this π-stacking interaction thus locks its methylene backbone group in a position that favors the hydrophobic interaction with the ethyl moiety of the carbene unit. In addition, the methyl groups of the substrate are stabilized by the methylene group of the S234 backbone and the isobutyl side chain of L246, while the phenyl ring is stabilized by hydrophobic interactions with the R232 backbone methylene group as well as the hydrophobic environment created by the sec-butyl and methyl side chains of I230 and A250, respectively (**Figure 2.12**). The hydrophobic interactions observed for the ethyl group of the carbene are weaker in **TS$_{triplet}$** and **TS$_{CSS}$**. Overall, all these interactions contribute to the stabilization of the transition state. The transition states relax to products (**PD$_{OSS}$**, **PD$_{CSS}$**, and **PD$_{triplet}$**), where the C1-Si bond is fully formed, and the Si-H bond is broken. The products formed in the three spin states are highly exothermic with energies of -77, -68, and -72 kcal/mol for **PD$_{OSS}$**, **PD$_{CSS}$**, and **PD$_{triplet}$**, respectively. Overall, the calculations show that the OSS spin state, which possesses the lowest transition state barrier of all the three spin states, is the most stable, implying that the formation of the C-Si bond product via the OSS spin state is both kinetically and thermodynamically favorable and preferred over the other spin states. The potential energy profile for the Si—H insertion reaction and the QM/MM-optimized stationary point geometries are presented in **Figures 2.11** and **10B**.

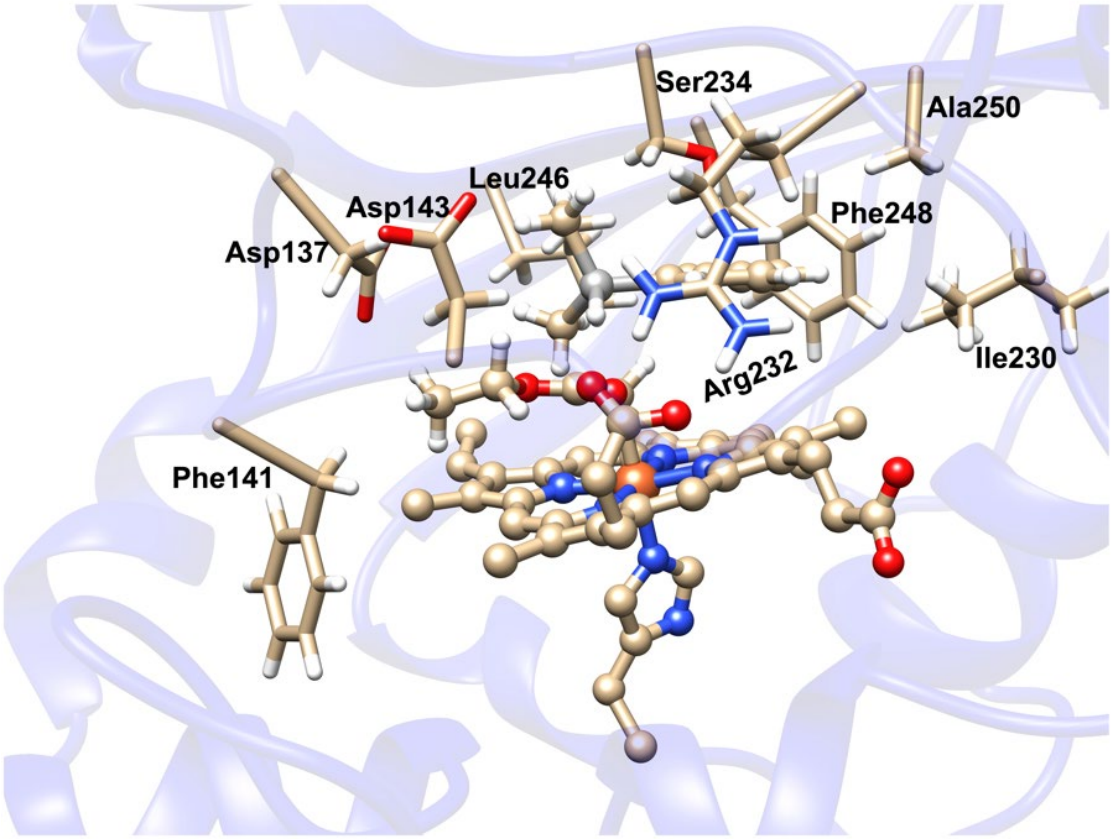

Figure 2.12 Second coordination sphere (SCS) residues that stabilize the open-shell singlet (OSS) transition state. The YfeX-IPC center and the dimethylphenylsilane substrate are represented in ball and stick while the SCS residues are in stick representation.

2.6 Discussion

In this chapter, we show that the enzyme YfeX is an excellent platform for further development of biocatalysts for carbene transfer reactions. Such carbene transferases are of particular interest for late-stage functionalization of drug precursors, allowing for the efficient synthesis of pharmaceuticals. These enzymes have the ability to form new C-C and C-heteroatom bonds under mild reaction conditions, where the tuning of the enzyme active site and beyond enables stereo- and even enantioselective reactions to be performed.[6, 29, 33-36, 55] So far, Cyt. P450s and myoglobin (Mb) have mainly served as the work horses for the development of carbene

transferases.[59, 105-106] However, the catalytic activity of WT Mb, for example, is somewhat limited. As pointed out by Arnold, for the development of robust biocatalysts it is of advantage to start from a WT enzyme that itself has a high catalytic activity for a desired transformation.[38] As we show in this work, the peroxidase YfeX is an excellent platform for further biocatalyst development, by either directed evolution and/or rational design. In particular, WT YfeX shines with high catalytic activity for the N-H insertion of aromatic and aliphatic primary and secondary amines that is comparable to those of the best Mb mutants available to this date from the Fasan group.[90] For example, WT YfeX has a 70% yield (at 0.1 mol% catalyst loading in just 1 hour), and up to a TON of >6000 (at 0.001 mol% loading after 20 hours) for the N-H insertion of aniline with EDA. Curiously, the cyclopropanation activity of YfeX, on the other hand, is comparable to that of Mb. As we show in this work, this is largely due to the lack of solubility of the corresponding test substrate, styrene, in buffer, and its inability to access the YfeX active site. So, whereas the intrinsic reactivity of the central carbene intermediate seems to be much higher in YfeX, Mb seems to profit from easier access to its heme cofactor (due to the lack of a real active site pocket) when substrates are used that lack water solubility. However, YfeX also shows remarkable stability in organic solvents, and in the presence of 30% methanol to improve styrene solubility, the yield for the cyclopropanation of styrene by WT YfeX increases to 47%. Under similar conditions, benzylamine gives a 56% yield for N-H insertion. Other styrene and aniline derivatives were tested as well, giving excellent yields for carbene transfer reactions, as shown in **Tables 2.3** and **2.4**. Even more impressively, WT YfeX is able to catalyze the Si—H insertion of dimethylphenylsilane with 11% yield (at 0.1 mol% catalyst loading in just 1 hour), which is superior to other WT proteins studied so far.[38-39, 95] These results show that YfeX and potentially other peroxidases have great potential to become the next universal work horses for the development of a broad range of new

carbene transferases, given its high intrinsic reactivity for carbene transfer reactions. A basic comparison between the reactivity of WT Mb and WT YfeX is given in **Table 2.8**.

Table 2.8 Product yield comparison between WT Mb and WT YfeX for standardized test substrates. All WT YfeX data were obtained at 0.1 mol% catalyst loading.

Substrate	Wt Mb	Time	Wt YfeX	Time
styrene	36% [b]	16 hrs	27% 59% [a]	1 hr
aniline	21% [c]	12 hrs	72%	1 hr
benzylamine	17% [d]	16 hrs	56% [a]	1 hr
dimethylphenyl-silane	35% [e]	12 hrs	11%	1 hr

[a] Using 30% DMSO (styrene) or 30% MeOH (benzylamine) as co-solvent. [b] Data from ref. [24] using 0.2 mol% Mb. [c] Data from ref. [89] using 0.2 mol% Mb. [d] Data from ref. [90] using 0.2 mol% Mb. [e] Data from ref. [92] using 0.2 mol% Mb.

To explore the substrate scope of YfeX for the N−H insertion and cyclopropanation reaction, a variety of *para*-substituted anilines and styrenes with electron-donating and electron-withdrawing substituents where subjected to reactivity with EDA. Similar to previous results with Mb and P450s,[33, 55, 58, 90, 107] it was shown that YfeX favors electron-rich substrates. The enhanced preference to electron-rich substrates is due to their higher reactivity toward the electrophilic heme−carbene intermediate that facilitates these reactions.[55, 58, 91, 107] Moreover, YfeX cyclopropanation reactivity shows that it can generate the *trans* product in high yield with 87% selectivity for the (R,R) enantiomer, unlike WT Mb, which produces 47% (R,R) enantiomer.[24] It has been shown that SCS interactions play a major role in diastereo- and enantioselectivity for cyclopropanation reactivity;[55, 94, 99] therefore, differences in selectivity for WT YfeX compared to WT Mb are likely due to variations near the heme active site. This point requires further investigation. Fasan and coworkers have further explored cyclopropanation selectivity using crystallographic, computational, and reactivity/mutagenesis studies in Mb and mutants.[94] They

highlight the importance of steric complementarity and noncovalent interactions to guide stereochemical selectivity during cyclopropanation reactivity, and corresponding studies on YfeX are currently in progress.[94]

We further investigated if an improvement of catalytic activity of YfeX could be achieved using other transition metals. For this purpose, we reconstituted YfeX with Co- and Ru-heme cofactors, which have shown promise for improving carbene transfer reactivity for Mb.[53-54] However, in the case of YfeX, no improvements in carbene transfer activity are observed in these cases. In agreement, the previously noted instability of RuMb persists for RuYfeX, emphasizing that carbene insertion into the porphyrin ring is a general reactivity feature of (biological) Ru-hemes, which would otherwise be highly active catalysts.[53] Therefore, the cheapest metal, iron, turns out to also give the most active and robust catalyst of all transition metals tested thus far with YfeX.

Since the Si—H insertion reaction is unique, we investigated this reaction further using computational methods. Whereas many WT heme proteins are able to catalyze the N—H insertion or cyclopropanation reaction, albeit often with very low yields, the Si—H reaction is much more challenging, and there are very few WT heme proteins that are able to mediate this process efficiently.[38] Here, we investigated this reaction starting from the three possible electronic ground states of the iron-porphyrin carbene (IPC) intermediate, which are the closed shell singlet (CSS) and open shell singlet (OSS) state, and the corresponding triplet state. As observed previously, these three states are very close in energy (within 5 kcal/mol), making it impossible to determine which form corresponds to the ground state of the IPC based solely on the computational results.[91, 107] Previous studies on truncated DFT models indicated that there is no energy barrier for either

the N—H insertion and cyclopropanation reactions, but there is a free energy barrier due to the entropic contribution, corresponding to 9 – 14 kcal/mol.[94, 103] In contrast, for the Si—H insertion by YfeX, the calculated energy barriers are 16.4 (OSS), 22.8 (CSS) and 27.6 (triplet) kcal/mol, indicating that the OSS state is ultimately allowing for this reaction to go forward. Overall, these results show that the Si—H insertion reaction is energetically much less favorable compared to the N—H insertion and cyclopropanation reactions, in agreement with the lack of reactivity of many WT heme proteins towards carbene transfer to Si-H bonds.

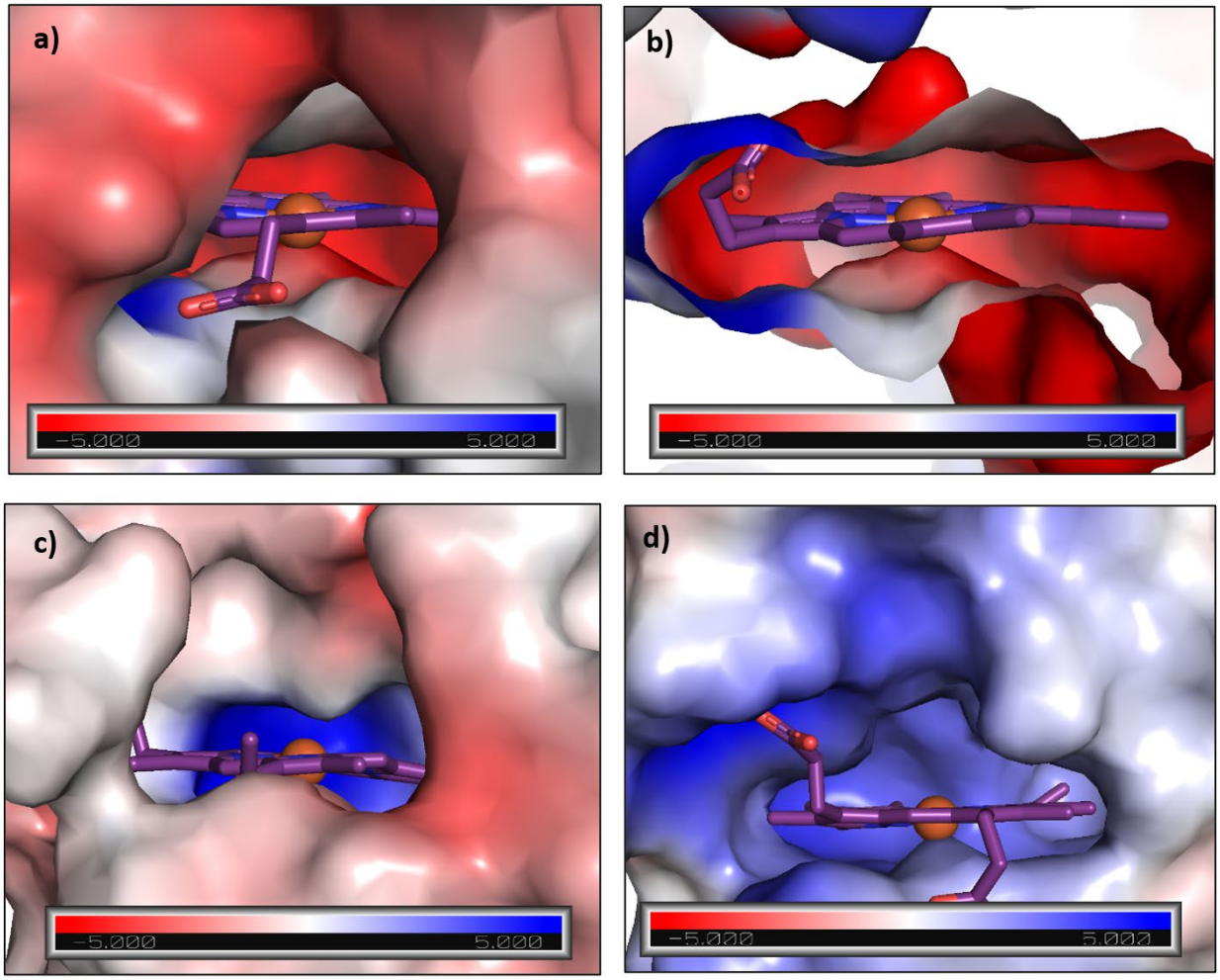

Figure 2.13 Electrostatic potential surfaces for the active site of (a) YfeX (PDB code 2IIZ) from the outside, and (b) zoomed-in version for YfeX, (c) Rma TDE (PDB code 6CUN), and (d) Mb (H64V, V68A) (PDB code 6M8F). Electrostatic potential surfaces were drawn in PyMOL using

APBS electrostatics (the red color corresponds to negative potential and the blue color corresponds to positive potential).

As shown by our results, the YfeX active site is uniquely equipped to stabilize the transition state for the Si—H insertion with dimethylphenylsilane, by locking the IPC complex and the substrate into a conformation that is productive for catalysis. During the MD simulations, the orientation of the substrate relative to the IPC intermediate shows little variation, thereby promoting this reaction despite the rather large activation barrier. Recently, Arnold, Houk and coworkers investigated the Si—H insertion mechanism as catalyzed by the *Rma* Cyt. *c* V75T M100D M103E triple variant (termed "*Rma* TDE") through experimental and computational studies.[39] They determined that Rma TDE catalyzes carbene insertion into Si-H bonds through a concerted, nonradical mechanism, and in their DFT and QM/MM calculations, the CSS is the most favorable transition state.[39] The transition state energies obtained from their QM/MM studies are rather similar to the ones obtained by us for YfeX, again emphasizing that YfeX is intrinsically suited for the Si—H insertion reaction, and thus, has the potential to be further optimized for this reaction to achieve high turnover numbers. Similarly, Fasan, Zhang and coworkers investigated the Mb-catalyzed carbene insertion into Si-H bonds, using a truncated DFT model for the calculations and radical trap experiments. Based on their results, it was concluded that the carbene insertion into Si-H bonds occurs through a concerted mechanism involving a CSS transition state.[95] As discussed above, our calculations predict that in the case of YfeX, the mechanism of Si—H insertion with dimethylphenylsilane involves an OSS transition state rather than a CSS transition state, as found for *Rma* TDE and Mb. These differences could be related to variations within the active sites of these proteins. **Figure 2.13** compares the electrostatic potential surface maps for the active sites of YfeX, *Rma* TDE, and Mb (H64V, V68A; one of the most active Mb-based carbene transfer catalyst), indicating key differences in YfeX compared to these other catalysts. Whereas

YfeX has a polar active site with both negatively and positively charged regions, and a narrow tunnel that leads into the active site, both *Rma* TDE and Mb (H64V, V68A) have much more open active sites with neutral to positive electrostatic potential. This explains why YfeX has intrinsically a high reactivity for N-H insertion, where polar aniline has a relatively high affinity for the active site of YfeX, whereas non-polar styrene does not. Styrene cyclopropanation is therefore drastically enhanced in the presence of organic co-solvents that help improve the availability of this substrate in solution for WT YfeX, whereas for aniline, the effect of an organic co-solvent is small. In addition, YfeX is able to better confine dimethylphenylsilane in the active site, which promotes reactivity. As evident from **Figure 2.13**, YfeX clearly contrasts with *Rma* TDE and Mb (H64V, V68A) with respect to its active site properties, which again emphasizes the great potential of YfeX and other peroxidases to access unprecedented reactivity space in biocatalytic transformations. Investigations in this regard are ongoing.

In conclusion, our results show that YfeX is a highly reactive and versatile catalyst for carbene transfer reactions, and in its WT form, shows excellent reactivity for the reactions we explored here, compared to WT Mb and diverse WT Cyt. P450s. In addition, the protein shows high stability against organic solvents, thereby enabling the use of organic co-solvents whenever necessary in order to improve turnover for hydrophobic substrates. Utilizing MeOH and DMSO co-solvents we show that cyclopropanation reaction yields significantly increase for WT YfeX, overcoming some of the low solubility barrier faced by styrene in aqueous buffer. The rather large active site of YfeX further promises exciting applications of this protein in the synthesis of pharmaceuticals and fine chemicals, allowing for the processing of rather large substrates, especially after (potentially) opening the tunnel into the active site via site-directed mutagenesis. Such studies are in progress, further explored in Chapter 3, combined with site-directed

mutagenesis studies that aim to explore the role of important second coordination sphere groups in the YfeX active site during various carbene transfer reactions. YfeX is an exciting new target for the design of new carbene transferases, with many potential applications in the pharmaceutical industry in the future.

2.7 Experimental Section

General Procedures

Materials. All chemicals and reagents were purchased from commercial suppliers (Sigma-Aldrich, Fisher Scientific, Acros, Frontier Scientific) and used without further purification unless otherwise noted. UV-visible spectra were recorded on an Analytic Jena Specord S600 spectrophotometer using sealed quartz cuvettes. ^{13}C- and ^{1}H-NMR spectra were measured on either a Varian MR400 (operating at 400 MHz), a Varian Inova 500 (operating at 500 MHz), or a Varian VNMRS 500 (operating at 500 MHz). Tetramethylsilane (TMS) served as the internal standard (0 ppm) for ^{1}H-NMR measurements.

Gas chromatography/mass spectrometry (GC/MS) analyses were performed using a Shimadzu QP-2010 GC/MS equipped with a 30 m long DB-5 column with 0.25 mm ID. Separation method: 1 μL injection, injector temperature: 200 °C, detector temperature: 250 °C. Gradient: column temperature set to 60 °C for 3 min, then to 250 °C at 20 °C/min and held at 250 °C for 2.5 min (7.5 min for derivatives). Total run time was 15.00 min for the aniline and styrene reactions, and 20.00 min for the reactions with the aniline and styrene derivatives.

Supercritical fluid chromatography (SFC) used to resolve the enantiomer products for cyclopropane compounds was performed using a Waters SFC instrument equipped with a column oven (35 °C), photodiode array detector, a backpressure regulator (12.0 MPa), a carbon dioxide pump and a sample injection volume of 3 μL. A Daicel Chiralpak IC column (5 μm, 4.6 × 250 mm analytical chiral column) was used for separation of the enantiomers and % ee determination. All samples were eluted using an isocratic solvent system with the indicated modifier in liquid CO_2,

containing 10% isopropanol as co-solvent, at an elution rate of 4 mL/min and detection at λ = 250 nm with a total run time of 6.0 min.

YfeX protein expression, purification. Protein expression and purification followed a protocol by the Weissenborn group (Martin-Luther-University Halle-Wittenberg in Halle (Saale), Germany).[78] The YfeX genes (pCA24N) were transformed into chemocompetent *E. coli* BL21 (DE3) cells by heat shock. Freshly plated transformants were grown overnight in 5 ml Terrific Broth (TB) medium containing 50 µg/ml chloramphenicol. 2 ml of the pre-cultures were inoculated in 400 ml TB autoinduction medium containing 50 µg/ml chloramphenicol. Cells were incubated at 37 °C and 120 rpm. After 4 h of cultivation, aqueous solutions of $FeCl_3$/5-aminolevulinic acid (final concentration: 100 µM) were added, the temperature was reduced to 30 °C and the cells were incubated for further 16.5 h. Cells were harvested by centrifugation (3000 x g, 20 min, 4 °C). The supernatant was discarded, and the pellets were resuspended in binding buffer (50 mM Kpi, pH = 7.4, 200 mM NaCl). Cells were lysed by sonication (Bandelin Sonoplus HD3100: 6x30 s, 70 % amplitude, pulse mode) and the lysate was incubated with hemin (final concentration: 600 µM) at room temperature for 30 min with a final DMSO concentration of 2 %. The cell debris was removed by centrifugation for 45 min at 4 °C and 6000 x g. Excess of hemin and traces of DMSO were removed during the protein purification steps. The protein exhibits a hexahistidine-tag and was purified by IMAC (immobilized metal ion affinity chromatography) using 1 mL His GraviTrap TALON columns (GE Healthcare Europe GmbH, Freiburg, DE). Washing buffer consisting of 50 mM Kpi (pH = 7.4), 200 mM NaCl and 5 mM imidazole was used to remove unspecific proteins. Protein was finally eluted by the addition of elution buffer (50 mM Kpi (pH = 7.4), 200 mM NaCl and 250 mM imidazole). PD-10 desalting columns (GE Healthcare Europe GmbH, Freiburg, DE) were used for buffer exchange of the

pooled elution fractions, yielding the purified protein in 50 mM Kpi (pH = 7.4) and 10 % glycerol (v/v). These stocks were flash-frozen in liquid N_2 and stored at -20 °C. Protein and heme *b* amounts were determined in duplicates using the BSA Protein Assay and the Pyridine Hemochromagen Assay (reduced form, $\varepsilon = 34.7\ mM^{-1}cm^{-1}$ at 557 nm).

Protein mass spectrometry analyses were performed using an Agilent Q-TOF HPLC-MS equipped with a Poroshell 300SB-C8 column. Separation method: 20 µL injection, flow rate: 0.5 mL/min, gradient: 95:5 water/acetonitrile for 3 min, followed by an increase over 10 min to 100% acetonitrile to elute the protein. Total run time was 13 min. Porphyrin mass spectrometry analyses were performed using an Agilent 6230 TOF HPLC-MS.

N−H Insertion Reactions. Reactions were performed as previously described,[53] at a ~450 µL scale using 20 µM YfeX, 20 mM aniline (or aniline derivative), 40 mM ethyl diazoacetate (EDA), and 10 mM $Na_2S_2O_4$. The sodium dithionite (100 mM stock solution) in potassium phosphate buffer (100 mM, pH 7.0) was purged by bubbling nitrogen through the solution for 10 min in a sealed vial. All reagents and proteins were brought into a Coy vinyl anaerobic chamber (10−30 ppm of O_2, 1.5−3.0% H_2) before running the reactions. The as-isolated, ferric YfeX was first reduced to ferrous YfeX through addition of 40 µL of $Na_2S_2O_4$ solution, followed by the addition of 4 µL of aniline or aniline derivatives from a 2 M stock solution in methanol, and 8 µL of EDA (2 M stock solution in methanol), which translates to a total MeOH content of 2.65%. The reactions were left under magnetic agitation for 1 h at room temperature (or as indicated).

Cyclopropanation Reactions. Reactions were performed in the same manner as the N−H insertion reactions, using 20 mM styrene (or styrene derivatives) instead of aniline. All 2 M styrene solutions were prepared in methanol.

Si-H Insertion Reactions. Reactions were performed in the same manner as the N−H insertion reactions, using 20 mM dimethylphenylsilane (or silane derivatives) instead of aniline. All 2 M silane solutions were prepared in methanol.

Product Analysis. The reactions were analysed, as previously described,[15] by addition of 20 μL of internal standard (2-phenyl-ethanol, 1 M in methanol) to the reaction mixture, followed by extraction with 1.5 or 3 mL of ethyl acetate, depending on the reaction. The organic layers were dried with magnesium sulfate and later filtered and analysed by GC/MS and/ SFC (see General Procedures section for details on GC/MS and SFC analyses). Calibration curves for quantification of the N−H insertion products of aniline and aniline derivatives and the cyclopropanation products of styrene and styrene derivatives were constructed using authentic standards produced synthetically (using 1−2 mol% $Rh_2(OAc)_4$ as the catalyst). These products were used to generate calibration curves for quantification of the aniline and styrene products in the catalytic reactions with YfeX. The reactions to produce authentic standards were conducted according to the same methods previously reported by our laboratory.[53] All measurements reported in the Results tables were performed in triplicate. Negative control experiments were performed in the absence of YfeX.

Computational Methods: System Preparation and MD Simulation. The initial coordinates of the system were generated using an X-ray crystal structure of YfeX (PDB code:

5GT2).[74] The precursor for the iron porphyrin carbene (IPC) intermediate and the dimethylphenylsilane substrate were modelled in the active site using GaussView 6.0.[108] The protonation states of the ionizable side chains were accessed with Propka software,[109] while the axial His215 that is coordinated to the Fe center of the heme was assigned a protonation state based on visual inspection of its local environment. The active center parameters were generated using Metal Center Parameter Builder (MCPB.py),[110] as implemented in Amber18. The bond and angle force constants were derived using the Seminario method,[111] while point charge parameters for the electrostatic potentials were obtained using the ChgModB method. The parameters for the carbene precursor complex and the silane substrate were generated using the Antechamber module of Amber18.[112] All the missing hydrogen atoms in the crystal structure were added with the Leap module in Amber and charges were neutralized using Na^+ counterions. The system was solvated with TIP3P water molecules in a rectangular box within a distance of 10 Å from the protein's surface.[113] Several MD and QM/MM studies on both heme and non-heme Fe containing enzymes have successfully used the parameters generated via this procedure to study both the dynamics and the catalytic mechanism of the Fe containing systems.[39, 91, 114-115]

A two-stage minimization of the geometries was first performed using MM to eliminate clashes of atoms. In the first stage of minimization, only the water molecules and the Na^+ counterions were minimized, while the solute molecules were restrained with a harmonic potential of 500 kcal/(mol$Å^2$). In the last minimization stage, all the atoms were geometrically optimized without any restraint. The system was subjected to 5000 steps of steepest descent, followed by 5000 steps of conjugate gradient energy minimization. The minimized system was first slowly heated from 0 to 300 K for 50 ps in an NVT ensemble using a Langevin thermostat.[116] The heated system was further subjected to constant temperature heating at 300 K for 1 ns in an NPT ensemble.

The solute molecules were restrained with a harmonic potential of 10 kcal/(molÅ^2) during all the heating processes. After that, the system was equilibrated for 3 ns in an NPT ensemble at a fixed temperature and pressure of 300 K and 1 bar, respectively, without any restraints on solute molecules. After equilibration, a restrained productive MD was then run for 200 ns using the distance NMR refinement module in Amber18 by restraining the distance between the Si atom of the silane substrate and the carbene carbon from 2.8 and 3.5 Å, followed by an unrestrained productive MD for another 200 ns in an NPT ensemble with a target pressure set at 1 bar and constant pressure coupling of 2 ps.[117] The pressure was held constant using Brendsen barostat[118] and the SHAKE algorithm[119] was used to constrain the bond lengths of those bonds involving hydrogen atoms. The simulations were performed using the GPU version of the PMEMD engine integrated in Amber18.[120] The Amber FF14SB force field was used for the simulations,[121] and periodic boundary conditions were employed. The obtained trajectories were processed and analysed using the CPPTRAJ module from Ambertools utilities.[122]

QM/MM Calculations. QM/MM calculations were performed with the ChemShell program,[102] which combines Turbomole[100] for the QM region and DL_POLY[101] for the MM region. The electrostatic embedding scheme was used to describe the interactions between the two regions, while hydrogen link atoms were used to treat the boundary between the QM and the MM region. The QM region was represented using the UB3LYP functional with the 6-31G(d) basis set for all atoms except Fe where the LANL2DZ basis set with an effective core potential (ECP; labelled BS1) was used, as in previous, similar studies on carbene transfer reactions.[93-94, 103, 123] The MM region was described with the Amber force field. The QM region consists of the Fe-porphyrin carbene intermediate, dimethylphenylsilane and the methylene imidazole group of the axial His215 ligand. After the initial QM/MM geometry optimization, linear transit scans along

the reaction coordinate were performed with 0.1 Å increment to obtain the transition states using a DL_find optimizer.[124] The transition states were reoptimized using the P-RFO algorithm implemented in the HDLC optimizer.[125] The fully optimized geometries of the minima and the transition states were characterized via frequency calculations. The final energies of the optimized stationary points were recomputed via single-point energy calculation using the all electron def2-TZVP basis set (labelled BS2) for all atoms. To obtain the open-shell singlet state (OSS) structures, the optimized triplet state structure was used as a starting point, followed by flipping one α-electron to a β-electron, and then an unrestrained geometry optimization was performed on this structure. To do the spin flip, the 'flip' module in Turbomole was used.

Chapter 3 YfeX: A Biocatalytic Carbene Transferase

In this chapter, the biocatalytic carbene transferase properties of YfeX variants were investigated. The following work was performed in collaboration with Professor Martin Weissenborn and student Anja Knorrscheidt from Martin-Luther-University Halle-Wittenberg, who provided protein plasmids, with Professor Christo Z. Christov from Michigan Technological University, who helped with the computational calculations, and undergraduate student Hannah Palomino who contributed with reactivity and computational studies. The following work will contribute to a manuscript tentatively titled: **Victor Sosa Alfaro**, Hannah Palomino, Anja Knorrscheidt, Martin Weissenborn, Christo Christov, Nicolai Lehnert. "Rational Design of YfeX Biocatalyst for Enhanced Carbene Transferase Reactivity", *Manuscript in preparation.* The following manuscript was published for YfeX R232A data used in this chapter: **Victor Sosa Alfaro**, Sodiq Waheed, Hannah Palomino, Anja Knorrscheidt, Martin Weissenborn, Christo Christov, Nicolai Lehnert. "YfeX – A New Platform for Carbene Transferase Development with High Intrinsic Reactivity", *Chem. Eur. J.* **2022,** e202201474.[79]

3.1 Introduction

As described in Chapter 2, YfeX styrene cyclopropanation and Si-H insertion reactions have moderate product yields and, in the case of the former, a low diastereomer selectivity. The active site of YfeX has an overall hydrophilic pocket due to three prominent amino acids, D143,

R232, and S234 (see **Figure 3.1**). To explore the steric and electrostatic effects of the second coordination sphere (SCS) in the active site on YfeX catalysis, studies on the catalytic carbene transferase activity of these YfeX variants were conducted. Furthermore, styrene is a non-polar substrate with low water solubility requiring hydrophobic interactions for solubilizing and entrance into the active site pocket. One of the important steps in reactivity is substrate binding into the active site, and low cyclopropanation and Si-H insertion yields could be due to a lack of substrate binding inside the polar YfeX active site. We therefore hypothesized that cyclopropanation and Si insertion reactivity could improve when making the active site more hydrophobic, by improving substate binding and retention for reactivity with the carbene intermediate.

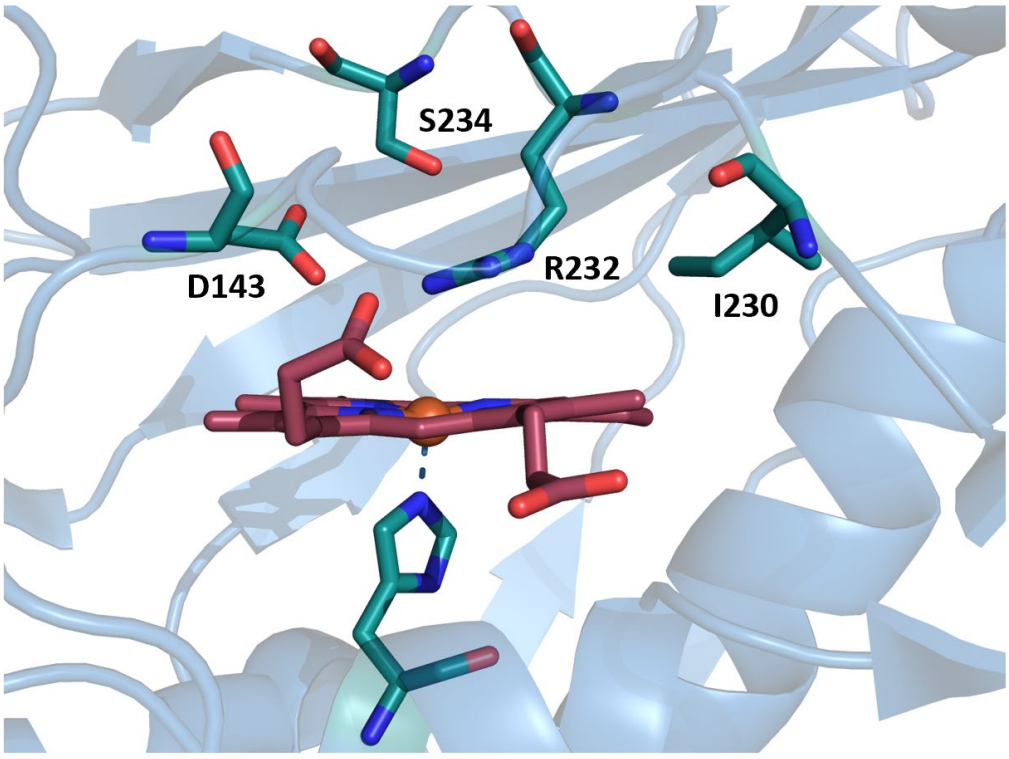

Figure 3.1 PyMOL image of the WT YfeX active site. The important second coordination sphere amino acids are highlighted. The image was generated from PDB code: 2IIZ.

These three key amino acids within the active site, D143, R232, and S234 play an important role in keeping the active site hydrophilic. Therefore, the initial approach is to mutate each of these three amino acids to an alanine, a small hydrophobic amino acid, generating three distinct mutants, D143A, R232A, and S234A, and then study their reactivity. Not only does adding an alanine increase the pocket size, but it also changes the electrostatic interactions by enhancing the hydrophobicity of the active site. Lastly, amino acid I230, found in the entrance pocket near the active site, may have an important role in substrate binding for YfeX (see **Figure 3.1**). Not only is I230 a relative bulky amino acid and hydrophobic, but it is also positioned in between the heme and the entrance channel. The goal is to further open the active site channel and guide substrates into the active site. To do probe this idea the YfeX I230A variant was generated. By introducing an alanine, the active site channel will potentially expand, and this mutation could allow substrate to go into the active site and would lead to increased carbene transfer reactivity.

The most promising mutation is R232A since arginine sits right above the heme plane. R232 not only has a positively charged side chain that repels hydrophobic substrates, but it can potentially block substrates from interacting with the carbene intermediate. D143A and S234A are interesting targets since they could potentially have similar effects as R232A, but they can also change the way styrene binds and hence, change the stereoselectivity of products generated. Interestingly, both R232 and D143 have previously been investigated in peroxidases and it was found that they have an important role in the overall mechanism and hence may also contribute to carbene transferase activity.[74] The study of these variants offers general insight into the role of the SCS in YfeX for carbene transfer reactions, and in this way, identifies targets for future mutagenesis studies to further improve catalysis with YfeX, especially selectivity, as further discussed in this chapter.

3.2 YfeX R232A Variant

To begin analyzing the role of the SCS within the YfeX active site for carbene transfer reactivity, the YfeX variant R232A was investigated, where the R232 residue that sits right above the heme is replaced with Ala. This choice was inspired by work on Mb, where removal of the distal His has a notable effect on catalysis.[53, 55] The N-H insertion with aniline and aniline derivatives for YfeX R232A shows interesting results: although the reactivity for aniline and its *para*-substituted derivatives is similar to that of WT YfeX, there is a difference in the results for *ortho*-, *meta*-, and *para*-toluidine (see **Table 3.1**). These results suggest that Arg232 plays a subtle role in substrate orientation in the active site, influencing the reaction of the carbene intermediate with these bulkier substrates. When R232 is replaced by a smaller amino acid like Ala, the discrimination against the *ortho*- and *meta*-substituted compounds is eliminated, and similar yields are obtained for all toluidine substrates (see **Table 3.1**).

Table 3.1 Results for the N-H insertion reaction of anilines with YfeX R232A.

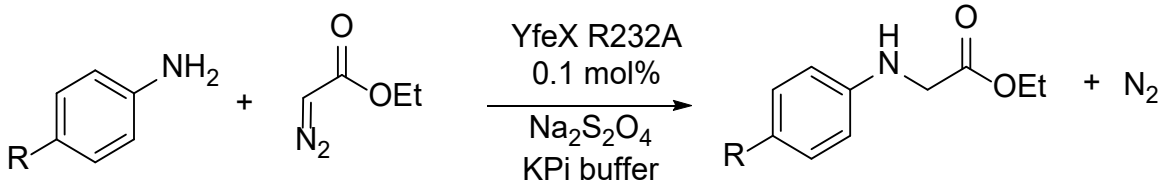

Substrate	Total Yield [a] (%)	TON	Mono: Di
aniline	75	756 ± 64	83:17
p-toluidine	40	408 ± 4	67:33
o-toluidine	50	502 ± 8	80:20

m-toluidine	51	512 ± 96	54:46
4-bromoaniline	43	434 ± 78	87:13
p-anisodine	54	544 ± 23	56:44
4-trifluormethylaniline	51	505 ± 67	83:17

[*a*] Reaction conditions: 20 μM YfeX R232A (0.1 mol%), 20 mM aniline and derivatives, 40 mM EDA, 10 mM dithionite, 1 hour reaction time. Yields are based on GC/MS analysis.

In contrast and surprisingly, cyclopropanation reactions with YfeX R232A show no enhanced reactivity, but instead, a slight decrease of the yields is observed (see **Table 3.2**). To help increase styrene solubility in buffer, 30% methanol co-solvent was again used, similar to WT YfeX. This approach enhanced WT YfeX cyclopropanation reactivity, but unfortunately, this method did not improve catalysis with YfeX R232A. The reason for this became evident from circular dichroism (CD) spectroscopy. The CD data indicate that there is a subtle difference in protein folding between WT YfeX and YfeX R232A, with a slightly increased β-sheet contribution to the fold in the R232A variant (**Figure 3.2**). In addition, the folding of the variant is modified with increasing concentrations of methanol; this trend is not seen in WT YfeX where folding remains essentially unchanged for up to 50% methanol concentrations (see Chapter 2). These results indicate that YfeX R232A has a decreased stability compared to WT, and the structural changes that occur in the presence of methanol are counterproductive for catalysis.

Table 3.2 Results for the cyclopropanation reaction of styrene derivatives with YfeX R232A.

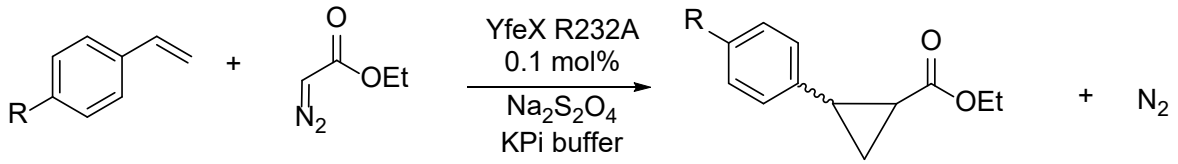

R= -H, -Me, -Cl, -O-Me

Substrate	Total Yield [a] (%)	TON	Cis:Trans
styrene	11	119 ± 12	11:89
styrene[b]	9	89 ± 12	7:93
4-methylstyrene	4	41 ± 5	23:77
vinylanisole	5	46 ± 10	14:86
4-chlorostyrene	5	50 ± 2	13:87

[*a*] Reaction conditions: 20 µM YfeX R232A (0.1 mol%), 20 mM styrene and derivatives, 40 mM EDA, 10 mM dithionite, 1 hour reaction time. Yields are based on GC/MS analysis. [*b*] Reactions were run in 30% methanol.

(A)

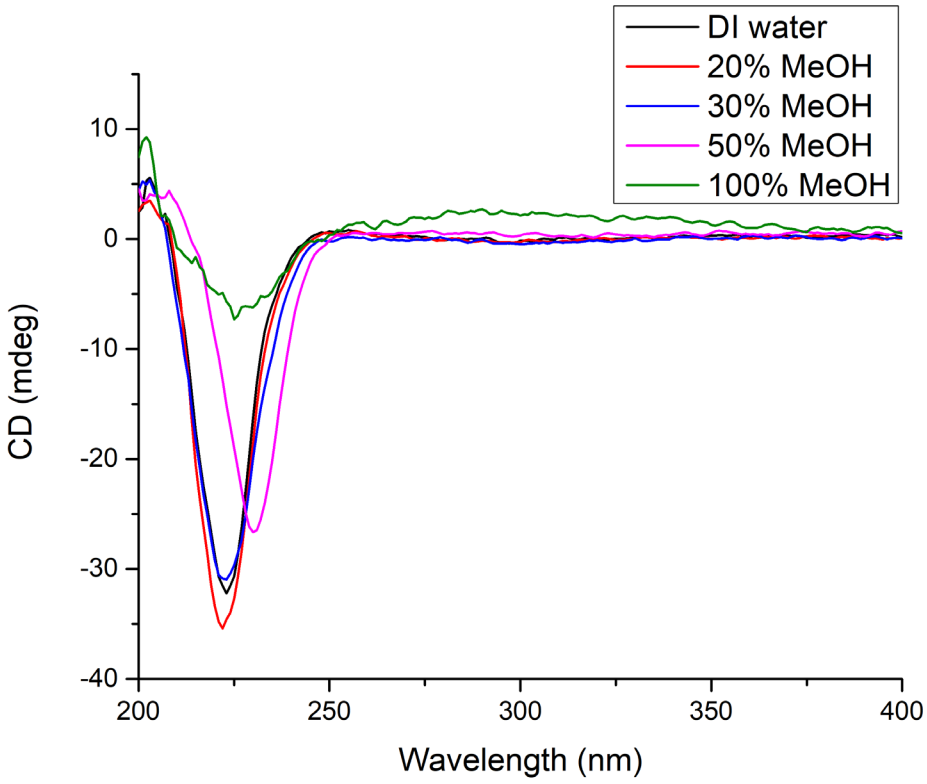

(B)

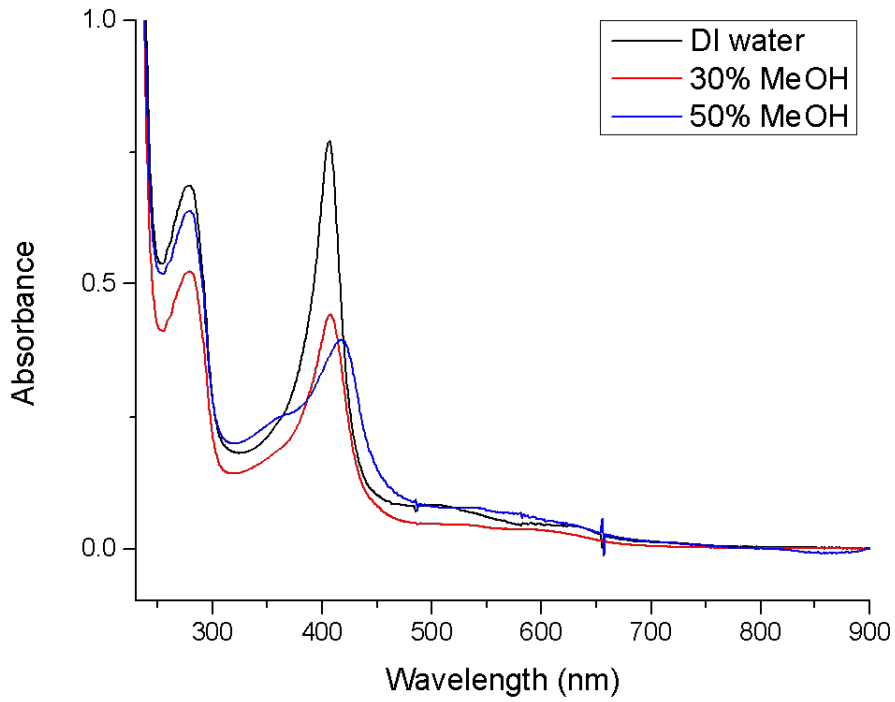

Figure 3.2 (A) Circular dichroism spectra of YfeX R232A [20μM] at various buffer/methanol mixtures. (B) UV-visible spectra of YfeX R232A [30μM] at various buffer/methanol mixtures.

Utilizing molecular dynamics (MD) calculations, conducted by Ms student Hannah Palomino in collaboration with the Christov lab, we are able to see changes that occur in the active site of the R232A variant. Here, one of the propionate groups of the heme changes position and hydrogen bonds with the nearby R195 side chain, instead of interacting with R232 (see **Figure 3.3**). The heme also slightly distorts compared to the heme in WT YfeX, likely due to the new hydrogen bonding network created in the variant. Work by Pfanzagl et al. shows that similar heme movements can be seen in the crystal structure of the dye decolorizing peroxidase (KpDyP) Arg mutant of the pathogenic bacterium *Klebsiella pneumoniae*.[126] These changes in the active site play a role in substrate binding and therefore affect the selectivity, as seen with the changes between *ortho*-, *meta*-, and *para*-toluidine product yields. Furthermore, the removal of R232 opens

the pocket above the heme group. Initially, this exposed active site was thought to be a good approach to enhance reactivity with styrene, but further reactivity studies as described above show that this substitution has more deleterious effects for cyclopropanation reactivity, and there is also a reduced stability of the variant as shown by the CD and UV-vis spectroscopy (**Figure 3.1**).

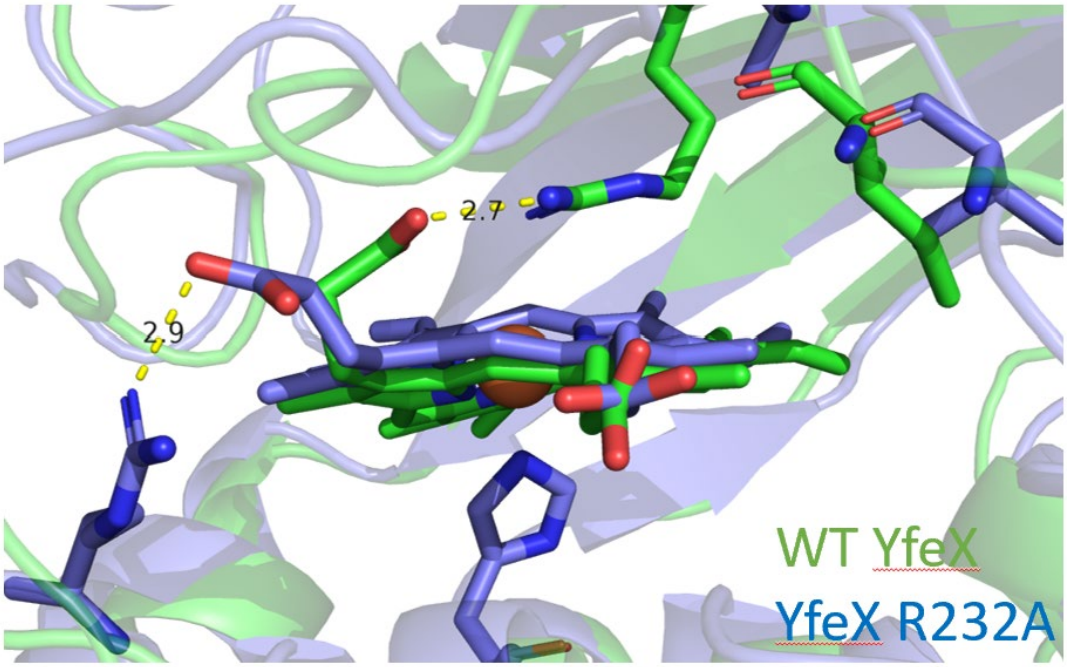

Figure 3.3 Molecular dynamics (MD) results comparing the active site of WT YfeX (in green) to that of YfeX R232A (in blue). Image was generated in PyMOL from MD simulations.

3.3 YfeX I230A Variant 2

The YfeX variant I230A was investigated because of its enhanced carbene transfer reactivity. The I230 residue sits right near the active site tunnel where natural substrates such as hydrogen peroxide are guided into the heme active site.[74] It is proposed that this specific modification may open up the overall tunnel, which would allow other, non-natural substrates to enter. The N-H insertion with aniline and aniline derivatives for YfeX I230A demonstrates

excellent results: compared to WT, the reactivity for aniline increases, giving up to 92% yield, and other *para*-substituted aniline substrates have relative high yields as well. In addition, there is a difference in selectivity between *ortho*-, *meta*-, and *para*-toluidine compared to WT YfeX. We have previously shown that *para*-toluidine is preferred over the other isomers in WT YfeX. Interestingly, with the I230 mutation the *meta*-substituted toluidine derivative generates the highest yield (giving 93% yield) and *para*-toluidine now gives the lowest yield (44%) amongst the three isomers. These results show that I230 plays a subtle role in substrate entrance and that it might somehow affect the orientation of substrates in the active site.

Table 3.3 Results for the N-H insertion reaction of anilines with YfeX I230A.

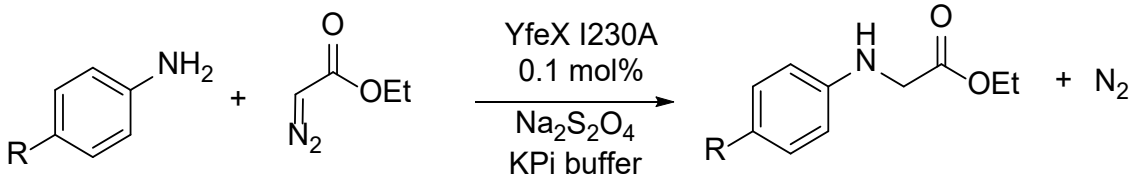

R= -H, -Me, -Br, -OMe

Substrate	**Total Yield [a] (%)**	**TON**	**Mono: Di**
aniline	92	922 ± 87	90:10
p-toluidine	44	447 ± 19	65:35
o-toluidine	74	737 ± 49	89:11
m-toluidine	93	935 ± 17	90:10
4-bromoaniline	37	367 ± 47	92:8
p-anisodine	46	458 ± 17	59:41

[*a*] Reaction conditions: 20 μM YfeX I230A (0.1 mol%), 20 mM aniline and derivatives, 40 mM EDA, 10 mM dithionite, 1 hour reaction time. Yields are based on GC/MS analysis.

Distinct to N-H insertion reactivity, cyclopropanation reactions with YfeX I230A show no enhanced reactivity, but again, a decrease of the yields is observed (see **Table 3.4**). To help increase styrene solubility in buffer, 30% methanol co-solvent was again used, similar to WT YfeX and YfeX R232A. This approach enhanced WT YfeX cyclopropanation reactivity, but unfortunately, this method did not improve catalysis with YfeX I230A, as seen for R232A YfeX as well. The CD data show that there is a difference in protein folding between WT YfeX and YfeX I230A, with a slightly increased β-sheet contribution to the fold in the I230A variant (**Figure 3.4**). These results show that YfeX I230A has structural changes compared to WT, and potentially decreased stability in the presence of methanol, which are all adverse properties for catalysis. The increased tunnel size, as shown by molecular dynamics (discussed below), does not help styrene binding as initially hypothesized, indicating more complex interactions occur during styrene and styrene derivative binding into the active site.

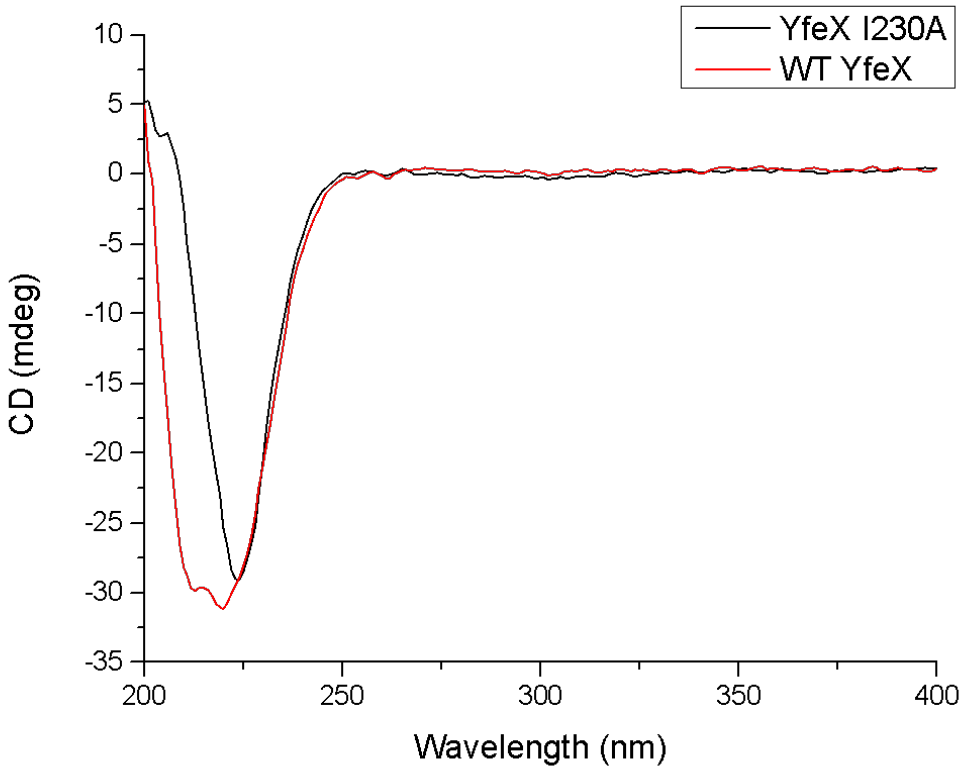

Figure 3.4 Circular dichroism spectra of YfeX I230A [20μM] compared to WT YfeX.

Table 3.4 Results for the cyclopropanation reaction of styrene derivatives with YfeX I230A.

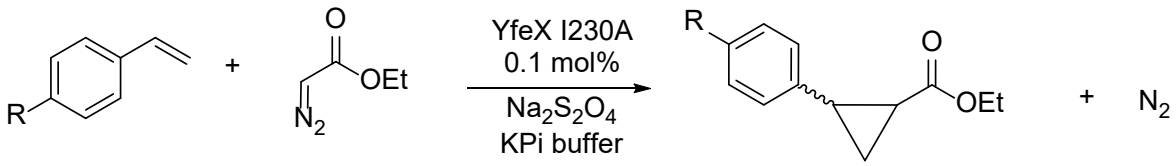

R= -H, -Me, -Cl, -O-Me

Substrate	Total Yield [a] (%)	TON	Cis:Trans
styrene	13	128 ± 14	8:92
styrene[b]	7	70 ± 8	5:95
4-methylstyrene	5.3	53 ± 2	1:99

vinylanisole	6.7	67 ± 8	8:92
4-chlorostyrene	5.9	59 ± 10	9:91

[*a*] Reaction conditions: 20 μM YfeX I230A (0.1 mol%), 20 mM styrene and derivatives, 40 mM EDA, 10 mM dithionite, 1 hour reaction time. Yields are based on GC/MS analysis. [*b*] Reactions were run in 30% methanol.

To investigate the effects of I230 on the overall protein structure, molecular dynamics and electrostatic potential surface maps studies were conducted (by Ms student Hannah Palomino). Electrostatic potential surface analysis shows a drastic change in overall electrostatic charge near the tunnel of I230A compared to WT YfeX, which has a higher positive electrostatic charge (see **Figure 3.5**). The tunnel entrance in I230A also becomes slightly wider as seen in the MD calculations, with the WT YfeX tunnel being ~8 Å wide compared to I230A YfeX tunnel with a ~10 Å diameter. Molecular dynamics results for the I230A variant further show changes that occur near the active site and specifically with the heme cofactor. Here, the propionate group from the heme that does not interact with R232 changes position and hydrogen bonds with a nearby Lys's residue (2.7 Å away) instead of the protein backbone and moves away from the entrance tunnel (see **Figure 3.6**). This heme orientation may influence the way substrates enter the active site and interact with the carbene intermediate, therefore affecting the yields of the *para*- and *meta*-substituted compounds, as seen with toluidine (see **Table 3.4**).

(A) (B)

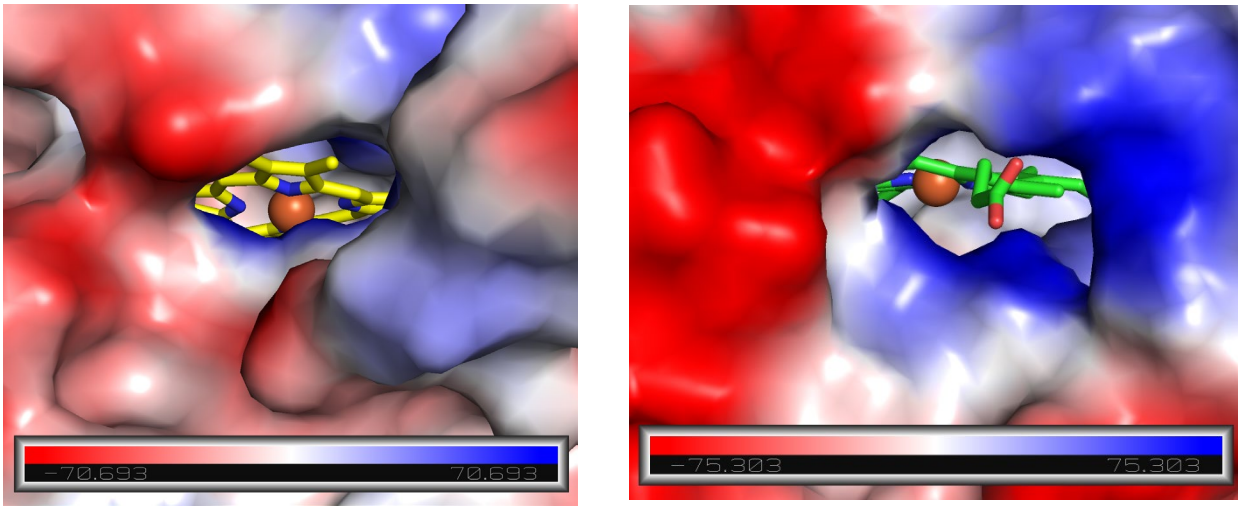

Figure 3.5 Electrostatic potential surface for the active site of (A) YfeX I230A and (B) WT YfeX. Electrostatic potential surfaces were drawn from optimized molecular dynamics calculations using PyMol APBS electrostatics (the red color corresponds to negative potential and the blue color corresponds to positive potential). Image was generated in PyMOL from MD simulations.

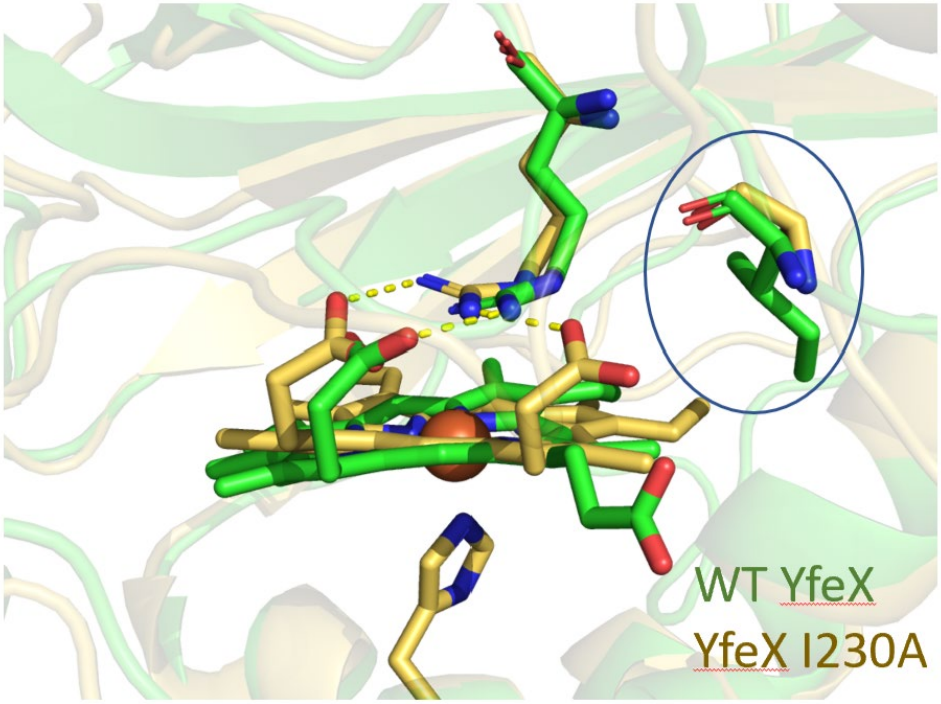

Figure 3.6 Molecular dynamics results comparing the active site of WT YfeX (in green) to that of YfeX I230A (in yellow). The I230 amino acid mutation is circled for clarity. Image was generated in PyMOL from MD simulations.

3.4 YfeX S234A Variant 3

The YfeX variant S234A was also investigated for enhanced carbene transfer reactivity. The S234 residue is positioned above the heme in the active site, ~7.1 Å away. The mutation of this serine near the active site to an alanine may alter the hydrogen bonding network within the active site and play an important role for substrate binding. The N-H insertion with aniline and aniline derivatives for YfeX S234A turned out to be inferior to WT enzyme: the reactivity for aniline decreased giving up to 54% yield, and other *para*-substituted aniline substrates have moderate yields as well. There is also no drastic difference in selectivity between *ortho*-, *meta*-, and *para*-toluidine compared to WT YfeX (see **Table 3.5**). These results show that Ser234 plays a subtle role in reactivity and substitution with Ala is more deleterious than productive.

Table 3.5 Results for the N-H insertion reaction of anilines with YfeX S234A.

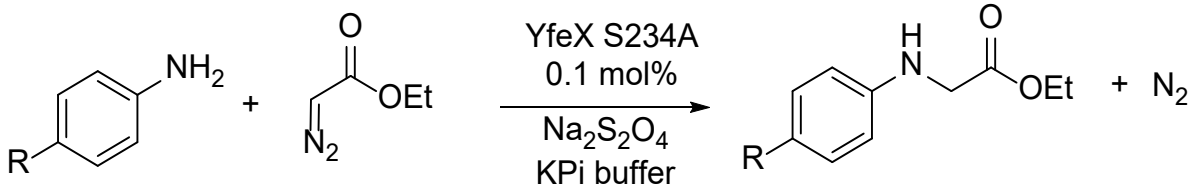

R= -H, -Me, -Br, -OMe

Substrate	Total Yield [a] (%)	TON	Mono: Di
aniline	54	537 ± 62	80:20
p-toluidine	43	429 ± 10	64:36
o-toluidine	61	615 ± 18	81:19
m-toluidine	60	604 ± 31	54:46

4-bromoaniline	53	534 ± 69	87:13
p-anisodine	48	479 ± 31	97:3

[*a*] Reaction conditions: 20 μM YfeX S234A (0.1 mol%), 20 mM aniline and derivatives, 40 mM EDA, 10 mM dithionite, 1 hour reaction time. Yields are based on GC/MS analysis.

Similar to the other variants, cyclopropanation reactions with YfeX I234A show no enhanced reactivity, but again, a decrease of the yields is observed (see **Table 3.6**). To aid styrene solubility in buffer, 30% methanol co-solvent was applied for catalysis. However, this approach did not improve cyclopropanation catalysis with YfeX S234A. The CD data show that there is a difference in protein folding for YfeX S234A compared to that of WT YfeX, with an increased β-sheet contribution to the folding (**Figure 3.7**). These results show that YfeX S234A generates structural changes that are antagonistic for catalysis, in comparison to the other variants discussed above.

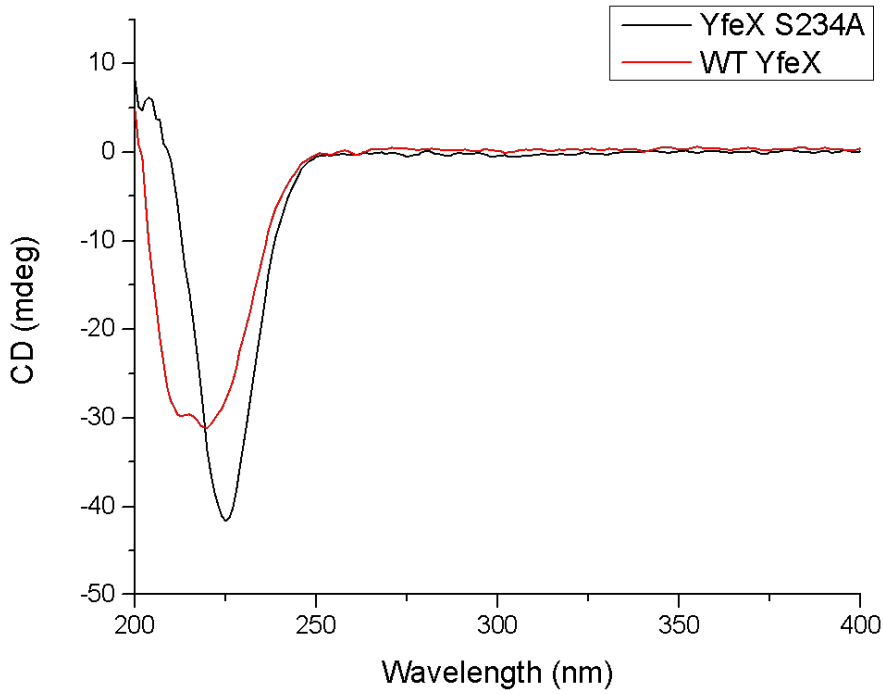

Figure 3.7 Circular dichroism spectra of YfeX S234A [20μM] compared to WT YfeX.

Table 3.6 Results for the cyclopropanation reaction of styrene derivatives with YfeX S234A.

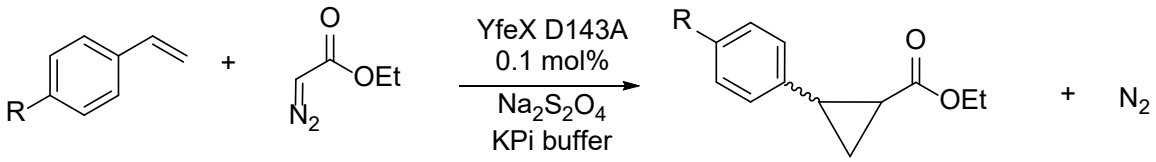

R= -H, -Me, -Cl, -O-Me

Substrate	Total Yield [a] (%)	TON	Cis:Trans
styrene	9	85 ± 7	8:92
styrene[b]	10	96 ± 9	7:93
4-methylstyrene	4.1	41 ± 4	0:100
vinylanisole	5.4	54 ± 3	0:100

4-chlorostyrene	3.3	33 ± 1	0:100

[*a*] Reaction conditions: 20 μM YfeX R232A (0.1 mol%), 20 mM styrene and derivatives, 40 mM EDA, 10 mM dithionite, 1 hour reaction time. Yields are based on GC/MS analysis. [*b*] Reactions were run in 30% methanol.

3.5 YfeX D143A Variant 4

Lastly, the YfeX D143A variant was investigated for carbene transferase activity. Replacement of the D143 residue that sits right above the heme, 3.7 Å away, with Ala it opens the active site pocket. This amino acid substitution has a drastic effect for the overall electrostatic charge within the active site, as seen in the electrostatic potential surface (**Figure 3.8**). Compared to WT YfeX, D143A reduces the negative electrostatic charge within the active site. Furthermore, it has been shown by Pfanzagl et al. that D143 in KpDyP helps hydrogen peroxide bind in the active site, and it stabilizes Compound I via specific hydrogen bonds during the native peroxidase activity of this enzyme.[73, 126] Similarly, we hypothesized that the D143 residue could also participate in carbene transferase reactivity. The N-H insertion with aniline and aniline derivatives for YfeX D143A revealed interesting results: the reactivity for aniline decreases compared to WT YfeX, giving up to 50% yield, but electron withdrawing *para*-substituted aniline substrates show relative high yields, especially for 4-bromo-aniline. In the latter case, D143A YfeX generates the highest yield among WT and all variants studied so far (see **Table 3.7**). D143A YfeX also shows a difference in selectivity between *ortho*-, *meta*-, and *para*-toluidine compared to WT YfeX. In the WT enzyme, *para*-toluidine is the preferred isomer, whereas with D143A the *meta*-substituted toluidine derivative generates the highest yield (88%), and *para*-toluidine shows the lowest yield (54%) amongst the three toluidine isomers. These results show that D143 plays an important role in substrate orientation in the active site.

(A) (B)

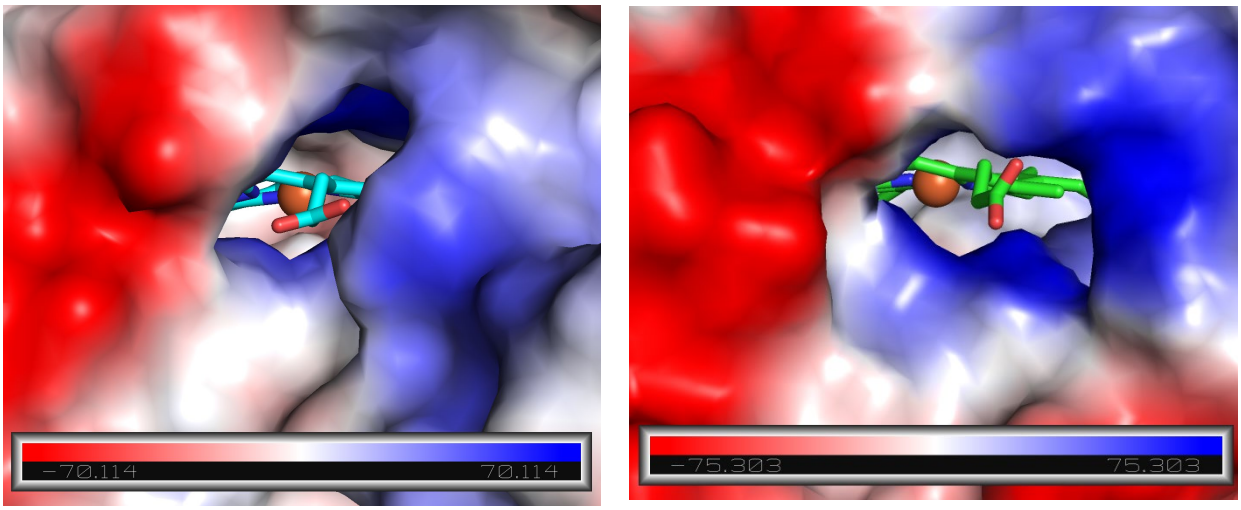

Figure 3.8 Electrostatic potential surface for the active site of (A) YfeX D143A and (B) WT YfeX. Electrostatic potential surfaces were drawn from optimized molecular dynamics calculations using PyMol APBS electrostatics (the red color corresponds to negative potential and the blue color corresponds to positive potential). Image was generated in PyMOL from MD simulations.

Table 3.7 Results for the N-H insertion reaction of anilines with YfeX D143A.

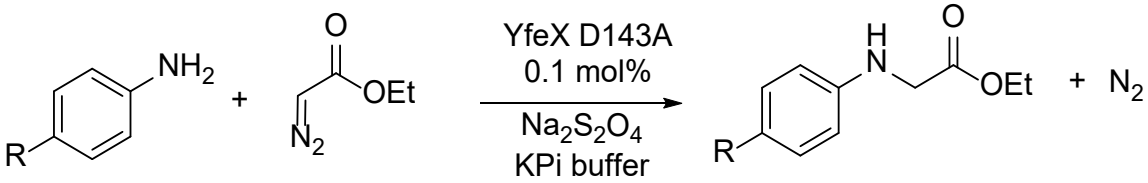

R= -H, -Me, -Br, -OMe

Substrate	Total Yield [a] (%)	TON	Mono: Di
aniline	50	498 ± 15	97:3
p-toluidine	54	540 ± 31	45:55
o-toluidine	78	787 ± 23	87:13
m-toluidine	88	881 ± 42	45:55

4-bromoaniline	84	841 ± 70	77:23
4-trifluormethylaniline	76	764 ± 52	94:6

[*a*] Reaction conditions: 20 μM YfeX D143A (0.1 mol%), 20 mM aniline and derivatives, 40 mM EDA, 10 mM dithionite, 1 hour reaction time. Yields are based on GC/MS analysis.

Lastly, cyclopropanation reactions with YfeX D143A show no enhanced reactivity, but again, a decrease of the yields is observed (see **Table 3.8**). The CD data show that there is a small difference in protein folding for YfeX D143A with a slightly increased β-sheet contribution to protein folding (see **Figure 3.9**), but not as drastic as observed for the variants discussed above. These results show that YfeX D143A has some structural changes compared to WT, and the positively charged active site might help binding of substrates with electron withdrawing substituents and/or their reaction with the heme-bound carbene.

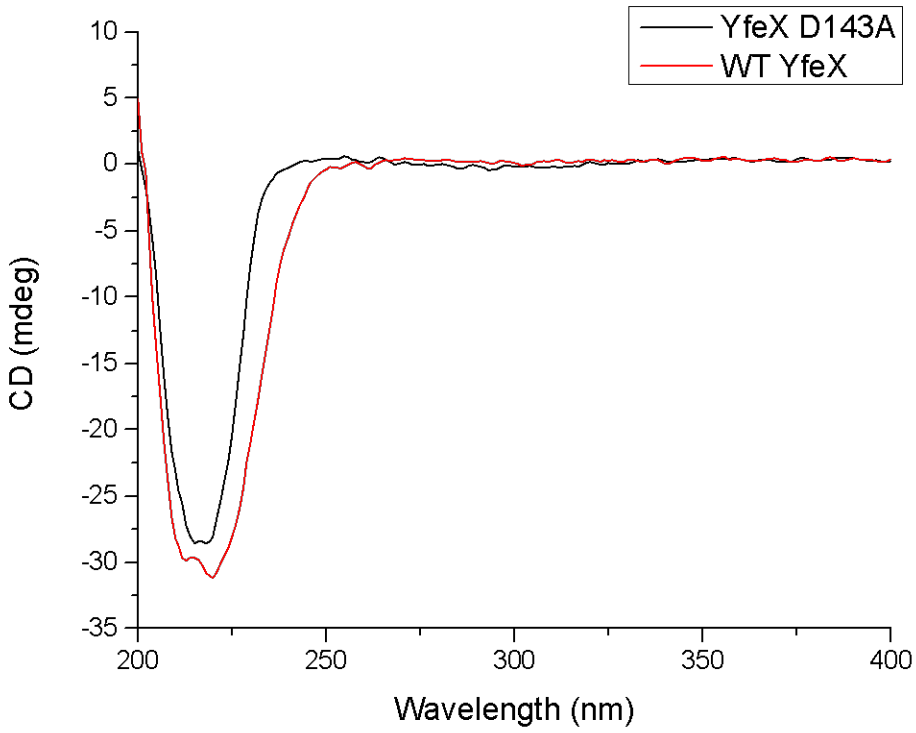

Figure 3.9 Circular dichroism spectra of YfeX D143A [20μM] compared to WT YfeX.

Table 3.8 Results for the cyclopropanation reaction of styrene with YfeX D143A.

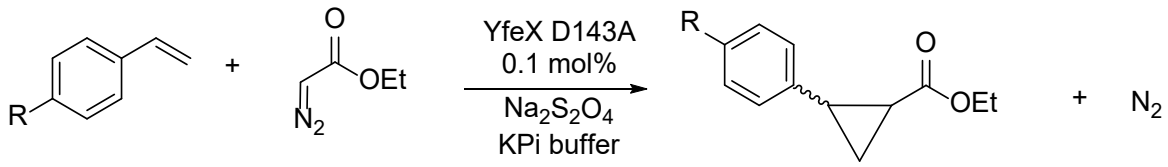

R= -H, -Me, -Cl, -O-Me

Substrate	Total Yield [a] (%)	TON	Cis:Trans
styrene	7	71 ± 16	5:95

[*a*] Reaction conditions: 20 μM YfeX D143A (0.1 mol%), 20 mM styrene and derivatives, 40 mM EDA, 10 mM dithionite, 1 hour reaction time. Yields are based on GC/MS analysis.

3.6 Discussion

As discussed in Chapter 2, WT YfeX is a great target for the design of a novel carbene transferases due to its high intrinsic reactivity.[79] The goal of this chapter is to begin the development of an effective YfeX variant with enhanced biocatalytic reactivity. The approach used was to analyze the effect of key amino acids in second coordination sphere (SCS) near the heme active site, many of them known to be important in the native peroxidase reactivity of the enzyme, on carbene transfer reactivity and regioselectivity. Specifically, four separate YfeX mutants, R232A, I230A, S234A, and D143A, where investigated. It has been shown that SCS interactions play a major role in enhancing biocatalytic activity as well as influencing product diastereo- and enantioselectivity;[55, 94, 99] Previously, Fasan and coworkers explored cyclopropanation selectivity of Mb using crystallographic, computational, and reactivity/mutagenesis studies in myoglobin (Mb) and Mb mutants.[55, 94] They highlight the importance of steric complementarity and noncovalent interactions to guide stereochemical selectivity during cyclopropanation reactivity.[55, 94] They showed that two key SCS amino acids substitution improved carbene transfer catalysis, generating the very active double mutant Mb(H64V,V68A). These two key mutations on the distal face of the heme (residues H64 and V68) enhance activity and stereoselectivity by creating a hydrophobic cavity that helps carbene transfer reactions. Overall, this Mb double mutant displays excellent efficiency for the cyclopropanation of styrene and EDA with yields >99% and over 9999 TON.[55, 94] This double Mb variant is also highly selective for the trans-cyclopropane product with a *de* of 99.9% and an *ee* of the (1S,2S)-trans-cyclopropane of 99.9%.[55, 94] By comparison, wild-type Mb has base reactivity of 36% yield with 180 TON and 87% *de* for the trans-cyclopropane. Therefore, this approach is implemented with YfeX in hope to enhance carbene transferase reactivity.

To investigate the effect of key SCS interactions in the YfeX active site, four different amino acid modifications were targeted and applied to WT YfeX. The first mutation studied in YfeX was Arg232, a positively charged amino acid that could interact with the carbene intermediate and/or the substrates, located right above the heme plane (5.9 Å away from the heme). Interestingly, work done with the peroxidase KpDyP shows that both D143 and R232 have an important role in natural peroxidase activity and it is proposed that they help deprotonate hydrogen peroxide once it is bound to the heme active site and stabilize Compound 0 formation, the ferric hydroperoxo intermediate.[126] Due to its location within the active site, this amino acid could therefore have a direct effect on reactivity. To investigate this point further, the YfeX mutant R232A was generated. The work on YfeX R232A shows that for N-H insertion, an overall similar reactivity is observed for aniline and its *para*-substituted derivatives as in the case of WT enzyme, so the Arg232 residue is flexible enough (in contrast to the distal His in Mb) to not impact overall carbene transfer reactivity significantly. However, a change in selectivity is observed for the toluidine derivatives, with enhanced reactivity towards *ortho*- and *meta*-toluidine, indicating that Arg232 does impact substrate orientation in the active site for bulkier molecules. Interestingly, a slight decrease in yield is observed for cyclopropanation with YfeX R232A compared to WT enzyme. This is in agreement with the proposal that access into the active site is the major hindering factor for cyclopropanation with YfeX, so the R232A mutation only has a small impact on catalysis. We further show that YfeX R232A is not as stable as WT YfeX, and this could contribute to the lower reactivity.

YfeX I230A is also expressed, purified, and studied for enhanced carbene transfer reactivity. The I230 residue is located near the active site channel, where the natural substrate H_2O_2 enters, and it is in the area where non-natural substrates also enter the active site. This mutation

impacts the entrance channel by increasing the overall size of the channel and by allowing for an easier entrance point for non-natural substrates, as shown by MD calculations. N-H insertion reactivity studies on YfeX I230A indeed show an enhanced reactivity for aniline and its *para*-substituted derivatives compared to WT enzyme. Furthermore, a change in selectivity is shown for the toluidine derivatives, with enhanced reactivity towards *meta*-toluidine, indicating that I230 has an influence in substrate orientation in the active site. Computational studies show that when I230 is mutated to the smaller Ala residue, one of the heme's propionate groups, the one near to the protein back bone (and not the propionate that is hydrogen binding to R232) slightly moves away from its original position in WT YfeX and this may influence substrate binding (see **Figure 3.6**). Unfortunately, a decrease in yield is observed for cyclopropanation with YfeX I230A. To help styrene solubility, co-solvent (30% methanol) was used, but regrettably I found that YFeX I230A is not stable under these conditions and has no enhanced activity. Overall, I230A is seen as a positive mutation for enhanced N-H insertion reactivity, but further work needs to be performed to understand the decline in cyclopropanation reactivity.

To continue exploring the effects of SCS groups near the YfeX heme active site, both S234 (7.9Å away from the heme) and D143 (3.7Å away from the heme) amino acids were analyzed by generating the corresponding YfeX mutants, S234A and D143A. Both S234 and D143 aid in maintaining an overall negative electrostatic potential and polar environment in the active. These amino acids side chains are also a part of the hydrogen binding network near the active site that participates in natural substrate binding. It was hypothesized that the S234A and D143A substitutions would have an impact on YfeX's carbene transferase activity, similarly to native peroxidase activity. To investigate their potential influence in carbene transfer reactivity, both the YfeX variants S234A and D143A were expressed and purified. The work on S234A and D143A

shows that for N-H insertion, an overall similar reactivity is observed for aniline and its *para*-substituted derivatives as in the case of WT enzyme, and no enhancement of overall carbene transfer reactivity is observed. However, a change in selectivity is observed for the toluidine derivatives, with enhanced reactivity towards *meta*-toluidine for both S234A and D143A, indicating that both amino acids have a slight influence on substrate orientation in the active site. D143 also showed the highest activity with halogenated, *p*-bromoaniline substrate compared to WT and the other variants. Further work needs to be conducted to understand these interactions, but it is proposed that D143 opens the active site pocket and allows larger halogenated substrates to bind and react with the carbene intermediate. Interestingly, a decrease in yield is observed for cyclopropanation for both YfeX S234A and D143A variants, even after the addition of co-solvent. In general, both S234A and D143A substitutions only have a small impact on catalysis.

Throughout the series of four YfeX variants, it was shown that there is no improvement with cyclopropanation activity compared to N-H insertion reactivity. Since N-H insertion reactivity does in fact increase, for two different variants YfeX R232A and I230A, it indicates that the carbene intermediate is still being generated and it is active. One possible factor that blocks cyclopropanation reactivity is a lack of styrene binding into the active site, which will then allow for reactivity to occur. Styrene does have low buffer solubility and it was proposed the higher concentrations of styrene in solution would help reactivity. It is shown, in Chapter 2, that this is the case: utilizing co-solvents (30% methanol or 30% DMSO) helps increase styrene concentrations in buffer, but this approach did not help with neither of the four variants. The addition of co-solvents may have unintended consequences to the protein structure and reduce overall reactivity. Future work using computational analysis may help understand the reasons why styrene reactivity is low. It could be that there are very specific amino acids that block its entrance

or binding into the heme active site, and hence, reduce its ability to be near the carbene intermediate and react.

In conclusion, our results show that the YfeX variants studied in this Chapter enhance carbene transfer reactivity. Specifically, YfeX R232A and YfeX I230A variants show an increase in N-H insertion reactivity and are therefore good starting points to further improve YfeX for this reaction. We further show that all the SCS amino acids near the heme active site affect regioselectivity in some way, as shown by the changes in *ortho*, *meta*, and *para*- toluidine reactivity. However, and curiously, none of the four amino acid substitutions help with cyclopropanation reactivity, which is difficult to rationalize. Further computational analysis is underway to help identify the factors that limit YfeX' ability to excel in this reaction. We show that simply adding co-solvents is not effective, since protein stability is lowered due to the amino acid substitutions around the active site. Ongoing work will investigate the effects of combining the two most promising single mutants by generating a double variant, such as YfeX R232A I230A. Computational analysis will be used to further analyze these proposed amino acid substitutions, which can help identify other promising mutations. Furthermore, these beneficial mutations can be utilized for the synthesis of pharmaceuticals synthons via its enhanced N-H insertion reactivity.

3.7 Experimental Section

General Procedures

All chemicals and reagents were purchased from commercial suppliers (Sigma-Aldrich, Fisher Scientific, Acros, Frontier Scientific) and used without further purification unless otherwise noted. UV-visible spectra were recorded on an Analytic Jena Specord S600 spectrophotometer using sealed quartz cuvettes.

Gas chromatography/mass spectrometry (GC/MS) analyses were performed using a Shimadzu QP-2010 GC/MS equipped with a 30 m long DB-5 column with 0.25 mm ID. Separation method: 1 μL injection, injector temperature: 200 °C, detector temperature: 250 °C. Gradient: column temperature set to 60 °C for 3 min, then to 250 °C at 20 °C/min and held at 250 °C for 2.5 min (7.5 min for derivatives). Total run time was 15.00 min for the aniline and styrene reactions, and 20.00 min for the reactions with the aniline and styrene derivatives.

YfeX Mutants Protein Expression and Purification. Protein expression and purification followed a protocol by the Weissenborn group (Martin-Luther-University Halle-Wittenberg in Halle (Saale), Germany).[78] The YfeX genes (pCA24N) were transformed into chemocompetent *E. coli* BL21 (DE3) cells by heat shock. Freshly plated transformants were grown overnight in 5 ml Terrific Broth (TB) medium containing 50 μg/ml chloramphenicol. 2 ml of the pre-cultures were inoculated in 400 ml TB autoinduction medium containing 50 μg/ml chloramphenicol. Cells were incubated at 37 °C and 120 rpm. After 4 h of cultivation, aqueous solutions of $FeCl_3$/5-aminolevulinic acid (final concentration: 100 μM) were added, the

temperature was reduced to 30 °C and the cells were incubated for further 16.5 h. Cells were harvested by centrifugation (3000 x g, 20 min, 4 °C). The supernatant was discarded, and the pellets were resuspended in binding buffer (50 mM Kpi, pH = 7.4, 200 mM NaCl). Cells were lysed by sonication (Bandelin Sonoplus HD3100: 6x30 s, 70 % amplitude, pulse mode) and the lysate was incubated with hemin (final concentration: 600 µM) at room temperature for 30 min with a final DMSO concentration of 2 %. The cell debris was removed by centrifugation for 45 min at 4 °C and 6000 x g. Excess of hemin and traces of DMSO were removed during the protein purification steps. The protein exhibits a hexahistidine-tag and was purified by IMAC (immobilized metal ion affinity chromatography) using 1 mL His GraviTrap TALON columns (GE Healthcare Europe GmbH, Freiburg, DE). Washing buffer consisting of 50 mM Kpi (pH = 7.4), 200 mM NaCl and 5 mM imidazole was used to remove unspecific proteins. Protein was finally eluted by the addition of elution buffer (50 mM Kpi (pH = 7.4), 200 mM NaCl and 250 mM imidazole). PD-10 desalting columns (GE Healthcare Europe GmbH, Freiburg, DE) were used for buffer exchange of the pooled elution fractions, yielding the purified protein in 50 mM Kpi (pH = 7.4) and 10 % glycerol (v/v). These stocks were flash-frozen in liquid N_2 and stored at -20 °C. Protein and heme *b* amounts were determined in duplicates using the BSA Protein Assay and the Pyridine Hemochromagen Assay (reduced form, $\varepsilon = 34.7\ mM^{-1}cm^{-1}$ at 557 nm).

Protein mass spectrometry analyses were performed using an Agilent Q-TOF HPLC-MS equipped with a Poroshell 300SB-C8 column. Separation method: 20 µL injection, flow rate: 0.5 mL/min, gradient: 95:5 water/acetonitrile for 3 min, followed by an increase over 10 min to 100% acetonitrile to elute the protein. Total run time was 13 min. Porphyrin mass spectrometry analyses were performed using an Agilent 6230 TOF HPLC-MS.

N−H Insertion Reactions. Reactions were performed as previously described,[53] at a ~450 μL scale using 20 μM YfeX, 20 mM aniline (or aniline derivative), 40 mM ethyl diazoacetate (EDA), and 10 mM $Na_2S_2O_4$. The sodium dithionite (100 mM stock solution) in potassium phosphate buffer (100 mM, pH 7.0) was purged by bubbling nitrogen through the solution for 10 min in a sealed vial. All reagents and proteins were brought into a Coy vinyl anaerobic chamber (10−30 ppm of O_2, 1.5−3.0% H_2) before running the reactions. The as-isolated, ferric YfeX was first reduced to ferrous YfeX through addition of 40 μL of $Na_2S_2O_4$ solution, followed by the addition of 4 μL of aniline or aniline derivatives from a 2 M stock solution in methanol, and 8 μL of EDA (2 M stock solution in methanol), which translates to a total MeOH content of 2.65%. The reactions were left under magnetic agitation for 1 h at room temperature (or as indicated).

Cyclopropanation Reactions. Reactions were performed in the same manner as the N−H insertion reactions, using 20 mM styrene (or styrene derivatives) instead of aniline. All 2 M styrene solutions were prepared in methanol.

Product Analysis. The reactions were analysed, as previously described,[15] by addition of 20 μL of internal standard (2-phenyl-ethanol, 1 M in methanol) to the reaction mixture, followed by extraction with 1.5 or 3 mL of ethyl acetate, depending on the reaction. The organic layers were dried with magnesium sulfate and later filtered and analysed by GC/MS and/ SFC (see General Procedures section for details on GC/MS and SFC analyses). Calibration curves for quantification of the N−H insertion products of aniline and aniline derivatives and the cyclopropanation products of styrene and styrene derivatives were constructed using authentic standards produced synthetically (using 1−2 mol% $Rh_2(OAc)_4$ as the catalyst). These products were used to generate calibration curves for quantification of the aniline and styrene products in the catalytic reactions

with YfeX. The reactions to produce authentic standards were conducted according to the same methods previously reported by our laboratory.[53] All measurements reported in the Results tables were performed in triplicate. Negative control experiments were performed in the absence of YfeX.

The active site is connected to the protein surface via a tunnel, which, in the native peroxidase reaction of YfeX, is proposed to guide hydrogen peroxide to the active site.[74] This tunnel is important, as the substrates for abiological carbene transfer catalysis with YfeX also must enter the active site via this tunnel. Further exploration of the tunnel was done my mutating I230 amino acid that is placed in the active site tunnel.

Computational Methods: System Preparation and MD Simulation. The initial coordinates of the system were generated using an X-ray crystal structure of YfeX (PDB code: 5GT2).[74] The precursor for the iron porphyrin was modelled in the active site using GaussView 6.0.[108] The protonation states of the ionizable side chains were accessed with Propka software,[109] while the axial His215 that is coordinated to the Fe center of the heme was assigned a protonation state based on visual inspection of its local environment. The active center parameters were generated using Metal Center Parameter Builder (MCPB.py),[110] as implemented in Amber18. The parameters for the carbene precursor complex was generated using the Antechamber module of Amber18.[112] All the missing hydrogen atoms in the crystal structure were added with the Leap module in Amber and charges were neutralized using Na^+ counterions. The system was solvated with TIP3P water molecules in a rectangular box within a distance of 10 Å from the protein's surface.[113] Several MD studies on both heme and non-heme Fe containing enzymes have successfully used the parameters generated via this procedure to study both the dynamics and the catalytic mechanism of the Fe containing systems.[39, 91, 114-115]

Chapter 4 NrfA: Mechanistic Insight into Cytochrome *c* Nitrite Reductase (NrfA): Elucidating Electron Storage and Distribution within the Pentaheme Scaffold

In this chapter, the electron storage and distribution properties within the pentaheme protein of *Geobacter lovleyi* NrfA were investigated utilizing electron paramagnetic resonance (EPR) spectroscopy coupled with chemical titration experiments. The following work was done in collaboration with Professor Eric Hegg and post-doc Dr. Julius Campeciño from Michigan State University, who expressed and purified NrfA, and with Professor Sean J. Elliott and graduate student Matthew Tracy from Boston University, who conducted all the electrochemistry experiments. The following manuscripts were published for this chapter: J. Campeciño, S. Lagishetty, Z. Wawrzak, **Victor Sosa Alfaro,** N. Lehnert, G. Reguera, J. Hu, E. Hegg. "Cytochrome *c* nitrite reductase from *Geobacter lovleyi* represents a new NrfA subclass", *J. Biol. Chem.* **2020**, *295*, 11455-11465;[80] and **Victor Sosa Alfaro**, Julius Campeciño, Matthew Tracy, Sean J. Elliott, Eric L. Hegg, Nicolai Lehnert. "Elucidating Electron Storage and Distribution within the Pentaheme Scaffold of Cytochrome *c* Nitrite Reductase (NrfA)" *Biochemistry* **2021**, *60*, 1853-1867.[88]

4.1 Introduction

4.1.1 Cytochrome c Nitrite Reductase (NrfA) Environmental Importance

Nitrogen is a critical building block of many essential biomolecules in all forms of life. In the biosphere, nitrogen is mostly found in the form of gaseous dinitrogen (N_2) which makes up 78% of the earth's

atmosphere.[127] For plants and other organisms to be able to use N_2 it must be "fixed" (reduced to ammonia, NH_3) first. In biological nitrogen fixation, nitrogenase enzymes are responsible for this reaction, which are found in microbes that live in association with leguminous plants, like alfalfa, clover, beans, peas, lentils and lupins.[128-130] Nature alone, however, often does not produce sufficient fixed nitrogen for robust crop cultivation. Because of this, farmers augment this process using synthetic fertilizer, produced by the Haber-Bosch process ($N_2 + 3\,H_2 \rightarrow 2\,NH_3$), to ensure that nitrogen is never a limiting nutrient for crop growth. This supplementation stimulates other pathways in the global nitrogen cycle, a vital biogeochemical cycle driven by microorganisms,[127, 131-132] which ultimately leads to the depletion of ammonia in the soil. Here, nitrification is a major pathway that competes with crops for ammonia, leading to the oxidation of ammonia to nitrite (NO_2^-) and nitrate (NO_3^-). These oxidized forms of nitrogen are detrimental for the environment, since they easily leach into bodies of water, eventually contributing to eutrophication in lakes and oceans.[133-135] Furthermore, nitrate and nitrite can then be taken up by microbes and enter the denitrification process, ultimately being reduced to the gaseous products nitrous oxide (N_2O) and N_2. This process leads to the pollution of the atmosphere (N_2O) and results in general nitrogen loss from the soil. In contrast, the dissimilatory nitrate reduction to ammonium (DNRA) pathway reverses nitrification and, therefore, conserves the usable nitrogen in the soil.[81] Dissimilatory nitrate reduction is a two-step process, mediated by chemoorganic heterotrophic anaerobes,[82-83] where nitrate is first reduced to nitrite by nitrate reductases. This is followed by the reduction of nitrite all the way to ammonium by Cytochrome *c* nitrite reductases (C*c*NIR or NrfA) in one multi-step reaction, as described by the following equation:

$$NO_2 + 8H^+ + 6e^- \rightarrow NH_4^+ + 2H_2O \qquad (1)$$

NrfA is a bacterial enzyme that is located in the periplasm and receives electrons from a designated membrane-bound reductase, which is either NrfH or the NrfBCD complex.[136-139] NrfA homologs have been previously isolated and characterized from a number of organisms, including *Wolinella succinogenes*,[140] *Escherichia coli*,[141] *Shewanella oneidensis*,[142] *Desulfovibrio desulfuricans*,[143] *Desulfovibrio vulgaris*,[144] and *Sulfurospirillum deleyianum*.[145] X-ray crystallography generally shows homodimeric (α_2) structures for these enzymes, where the dimerization occurs along the interface of two alpha-helices via various salt bridges, (**Figure 4.1**) with a molecular mass ranging from 52 to 65 kDa. One exception includes NrfA from the haloalkaliphilic bacterium *T. nitratireducens*, which stabilizes a hexamer containing 48 hemes.[146] NrfA crystal structures reveal that each monomer contains five ferric *c*-type hemes (**Figure 4.2**) within each monomer of the enzyme. These hemes are numbered according to the sequence of occurrence of their binding sites in the polypeptide chain. The active site Heme 1 is presumed to be five-coordinate (5C) and high-spin in the ferric resting state of the enzyme and features an unusual proximal lysine ligand. However, the exact role of the Lys residue for catalysis is not known. The remaining four hemes (Heme 2-5; see **Figure 4.2B**) are bis-histidine coordinated and are low-spin in both the ferrous and ferric state and help shuttle electrons to the active site. These four hemes are covalently linked to the peptide backbone by thioether bonds via cysteine residues of a classical heme-binding motif for periplasmic proteins such as (Cys-X_1-X_2-Cys-His) or (Cys-X_1-X_2-Cys-Lys). Heme 2 is believed to be the initial entry point for electrons from either NrfH or the NrfBCD complex, and it shuttles electrons to the other hemes and ultimately Heme 1 during catalysis. For example, it has been shown that the *E. coli* NrfA utilizes soluble penta-heme cytochrome, NrfB, as a redox partner, but in comparison, *W. succinogenes* and *S. deleyianum* NrfA accept electrons from a membrane-anchored tetra-heme cytochrome (NrfH). One of the

distinguished differences between these proteins is the surface around heme 2, which again may be the docking site for the redox partner.[147]

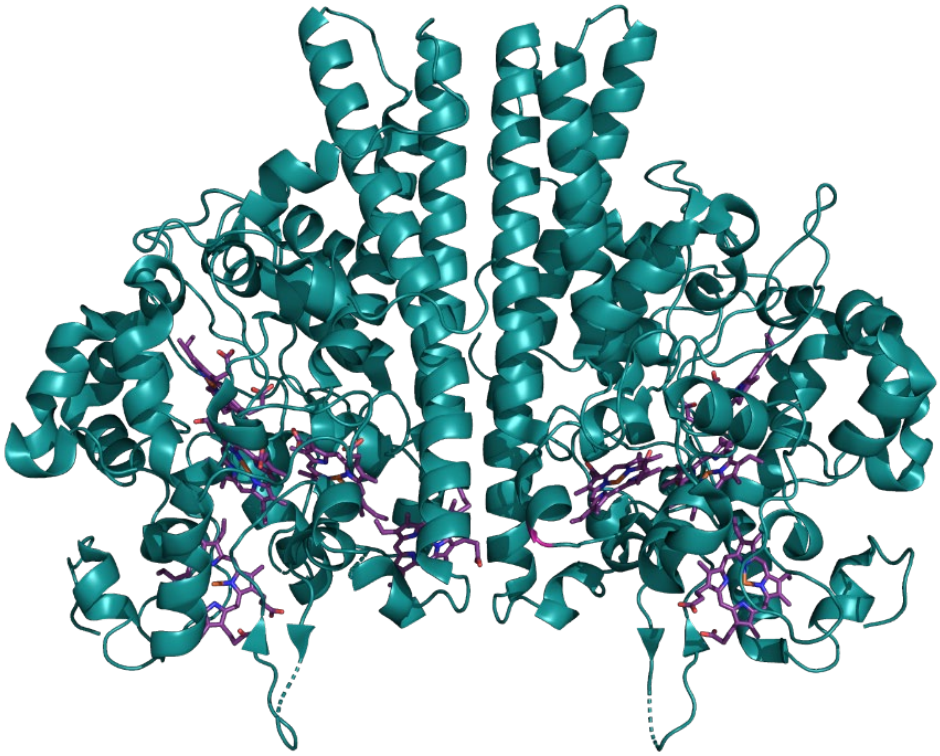

Figure 4.1 Crystal structure of fully oxidized G. lovleyi NrfA (PDB: 6V0A).

All five hemes in the *S. deleyianum* NrfA crystal structure, within a monomer, are in near contact with one another, having Fe-Fe distances of between 9-12.8 Å (**Figure 4.2B**). Hemes 1, 3 and 4 are arranged almost coplanar with edge-to-edge distances below 4 Å and are close enough to allow direct π-electron interactions of the porphyrin rings. Hemes 2 and 5 are farther apart and are perpendicular to their nearby heme (see **Figure 4.2B**). Heme 5 lies close to the dimer interface (dimerization occurs along the interface of two alpha-helices via various salt bridges) with a short Fe-Fe distance of 11.7Å and it is suggested that an electronic interaction between two dimers

occurs via these two heme centers.[148] One of the key questions in this regard is whether Hemes 2-5 act only as a wire to shuttle electrons to the catalytic heme, or whether they could also function as capacitors, storing electrons before, during, or after each catalytic cycle. The fact that NrfA catalyzes the reduction of nitrite to ammonia without the release of any partially reduced species indicates that electrons can be stored on-site, but the details of how electrons are distributed in the electron storage unit are not exactly known. A catalytic mechanism of NrfA for nitrite reduction has been proposed based on crystallographic and computational analysis,[84-86] but many details, especially concerning the nature of key intermediates, are still lacking experimental verification.

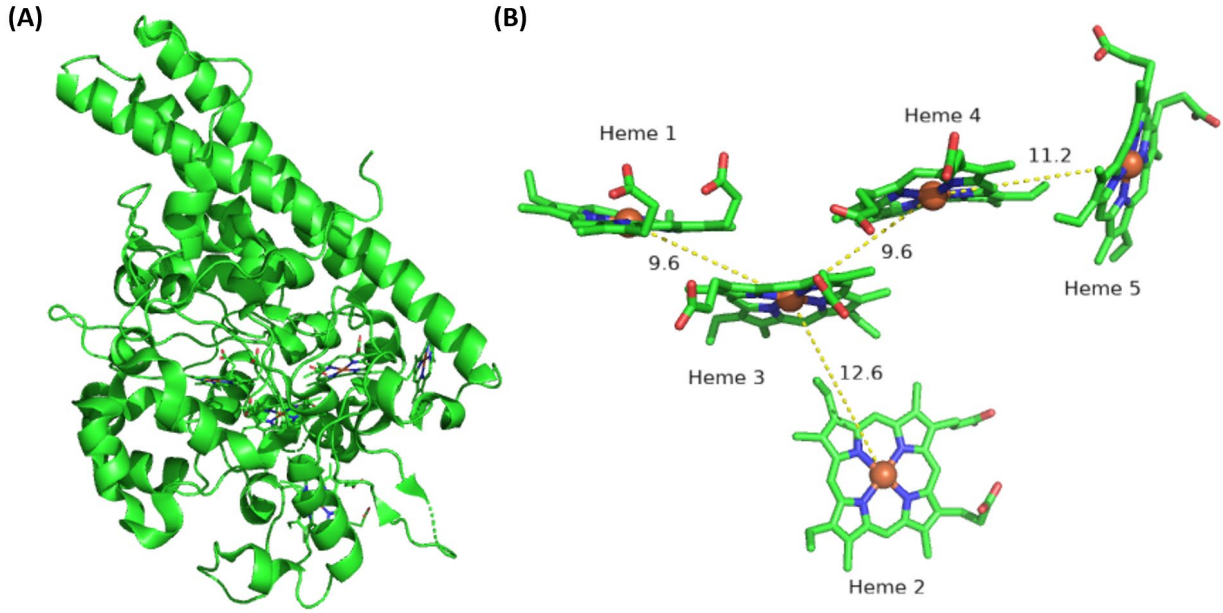

Figure 4.2 A. Crystal structure of one monomer of fully oxidized *G. lovleyi* NrfA (note that the protein crystallizes as a homodimer; PDB: 6V0A). B. Spatial arrangement of the five hemes, along with their numbering scheme. Note that Heme 1 is the active site, and Hemes 1-3-4 are exchange coupled in the fully oxidized form of the enzyme. Distances between the iron centers of neighboring hemes are also indicated.

4.1.2 NrfA Proposed Mechanism

The catalytic mechanism of NrfA for nitrite reduction has been proposed based on crystallographic and computational analysis,[84-87] but many details, especially concerning the nature of key intermediates, are still under investigation. NrfA reduces nitrite to ammonia with high turnover rates including: *S. deleyianum* (962 s^{-1}), *E. coli* (777 s^{-1}), and *D. desulfuricans* (415 s^{-1}) and with high specific activity, for example *S. deleyianum* NrfA with up to 1,050 (μmol min^{-1} mg^{-1}) of nitrite at pH 7.[149] The first proposed reaction mechanism proposed by Neese and coworkers was based on crystallographic analysis and DFT calculations (**Figure 4.3**).[150] The overall proposed mechanism initiates once nitrite binds to the ferrous active site heme. Heterolytic cleavage of the first N−O bond occurs via the assistance of two external protons. Next, two rapid reductions generate a series of heme-nitrosyl intermediates, $\{FeNO\}^6$ −$\{FeNO\}^8$, and a following protonation step is proposed to generate an Fe^{II}–HNO intermediate. Further reduction by two electrons and protonation yield the hydroxylamine intermediate Fe^{II}–H_2NOH.[151] The cleavage of the second N−O bond occurs after an additional reduction and protonation event that allows the release of another water molecule from the active site. The final product, ammonia, is produced and closes the catalytic cycle once it dissociates out of the active site.

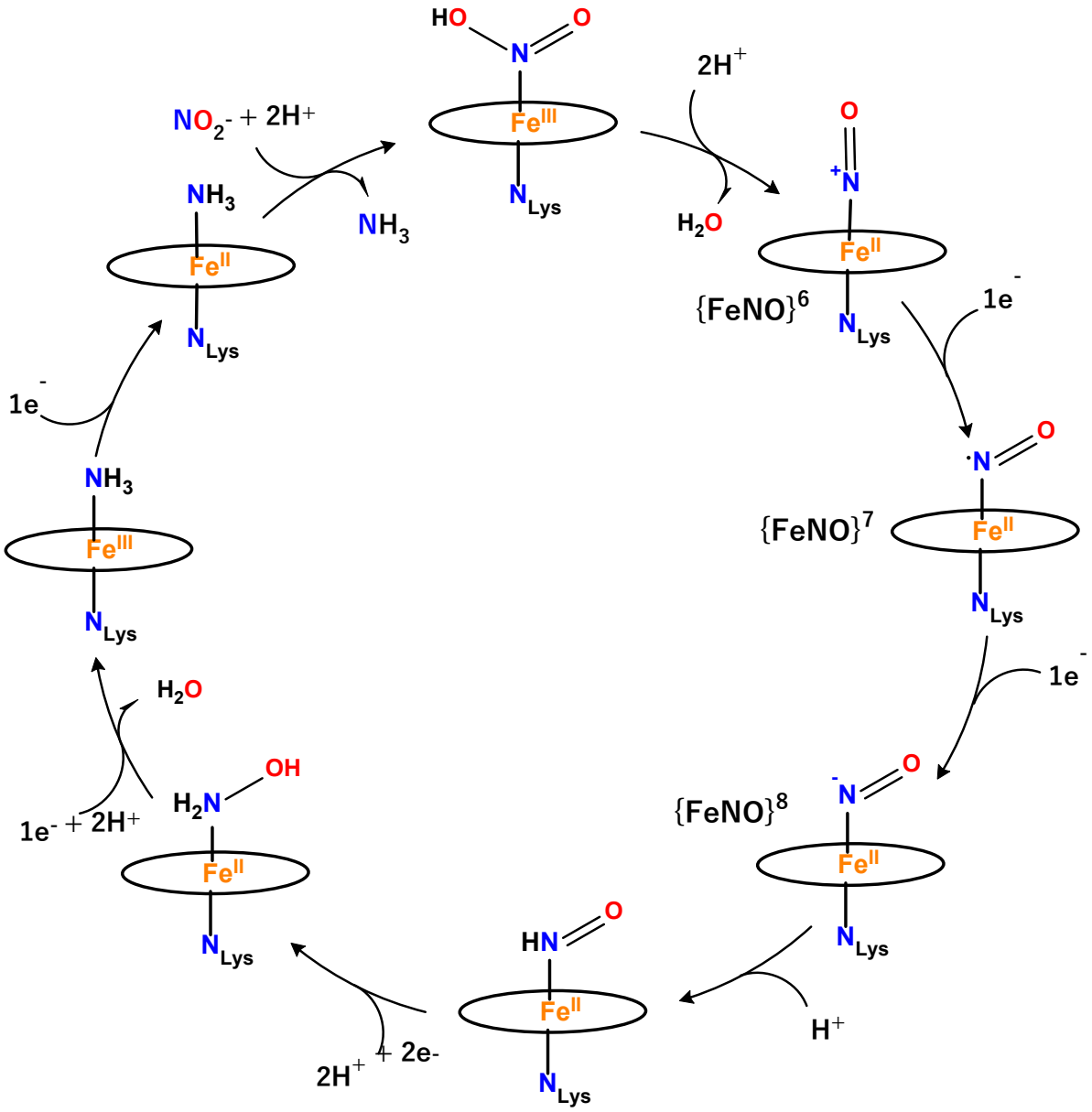

Figure 4.3 Scheme of the proposed reaction mechanism of NrfA nitrite reduction.

Two important components are necessary during nitrite reduction catalysis once nitrite binds to the active site. First is fast electron shuttle into the active site. The required electrons are donated from a designated membrane-bound reductase, which is either NrfH or the NrfBCD complex (species dependent).[136-139] The second critical component are protons, which are supplied through a positively charged substrate channel.[152] Importantly, the substrate channel contains a

bound calcium site (for example in *S. deleyianum* NrfA) or a critical arginine residue (for example in *G. lovleyi* NrfA) that are in direct proximity to the active site (**Figure 4.4**). The role of Ca^{2+} in *S. deleyianum* NrfA within the substrate channel, located only 10.7 Å away from the iron catalytic center, is to help with structural stability of the active site combined with electrostatic interactions, and to assist with proton-transport during catalysis. During turnover hydroxide ions can be stabilized within the Ca^{2+} coordination sphere, while protons can shuttle to the active site and take part in the catalytic nitrite reduction. It was also demonstrated that calcium or arginine are essential for enzyme activity, and when either calcium is removed (for *S. deleyianum* NrfA) or R277 is mutated out (for *G. lovleyi* NrfA) there is no observed enzymatic activity.[80, 153-154]

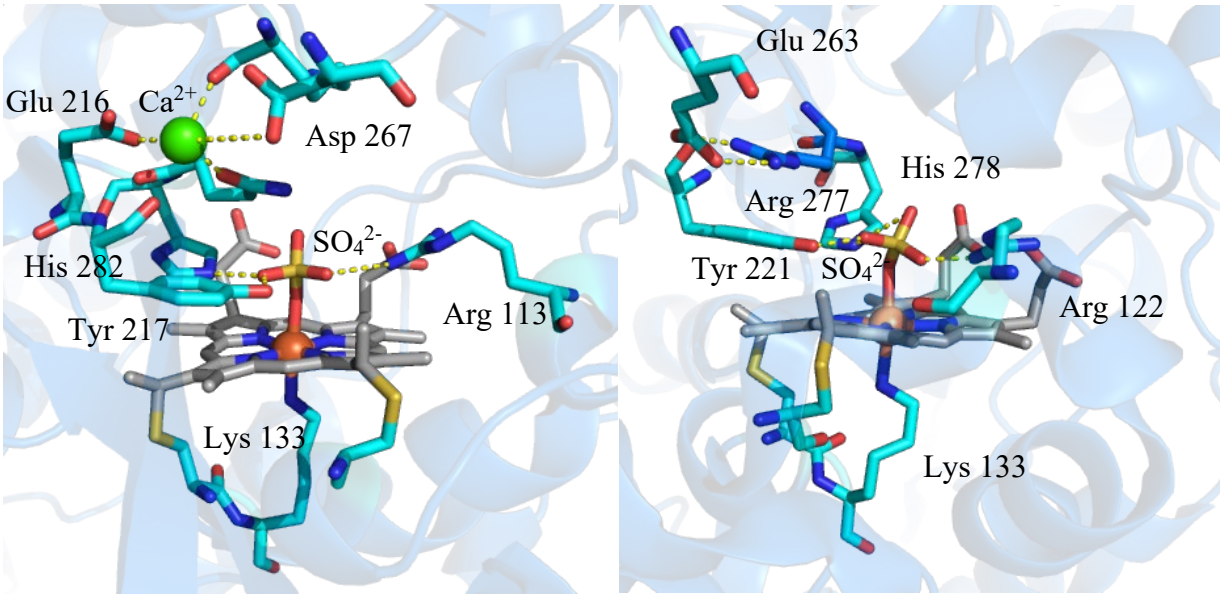

Figure 4.4 Crystal structures of NrfA active site channel from *S. deleyianum* (left) and the *G. lovleyi* NrfA (right). The images were generated using PyMOL from PDB codes 1QDB and 6V0A.

4.1.3 Scope of this Chapter

In previous work, Stein *et al.* made specific midpoint potential assignments to each of the five hemes in *S. oneidensis* NrfA using spectropotentiometric titrations in the presence and absence of a strong field ligand, cyanide, as a mimic of the enzyme's natural substrate, nitrite.[155] The redox potentials of the five hemes were determined, in addition to assigning features of the enzyme's EPR spectrum to individual hemes, by following the appearance and disappearance of the EPR features upon reduction by bulk electrolysis. These results provided insight into the sequence of electron transfers to the pentaheme scaffold of NrfA, but important questions remained, in large part because a complete assignment of the complex EPR spectrum of fully oxidized NrfA has not been accomplished. In addition, due to the close redox potentials of some of the hemes, a clean, step-by-step titration of the enzyme with equivalents of reductant is hard to achieve by electrochemical methods (*e.g.*, bulk electrolysis).

In this chapter, the electron storage and distribution properties within the pentaheme scaffold of *Geobacter lovleyi* NrfA were investigated via EPR spectroscopy coupled with chemical titration experiments. Initially, a chemical reduction method was established to sequentially add electrons to the fully oxidized protein, one equivalent at a time. The step-by-step reduction of the hemes was then followed using UV-Vis and EPR spectroscopy. EPR-spectral simulations elucidate the sequence of heme reduction within the pentaheme scaffold and identify the signals of all five hemes in the EPR spectra. Work performed by our collaborators, the Elliott Lab at Boston University, allowed us to experimentally ascertain the reduction potentials for each heme, observed in a narrow +11 (Heme 5) to -212 mV (Heme 3) range (vs SHE). Based on quantitative analysis/simulation of the EPR data, we demonstrate that Hemes 4 and 5 are reduced first (before the active site Heme 1) and serve the purpose of an electron storage unit within the protein. To

probe the role of the central Heme 3, a H108M NrfA variant was generated where the reduction potential of Heme 3 is shifted positively. The H108M mutation significantly impacts the distribution of electrons within the pentaheme scaffold and the reduction potentials of the hemes. We propose that this is due to Heme 3's important role as an electron gateway in the wild-type enzyme. Overall, this work gives insight into the complicated NrfA mechanism. This chapter has been reproduced in part from a manuscript published in *Biochemistry* (**Victor Sosa Alfaro**, Julius Campeciño, Matthew Tracy, Sean J. Elliott, Eric L. Hegg, Nicolai Lehnert. *Biochemistry* **2021**, *60*, 1853-1867).[88]

4.2 Redox Titrations Followed by UV-Vis Spectroscopy

In order to conduct redox titrations on wild-type (WT) NrfA, a reductant is needed that can cleanly reduce NrfA stoichiometrically, one heme at a time, without the need for excess reductant. To identify a suitable compound, we conducted titrations with several reductants and followed them by UV-Vis spectroscopy. Here, changes in the UV-Vis spectrum are used to follow the reduction of NrfA. In the fully oxidized form of the enzyme, the Soret band is observed at 410 nm (see **Figure 4.5**), which, upon addition of reductant, decreases in intensity. Fully reduced enzyme shows the Soret band at 420 nm. Different reductants that were initially tested include sodium dithionite (E^0 = -660 mV vs NHE at pH = 7.0, referred to as $E^{0'}$), sodium borohydride (E^0 = -1240 mV at pH = 14), [Ti(III)(Cit)$_3$] ($E^{0'}$ = -702 mV) and europium(II) diethylenetriamine pentaacetate (DTPA), [Eu(II)(DTPA)] ($E^{0'}$ = -902 mV). **Figure 4.5** shows the UV-Vis-spectral changes for two representative examples, dithionite and [Ti(III)(Cit)$_3$]. Here, the reductant was added to a solution of 2.0 μM fully oxidized NrfA in 1 equiv steps. Sodium dithionite requires excess of up to 10 equiv (relative to the number of hemes per NrfA monomer, based on the extinction coefficient 547 mM^{-1} cm^{-1} of the Soret band, or a 2-fold excess per heme) to fully reduce all five hemes of the protein (see **Figure**

4.5A). On the other hand, [Ti(III)(Cit)$_3$], a more potent reductant, enabled the stoichiometric reduction of NrfA, one heme at a time (see **Figure 4.5B**). The same is true for [Eu(II)(DTPA)] (data not shown). Therefore, [Ti(III)(Cit)$_3$] was ultimately chosen as the preferred reductant for the EPR titrations. In this regard, it should be noted that [Ti(III)(Cit)$_3$] is not particularly stable in solution and decomposes over time. To address this problem, fresh stock solutions of [Ti(III)(Cit)$_3$] were prepared prior to the titration experiments and calibrated by titration against met-Mb.

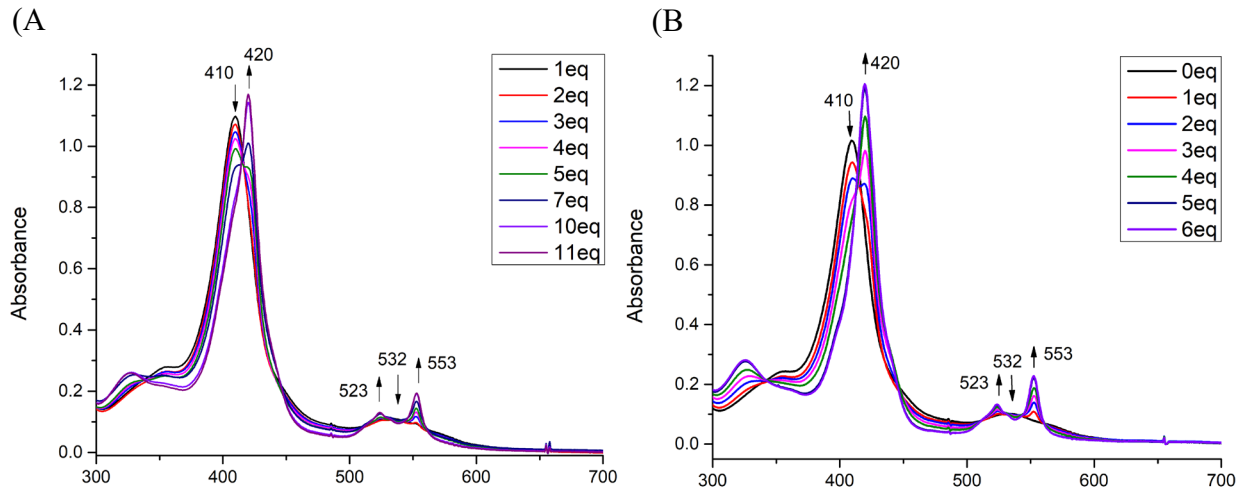

Figure 4.5 UV-Vis-spectral changes of as-isolated, fully oxidized *G. lovleyi* NrfA upon addition of reductant in different equiv as indicated (given relative to the number of hemes per NrfA monomer): (A) sodium dithionite; (B) [Ti(III)(Cit)$_3$] (in this case, note the that the spectra for 5 and 6 equiv overlay exactly).

4.3 Analysis of the EPR Spectra of Fully Oxidized NrfA and Comparison to the Literature

As-isolated, fully oxidized NrfA contains five *c*-type ferric hemes with unique EPR spectroscopic signatures, based on axial ligand coordination/orientation and the coupling between the hemes in the pentaheme unit. Heme 1 is presumably 5C in as-isolated protein, with proximal lysine coordination and a high-spin ferric (S = 5/2) ground state. However, the typical g_{eff} = ~6 and 2 signals of high-spin ferric hemes that would therefore be expected for Heme 1 are obstructed

by exchange coupling with Heme 3, as previously noted,[155] but the details of this interaction were not investigated in the previous work (which requires detailed spectral simulations as performed here; see below). In the previous report, direct evidence for the Heme 1-3 coupling was derived from electrochemical titration experiments, where upon reduction of Heme 1 to the ferrous state, the signals of Heme 3 appear in the EPR spectrum.[155] In addition, Hemes 2-5 have been shown to be low-spin, bis-His ligated hemes with S = 1/2 ground states in the ferric form. In order to assign the signals for Hemes 2-5, it is important to first review the basic structural properties of bis-His ligated hemes, and how this relates to their EPR properties.

In many previous studies on metalloproteins and synthetic model complexes, it has been established that structural factors and electronic properties of bis-His ligated hemes are clearly reflected by their EPR properties.[156-157] In short, these studies have shown that the relative orientation of the imidazole planes of the axially-coordinated His ligands is the key determining factor for the EPR-spectroscopic properties of a bis-His ligated heme, giving rise to unique spectral features. Hemes with axial imidazole groups with close to parallel orientation exhibit rhombic EPR spectra with pronounced g anisotropy. Signals for all three g values are usually observed in the spectra, where $g_z > g_y > g_x$ (the latter two by convention). Hemes with axial His ligation with close to perpendicular orientation of the imidazole planes give rise to so-called "g_{max}" (or HALS) spectra with large g anisotropy ($g_{max\ (z)} = 3 - 4$).[156] The EPR features are relatively weak, and other than g_z, the remaining resonances are often difficult to observe.

In the case of Hemes 2 and 3, the axial imidazole groups show a parallel orientation, which should lead to the generation of rhombic EPR spectra as described above. Indeed, previous studies identify very similar Heme 2 signals at g = 2.94, 2.29, 1.52 and 2.92, 2.3, 1.52 in the spectra of *S.*

oneidensis and *E. coli* NrfA,[147, 155] respectively. The Heme 3 signals are not observed in fully oxidized enzyme, due to exchange coupling with Heme 1 (see above). In contrast, Hemes 4 and 5 show axial His ligation with a perpendicular orientation of the imidazole planes and should therefore give rise to weaker g_{max} signals. The position of these signals is not easily determined in the EPR spectrum of fully oxidized NrfA. Based on electrochemical titration experiments, the Heme 4 signals were assigned to a feature at g = 3.39 in *S. oneidensis* NrfA, whereas the signal for Heme 5 could not be identified unambiguously.[155] In the study on *S. oneidensis* NrfA, it is proposed that Heme 5 is coupled to the Heme 5' of the other subunit in the assumed NrfA homodimer. However, because our recent studies have shown that the homodimeric structure of the protein, observed by crystallography (see **Figure 4.1**), is not necessarily maintained in solution,[80] this explanation given by Stein *et al.* in their report is questionable.

A typical EPR spectrum of as-isolated, fully oxidized *G. lovleyi* NrfA, obtained in this work, is shown in **Figure 4.6** (black line). The data contain prominent features that include the rhombic signal with g values of $g_z = 3.01$, $g_y = 2.21$ and $g_x = 1.52$, which are assigned to Heme 2 based on literature precedence, and its bis-His coordination with parallel imidazole planes. This heme is magnetically isolated from the other hemes in the scaffold and would therefore be expected to give relatively unperturbed EPR signals. The EPR signals observed at g_{eff} = 10, 3.6 were previously assigned to the exchanged-coupled Heme 1-3 pair.[147, 158] Similar EPR signals were reported for *S. oneidensis* NrfA with g_{eff} = 15, 3.42 and *E. coli* NrfA with g_{eff} =10.8, 3.5 (with the 3.5 signal being more intense than in the other cases).[147, 155] As discussed below, we propose that Hemes 1-3-4 form a triad of exchange coupled hemes, based on our EPR simulations. Overall, the as-isolated, fully oxidized *G. lovleyi* NrfA has EPR features that are similar to those of both *S. oneidensis* and *E. coli* NrfA.

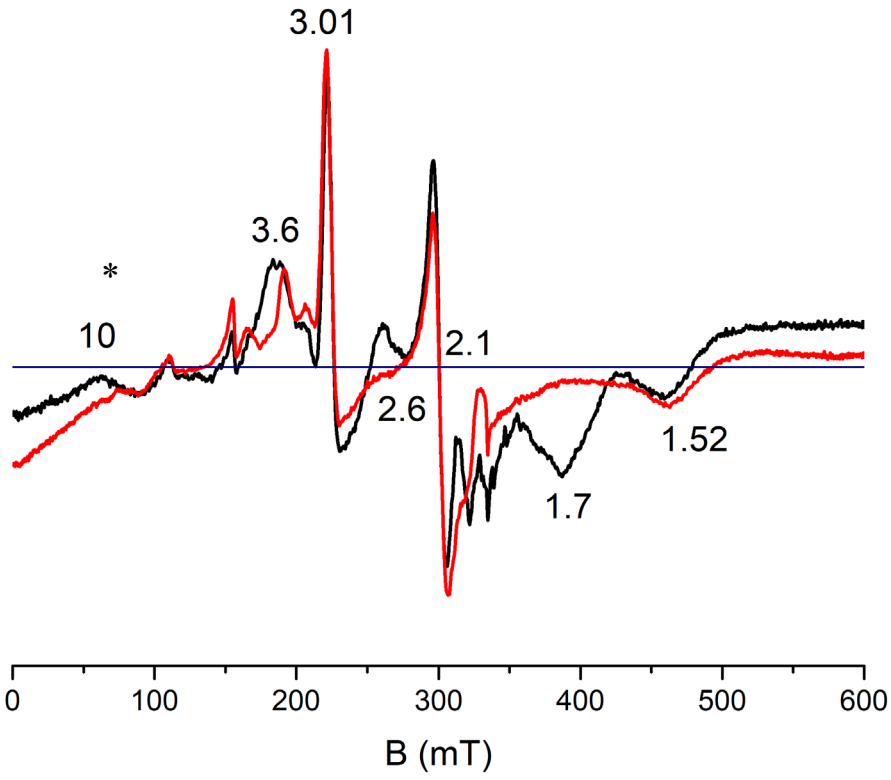

Figure 4.6 Typical X-band EPR spectrum obtain for as-isolated, fully oxidized *G. lovleyi* NrfA in 50 mM HEPES buffer with 150 mM NaCl at pH 7.0 (black line), and oxidized NrfA with [400 μM] cyanide added (red line). The derivative signal marked with an asterisk (*) in the cyanide-bound enzyme corresponds to an impurity (from the treatment of the sample with chelex).

Cyanide-bound NrfA. To further investigate Heme 1 and its coupling pattern to the other hemes, excess cyanide (CN^-) was added to the as-isolated, fully oxidized protein sample to mimic nitrite binding and switch Heme 1 to low-spin ferric (S = 1/2), as previously shown.[155] The EPR-spectral changes observed when a 100 μM solution of as-isolated, fully oxidized NrfA was exposed to 400 μM CN^- are shown in **Figure 4.6** (red). The addition of cyanide to the protein causes complex changes to the EPR spectrum that are not easily rationalized. As shown in **Figure 4.6**, the features at g = 10, 3.6 and 1.7 as well as the derivative-shaped signal centered at g = 2.6 disappear upon cyanide binding to Heme 1. Hence, all of these spectral changes must relate to the spin state change

at Heme 1, and the concomitant change in the exchange coupling with Heme 3. The isolated rhombic signals of Heme 2 do not change upon the addition of cyanide, as shown in **Figure 4.6**. This is due to a lack of magnetic interactions between Heme 2 and Heme 1.

Previous work on *S. oneidensis* NrfA reported similar EPR-spectral changes in the g = 10, 3.6 region upon cyanide binding. In addition, an intense signal at g = 2.87 disappears and is thought to become a sharp signal at g = 2.94 in cyanide-bound *S. oneidensis* protein.[155] In contrast, the changes at g = 2.6 and 1.7 in *G. lovleyi* NrfA are not observed in the previous studies on *S. oneidensis* NrfA.[155]

4.4 EPR Simulations and Assignments

To simulate the EPR spectrum of the as-isolated, fully oxidized *G. lovleyi* NrfA, we began to analyze the different components discussed above and previously assigned in the literature. As noted, the signals at $g_z = 3.01$, $g_y = 2.21$, and $g_x = 1.52$ arise from Heme 2, and the corresponding simulation is shown in **Figure 4.7B** (red; see also **Table 4.1**). In *S. oneidensis* and *E. coli* NrfA, the corresponding signals are observed at $g_z = 2.94$, $g_y = 2.29$ and $g_x = 1.51$ and $g_z = 2.92$, $g_y = 2.3$ and $g_x = 1.52$, respectively,[147, 155] which indicates an interesting variation in the properties of Heme 2 in different NrfA homologs. In the literature, an EPR analysis of the triheme periplasmic Cytochrome A (PpcA) from *Geobacter sulfurreducens* was reported by Ponomarenko et al.[159] PpcA contains one rhombic heme and two g_{max} hemes, and similarly to NrfA, the spectrum of the rhombic heme is clearly distinguished from the other signals. In this case, the rhombic heme shows EPR signals at $g_z = 2.96$, $g_y = 2.21$, and $g_x = 1.47$, similar to Heme 2 of *G. lovleyi* NrfA.

Since Hemes 4 and 5 are expected to show g_{max} EPR signals due to their bis-His coordination with perpendicular imidazole planes (with $g_z > 3$), the remaining signals with $g < 3$ of the fully oxidized protein must therefore correspond to the Heme 1-3 coupled dyad. However, despite many efforts, we were not able to obtain satisfactory spectral simulations with this model. On the other hand, as shown in **Figure 4.2**, Hemes 3 and 4 are at a similar, π-π stacking distance to each other as Hemes 1 and 3. Here, the iron-iron distances are ~9.6 Å for both heme pairs (Hemes 1 and 3 and Hemes 3 and 4, respectively; see **Figure 4.2**). We therefore started to explore the possibility that all three hemes, 1, 3 and 4, actually form an exchange-coupled triad.

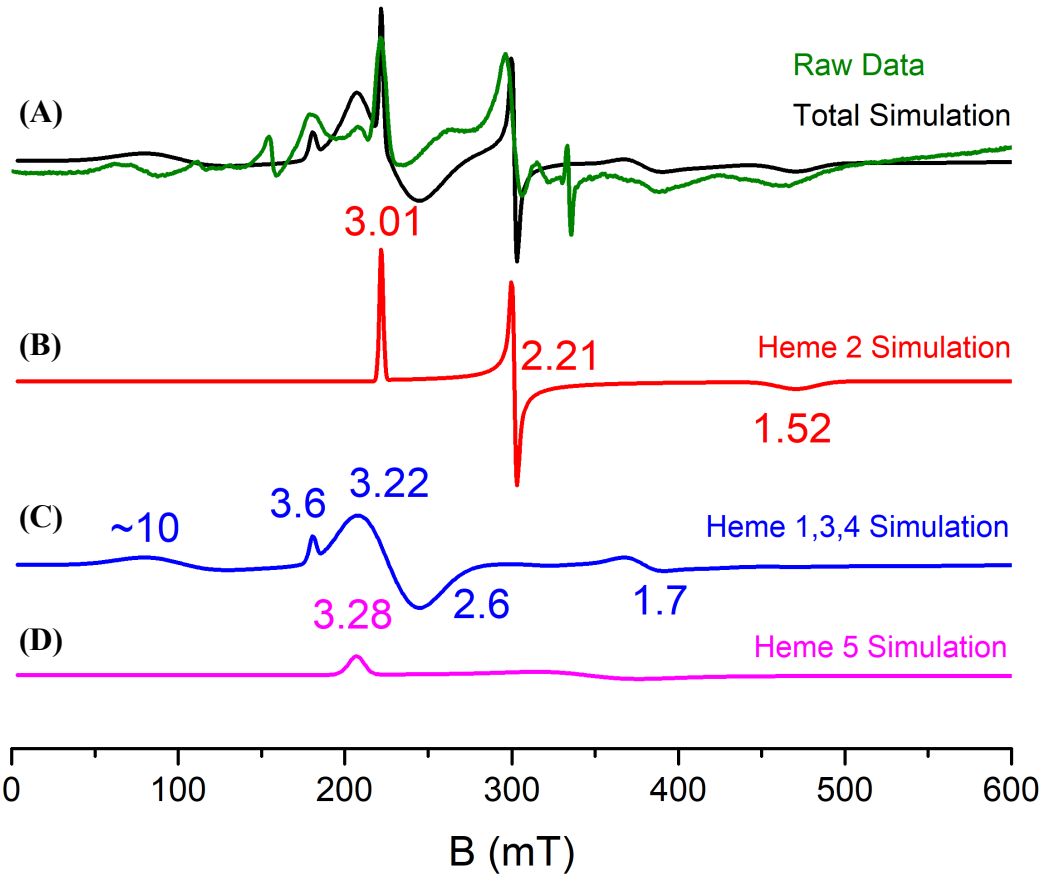

Figure 4.7 A. Overlay of the EPR spectrum of as-isolated, fully oxidized *G. lovleyi* NrfA (green line; highly purified protein via multiple rounds of chromatography) and the total simulation (=

sum of the spectra shown in panels B-D, black line). The three simulate components consist of [Heme 2] (red, panel B), [Heme 1 (S=5/2)-Heme 3-Heme 4] (blue, panel C), and [Heme 5] (magenta, panel D).

Because Heme 1 is in the high-spin ferric state, its three g values are about 2. As a starting point for the simulations, we assumed ZFS parameters of this heme that are typical for high-spin ferric hemes in the literature ($|D| < 10$ cm^{-1}, $E/D \sim 0$).[160] The EPR parameters of Heme 3 can be obtained from the EPR redox titration (see below), as this heme becomes visible in the EPR spectrum once Heme 1 is reduced. The EPR parameters for Heme 3 are therefore: $g_z = 3.22$, $g_y = 2.2$, and $g_x = 1.41$ (see below and **Table 4.1**). Finally, since Heme 4 is a g_{max} heme, we know that its main EPR signal is roughly located in the $3.1 \leq g_z \leq 3.8$ region. Unlike Heme 3, Heme 4 does not show up with prominent signals in the redox titration. Finally, for the simulations, we also took into consideration the spectral changes that are observed upon cyanide binding to Heme 1, as further discussed below. To simulate the three-heme coupling, a range of possible values for the exchange coupling constants, *J*, between Heme 1-Heme 3 (J_{13}) and Heme 3-Heme 4 (J_{34}) were explored in EasySpin. It should be noted here that we treated all exchange coupling interactions as isotropic, to limit the parameter space, but this is certainly an approximation. As (J_{13}) increases from 0.5 cm^{-1} to 3.0 cm^{-1} (**Figure 4.8**), the derivative signal at 240 mT (see **Figure 4.7**) moves to lower magnetic fields (~350 - 400 mT), allowing us to accurately estimate the value of this coupling constant, which must be $J_{13} < 0.5$ cm^{-1}. Next, we analyzed the coupling between Hemes 3 and 4 and simulated spectra where (J_{34}) increases from 0.01cm^{-1} to 2.0 cm^{-1} (**Figure 4.9**). As J_{34} increases, the signal at 200 mT and the derivative signal at 240 mT move to lower magnetic fields, and when $J_{34} > 1$ cm^{-1}, all signals converge into a broad signal at 120 mT. From these findings, we conclude that $J_{34} < 0.01$ cm^{-1}.

(A)

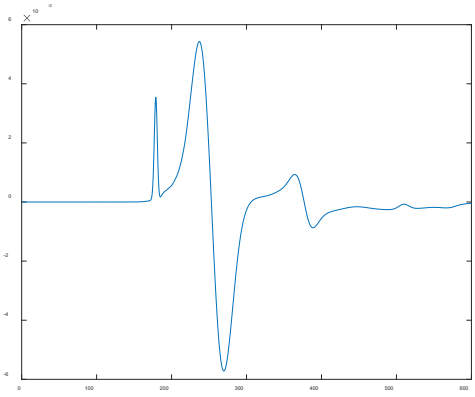

(B)

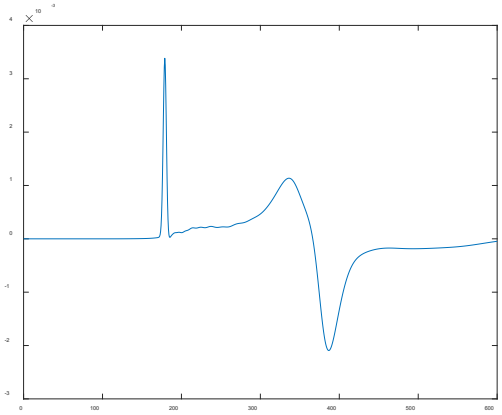

(C)

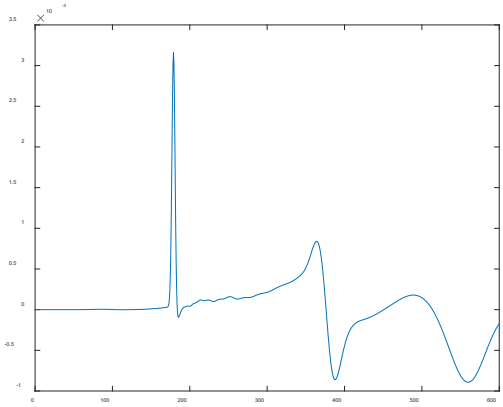

(D)

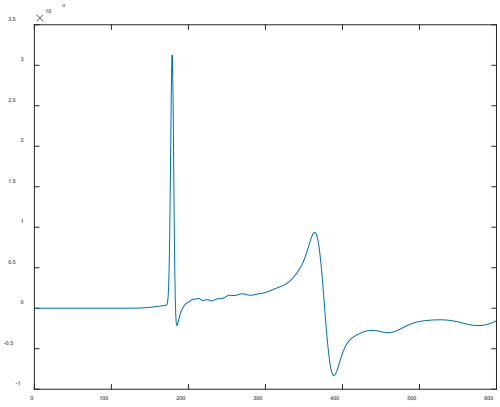

Figure 4.8 EPR simulations of the Heme 1-3-4 triad. Variation of the J_{13} value (coupling of Hemes 1 and 3) with (A) J_{13} = 0.5 cm^{-1}, (B) J_{13} = 1.0 cm^{-1}, (C) J_{13} = 2.0 cm^{-1}, (D) J_{13} = 3.0 cm^{-1}. All simulations were conducted with: D = 2.5 cm^{-1}, E = 0.005 cm^{-1}, E/D = 0.002, and J_{34} = 0.001 cm^{-1}. For the g values used in the simulations see **Table 4.1**. As evident from panels A-D, the position and intensity of the derivative-shaped signal at ~250 mT in panel A is highly dependent on the magnitude of J_{13}, allowing us to fit the value of this exchange coupling constant.

(A) (B)

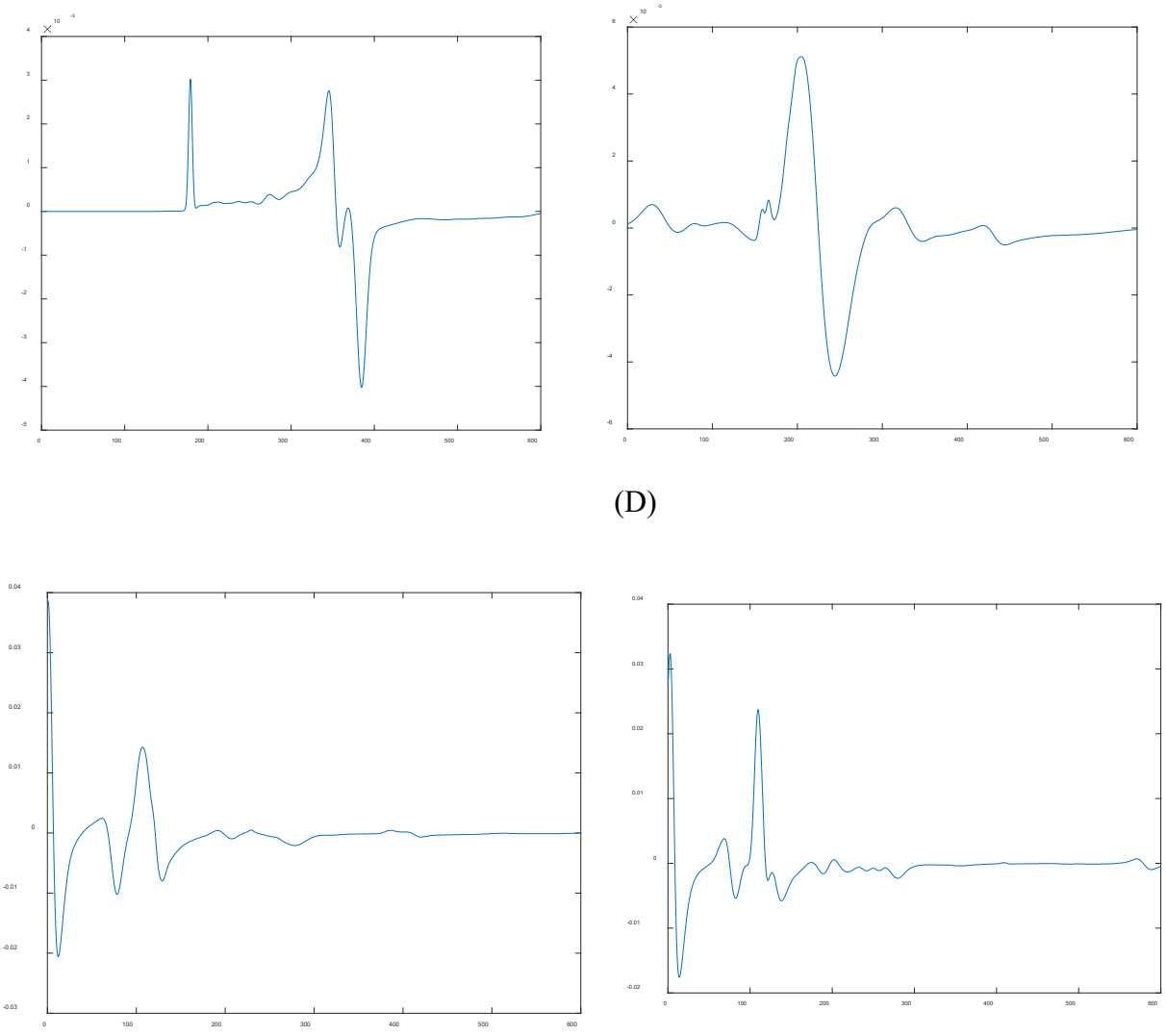

(C) (D)

Figure 4.9 EPR simulations of the Heme 1-3-4 triad. Variation of the J_{34} value (coupling of Hemes 3 and 4) with (A) $J_{34} = 0.01$ cm^{-1}, (B) $J_{34} = 0.1$ cm^{-1}, (C) $J_{34} = 1.0$ cm^{-1}, (D) $J_{34} = 2.0$ cm^{-1}. All simulations were conducted with: $D = 2.5$ cm^{-1}, $E = 0.005$ cm^{-1}, $E/D = 0.002$, and $J_{13} = 0.334$ cm^{-1}. For the g values used in the simulations see **Table 4.1**. As evident from panels A-D, the shape of the spectra is highly dependent on J_{34}, allowing us to fit the value of this exchange coupling constant.

For the simulation, the ZFS parameters of Heme 1 were also varied, starting with *D* in the 2 - 5 cm^{-1} range and using the constraint that *E*/*D* remains close to axial. When increasing the *D* value further in the simulation (**Figure 4.10**), the signals at 100 mT become more intense and shift

to lower magnetic field, which is not in agreement with experiment. The simulation is less sensitive to E/D if $E/D < 0.01$. When $E/D > 0.01$, new spectral features appear in the simulations that are not observed experimentally (**Figure 4.11**). Lastly, the g-strain of Heme 1 (see **Figure 4.12**) was adjusted to finalize the three-heme simulation. Ultimately, it was found that a D value of 2.5 cm^{-1} along with J_{13} = 0.334 cm^{-1} (relatively strong coupling between Hemes 1 and 3) and J_{34} = 0.001 cm^{-1} (weak coupling between Hemes 3 and 4) best fit the EPR data of as-isolated, fully oxidized *G. lovleyi* NrfA (see **Table 4.1**). The resulting simulation of the Heme 1-3-4 triad is shown in **Figure 4.7C**, which reproduces key features of the NrfA EPR data, including the g = 10, g = 3.6, g = 1.7 signals, and the derivative signal at g = 2.6.

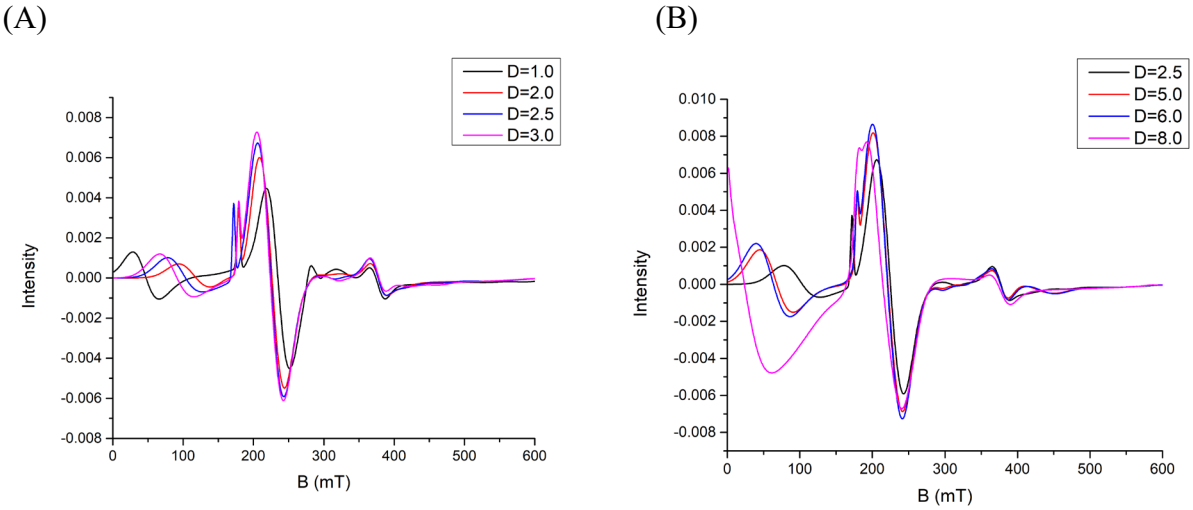

Figure 4.10 EPR simulations of the Heme 1-3-4 triad. Variation of the D value for Heme 1 (S = 5/2) between 1 - 3 cm^{-1} (A) and 2.5 - 8 cm^{-1} (B). All simulations were conducted with: E = 0.005 cm^{-1}, J_{13} = 0.334 cm^{-1} and J_{34} = 0.001 cm^{-1}. For the g values used in the simulations see **Table 4.1**. As evident from panels A and B, the low-field signals are very sensitive to the value of D, allowing us to fit the value of this parameter.

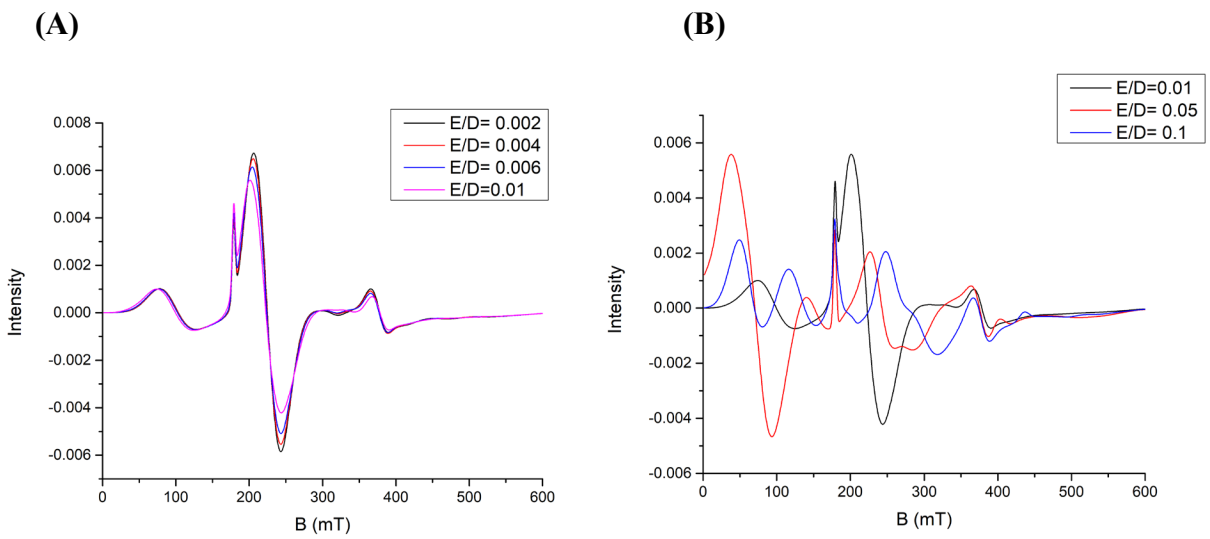

Figure 4.11 EPR simulations of the Heme 1-3-4 triad. Variation of the E/D ratio of Heme 1 (S = 5/2) between 0.002-0.01 (A) and 0.01-0.1 (B). All simulations were conducted with: D = 2.5 cm^{-1}, J_{13} = 0.334 cm^{-1}, and J_{34} = 0.001 cm^{-1}. For the g values used in the simulations see **Table 4.1**. As evident from panels A and B, the simulations do not depend much on the E/D ratio, as long as E/D < 0.01.

The EPR signal for Heme 5 was again identified in the EPR redox titrations (see below), by very careful experimentation, and it was found that the g_{max} signal of this heme, located at g_z = 3.28, is very weak. Similarly, in the case of PpcA, the signals of the two g_{max} hemes are weak and overlaid, and assigned to spectral features in the g = 3.2 - 3.5 region, generating a broad peak in the EPR spectrum.[159] The corresponding simulation for Heme 5 is shown in **Figure 4.7D**.

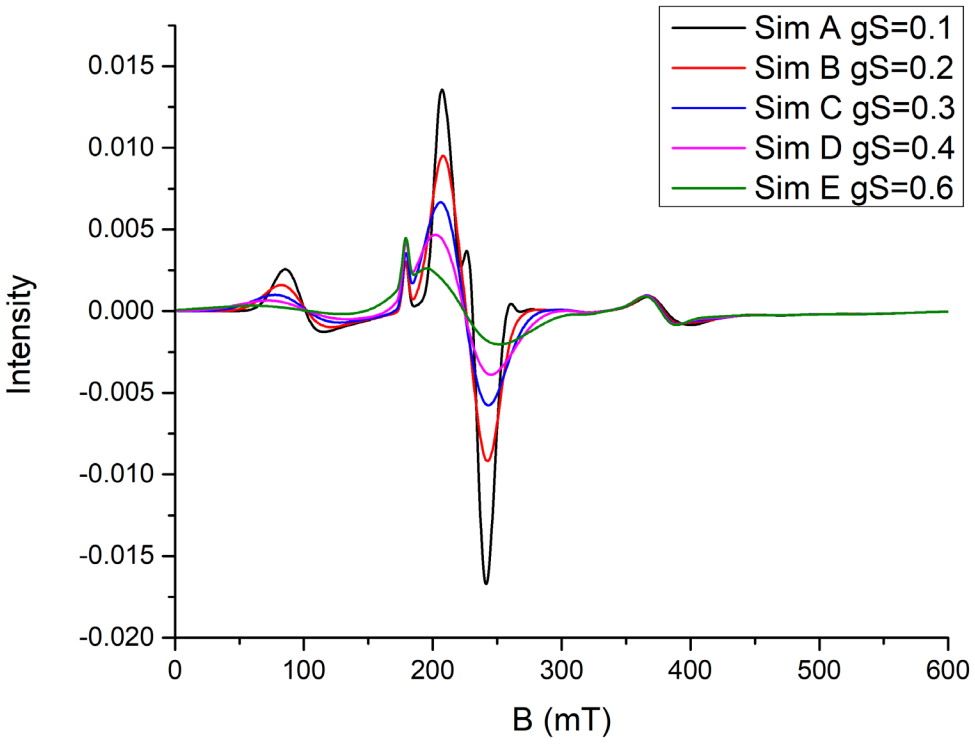

Figure 4.12 EPR simulations of the Heme 1-3-4 triad. Variation of the Heme 1 g-strain. All simulations were conducted with: D = 2.5 cm-1, E = 0.005 cm-1, E/D = 0.002, J13 = 0.334 cm-1 and J34 = 0.001 cm-1. For the g values used in the simulations see Table 4.1.

The combined EPR spectrum obtained from the simulations of the EPR signals of all five hemes is shown in **Figure 4.7A** in black, overlaid with the experimental spectrum of as-isolated, fully oxidized *G. lovleyi* NrfA in green. As evident from this comparison, excellent agreement between the simulation and the experimental data is obtained (see **Table 4.1** for all simulation parameters). In particular, the broad signals at 3.2 and 3.6 corresponding to an overlaid signal from Heme 5 and the coupled Heme 1-3-4 triad, the derivative signal at g = 2.6, and the high-field signals at g = 1.7 and 1.5 are all reproduced in our simulation.

Table 4.1 EPR parameters of the simulated EPR spectra of fully oxidized *G. lovleyi* NrfA in the absence (high-spin Heme 1) and presence (low-spin Heme 1) of cyanide (see Figures 4.6 and 4.7).

	g_x	g_y	g_z	Linewidths (x,y,z)
Heme 2 (S = 1/2)	1.52	2.21	3.01	0.08, 0.03, 0.05
Heme 3 (S = 1/2)	1.41	2.20	3.22	0.1, 0.02, 0.05
Heme 4 (S = 1/2)	0.7	1.75	3.7	0.1, 0.1, 0.07
Heme 5 (S = 1/2)	1.11	1.9	3.28	0.3, 0.3, 0.15
Heme 1 (S = 5/2)	2	2	2	0.35, 0.35, 0.35
Heme 1 (S = 1/2)	0.93	1.7	3.2	0.35, 0.35, 0.35
	J [cm^{-1}]	D [cm^{-1}]	E [cm^{-1}]	E/D
Heme 1 (S = 5/2)	J_{13} = 0.334 J_{34} = 0.001	2.5	0.0049	0.002
Heme 1 (S = 1/2)	J_{13} = 0.333 J_{34} = 2.0			

4.5 EPR Simulations and Assignments of Cyanide-Bound NrfA

The cyanide-bound NrfA EPR spectrum is simulated to further explore the three-heme coupling that occurs between Hemes 1, 3 and 4, and how these change upon cyanide binding, which causes Heme 1 to become low-spin (S = 1/2). As mentioned above, EPR features that change upon addition of cyanide, especially at g = 10, 3.6, 1.7 but also the derivative-shaped signal centered at g = 2.6, must only relate to the spin state change at Heme 1, and the accompanying alterations of the exchange couplings within the Heme 1-3-4 triad. To begin the simulations, the EPR-parameters of the cyanide-bound Heme 1 were evaluated. EPR analysis of low-spin forms of ferricytochrome *c* hemes show that they can give a range of EPR signals with g_z = 3.05-3.4, g_y = 2.05-2.25, and g_x = 1.25-1.40 at neutral pH.[161] More relevantly, cyanide-bound ferric horse cytochrome *c* gives EPR signals at g_z = 3.45, g_y = 1.89, and g_x = 0.93.[161] Taking this into consideration, we started our simulations with g_z = 3.2, g_y = 1.7, and g_x = 0.93 for low-spin Heme 1 to best fit the raw data (**Figure 4.13C, Table 4.1**).

Next, the coupling constants of Heme 1-Heme 3 (J_{13}) and Heme 3-Heme 4 (J_{34}) were fit to reproduce the EPR spectral changes. Our analysis shows that the simulated spectrum is moderately sensitive to J_{13}, with the best results obtained when this parameter stays within similar values (J_{13} = 0.334 to 0.333 cm^{-1}). On the other hand, J_{34} is distinctively increased from J_{34} = 0.001 to 2.0 cm^{-1} when Heme 1 becomes low-spin. This change in the Heme 3-4 coupling is necessary to affect the g = 3.6 signal upon cyanide binding, as observed experimentally. Since Heme 4, which is largely responsible for the g = 3.6 signal, does not interact with cyanide, the spectral changes in this region must be due to a secondary effect. Here, the increase in the Heme 3-4 coupling constant shifts the g = 3.6 signal and turns it into a broad signal around g = 3.4, which reproduces the

experimental observations (see **Figure 4.13**). Other than this, the same simulation parameters were used for Hemes 3 and 4 as in the absence of cyanide (**Table 4.1**). The spectral features of Heme 2 and Heme 5 are not affected by cyanide addition, and similarly, the same simulation parameters are used for these hemes (**Figures 4.13B** and **4.13D**). The combined EPR spectrum obtained from the simulations of the EPR signals of all five hemes is shown in **Figure 4.13A** in black, overlaid with the experimental spectrum of fully oxidized, cyanide-bound *G. lovleyi* NrfA in green. The EPR simulation shows excellent agreement with the experimental data. The only deviation is the broad shoulder observed in the g = 330 mT region, which is absent in our simulations. We believe that this shoulder is due to an impurity, since it is not observed in the EPR spectra of all protein preparations (compared to **Figure 4.6**, for example).

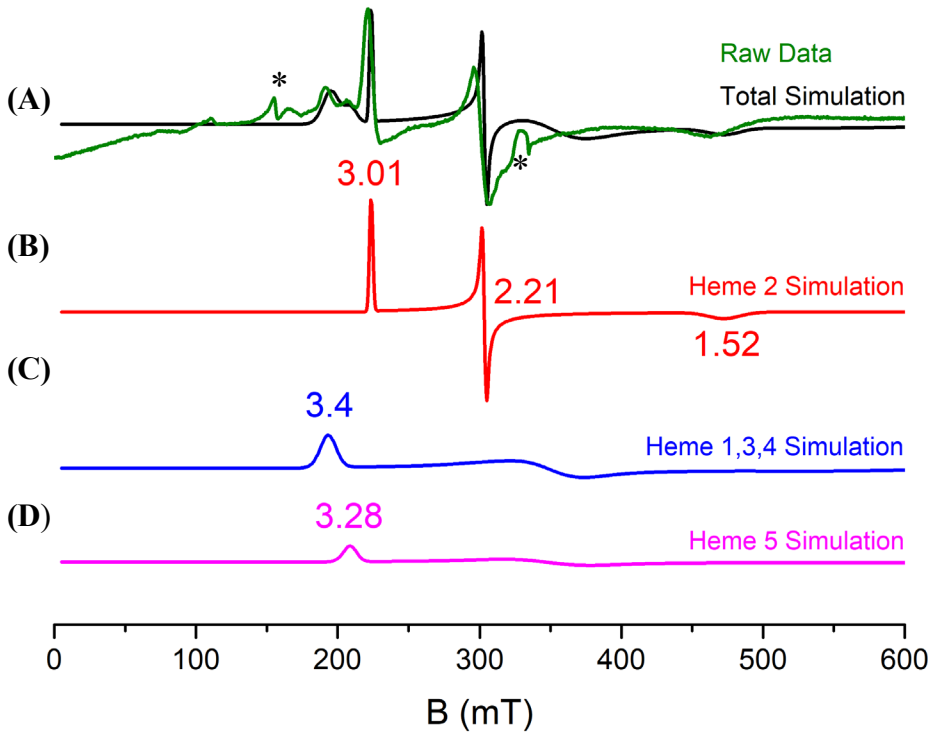

Figure 4.13 A. Overlay of the EPR spectrum of fully oxidized, cyanide-bound *G. lovleyi* NrfA (green line) and the total simulation (= sum of the spectra shown in panels B-D, black line). The

three simulated components consist of [Heme 2] (red, panel B), [Heme 1 (S=1/2)-Heme 3-Heme 4] (blue, panel C), and [Heme 5] (magenta, panel D). The signals marked with an asterisk (*) correspond to impurities.

4.6 Redox Titration of WT NrfA Followed by EPR Spectroscopy

A redox titration of 100 μM fully oxidized WT *G. lovleyi* NrfA was conducted via stepwise addition of [Ti(III)$(Cit)_3$] as the reductant and monitored by EPR spectroscopy to determine the sequence in which Hemes 1 – 5 are reduced. **Figure 4.14** shows an overview of the data obtained this way, and **Figure 4.16** better illustrates the observed EPR changes. Upon addition of the first equivalent of reductant, only very small spectral changes were observed. Careful analysis of multiple data sets shows that the broad signal at g ≈3.4 decreases in intensity upon the addition of the first equivalent of reductant (**Figure 4.16A** and **4.15**), and that intensity further decreases in the g = 1.7 region. Based on our spectral simulations and analysis (see above), these spectral changes are clearly due to reduction of either Heme 4 or Heme 5, with the g_{max} signals of these hemes being located in the g = 3.2 - 3.6 region. In contrast, in the electrochemical titration of *S. oneidensis* NrfA, the first reduction event was suggested to cause a decrease in the g = 2.87 signal.[155] These spectral changes were attributed to the reduction of Heme 1.

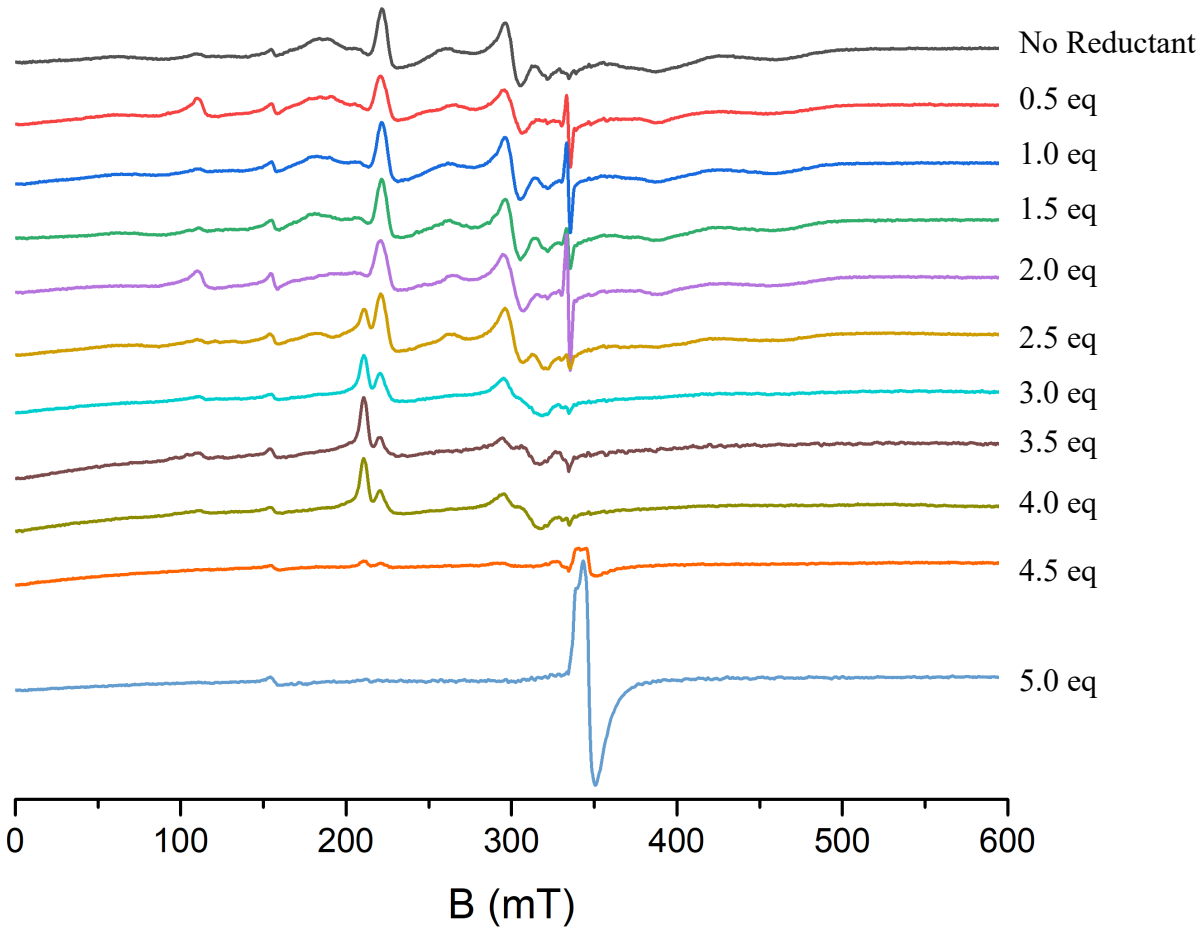

Figure 4.14 Titration of fully oxidized NrfA in 50 mM HEPES buffer with 150 mM NaCl at pH 7.0, followed by EPR spectroscopy. Here, the addition of half-equivalents of reductant [Ti(III)(Cit)3], up to 5 equivalents, causes characteristic spectral changes that are further analyzed in the text. The large signal observed at g = 1.9 upon addition of 5 equiv of reductant corresponds to excess [Ti(III)(Cit)3] (S = 1/2).

Addition of the second equivalent of [Ti(III)$(Cit)_3$] to *G. lovleyi* NrfA causes further changes in the g = 3.2 - 3.6 region, as shown in **Figure 4.16B**. This clearly indicates reduction of the second g_{max} heme. Addition of the second reductive equivalent causes further, subtle changes in the high field region of the EPR spectra (for example, around g ~ 2.6), which would indicate that Heme 5 becomes reduced before Heme 4, but it is also possible that both hemes are reduced concomitantly. So, at this point, the exact order in which the g_{max} hemes become reduced is not clear. Nevertheless, *our EPR titration demonstrates that the two* g_{max}

hemes are reduced first in G. lovleyi NrfA. Interestingly, in the *S. oneidensis* NrfA redox titration, the second heme to be reduced was proposed to be Heme 4, which was identified with a decreasing signal at g = 3.41, while simultaneously, a signal at g = 2.93 increased in intensity as well.[155]

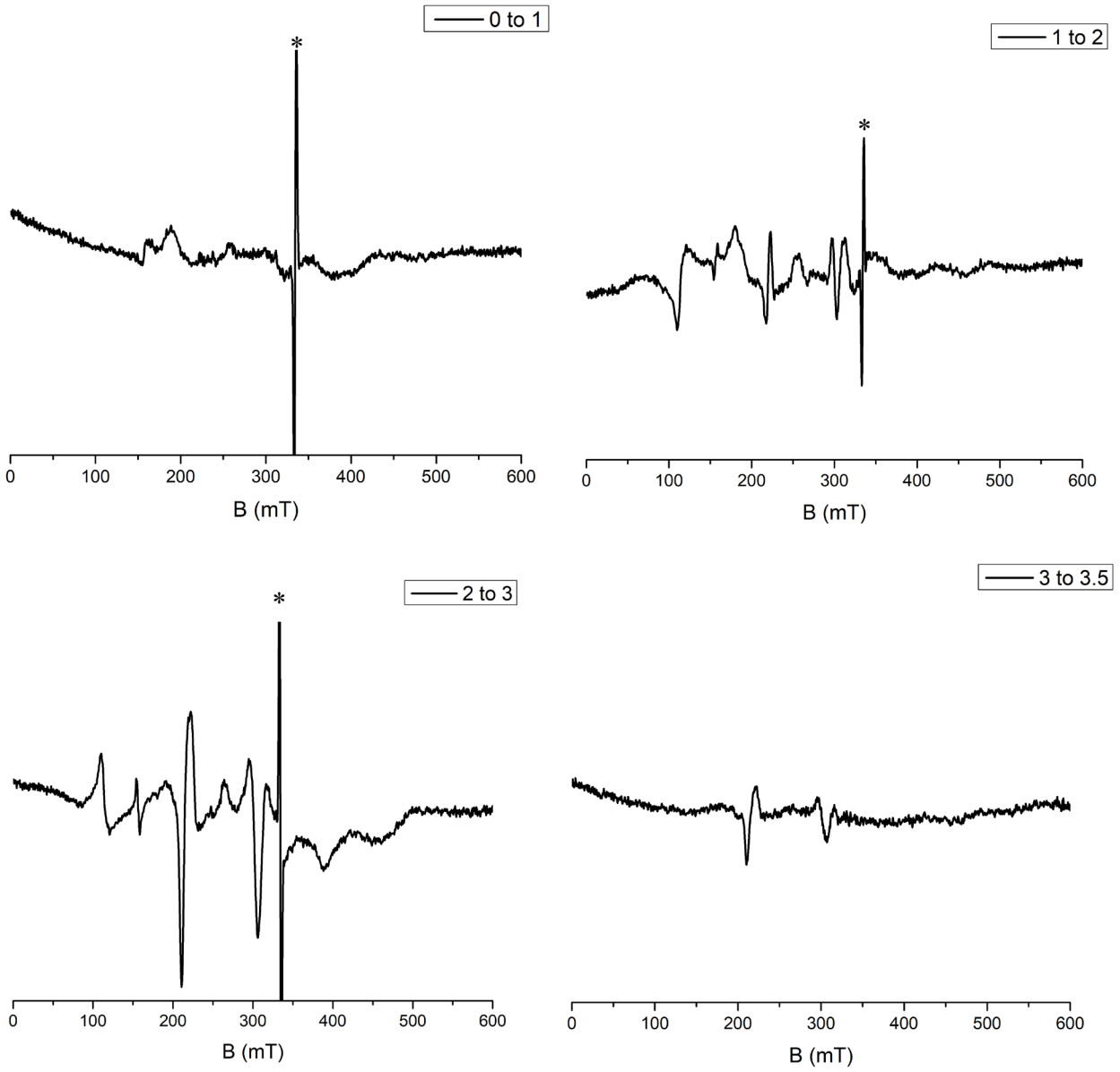

Figure 4.15 Titration of fully oxidized WT NrfA in 50 mM HEPES buffer with 150 mM NaCl at pH 7.0, followed by EPR spectroscopy. Here, we show the respective difference spectra from **Figure 8** after the addition of half-equivalents of reductant [Ti(III)$(Cit)_3$], up to 5 equivalents. This causes characteristic spectral changes that are further analyzed in the text. Spectra shown in the panels correspond to the subtraction of spectra with different equiv of [Ti(III)$(Cit)_3$] added, as indicated: (A) 0 equiv - 1 equiv; (B) 1 equiv - 2 equiv, (C) 2 equiv - 3 equiv, and (D) 3 equiv - 3.5 equiv. * The g = 2 peak is due to a residual radical from the reductant and not the protein.

Following the reduction of Hemes 4 and 5, addition of the next reductive equivalent to *G. lovleyi* NrfA causes clear spectral changes as shown in **Figure 4.16C**. Here, Heme 1 is reduced and

in this way, decoupled from Heme 3, which allows the EPR-spectral signals of Heme 3 to appear at $g_z = 3.22$, $g_y = 2.2$, and $g_x = 1.41$. Heme 3 contains bis-His ligation with parallel imidazole planes and is therefore expected to show a rhombic EPR spectrum (see above). Because Heme 4 is already reduced at this point and diamagnetic, it seems that upon reduction of Heme 1, Heme 3 is now magnetically isolated. In addition to the appearance of the spectral features of Heme 3, reduction causes the derivative signal at g=2.6 and the signals at g=10 and g=1.7 to disappear, again confirming that these signals arise from the exchanged coupled Heme 1-3 dyad. These spectral changes are similar to those observed upon CN^- binding to Heme 1 (see above). Finally, it is notable that as the signals of Heme 3 appear, the signals of Heme 2 are starting to decrease in intensity. This indicates that the reduction potential of Heme 1 is only slightly more positive than that of Heme 2, causing a distribution of the 3rd reductive equivalent over Heme 1 (major acceptor) and Heme 2 (minor acceptor).

This trend continues upon the addition of the 4th equivalent of reductant to *G. lovleyi* NrfA (see **Figure 4.16C**), where the signal of Heme 3 further increases and reaches maximum intensity, indicating complete Heme 1 reduction, whereas the signal of Heme 2 further decreases. Because of this, the Heme 3 signals at $g_y = 2.2$ and $g_x = 1.41$ become more pronounced in the EPR spectrum as well.

Lastly, upon the addition of the final reductive equivalent to *G. lovleyi* NrfA (see **Figure 4.14**), both Heme 3 and Heme 2 signals begin to decrease, with the decrease in the Heme 3 signal lagging behind the reduction in the Heme 2 signal. This indicates that Hemes 2 and 3 have quite similar redox potentials (see **Table 4.2**), but that the potential of Heme 3 is the most negative in the pentaheme unit of *G. lovleyi* NrfA.

In summary, the chemical titration of *G. lovleyi* NrfA allows us to cleanly track the reduction of the hemes in the pentaheme scaffold of the enzyme by EPR spectroscopy. Combined with our detailed analysis of the WT EPR spectrum, we demonstrate a sequence where initial reduction of Hemes 4 and 5 is followed by reduction of Hemes 1, 2 and 3. However, the latter three hemes have somewhat similar reduction potentials (especially Hemes 2 and 3), causing a distribution of electrons over these hemes as evident from the EPR data.

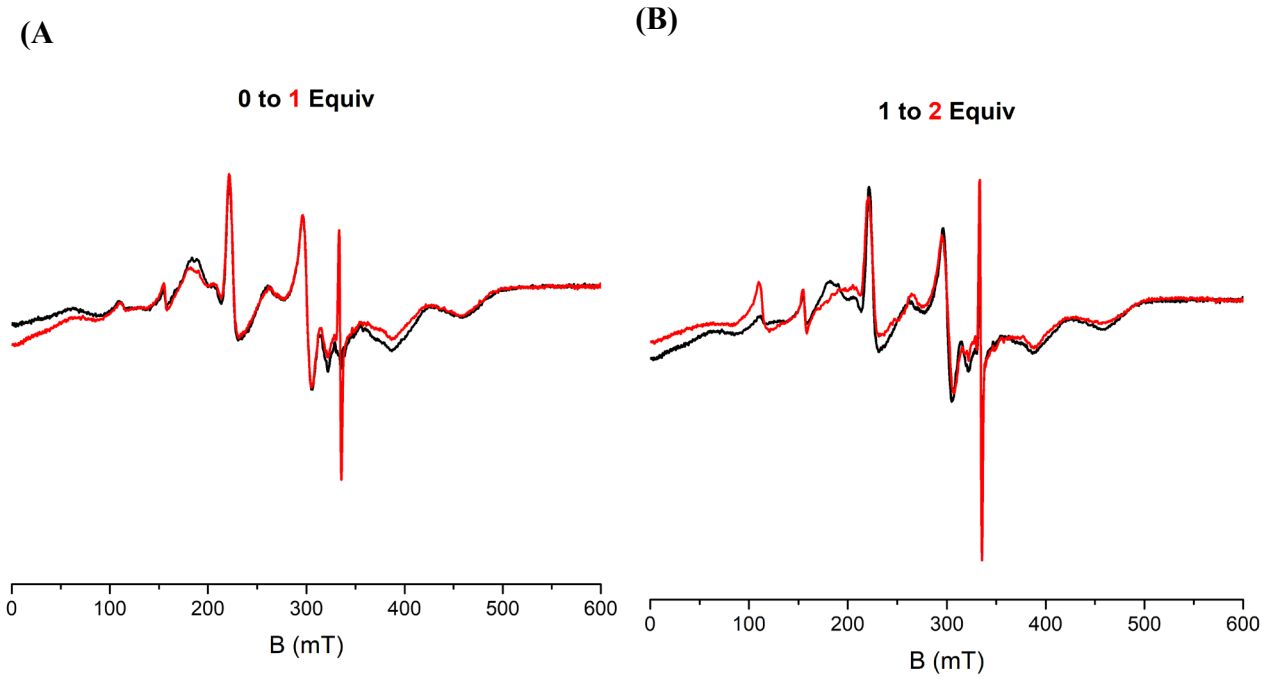

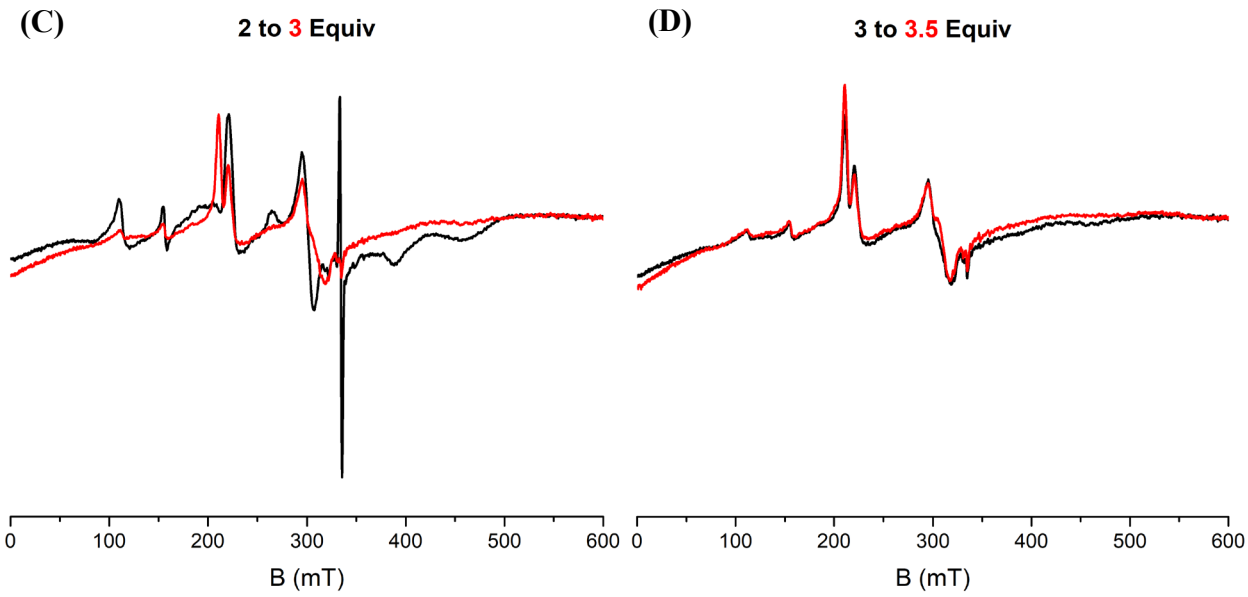

Figure 4.16 Titration of fully oxidized NrfA in 50 mM HEPES buffer with 150 mM NaCl at pH 7.0, followed by EPR spectroscopy. Here, the addition of half-equivalents of reductant [Ti(III)(Cit)$_3$], up to 5 equivalents, causes characteristic spectral changes that are further analyzed in the text. Spectra shown in the panels correspond to different equiv of [Ti(III)(Cit)$_3$]: (A) 0 (black) to 1 (red) equiv; (B) 1 (black) to 2 (red) equiv, (C) 2 (black) to 3 (red) equiv, and (D) 3 (black) to 3.5 (red) equiv. The respective difference spectra from each panel are shown in **Figure 4.14**.

4.7 Determination of Reduction Potentials (Elliott laboratory)

The work described in this section was performed by our collaborators in the Elliott Lab at Boston University. Non-turnover protein film voltammetry (PFV) experiments performed on *G. lovleyi* NrfA in the absence of substrate gave rise to an overlapping envelope of reversible signals spanning about 400 mV. These signals, once deconvoluted and fit to Nernstian one-electron peaks, are separable into five reversible signals corresponding to the reduction and oxidation of the five heme cofactors within one protomer of the enzyme (**Figure 4.17**). Fitting to account for a combination of three one-electron centers and one two-electron center was also investigated (data not shown) which yielded poor fits. Electrochemical data taken at pH 6.0 were used for determination of midpoint potentials, since at higher pH values, the signal envelope was observed

to crowd together in a fashion which obscured the precision of our analysis using fits. The overall signal shape is similar to previous work on *E. coli* NrfA,[162] and the assignment of five one-electron reversible peaks is applicable for *G. lovleyi* NrfA (see **Table 4.2**) as for other NrfA homologs including *E. coli* (with midpoint potentials of $E_{m=}$ -37 mV [H2], -107 mV [H1], - 323 mV [H3], and -250 to -400 mV [H4 and H5])[147] and *D. desulfuricans* (with midpoint potentials of $E_{m=}$ +7 mV, -20 mV, -55 mV, -120 mV, and -325 mV).[163]

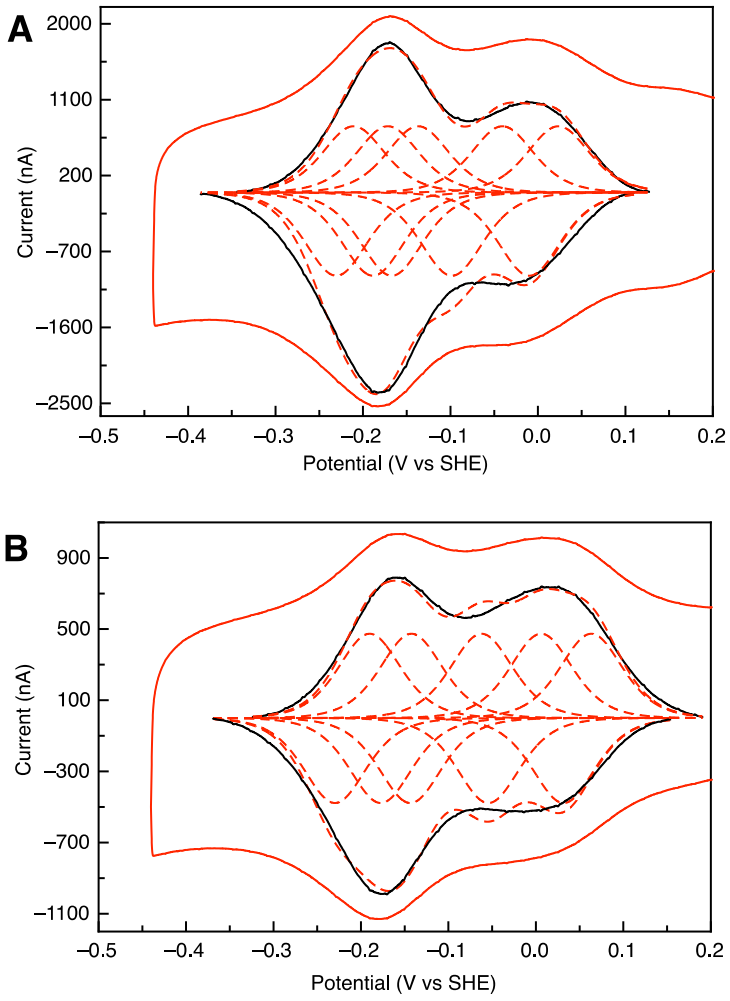

Figure 4.17 Non-turnover voltammograms of (A) G. lovleyi WT NrfA (red) recorded at pH 6.0, 4oC. Non-faradaic current subtracted data (black) is super-imposed with fitting of the data to five individual redox couples (inset, red dash) and the sum of those fitted component (red dash). Em values are -226, -180, -152, -66, and +10 mV. (B) Comparison with G. lovleyi H108M NrfA (red),

with non-faradaic current subtracted data (black), inset with fitting of the data to five individual redox couples (inset, red-dash). Em values are -210, -160, -103, -24, and +48 mV for both panels, scan rate: 10 mV/s.

The H108M amino acid variant, whereby the bis-His Heme 3 was converted to a His-Met heme, shows a broader signal envelope (**Figure 4.17B**). Compared to the WT enzyme, the signal envelope spreads out in a wider distribution in both directions. The most positive signal was seen to shift 38 mV more positive, while the other four signals shifted slightly more positive by varying amounts (see **Table 4.2**). If all five heme signals were fully independent, an axial histidine to methionine mutation would be likely to shift a single signal, corresponding to the midpoint potential of Heme 3, to relatively higher potentials, as in previous observations of heme midpoint potentials associated with bis-His and His/Met ligation.[164] Since a more complex change in the voltammogram was observed in the H108M mutant NrfA, this further indicates electronic coupling between heme cofactors, causing two or more hemes to change their midpoint potentials significantly. It is possible that the broad change in the signal envelope was the result of a small (relative to each other) modulation in the midpoint potentials of all five hemes, or the result of one or more heme signals changing in potential sufficiently as to cross over each other and change the ordering of all five signals. This point is further analyzed using a titration experiment followed by EPR spectroscopy (see below).

Table 4.2 Midpoint potentials of wild-type and H108M mutant NrfA, determined at 4ºC and pH 6.0.[a]

WT NrfA E_m (mV vs. SHE) [b]	H108M NrfA E_m (mV vs. SHE)	*S. oneidensis* WT NrfA[155]
+10 ±2 (H4/5)	+48 ±8 (H3)	-44 (H1)
-66 ±11 (H4/5)	-24 ±17 (H4)	-110 (H4)

-152 ±27 (H1)	-103 ±22 (H5)	-210 (H2)
-180 ±10 (H2)	-160 ±13 (H1)	-257 (H5)
-226 ±7 (H3)	-210 ±9 (H2)	-382 (H3)

[a] All electrochemical parameters were determined by PFV as described in the Experimental Section. [b] Errors were determined as standard deviation of three experimental replicates in identical conditions.

We note that the fits of one-electron peaks for H108M NrfA are not as precise (they have larger total residuals, **Figure 4.18**) compared to WT, which is also evident in the disagreement between simulated electrochemical signals and experimental data for H108M NrfA in **Figure 4.17B**, especially in the region -0.15 V to +0.05 V. This points to some complicating signal arising in the mutant H108M NrfA which is not present in WT NrfA. An explanation for this could be the existence of two distinct populations of H108M NrfA with different reduction potentials; for example, a population with Heme 3 existing in either a hexacoordinate or pentacoordinate state, characterized by the Met ligand bound axially in the former population, and unbound and distant in the latter. If this were true, it would give rise to a splitting of one or more of the electrochemical waves and produce a voltammetry less able to be fit to five one-electron peaks. The EPR titration of H108M NrfA shows some unusual behavior of the variant, supporting this idea.

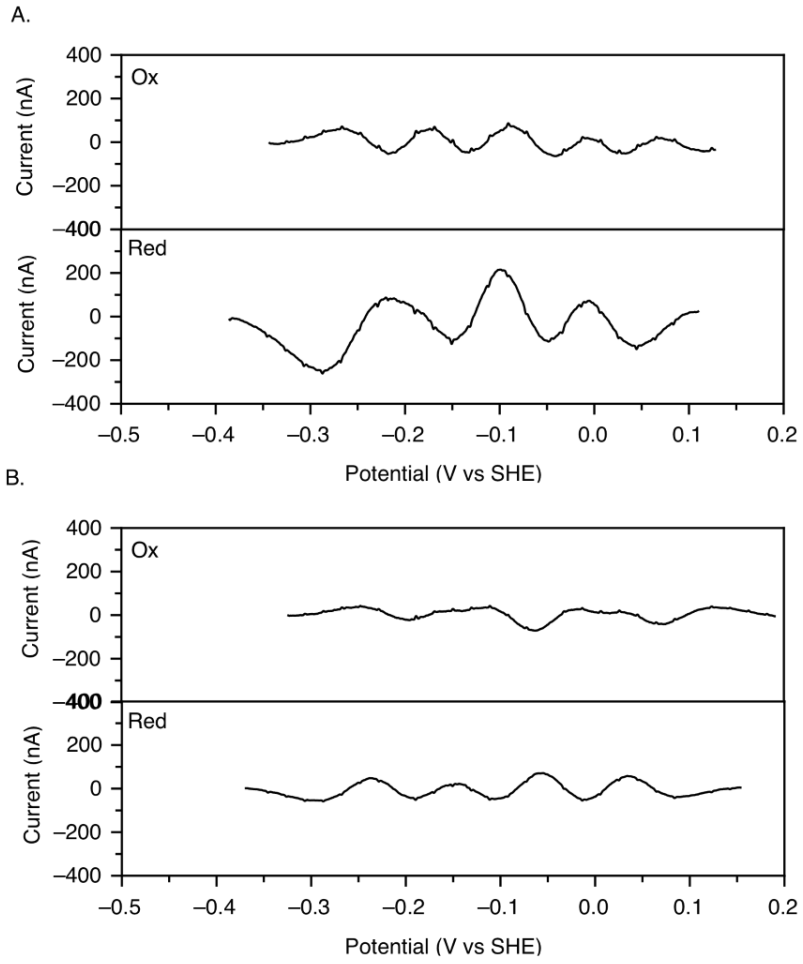

Figure 4.18 A. Residuals for fits of the oxidative and reductive scans of WT NrfA and B. Residuals for fits of the oxidative and reductive scans of H108M NrfA. Conditions are pH 6.0, 4ºC and 10 mV/sec.

PFV of WT NrfA taken at pH 8.0 (**Figure 4.19**) demonstrated a shift of all heme signals to lower potentials, indicating that the midpoint potentials of each heme depend on pH in some way, possibly by electrostatic effects of heme environment, or due to proton coupling to electron transfer. This observation implies that none of the heme cofactors are sufficiently buried from solvent as to possess fully pH-independent midpoint potentials. However, the two most positive electrochemical waves were shifted by the greatest degree during this change of two pH units: changes of –61 mV and –60 mV were observed. However, the most negative wave shifted by only

approximately –20 mV with the pH increase. Notably, neither correlates with a Nernstian prediction for a $1H^+$:1-electron process, where we might anticipate a downward change of ~ 120 mV.

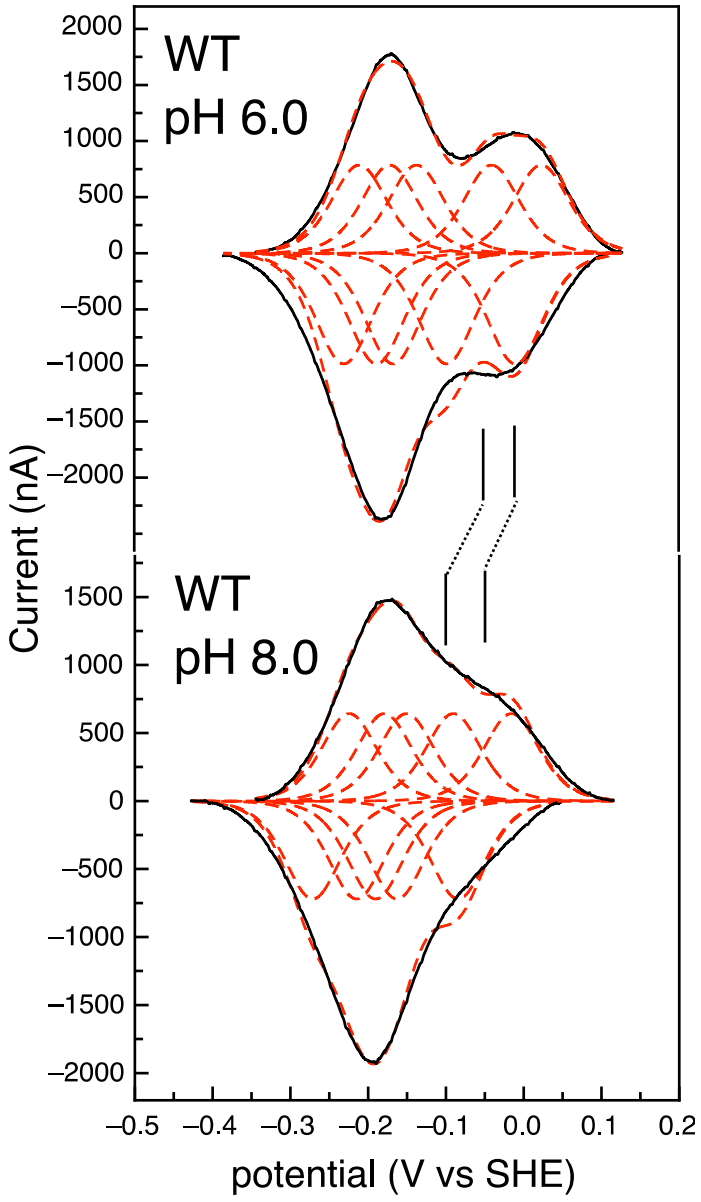

Figure 4.19 Non-Faradaic current-subtracted non-turnover *G. lovleyi* NrfA voltammograms recorded at pH 6.0 (top) and pH 8.0 (bottom), 4°C, scan rate: 10 mV/s. Em values for deconvoluted data for the pH 8.0 trace are: -248, -197, -171, -127, and -50 mV.

PFV data for WT and H108M NrfA exhibited some deviations from ideality, including separation of oxidative and reductive half-scans on the order of tens of mV, and quasi-reversibility (red dashed lines in Figures 7 and 8). To search for the underlying causes of this, we tested alternative fits where the value of n_{app} (the apparent number of electrons transferred per electrochemical event) was no longer fixed at 1.0, an assumption which used in the fits presented above. By allowing n_{app} to be a floatable parameter (**Figure 4.20** and **4.21**), fits improved, with n_{app} ranging from 1.0 to 0.69 (**Table 4.3**).

Table 4.3 Tabulation of calculated n values (electrons transferred) for each oxidative and reductive wave for wtNrfA and H108M NrfA.

	Most negative peak (peak 1)	Peak 2	Peak 3	Peak 4	Peak 5
Oxidative scan (wtNrfA)	0.91 ±0.007[a]	1.16 ±0.01	0.93 ±0.01	0.85 ±0.006	0.93 ±0.004
Reductive scan (wtNrfA)	0.79 ±0.007	1.09 ±0.01	1.06 ±0.01	0.69 ±0.008	0.81 ±0.004
Oxidative scan (H108M NrfA)	0.79 ±0.007	0.85 ±0.003	0.87 ±0.006	0.81 ±0.003	0.69 ±0.007
Reductive scan (H108M NrfA)	0.91 ±0.009	0.78 ±0.005	1.03 ±0.01	0.74 ±0.005	0.80 ±0.003

a. Errors shown are calculated statistical errors in fitting algorithm used by ODRPACK module in qSOAS.

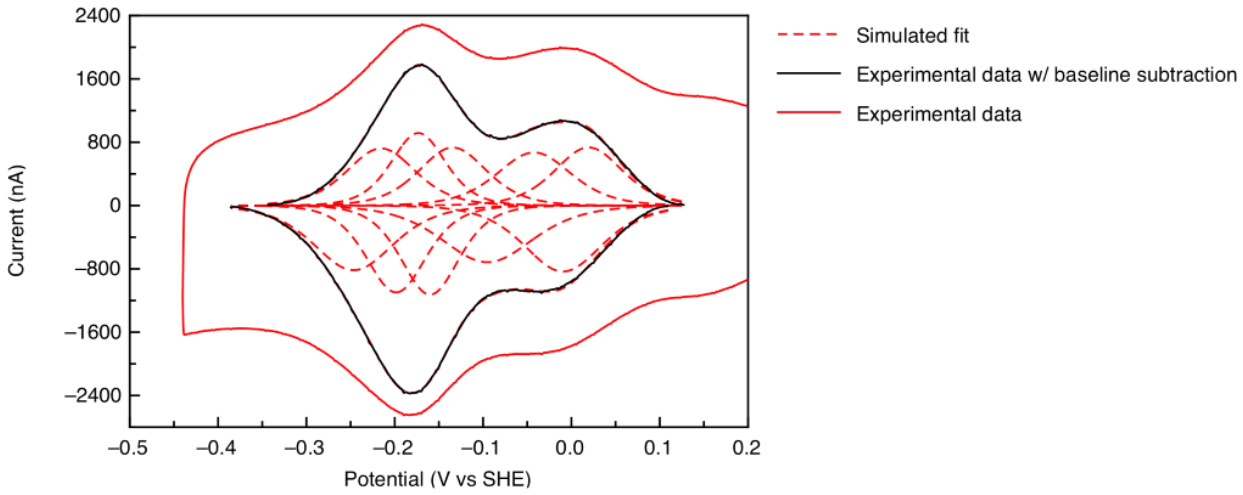

Figure 4.20 Alternative fits for baseline-subtracted non-turnover *G. lovleyi* WT NrfA voltammogram (pH 6.0, 4 ºC, 10 mV/sec) with n value (electrons transferred per electrochemical event) not fixed at n = 1, and instead calculated as a best fit.

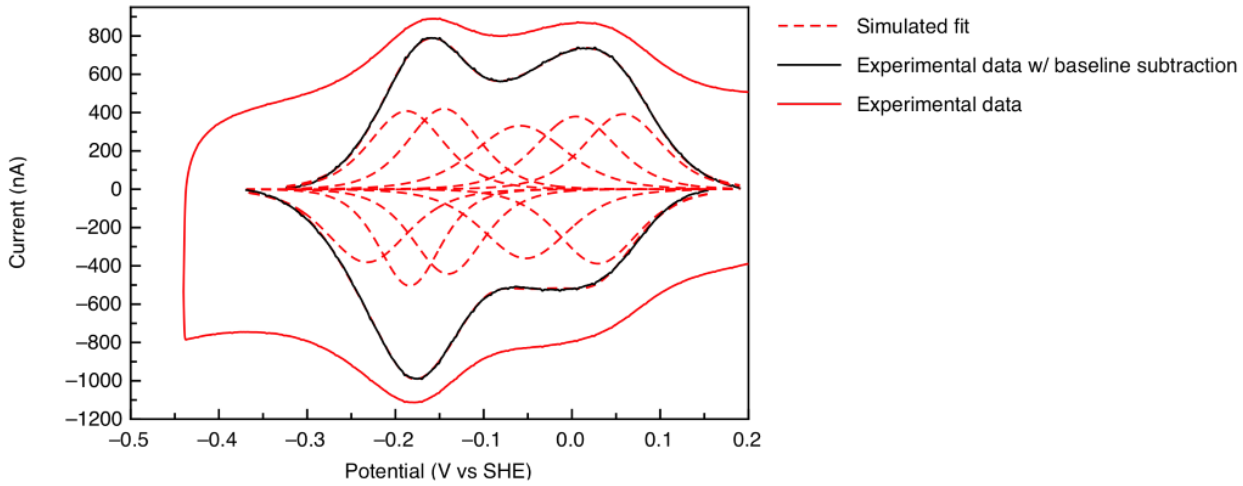

Figure 4.21 Alternative fits for baseline-subtracted non-turnover *G. lovleyi* H108M NrfA voltammogram (pH 6.0, 4ºC, 10 mV/sec) with n value (electrons transferred per electrochemical event) not fixed at n = 1, and instead calculated as a best fit.

While by theory, we would anticipate that all redox contributions should be marked by n_{app} being precisely 1.0, and that separation of oxidative and reductive half-scans be zero (REF LAVIRON),[165] such features are rarely observed in the PFE literature. This constant non-zero peak separation has been observed in other quasi-reversible PFV data of azurin and flavocytochrome

c_3,[166] among other cases involving multi-heme cytochromes *c* and even mono-heme cytochromes *c* at heterogenous carbon-based electrodes.[142, 167-171] The physical meaning of a non-integer n value lower than 1 is probably related to reduced accessibility of some of the redox cofactors to the electrode, resulting in inefficient interfacial electron transfer. This would neatly explain the minimum (the slight dip between the two peaks) in the middle of the observed signal envelopes at pH 6. By this explanation, the attenuation in some heme signals relative to others is the result of a buried or otherwise insulated heme cofactor being partially inaccessible to interfacial electron transfer, compared to the other heme cofactors. Critically, the E_m values for NrfA only shift by 4 to 6 mV whether simulated with free n values or with n values fixed at n = 1.0 (**see Table 4.4**), so this analysis implies that variations in the reversibility and relative amplitude of the fits in Figures 1 and 2 are negligible sources of error in assignment of midpoint potentials.

Table 4.4 Tabulated midpoint potential values, in mV vs. SHE, comparing fits with fixed n=1 and fits with free n values, for WT NrfA and H108M NrfA (data collected at pH 6.0, 4°C, and 10 mV/sec).

	Most negative peak (peak 1)	Peak 2	Peak 3	Peak 4	Peak 5
wtNrfA	-226	-180	-152	-66	+10
wtNrfA (free n)	-231	-186	-147	-69	+5
H108M NrfA	-210	-160	-103	-24	+48
H108M NrfA (free n)	-210	-164	-99	-24	+44

4.8 Redox Titration of H108M NrfA Followed by EPR Spectroscopy

To further explore the role of the central Heme 3 a H108M NrfA variant was generated. The H108M mutation significantly impacts the distribution of electrons within the pentaheme scaffold and the reduction potentials of the other hemes. This modification within the scaffold is drastic and it is shown by the reduced catalytic activity of the enzyme to 3% compared to wild-type (**Figure 4.22**). Replacement of the distal His ligand of Heme 3 by Met via site-directed mutagenesis (H108M variant) is expected to cause a dramatic positive shift of the reduction potential of this heme (from -212 mV to +29 mV), thereby altering the sequence of events in the EPR redox titration. Similar to WT NrfA, a redox titration on 100 μM fully oxidized H108M *G. lovleyi* NrfA was conducted via stepwise addition of $[Ti(III)(Cit)_3]$ as the reductant and monitored by EPR spectroscopy. The redox titration allows us to determine the sequence in which Hemes 1 – 5 are reduced in H108M NrfA. **Figure 4.23** shows an overview of the data obtained this way, and **Figure 4.24** illustrates the observed EPR changes.

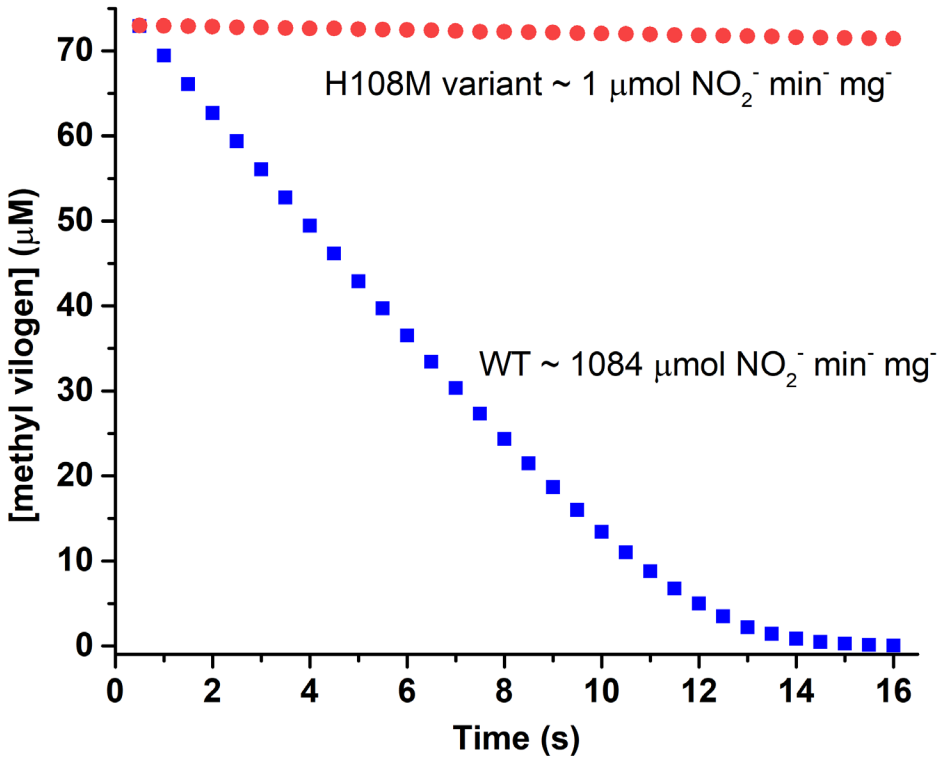

Figure 4.22 Nitrite reduction activity of the *G. lovleyi* NrfA H108M variant in comparison to the WT enzyme.

Upon addition of the first equivalent of reductant to H108M, Heme 3 is expected to be reduced first. Indeed, a strong increase of a signal at g_{eff} = 5.8 is observed, indicating reduction of Heme 3, which subsequently becomes diamagnetic and allows the signals of the now uncoupled high-spin Heme 1 to appear in the EPR data (**Figure 4.24A**). In addition, small spectral changes are observed around g = 3.6, indicating partial reduction of Heme 4 at the same time, *i.e.*, the sample is heterogeneous such that in some protein Heme 4 is reduced instead of Heme 3. The latter is evident from the fact that the derivative signal at g = 2.6 and the signal at 1.7 decrease in intensity but do not disappear, indicating that in some of the protein the oxidized Heme 1-3 dyad is still present.

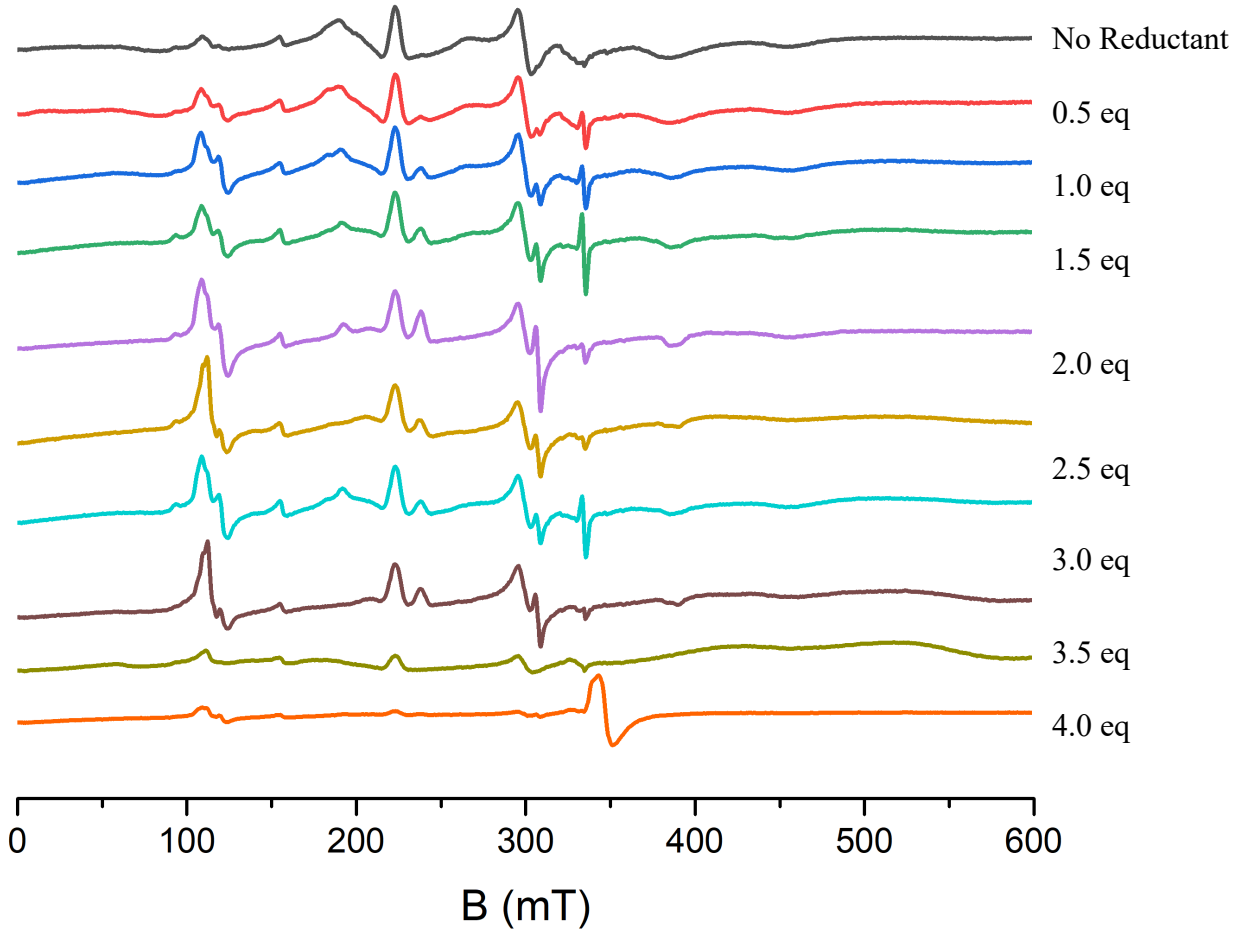

Figure 4.23 Titration of fully oxidized H108M NrfA in 50 mM HEPES buffer with 150 mM NaCl at pH 7.0, followed by EPR spectroscopy. Here, the addition of half-equivalents of reductant [Ti(III)(Cit)$_3$], up to 4.5 equivalents, causes characteristic spectral changes that are further analyzed in the text. The large signal observed at g = 1.9 upon addition of 4.5 equiv of reductant corresponds to excess [Ti(III)(Cit)$_3$] (S = 1/2).

These trends continue as the second equivalent of [Ti(III)(Cit)$_3$] is added to H108M NrfA. First, the signal at g_{eff} = 5.8 further increases, indicating additional reduction of Heme 3 (**Figure 4.24B**). Concomitantly, the intensity in the g = 3.6 region further decreases, demonstrating additional reduction of Heme 4. These results again indicate that in the H108M amino acid variant, Heme 3 and Heme 4 now have quite similar reduction potentials, and hence, become reduced simultaneously. Therefore, after addition of 2

equiv of reductant, it is expected that Heme 3 and Heme 4 are now fully reduced. Accordingly, the derivative signal at g = 2.6 and the signal at g = 1.7 further decrease in intensity upon addition of the second equiv of reductant. Curiously, besides these expected spectral changes, a new set of EPR signals also appears at g = 2.78 and g = 2.15 in the spectra. Since Heme 2 is still fully oxidized, evident from its typical EPR signals (g = 3.01, 2.21, 1.52), this new set of signals can only originate from Heme 3. This implies that upon two-electron reduction of H108M NrfA, a small fraction of protein has been generated where Heme 1 is reduced instead of Heme 3, allowing the signals of Heme 3 to appear in the spectra. Note that these EPR signals are altered compared to WT, based on the change in axial ligation (His vs Met) of Heme 3. One possible explanation for this observation is that Heme 3 can exist in two different states, with two different reduction potentials, as also indicated in the electrochemical data (see above). Here, the majority form of Heme 3 has the expected His/Met ligation with the more positive reduction potential, whereas the minority form has either a different sixth ligand or a somehow altered active site environment, leading to a change in reduction potential but keeping the heme low-spin (as evident from the EPR data). Alternatively, since Hemes 1-3-4 are coupled, the simultaneous reduction of Hemes 3 and 4 and artificial (= not observed in WT) accumulation of negative charge in close proximity might generate an equilibrium where in a fraction of the protein sample, an electron is "pushed" from Heme 3 to Heme 1:

$$[H1(III)\text{-}H3(II)\text{-}H4(II)]\ (major) \leftrightarrow [H1(II)\text{-}H3(III)\text{-}H4(II)]\ (minor) \quad \textbf{(1)}$$

In summary, after addition of 1 and 2 equiv of reductant, the protein sample shows heterogeneity in each case with two different species present in solution, which is not observed for WT enzyme.

Addition of the third reductive equivalent to H108M *G. lovleyi* NrfA causes interesting spectral changes as shown in **Figure 4.24C**. Here, Heme 3 appears fully reduced with minimal changes in the high-spin signal at g_{eff} = 5.8 for Heme 1. Small but distinct changes again appear in the g = 3.2 - 3.6 region, leading to a decrease of a signal at g ~ 3.4 which we associate with Heme 5. Here,

addition of 1.5 equiv of reductant is needed before this signal fully disappears, indicating that a small error in equiv was introduced into the titration at this point.

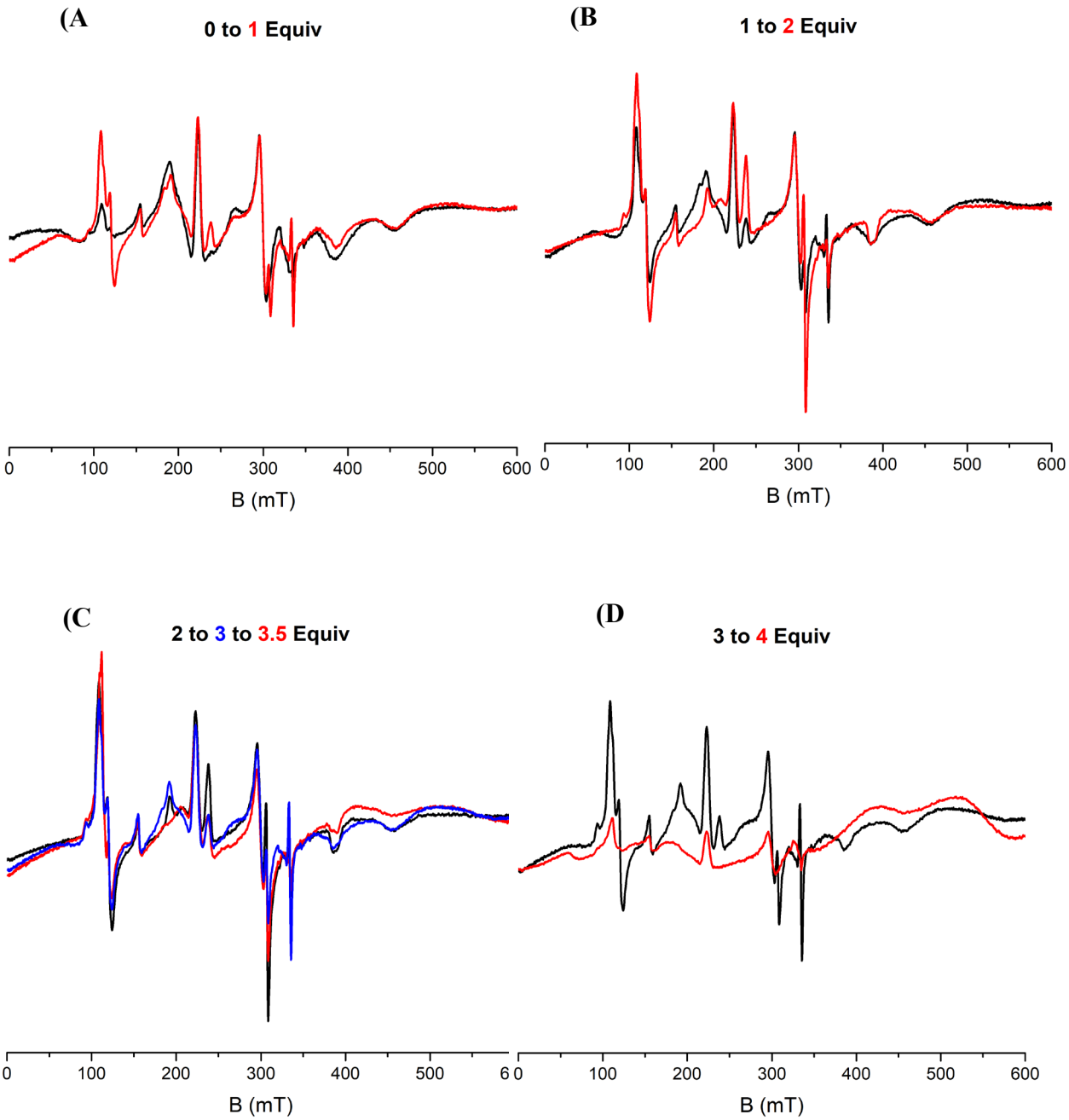

Figure 4.24 Titration of fully oxidized H108M NrfA in 50 mM HEPES buffer with 150 mM NaCl at pH 7.0, followed by EPR spectroscopy. Here, the addition of half-equivalents of reductant [Ti(III)(Cit)$_3$], up to 5 equivalents, causes characteristic spectral changes that are further analyzed in the text. Spectra shown in the panels correspond to different equiv of [Ti(III)(Cit)$_3$]: (A) 0 (black) to 1 (red) equiv; (B) 1 (black) to 2 (red) equiv, (C) 2 (black) to 3 (blue) to 3.5 (red) equiv, and (D) 3 (black) to 4 (red) equiv.

Lastly, upon addition of the fourth reductive equivalent to H108M *G. lovleyi* NrfA, the Heme 1 and Heme 2 signals both decrease simultaneously, as shown in **Figure 4.24D.** This implies that Hemes 1 and 2 have similar reduction potentials in the variant. Further addition of reductant continues the trend and ultimately leads to the disappearance of the signals of these hemes, as seen in **Figure 4.23**. Here, the reductions of Hemes 1 and 2 track almost perfectly, indicating that their reduction potentials are quite close.

4.9 Discussion

In this work, we use EPR spectroscopy coupled with chemical titration experiments and detailed spectral simulations to elucidate the sequence of heme reduction in the pentaheme scaffold of the dissimilatory multiheme nitrite reductase (Cytochrome *c* nitrite reductase (C*c*NIR) or NrfA) from *G. lovleyi*. The latter organism serves as a representative of the *Geobacter* genus, which are important soil bacteria that play a key role in the nitrogen cycle.[81-83] To reduce the hemes of NrfA in a stepwise fashion, we first developed a protocol where the chemical reductant titanium(III) citrate, [Ti(III)$(cit)_3$], is used to deliver electrons to the enzyme in clearly defined, one-electron steps. Since the redox potentials for some of the hemes in the pentaheme scaffold of NrfA are very close, this approach allows for a cleaner delivery of individual equivalents of reductant, compared to bulk electrolysis, which is the method that was used in previous work.[155] In addition, our previous work demonstrated that *G. lovleyi* NrfA is a monomer in solution, despite the dimeric structure observed by X-ray crystallography for this enzyme (and all other crystallographically characterized NrfA enzymes), which prevents any unwanted complications from monomer-dimer equilibria during the reductive titrations.

Using our new methodology combined with detailed EPR simulations, we identified the EPR-spectral signatures for all five hemes and simulated the data of as-isolated, fully oxidized (all-ferric) NrfA, including a form where the active site Heme 1 is shifted from the high-spin to the low-spin state by cyanide binding. The EPR spectra of fully oxidized NrfA are surprisingly complicated, evident from the lack of any signals for high-spin Heme 1 and the appearance of spectral features around g = 10, broad signals in the g = 3.2 - 3.6 region, a derivative signal at g = 2.6, and high-field signals at g = 1.7 and 1.5 (see **Figure 4.6**). Similar spectral features have previously been reported for *S. oneidensis* and *E. coli* NrfA.[155] Our results show that these unusual features are due to exchange coupling between Hemes 1, 3, and 4, where the magnitude of the coupling is influenced by the spin state of Heme 1 (see **Figures 4.7** and **4.8**). In addition, this is the first time that the EPR spectral signals of Heme 5 could be identified. This heme gives rise to a broad g_{max} signal at g = 3.28 that is quite weak, which we propose is due to the solvent exposure of this heme and the coupling to surrounding water molecules, increasing heterogeneity of this heme and relaxation times.

Based on the full quantitative analysis and simulation of the EPR data, we are then able to follow the reduction of each heme in the pentaheme scaffold of NrfA, when the protein is titrated with [Ti(III)$(cit)_3$]. Our data demonstrate that the g_{max} Hemes 4 and 5 are reduced first, but the exact order in which they are reduced could not be determined with certainty. Nevertheless, this provides clear evidence, for the first time, that these hemes indeed serve the purpose of an electron storage unit, as these hemes get charged before reduction of the active-site Heme 1 occurs. Hence, catalysis does not start until at least 3 electrons are available on site. In other words, *the four bis-His hemes present in NrfA do not merely serve as a wire to pass electrons to Heme 1, but they also serve as a storage unit*. In addition, based on X-ray crystallography, it has been proposed that *in*

vivo, NrfA is bound to its redox partner NrfH by formation of a NrfH(NrfA)$_2$ complex as the functional unit where the Heme 5 of the two NrfA subunits in the dimer would be in close proximity.[136-139] Hence, by charging Hemes 4 and 5 first, inter-subunit electron transfer (ET) to the other subunit would be enabled, *i.e.*, the electron(s) in Hemes 4 and 5 could be used to provide additional reductive equivalents for the other subunit if needed. This model of "cooperative catalysis", however, requires the dimer to be the functional unit, which is currently an unsettled question. In combination with the electrochemical data, we are further able to provide reduction potentials for each heme, in the relatively narrow +10 (Hemes 4/5) to -226 mV (Heme 3) range (reduction potentials vs SHE).

In this context, it is interesting to note that Heme 3, which sits at the branching point between the *active site* (Heme 1) and the *electron storage unit* (Hemes 4 and 5; see **Figure 4.2**), with electrons coming in through Heme 2 from external reductants, is the last heme to be reduced. We posit that this is functionally significant; by keeping Heme 3 oxidized, fast electron transfer from Heme 2 to either Heme 1 or Hemes 4 and 5 (electrons being delivered externally) or from Heme 4 to Heme 1 (electrons being delivered from the storage unit) is enabled. Heme 3, in this sense, is an open gateway allowing electrons to pass to Heme 1 from either direction, without any kinetic barrier. The reduction potentials of Hemes 2 and 3 are quite similar, allowing electrons to move between them quickly and "delocalize" in this way. In this sense, Hemes 2 and 3 serve as a *wire* that connects the *active site* and the *storage unit* to the protein surface where electrons are delivered (see **Figure 4.25**). We envision that under turnover and fast external electron delivery, electrons are brought into Heme 1 via the *wire* for turnover, while the *storage unit* remains reduced. If external electron delivery slows down, electrons can then be taken from the *storage unit* and transferred directly to the *active site* via the oxidized Heme 3 to keep catalysis going. As external

electron delivery speeds up or Heme 1 is idle (waiting for substrate), the *storage unit* can be replenished and turnover proceeds. In order to accomplish this, it is favorable to keep the *electron gateway*, Heme 3, oxidized. In contrast, if Heme 3 would have a more positive reduction potential than either Heme 1 and/or Hemes 4 and 5, then Heme 3 would be reduced first and this would considerably slow down electron transfer to the other hemes, as this would now add a thermodynamic and kinetic barrier to every following electron transfer step.

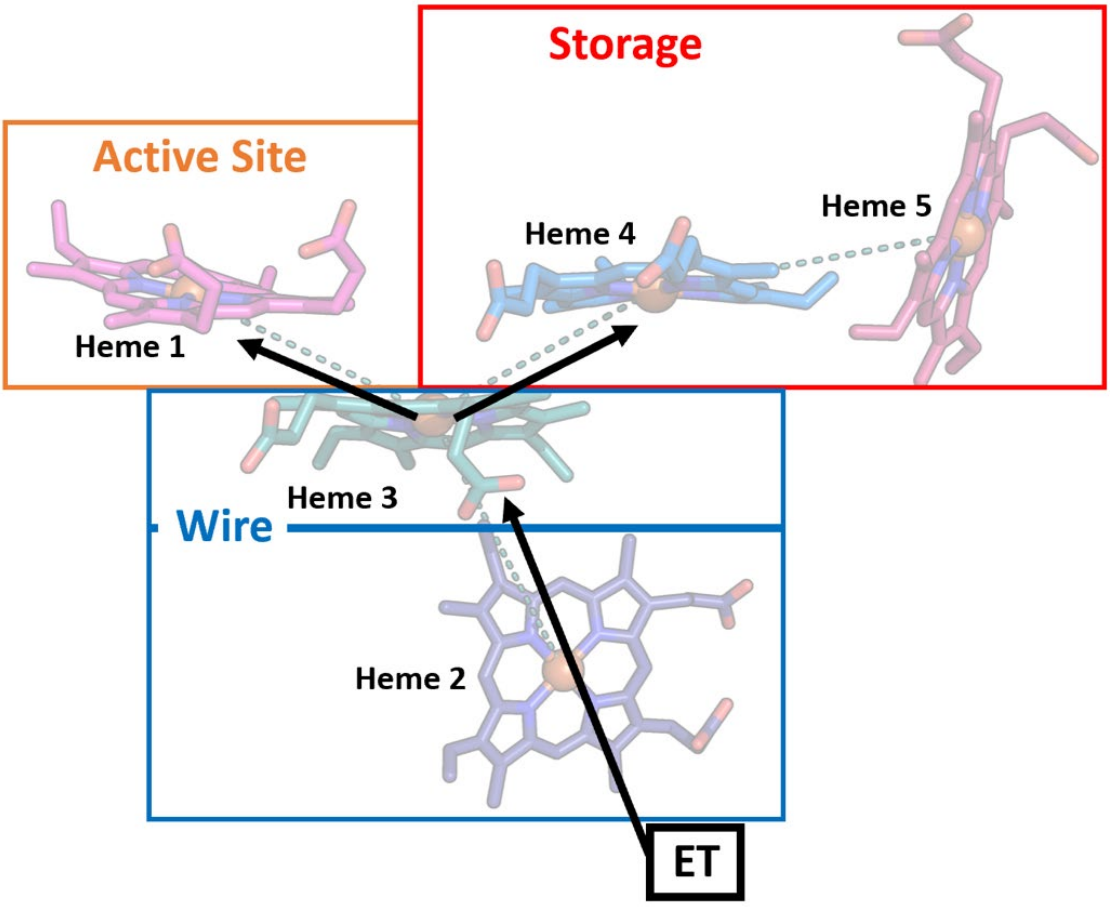

Figure 4.25 Representation of electron transfer (ET) within NrfA, where Heme 2 and Heme 3 act as a wire and Heme 3 distributes the electrons to the storage Hemes 4, 5 or the active site Heme 1.

This idea that Heme 3 has an important function as a gateway was further tested using the H108M mutant, where the H108 ligand to Heme 3 was changed to a methionine (resembling a heme *c* in a typical monoheme Cyt *c*).[172] Indeed, in the H108M variant, Heme 3 now has the most positive reduction potential (+48 mV) and is the first heme to be reduced. However, surprisingly, the sophisticated ET machinery of NrfA as a whole is greatly affected in this variant. First of all, the alteration made to Heme 3 has a significant impact on the reduction potential of Heme 1, which is shifted from -152 to -160 mV, indicating electronic coupling between Hemes 1 and 3. In addition, in the titration experiments, a distribution of electrons between Hemes 1, 3 and 4 is now observed, leading to sample heterogeneity and a blurring of the sequential reductions of the first three hemes as observed for the WT enzyme. Negative shifts in reduction potentials are also observed for Hemes 2 and 5, indicating extended interactions between the hemes. The latter observation could also be related to charge compensation effects: as hemes become reduced, protons should be transferred to their respective active site pockets, and the change in the sequence of heme reductions in the variant could affect the related, sequential proton transfers as well, thereby affecting the reduction potentials of the hemes. Finally, because Hemes 2 and 5 are located at the protein surface, the shifts in their reduction potentials could also be related to structural changes of the enzyme, but this point cannot be addressed without structural studies. In any case, we propose that the observed, low catalytic activity of H108M relates to (a) the low potential of Heme 1, potentially slowing ET kinetics to the active site heme due to the reduction of Heme 3 first, which blocks the ET chain, and (b) the general disorganization of ET in the pentaheme unit of NrfA caused by this mutant. In this sense, the H108M NrfA mutant again emphasizes the significance of Heme 3 as the branching point

in the ET chain, connecting Heme 2 either to the active site Heme 1, or the electron storage unit (Hemes 4 and 5).

In comparison to *S. oneidensis* NrfA studied previously, a couple of interesting differences should be noted. First and most significantly, the reduction potentials of the five hemes of *S. oneidensis* NrfA all lie between -44 to -382 mV and are shifted negative compared to those of the *G. lovleyi* enzyme (see **Table 4.2**). Most significant is the shift for Heme 3, the heme with the most negative reduction potential in the chain, which is observed at -226 mV in WT *G. lovleyi* versus -382 mV in WT *S. oneidensis* NrfA, a surprising shift of -156 mV. This could indicate a different electron source for NrfA in this organism, operating at different potentials. Accordingly, *S. oneidensis* does not have an obvious homolog of NrfH or the NrfBCD complex, which could explain this difference. The sequence of heme reduction is also different in these enzymes, and for *S. oneidensis* NrfA it was proposed that Heme 1 is reduced before Heme 4. However, it should be noted that Heme 5 could not be unequivocally identified in the EPR spectra of *S. oneidensis* NrfA, and hence, there is a bit of uncertainty as to when exactly this heme is reduced. Hence, it is possible that in *S. oneidensis* NrfA, Hemes 5 is reduced first, but that the corresponding EPR-spectral changes are masked due to the weakness of the EPR features of this heme.

In summary, using chemical and electrochemical titrations coupled to EPR spectroscopy and in-depth spectral simulations, we have identified the reduction potentials of the hemes in the pentaheme scaffold of *G. lovleyi* NrfA. Our data provide further insight into the potential roles of the four bis-His hemes of the enzyme, with Hemes 4 and 5 serving as an electron storage unit, and Heme 3 being the central heme important for efficient electron distribution in the circuit. Heme 5 has the potential additional role to allow for ET of stored electrons into the other NrfA subunit, assuming that the functional

unit, when bound to NrfH, is a $(NrfA)_2$ dimer. In total, our data provide strong evidence that the four bis-His hemes are much more than just a wire that allows for ET to the active site Heme 1.

4.10 Experimental Section

a. NrfA Protein Expression, Purification and Mutagenesis

The *G. lovleyi* wild-type (WT) NrfA enzyme (uniprot ID: B3E641 and NCBI ID: WP_012469115.1) and the variant H108M (Heme 3 distal ligand variant) were overexpressed and purified as previously described with minor modification.[80] The cell cultures expressing the H108 variant were incubated for 16 hours after induction as opposed to the 12-hour incubation for the cultures expressing the WT enzyme. Osmotic shock was employed to extract the enzyme from the cell pellets as opposed to the total lysis that was previously employed. Briefly, each liter worth of harvested cell pellets was resuspended to 50 ml in 100 mM Tris buffer at pH 8.0 containing 20% sucrose and 1 mM EDTA at room temperature for 10 min. The suspension was then centrifuged for 10 min at 100,000 rcf. The supernatant was discarded while the pellet was resuspended to 40 ml ice-cold water for 10 min. The suspension was then centrifuged for 10 min at 100,000 rcf. The pellet was discarded while the supernatant was added with 2 dissolved tablets of cOmplete^{TM}, Mini, EDTA-free Protease Inhibitor Cocktail (Roche) and 5 ml of 10 x 100 mM Tris buffer at pH 7.5 with 150 mM NaCl. The resulting mixture was topped-off to 50 ml using distilled water and then filtered using a 0.22 μm filter. In cases where samples were sticky and difficult to filter due to the leakage of genomic DNA and RNA during osmotic shock, 50 μL each of 10 mg/ml Dnase I and RNase were added, and the samples were stirred for approximately 30 min before filtering. The enzymes were then purified by strep-tag II affinity column chromatography (IBA Life Sciences), followed by size exclusion chromatography (GE Life Sciences) as previously described.[80] The H108M variant yield was ~4 mg per liter of culture. The activity of the variant was determined as previously described,[80] and the H108M variant was found to be only 3% as active (1 μmol NO_2^- min^{-1} mg^{-1}) as the WT enzyme (1084 μmol NO_2^- min^{-1} mg^{-1}; see **Figure 4.22**).

To generate the H108M variant, polymerase chain reaction (PCR) on the codon-optimized WT gene (**Figure 4.26**) inserted into pBAD202D-TOPO was performed using Phusion High Fidelity DNA Polymerase (New England Biolab) with 3% DMSO as an additive. The sequences of the primers and their corresponding annealing temperature are given in **Table 4.5**.

ATGAAATACCTGCTGCCGACCGCTGCTGCTGGTCTGCTGCTCCTCGCTGCCCA
GCCGGCGATGGCCGCGCCGCCGAAAGCGGAACAAGCGAAGATTGCGGAGAT
CCCGGATGGCACCATTGACCCGGCGGTTTGGGGCAAGAACTACCCGGAGGAG
TACCAGACCTGGAAAGACACCGCGCTGCCGACCCCGGAAGGCAAGAGCAAA
TATAAGAAAGGCAACGACGGTGGCAAGGTTTACGATAAACTGAGCGAGTATC
CGTTCATCGCGCTGCTGTTTAACGGCTGGGGTTTCGGCATTGAGTACAACGAA
CCGCGTGGTCACGTGTATATGATGAAGGACCAGAAAGAAATTGATCCGAGCC
GTCTGAAGGGTGGCGGTGCGTGCCTGACCTGCAAGACCCCGTACGCGCCGCA
GCTGGCGCAGAAGCAAGGTGTTACCTACTTTAGCCAAAGCTATGCGGATGCG
GTGAACCAGATCCCGAAAGAGCACCAAGAAATGGGCGTTGCGTGCATTGACT
GCCACAACAACAAGGATATGGGTCTGAAAATCAGCCGTGGCTTCACCCTGGT
TAAGGCGCTGGACAAAATGGGTGTGGATCAGACCAAGCTGACCAACCAAGA
CAAACGTAGCCTGGTTTGCGCGCAGTGCCACGTGACCTACACCATTCCGAAG
GATGCGAACATGAAAAGCCAAGACGTTTTCTTTCCGTGGGATGAGAGCAAGT
GGGGCAAAATCAGCATCGAAAACATCATTAAGAAAATGCGTAGCGACAAGA
GCTATGGTGAATGGACCCAGGCGGTGACCGGCTTTAAAATGGCGTACATCCG
TCACCCGGAGTTCGAAATGTATAGCAACCAAAGCGTTCACTGGATGGCGGGT
GTGAGCTGCGCGGATTGCCACATGCCGTACACCAAAGTGGGCAGCAAGAAA
ATCAGCGACCACCGTATTATGAGCCCGCTGAAAAACGATTTTAAGGGTTGCA
AACAGTGCCACAGCGAGAGCAGCGAATGGCTGAAGAACCAGGTTATCACCA
TTCAAGACCGTGCGGCGAGCCAATACATTCGTAGCGGTTATGCGCTGGCGAC
CGTGGCGAAGCTGTTCGAGATGACCCACAAACAGCAAGCGGCGGGCAAGCA
GATCGACCAAAAAATGTACGATCAGGCGAAATTTTACTATGAGGAAGGCTTC
TATCGTAACCTGTTCTTTGGTGCGGAGAACAGCATCGGCTTTCACAACCCGAC
CGAAGCGATGCGTATTCTGGGTGACGCGACCATGTACGCGGGCAAGGCGGAT
GGCCTGCTGCGTCAAGCGCTGACCAAAGCGGGTGTGGACGTTCCGGTGAAGA
TCGATCTGGAACTGAGCAAATATACCAACAACCGTGGCGCGAAAAAGCTGAT
GTTTAAGCCGGAGCAGGAGCTGAAAGACCCGTATGGCCCGCAGAAGTGGAG
CCACCCGCAGTTCGAAAAGTAA

Figure 4.26 The optimized *G. lovleyi* wild-type NrfA gene sequence (codons in black) fused with the pelB (codons in red) and strep-tag II (codons in blue).

Table 4.5 Primers and annealing temperature for the H108M variant of *G. lovleyi* NrfA.

Variant	Primers	Annealing Temp. [^{o}C]
H108M	5'-ATGGTGTATATGATGAAGGACCAGAAAGAAATTGATCC-3' 5'-ACCACGCGGTTCGTTGTAC-3'	**66**

b. Overview of Sample Preparation for UV-Vis and EPR Spectroscopy

Titanium Citrate Preparation. The protocol for preparing solutions of titanium(III) citrate, [Ti(III)(cit)$_3$], was adapted from prior reports.[173-174] Solutions of [Ti(III)(cit)$_3$] were made fresh daily. Under anaerobic condition inside an anaerobic chamber (Coy Laboratory Products; O_2 < 15.0 ppm), a 40 µL aliquot of 12% titanium(III) chloride in 10% HCl stock solution (Millipore) was added to 200 µL of a 0.2 M sodium citrate solution (Bio Basic, Amherst, NY). The pH of the resulting solution was then adjusted to pH 9 by slowly adding 160 µL of a saturated potassium carbonate solution, pH 10.6. A stock solution generated in this way has a concentration of 100 mM of [Ti(III)(cit)$_3$] and an approximate pH of 9. Working solutions of 9 mM or 1 mM concentration of the reducing agent were then prepared by appropriate dilution using 50 mM HEPES buffer at pH 7.0 with 150 mM NaCl.

UV-Visible Titrations. UV-Vis spectra of the oxidized, as-isolated wild-type *G. lovleyi* NrfA (1.65 µM NrfA) were obtained using a solution that contained 50 mM HEPES (pH 7.0) and 150 mM NaCl. In an anaerobic environment, UV-Visible spectropotentiometric titrations were performed on the as-isolated *G. lovleyi* NrfA by incremental addition of the reducing agent in a 1:1 equivalent per heme per NrfA monomer, based on the extinction coefficient 547 mM^{-1} cm^{-1} of the Soret band. The titration was performed by adding 1 µL of the 1 mM [Ti(III)(cit)$_3$] solution at a time, up to 5 equivalents (based on five hemes per monomer; 5 µL) to generate fully reduced

enzyme. The samples were placed in sealed quartz cuvettes, and the UV-Vis spectra were collected using an Analytic Jena SPECORD S600 spectrophotometer.

Electron Paramagnetic Resonance (EPR) Spectroscopy. Electron paramagnetic resonance spectra were collected using 20.5 mW microwave power and 9.277 GHz microwave frequency using a Bruker EMX 200 spectrometer equipped with an ESR 900 continuous-flow liquid helium cryostat (Oxford Instruments) to maintain the temperature at 10 K ± 1K.

Samples of oxidized, as-isolated WT *G. lovleyi* NrfA enzyme were prepared at a concentration of 100 μM in 50 mM buffer (HEPES at pH 7.0 with 150 mM NaCl). The cyanide-bound enzyme was prepared by adding 10x equimolar potassium cyanide to the oxidized, as-isolated NrfA, allowing the sample to incubate for 5 additional min at RT. Once prepared, samples were transferred into 4 mm wall x 250 mm EPR sample tubes (Quartz Glass) and flash frozen using liquid nitrogen.

Similarly, the EPR samples for the reductive titrations were obtained by the stepwise addition of 0.5 equivalent (per heme per NrfA monomer, 1 μL) of the 9 mM [Ti(III)$(cit)_3$] solution to oxidized, as-isolated WT NrfA, up to 5 equivalents (based on five hemes; 10 μL), to generate fully reduced enzyme inside an anaerobic chamber. The samples were placed in sealed quartz EPR tubes and flash frozen in liquid nitrogen.

EPR simulations. The EPR spectra were initially processed using the software SpinCount (by Prof. Michael Hendrich, Carnegie Mellon University).[175] The simulations were performed using both SpinCount and EasySpin (by Prof. Stefan Stoll, University of Washington).[176] Simulation parameters are provided in the text. As evident from **Figures 4.27** and **4.28**, data

obtained at different microwave energies overlay very well, which demonstrates minimal power saturation of the signals originating from NrfA in the 20 mW data used here for the analysis. This contrasts with the impurity signal in **Figure 4.27**, which shows a different power dependence.

(A)

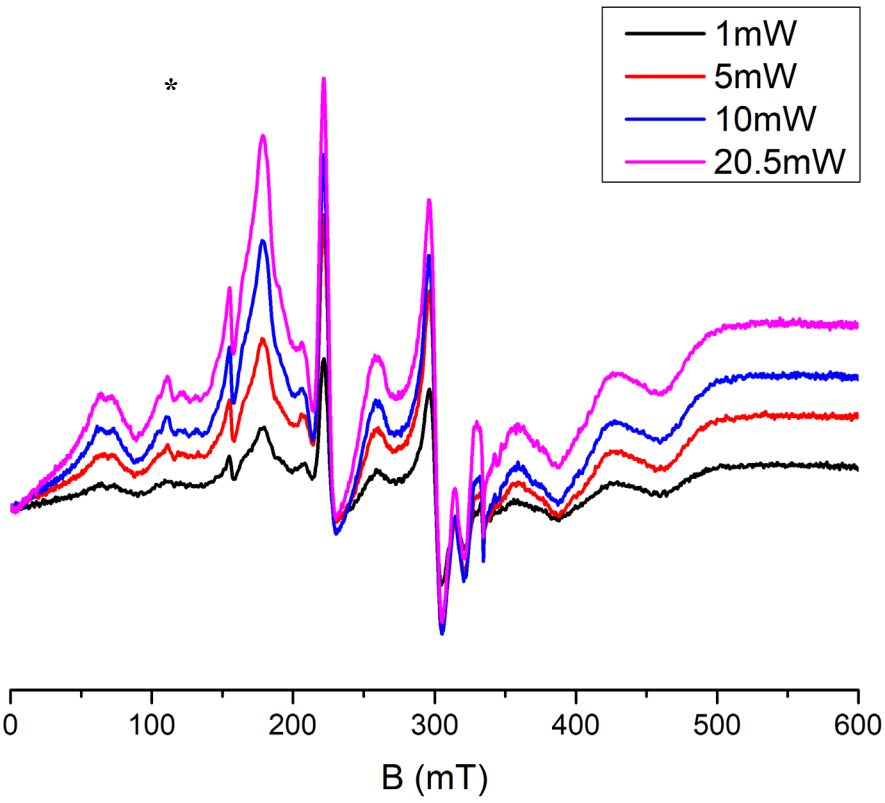

(B)

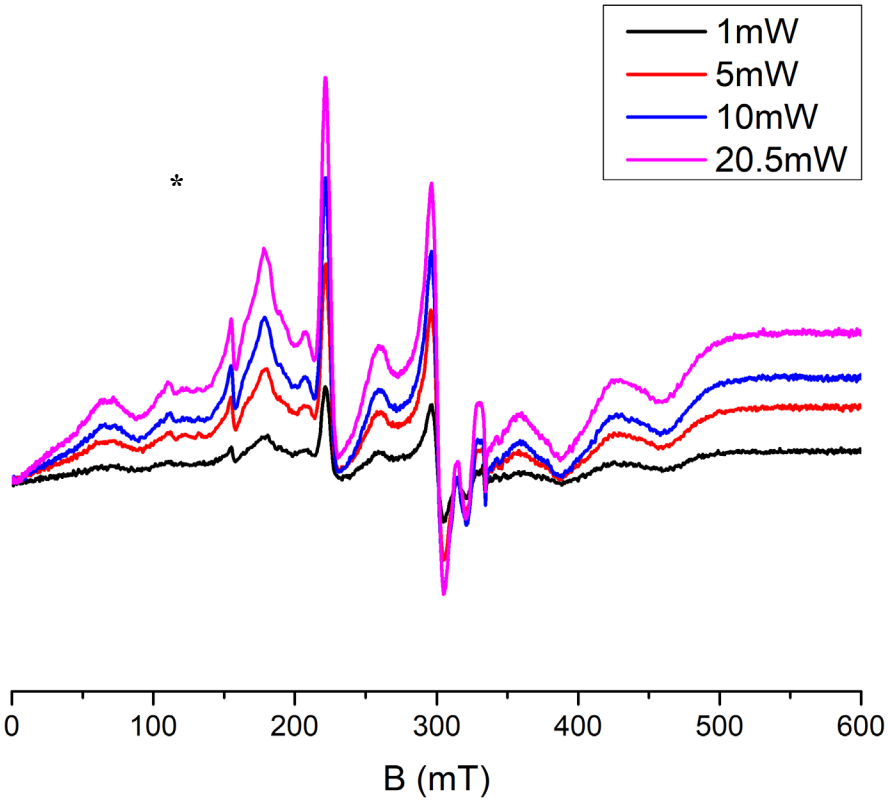

Figure 4.27 Power dependence of fully oxidized WT NrfA in 50 mM HEPES buffer with 150 mM NaCl at pH 7.0 EPR signals recorded at different microwave power at (A) 10K and (B) 15K. The signals marked with an asterisk (*) correspond to impurities.

(A)

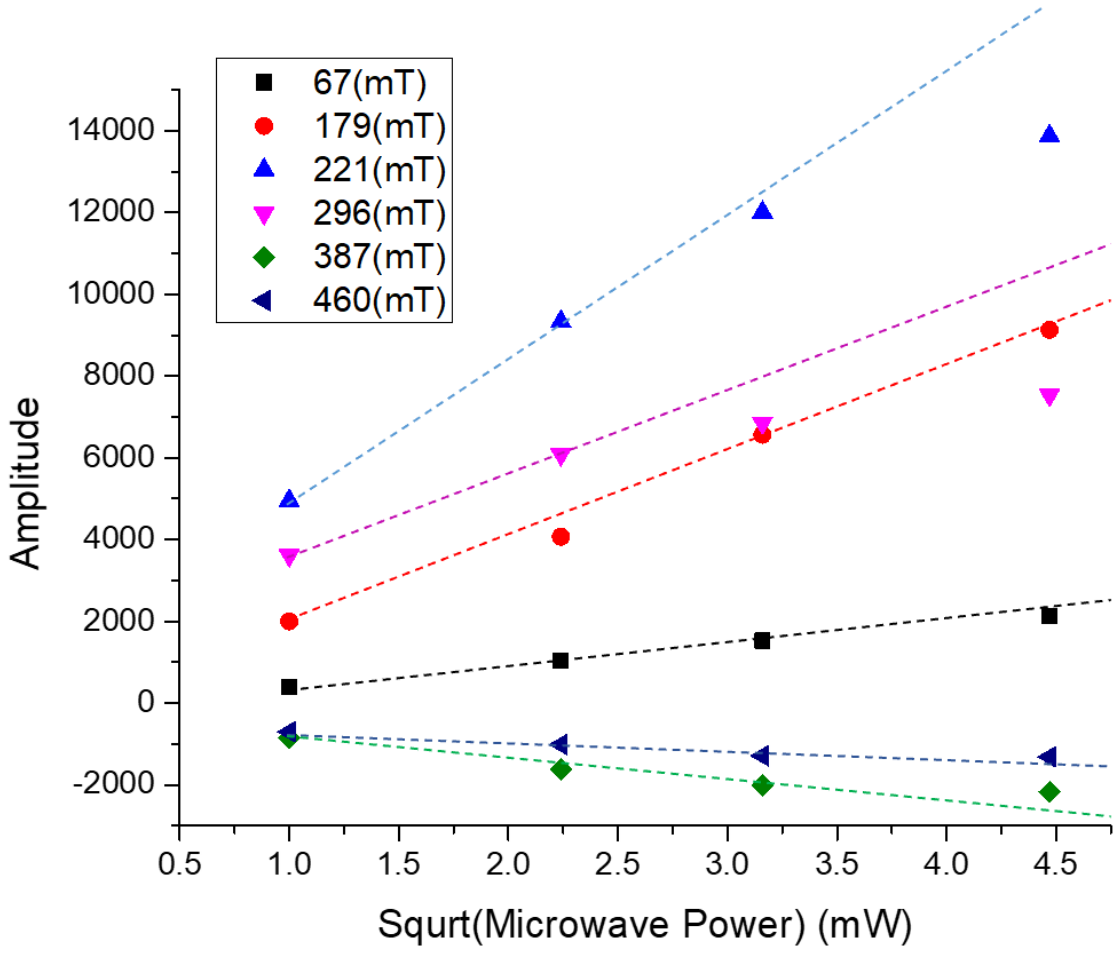
67(mT)
179(mT)
221(mT)
296(mT)
387(mT)
460(mT)
Amplitude
14000
12000
10000
8000
6000
4000
2000
0
-2000
0.5
1.0
1.5
2.0
2.5
3.0
3.5
4.0
4.5
Squrt(Microwave Power) (mW)

(B)

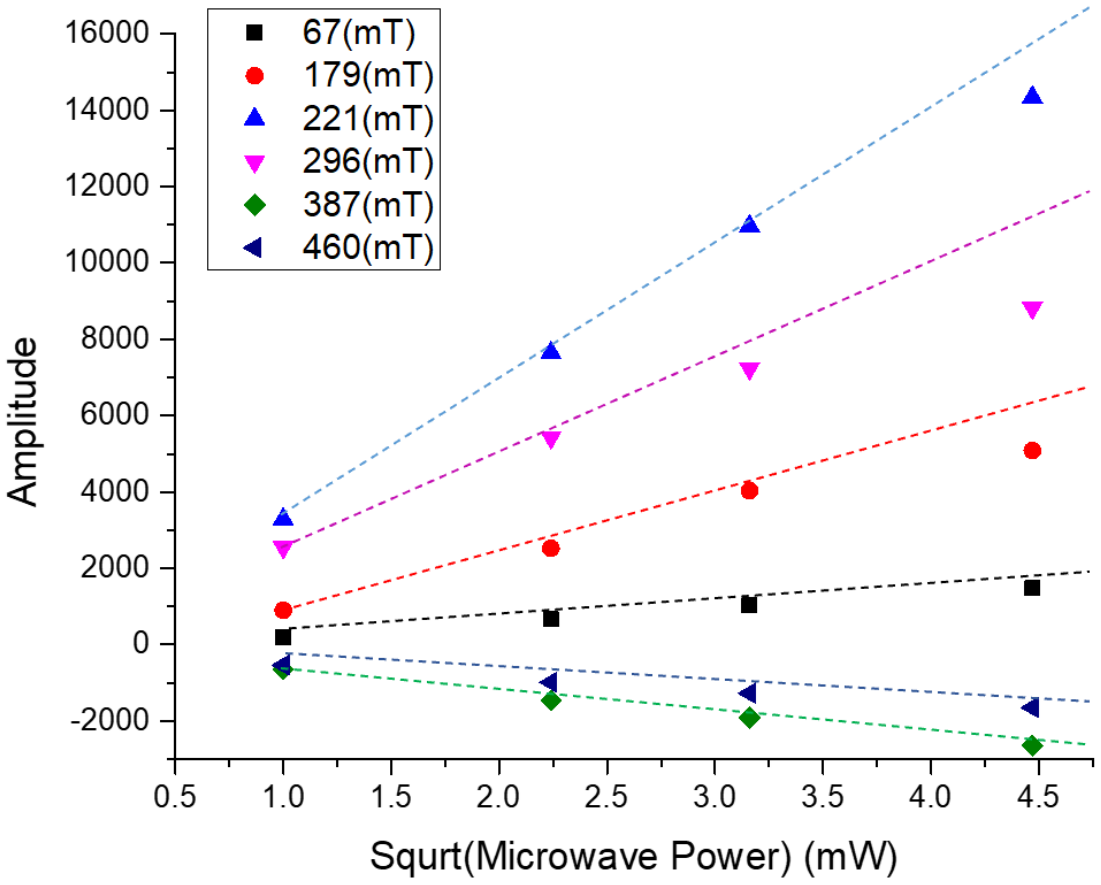

Figure 4.28 Power dependence plots of fully oxidized WT NrfA in 50 mM HEPES buffer with 150 mM NaCl at pH 7.0 at (A) 10K and (B) 15K (generated from Figure 4.27 data).

c. Protein Film Voltammetry Experiments

Pyrolytic graphite edge (PGE) electrodes were prepared by polishing with an aqueous slurry of 1.0 μm alumina, and then the alumina was removed by sonicating in water for several minutes. After drying, a 3 mg/mL solution of multiwalled carbon nanotubes (Sigma) in *N*,*N*-dimethylformamide (Fisher) was prepared and sonicated for several minutes. 14 μL of carbon nanotube solution were pipetted on the electrode surface and allowed to dry overnight. *G. lovleyi* NrfA was immobilized on dry carbon nanotube electrodes by pipetting 3 μL of 300 μM enzyme

solution onto the electrode surface, waiting approximately 20 s, then pipetting off excess enzyme solution. After generation of the enzyme film, electrodes were immersed in a multi-component buffer containing 10 mM each of MES, MOPS, TAPS, CHES, HEPES, and CAPS, 100 mM NaCl, and 2 mM $CaCl_2$, which was adjusted to pH 6.0. A three-electrode electrochemical cell was used, with a platinum wire as counter-electrode, and a saturated calomel reference electrode (SCE). All potentials were corrected by +260 mV, for a single calibrated SCE, and reported relative to the standard hydrogen electrode (SHE). The electrochemical cell was water-jacketed and cooled to 4°C for every experiment.

Protein film voltammetry (PFV) experiments were carried out anaerobically in a MBraun Labmaster glovebox under a nitrogen atmosphere, using a PGSTAT30 AutoLab (Ecochemie), equipped with FRA and ECD modules. All PFV data were collected using the GPES software package (Ecochemie). All cyclic voltammograms were analyzed using the qSOAS package,[162] through which background electrode capacitance was subtracted from the raw data, and data was filtered to remove electrical noise. Deconvolution of the electrochemical data was achieved within qSOAS using standard procedures,[142, 167-168] where a model of adsorbed redox-active species as described by Laviron is used,[177] where the stoichiometry of all redox cofactors (five hemes in this case) is set to 1.0, and n_{app} is allowed to be either a set or floatable parameter, to describe the ideality of the redox, by equation (2):

$$i) \quad \frac{n_s n_{app} F^2 \nu A \Gamma}{RT} \frac{\exp[n_{app} F(E - E_p)/RT]}{[1 + \exp[n_{app} F(E - E_p)/RT]]^2} \qquad \textbf{(2)}$$

Fits were compared where n_{app} was either 1.0 or a floatable parameter, the resulting E_m values for each redox cofactors was found to alter by only so much as 5 mV.

Chapter 5 Conclusion and Future Work

5.1 Conclusions

Carbene transferase development is an important area of interest in organic synthesis since these enzymes catalyze the production of hard to synthesize carbon-carbon or carbon-heteroatom bonds in late-stage functionalization of larger molecules.[6, 29, 33-36, 55] Furthermore, catalyzing organic reactions in water with highly controlled product stereoselectivity, large turnover number (TON) and turnover frequency (TOF), and long lifetime are ideal attributes for industrial applications.[12-14] Biocatalysts are attractive due to their ability to function under environmentally friendly conditions at high rates, with high stereo- and enantioselectivity.[2, 15] Designing novel biological catalysts leads to a significant reduction in waste and cost in industrial-scale synthesis compared to stoichiometric syntheses and other catalytic processes.[16-17] Herein, I focus on the devolvement of biocatalyst with enhance carbene transferase reactivity using YfeX and rational designed YfeX variants.

The initial contribution of this thesis was the investigation of carbene transfer reactivity of wild-type (WT) YfeX for N−H insertion, cyclopropanation, and Si-H insertion to give further insight into YfeX' biocatalytic profile. Chapter 2 focused on WT YfeX's reactivity, kinetic, and substrate scope studies on these carbene insertion reactions. First, the N−H insertion activity of YfeX with aniline as the substrate was investigated and results show high product yields with a 72% yield. Even higher compared to free porphyrin [Fe^{II}PpIX] with a 27% yield and sperm whale WT FeMb with a 21% yield.[89] Overall YfeX has a high TON of 6274 for the aniline N-H insertion

using 0.001% catalyst loading over 20 hours, with a k_{obs} = 0.210 min^{-1}. Furthermore, at higher YfeX loading aniline can produce the di-insertion product (diethyl 2,2-(phenylimino) diacetate) with EDA, and at 0.1% catalyst loading, 30% of the disubstitution product is obtained. As the catalyst loading is reduced (or, in other words, the excess of aniline is increased), the disubstitution reaction is suppressed, and at 0.01% catalyst loading, the di-insertion product only contributes 1% to the total yield. To further investigate the N−H insertion reaction of secondary amines, similar to the disubstitution reaction, using *N*-methyl aniline as a substrate it was shown that YfeX produces a 62% yield of product with a TON of 620. Additional substrate scope studies for the N−H insertion reaction using anilines with electron-withdrawing substituents (4-bromoaniline, 4-trifluoromethylaniline) gives 52% to 57% yields and electron-donating substituents (4-methylthioaniline, 4-methoxyl-6-methylaniline, *p*-toluidine) gives 40 - 51% yields. Lastly, using *para*-, *meta*-, and *ortho*- methyl aniline, substrate steric contribution was analyzed, and it is shown that as the methyl group moves closer to the reactive amine group, from -*para* to -*meta* to -*ortho* substitution, the N−H insertion yields decrease accordingly, from 57% to 37% to 23%. Overall, these studies demonstrate that WT YfeX is a fantastic N-H insertion biocatalyst with great potential for applications in drug synthesis.

Cyclopropanation reactivity with YfeX is also investigated utilizing styrene as substrate. Reactivity studies show that YfeX generates a 27% yield of styrene cyclopropane product with a TON of 268 and a k_{obs} = 0.096 min^{-1}, which is comparable to that of WT Mb (36% yield, with a TON of 180).[24] Stereoselectivity analysis of the styrene cyclopropane product displays a *cis* to *trans* ratio of the product of 11 to 89, comparable to WT Mb (9:91) and [Fe^{II}PpIX] (13:87). YfeX procedures the *trans* product with 87% selectivity for the (R,R) enantiomer, which is different from WT Mb, which produces 47% (R,R) enantiomer.[24] Furthermore, various *para*-substituted

styrene derivatives were examined for cyclopropanation activity, with the functional groups analogous to the aniline derivatives. 4-methylstyrene shows the highest yield with 48% compared to styrene and other derivatives. Vinylanisole, 4-chlorostyrene, and 4-trifluorormethylstyrene show a moderate conversion to the cyclopropane products with similar yields (30%, 23% and 29%, respectively). All the substrates exhibit similar diastereoselectivity, yielding 80 - 90% of the *trans* isomer. Organic co-solvents were used to help increase styrene substrate solubility and at a 30% methanol co-solvent concentration, the yield for the aniline-based product remains similar, but, importantly, a doubling of the yield for the styrene substrate is observed (47% yield). We further show that 30% DMSO as a co-solvent further improves the cyclopropanation yield, with an increase to 59%. Utilizing dimethylphenylsilane as a substrate, we explored whether YfeX is able to catalyze the carbene insertion into silicon-hydrogen (Si−H) bonds. WT YfeX is able to catalyze the carbene transfer to dimethylphenylsilane, generating ethyl[dimethyl(phenyl)silyl] acetate in 11% yield with a TON of 108 at 0.1 mole percent of catalyst after just one hour. In short, cyclopropanation and Si-H insertion reactivity with YfeX was not as robust as N-H insertion, but additional YfeX protein optimization can be conducted to help with reactivity.

To understand YfeX carbene insertion reactivity, specifically Si-H insertion, we further investigated reactivity using computational methods. Initial reactivity began from three possible electronic ground states of the iron-porphyrin carbene (IPC) intermediate, which are the closed shell singlet (CSS) and open shell singlet (OSS) state, and the corresponding triplet state. It was shown that Si—H insertion by YfeX, the calculated energy barriers are 16.4 (OSS), 22.8 (CSS) and 27.6 (triplet) kcal/mol, indicating that the OSS state is ultimately allowing for this reaction to go forward. Overall, these results show that the Si—H insertion reaction is energetically much less favorable compared to the N—H insertion and cyclopropanation reactions, in agreement with the

lack of reactivity of many WT heme proteins towards carbene transfer to Si-H bonds. Our findings are aligned to previous observations, where these three states are very close in energy (within 5 kcal/mol), making it impossible to determine which form corresponds to the ground state of the IPC based solely on the computational results.[91, 107] Previous studies on truncated DFT models indicated that there is no energy barrier for either the N—H insertion and cyclopropanation reactions, but there is a free energy barrier due to the entropic contribution, corresponding to 9 – 14 kcal/mol.[94, 103]

One of the advantages of rational design is the ability to modify the primary coordination sphere. Considering this benefit, the YfeX heme cofactor within the active site was removed and reconstituted with Co- and Ru-heme cofactors and carbene transfer reactivity studies were conducted with these two new catalysts. This approach has shown promising results when implemented with Mb.[53-54] RuYfeX N−H insertion reactivity in buffer was achieving with a 43% yield (TON of 433) at pH 7. The N−H insertion of a secondary amine, *N*-methyl aniline, gave a somewhat lower yield of 39% compared to aniline. Similar to Mb, the TONs decrease for the cyclopropanation of styrene upon RuMpIX substitution into YfeX, giving a yield of 20% for RuYfeX at pH 7, which is comparable to free [Ru^{II}MpIX] and WT Mb and variants. Notably though, the cyclopropanation activity of RuYfeX is greatly superior to RuMb.[53] Styrene cyclopropanation with RuYfeX delivers a *cis* to *trans* ratio of 15 to 85, showing a higher trans selectivity compared to free [Ru^{II}MpIX], which yields a *cis* to *trans* ratio of 38 to 62. CoYfeX can facilitate carbene transfer reactivity at pH 7 in buffer for the N−H insertion of aniline, albeit only with 29% yield (with a TON of 292), and for the cyclopropanation of styrene, a very small TON of only 49 is obtained. Previously, the Fasan group used the CoPpIX-reconstituted Mb(H64V, V68A) mutant to analyze carbene transfer reactivity.[51] Their results show that CoMb(H64V,

V68A) has a lower reactivity for the N−H insertion than CoYfeX, with 13 % yield (and a TON of 129), but similar styrene cyclopropanation activity with 4 % yield.[51] The catalytic activity of CoYfeX is relatively low compared to both WT YfeX and RuYfeX, and was therefore not further pursued.

YfeX variants were investigated for biocatalytic carbene transferase reactivity in Chapter 3. Structurally, YfeX contains a buried heme active site with hydrophilic secondary coordination sphere (SCS) amino acids and an entrance tunnel, where substrates and hydrogen peroxide enter during native peroxidase reactivity. These attributes make YfeX an ideal starting point for development of a novel robust carbene transferase catalyst. In order to improve reactivity, the initial approach taken is to study the effects amino acids in the SCS on carbene insertion reactivity. This was done by mutating three sites (R232, S234, and D143) to an alanine, a small hydrophobic amino acid, generating three distinct variants, R232A, S234A, and D143A. Additionally, to probe the entrance pocket near the active site the I230A variant was also investigated, to probe the effects of a wider tunnel into the active site.

Initially, the YfeX variant R232A was investigated for N-H insertion reactivity with aniline giving 75% yield. Substrate scope studies for the N−H insertion reaction using anilines with electron-withdrawing substituents (4-bromoaniline and 4-trifluoromethylaniline) gives 43% and 51% yields and electron-donating substituents (*p*-toluidine, *p*-anisodine) gives 40% and 54% yields. In contrast, the cyclopropanation reaction demonstrated no enhanced reactivity, but instead, a slight decrease with 11% yield and 9% yield with 30% MeOH co-solvent. The YfeX variant I230A was also investigated for N-H insertion reactivity with aniline giving the highest product yield of 92%. Substrate scope studies for the N−H insertion reaction using anilines with electron-withdrawing substituent (4-bromoaniline) gives 37% yields and electron-donating substituents (*p*-

toluidine, *p*-anisodine,) gives 44% and 94% yields. In contrast, the cyclopropanation reaction demonstrated no enhanced reactivity, but instead, a slight decrease with 13% yield and 7% yield with 30% MeOH co-solvent. Lastly, the YfeX variants S234A and D143A were investigated for N-H insertion reactivity with aniline giving the lowest yields (54 and 50%). Similarly, the cyclopropanation reaction demonstrated no enhanced reactivity, with 9% and 7% yields. In short, these new mutations give further insight into the effects of the SCS near the active site and the entrance tunnel that help design the next generation of YfeX carbene transferases.

The results in chapters 2 and 3 demonstrate that rational design is a great tool for the development of biocatalysts. Although modifications in the primary coordination sphere with YfeX, by introducing Ru^{II}MpIX and CoPpIX, did not enhance carbene transferase reactivity it did give insight into the complicated electronic effects metal complexes within biological scaffolds. Modification of the SCS displayed a more promising approach and two YfeX variants, R232A and I230A, showed enhancing N-H insertion reactivity. Computational analysis gives further insight into important interactions that occur within the active site and help illustrate nature's meticulous efforts in generating highly active enzymes.

In Chapter 4, the electron storage and distribution properties within the pentaheme protein cytochrome c nitrite reductase (NrfA), from *Geobacter lovleyi*, were investigated utilizing electron paramagnetic resonance (EPR) spectroscopy coupled with chemical titration experiments. Initial work focused on developing a technique to reduce NrfA's five hemes in a stepwise fashion, and it was found that the chemical reductant titanium(III) citrate, $[Ti(III)(cit)_3]$, can deliver electrons to NrfA in defined one-electron steps. Utilizing this new method, combined with detailed EPR simulations, we identified the EPR-spectral signatures for all five hemes and simulated the data of as-isolated, fully oxidized (all-ferric) NrfA. We demonstrated that the g_{max} Hemes 4 and 5 are

reduced first, hence, indicating that these hemes assist as an electron storage unit for Heme 1, the active site. The EPR spectrum of fully oxidized NrfA is complex, and there is a lack of any signals for the high-spin Heme 1. We demonstrate that these unusual observations are caused by exchange coupling between Hemes 1, 3, and 4, and it is confirmed using EPR simulations. Interestingly, Heme 3, which sits at the branching point between the active site (Heme 1) and the electron storage unit (Hemes 4 and 5), with electrons coming in through Heme 2 from external reductants, is the last heme to be reduced. The reduction potentials of Hemes 2 and 3 are quite similar, allowing electrons to move between them quickly and "delocalize" in this way. Therefore, it is proposed that Hemes 2 and 3 serve as a wire that connects the active site and the storage unit to the protein surface where electrons are delivered. We predict that under turnover and fast external electron delivery, electrons are brought into Heme 1 via the wire for turnover, while the storage unit remains reduced. The reduction potentials for each heme were further determined using electrochemical data and show that they have a relatively narrow +10 (Hemes 4/5) to -226 mV (Heme 3) range (reduction potentials vs SHE). In short, our data provide strong evidence that the four bis-His hemes are much more than just a wire that allows for electron transfer to the active site Heme 1.

Heme 3 has a significant function as a gateway between shuttling electrons from Heme 2 to the active site or the storage unit (hemes 4 and 5). To further study the role of Heme 3, a H108M variant was generated, where the H108 ligand to Heme 3 was changed to a methionine (resembling a heme *c* in a typical monoheme Cyt *c*).[172] In this new NrfA H108M variant, Heme 3 now has the most positive reduction potential (+48 mV) and becomes the first heme to be reduced. EPR studied showed that the overall electron transfer machinery of NrfA is greatly modified in this new variant. The H108M also has low catalytic activity, and it is probably due to the low potential of Heme 1, potentially slowing electron transfer to the active site heme due to the reduction of Heme 3 first, which blocks

the natural electron flow. In this sense, the H108M NrfA mutant again emphasizes the significance of Heme 3 as the branching point in the electron transfer chain.

The results in chapter 4 give further insight into the complicated mechanism of electron transport, storage, and distribution in NrfA. We demonstrate that Hemes 1, 3, and 4 have exchange coupling, not shown previously, that helps explain the complicated fully oxidized NrfA EPR spectrum. Additionally, to probe the important role of the central Heme 3, the H108M NrfA variant was generated. This H108M variant has a significant impact in the distribution of electrons within the pentaheme scaffold and decreases the catalytic activity of the enzyme to 3% compared to WT NrfA. Using this information, we were also able for the first time identified the EPR signals of all five hemes in the fully oxidized NrfA, which allowed to track electron flow within NrfA. Furthermore, EPR-spectral simulations were used to elucidate the sequence of heme reduction and reveal that Hemes 5 and 4 are reduced first (before the active site Heme 1) and can serve the purpose of an electron storage unit within the protein instead of simply serving as a wire to pass electrons into Heme 1.

5.2 Future Work

In this thesis I show that YfeX and variants are great carbene insertion biocatalyst with enhanced N-H insertion reactivity. Unfortunately, YfeX and variants have low product yields for the cyclopropanation of styrene. Future work will focus in improving YfeX's capabilities for cyclopropanation reactivity, specifically by utilizing and expanding on the results presented in Chapters 2 and 3 in combination with additional computational analysis. The limiting cyclopropanation reactivity is not due to a lack of carbene intermediate formation, since we see good N-H insertion reactivity, but instead we propose it is due to a lack of styrene entering the

active site. Initially it was thought that a deficiency of styrene solubility in aqueous buffer could contribute to the reduced reactivity, and the addition of organic co-solvents did not increase yields similar to those for N-H insertion. Therefore, it is proposed that styrene potentially has difficulty entering the active site or once inside it is not oriented properly in a way to react readily with the carbene intermediate. To explore this hypothesis, modifications in the SCS with the active site and near the entrance channel were made to YfeX. So far, none of the four variants investigated show enhanced cyclopropanation reactivity. Another approach for future work is to explore styrene cyclopropanation reactivity using styrene substrates with charged *para*-substituents. Cationic substrate (4-vinylphenyl) trimethylaminium or anionic substrate 4-styrene sulfonic acid would help scope any differences in charges (see **Figure 5.1**). These charged styrene substrates are water soluble and would allow to investigate their interactions within YfeX active site channel.

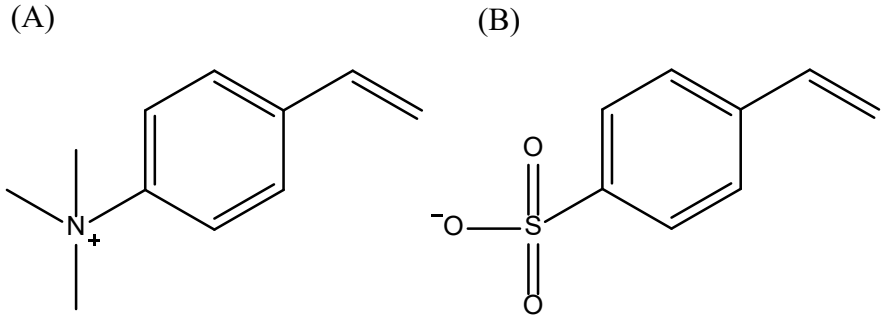

Figure 5.1 Charged styrene substrates (A) (4-vinylphenyl) trimethylaminium and (B) 4-styrene sulfonic acid.

Recently, Huang and coworkers rationally designed and engineered a variant of nitrophorin 2 (NP2), a nitric oxide transport hemoprotein, that catalyzes olefin cyclopropanation with high activity and stereoselectivity.[178] NP2 protein structure consists of an eight-stranded β-barrel typical for a lipocalin fold with a hydrophobic active site and contains a wide substrate channel. They

demonstrated that steric interactions from SCS amino acids near the heme active site have an important role in reactivity. They therefore designed a triple variant, NP2(L122V/ L132V/I120V), that is able to facilitate the styrene cyclopropanation reactivity with very high selectivity, (95%de, 93%ee), giving the (1S,2S)-isomer, by reducing the size of SCS amino acids while maintaining the highly hydrophobic active site pocket.[178] Inspired by these interesting results, future work may investigate the effects of multi-mutations on YfeX . Both YfeX R232A and I230A show improved N-H insertion reactivity and based on these results, a double mutant YfeX R232A, I230A would be a potential target for further investigation. Not only would this double variant enhance the active site cavity but also change the electrostatic interactions within the active site, and more importantly it would also modify the substrate channel, by removing Ile230. This double variant could have promising results for styrene cyclopropanation reactivity.

Furthermore, future work may investigate the effects of a new variant not yet investigated, for example YfeX F248A. This Phe248 is situated (~3.3 Å) above the heme active site and could potentially block styrene entrance or influence styrene orientation within the active site in a negative manner (see **Figure 5.2**). This Phe248 residue could potentially π-stack with styrene and prevent a productive orientation for carbene insertion to occur. By removing this Phe248 residue and replacing it with alanine the active site pocket size would also increase, again potentially allowing styrene to enter more readily to react with the carbene intermediate. Depending on the results, this mutation can also be implemented into a multi-mutation YfeX variant. So far, all amino acid replacements have been done with alanine and, although this is a great starting point, further investigations can be conducted by replacing these SCS residues with other amino acids. This approach would initially need to be tested using computational analysis to gain knowledge about suitable amino acids to introduce. Future work will also focus on characterizing the kinetic profile

of the different YfeX variants. This can be done similar to the kinetic studies of WT YfeX presented in Chapter 2, by monitoring the rate of reaction for N-H insertion of aniline with EDA and for cyclopropanation of styrene with EDA. Overall, these new proposed variants have potential positive characteristics for cyclopropanation reactivity and could help styrene enter the active site and react readily with the carbene intermediate. Further computational studies are underway to model some of the variants and get a better understanding of their interaction.

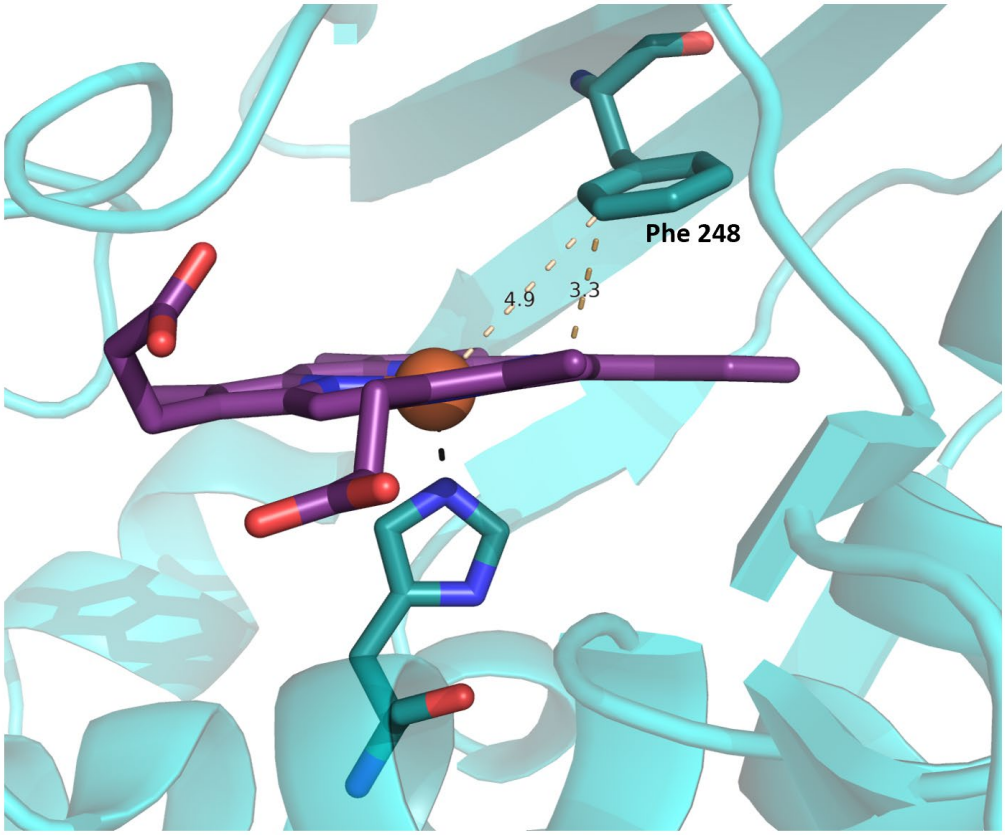

Figure 5.2 PyMOL image of YfeX heme active site highlighting the distance of Phe248 to the heme active site (PDB code: 2IIZ).

QM/MM modeling has been an essential tool for understanding reaction mechanisms of different metalloenzymes.[179-181] It can be used to further understand the limitations of YfeX for

cyclopropanation reactivity and hence help modify the active site accordingly to improve reactivity. As an example, Dim and co-workers used site-directed mutagenesis assisted with QM/MM modeling to enhance glutamate carboxypeptidase II activity.[182] They show that a single-point mutation, E424H, had positive effects on enzyme kinetics, via QM/MM, and the mutant was experimentally characterized to have enhanced reactivity.[182] Furthermore, QM/MM can also be used to improve selectivity of a specific stereoisomer of product, as shown by Arnold and coworkers (see Chapter 2).[39] This approach can be implemented to help improve stereoselectivity for N-H insertion or cyclopropanation reactivity to generate pharmaceutics or pharmaceutical synthons. As seen in Chapter 2, in collaboration with Prof. Chritov lab, we have analyzed the mechanism of Si—H insertion with dimethylphenylsilane via QM/MM and our calculations predict that YfeX goes through an open shell singlet (OSS) transition state. In addition, future computational work can focus on investigating the local environment for the carbene intermediate reaction center via analysis using steric contour maps, as conducted in Huang S. et al.[178] This approach helps understand any steric hinderance that occurs during substrate binding or any interactions that would orientate substrate in an unproductive manner. These proposed computational studies will help gain further information about the SCS interactions that occur during cyclopropanation reactivity and would lead the development of the next generation of YfeX carbene transferase catalysts.

Besides improving YfeX carbene insertion reactivity, via structural modifications, future work may focus on substrate scope and exploring novel reactivity. As highlighted previously, YfeX has high N-H insertion reactivity, and this can now be applied to different substates, such as aniline analogs. As an example, the benzimidazole core structure, a prominent drug synthon for antimycobacterial, analgesic, and anti-inflammatory agents,[183-184] can be potentially

biosynthesized utilizing YfeX's N-H insertion reactivity with *o*-phenylenediamine (see **Figure 5.3**). Once reactivity and products are confirmed further development can be done with *o*-phenylenediamine derivatives to generate other relevant synthons. This similar approach could be used to produce other pharmaceutical synthons and by specifically taking advantage of YfeX's high N-H insertion reactivity.

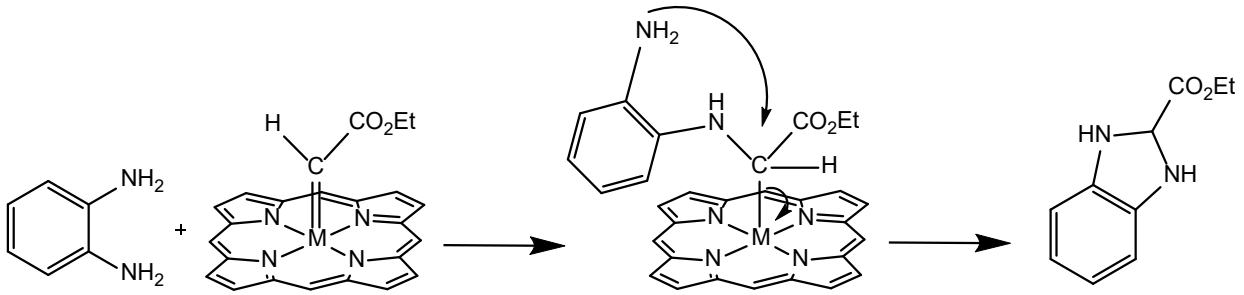

Figure 5.3 Mechanism for the generation of the benzimidazole core structure from a carbene intermediate that is reacted with o-phenylenediamine.

Chapter 4 focuses on the investigation of electron storage and distribution properties within the pentaheme scaffold of *Geobacter lovleyi* cytochrome C nitrite reductase (NrfA). In this project, I was able to establish a method to sequentially add electrons to the fully oxidized protein and track electron flow (by using electron paramagnetic resonance (EPR) and UV-Visible spectroscopy coupled with chemical titration experiments under anaerobic conditions). EPR-spectral simulations were further used to elucidate the sequence of heme reduction within the pentaheme scaffold. Ongoing research aims to capture NrfA intermediates to shed further light on the complicated NrfA mechanism.

The proposed mechanism of NO_2^- reduction by NrfA incorporates several different steps (see **Scheme 4.1** in Chapter 4), but direct experimental evidence of these proposed intermediates is lacking because intermediates have not been trapped and characterized. As a result, our current

understanding of the mechanism is mostly based on computational studies (see Section 4.2).[185-187] To obtain additional experimental insight, we propose to prepare NrfA in different redox states using chemical reduction in the presence of nitrite. Reactions will proceed only until they consume the available electrons, allowing us to trap and characterize any stable intermediates. Since these intermediates are potentially fleeting, the strategy is to utilize stopped-flow spectroscopy. These trapped intermediates can then also be studied using EPR spectroscopy.

To implement this approach, it is proposed that NrfA will be reduced with 1 to 5 electrons at a time chemically (as described in Chapter 4), and the reaction will be initiated by the addition of NO_2^-. These single-turnover reactions would help generate different types of intermediates as shown in **Figure 5.4**, which are based on the computational studies.[185-187] It would be expect that the $\{FeNO\}^6$, $\{FeNO\}^7$, and Fe(II/III)-hydroxylamine complexes are stable species, such that stopped-flow methods will track these reactions and determine the basic kinetics. Analogous studies to those described above can be performed with the alternate substrates NO and H_2NOH to provide additional mechanistic information. The $\{FeNO\}^6$ intermediate can also be obtained by reacting the fully oxidized form of the enzyme with NO. The $\{FeNO\}^7$ intermediate can be captured by reacting the one-electron reduced form of the enzyme with NO. The $\{FeNHO\}^8$ species can be captured by reacting the two-electron reduced form of the enzyme with NO or one-electron reduced form of the enzyme with HNO. Lastly, the other intermediates are accessible by coordinating H_2NOH to the fully oxidized and one-electron reduced form of the protein. These proposed studies will give insight into the complex NrfA mechanism.

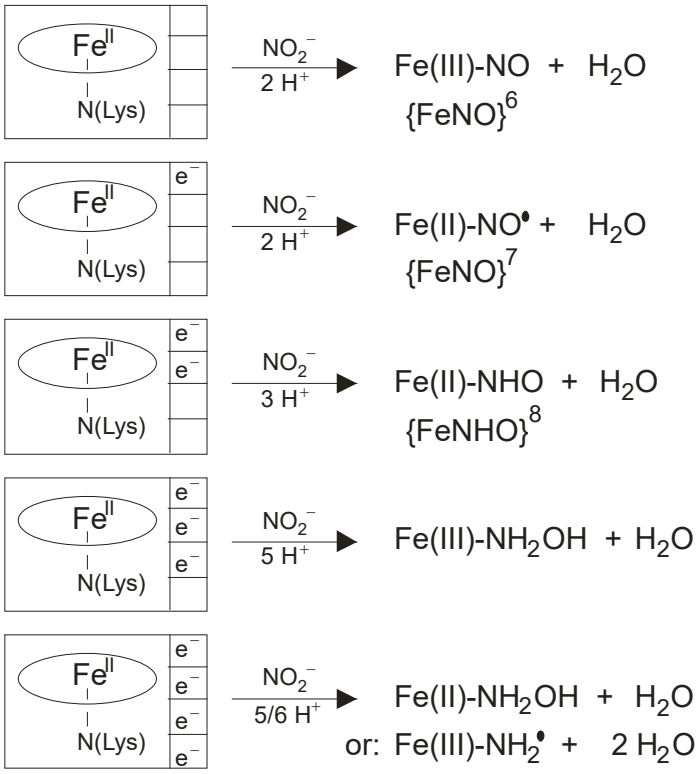

Figure 5.4 Reaction of 1-5 electron-reduced forms of NrfA with $NO2^{-}$. The indicated products are derived from comparison to other enzymes and DFT computations.

Initial work has focused on developing methods to investigate NrfA via stopped-flow spectroscopy. Under pseudo-anaerobic conditions a kinetic trace of NrfA reduction is obtained in the presence of excess reductant. We are able to see that NrfA is fully reduced after 0.6 seconds, after mixing fully oxidized NrfA with excess reductant in the stopped-flow chamber, generating a kinetic curve with no further spectral changes after 1 second (see **Figure 5.5**). From these preliminary experiments, a rate of reduction can be fitted, and we found that NrfA is fully reduced under these conditions with a k_{obs} = 0.7 (sec^{-1}) (see **Figure 5.5C**). To begin trapping any NrfA intermediates the next step is to reduce NrfA by one equivalent of reductant at a time under anaerobic conditions, since once NrfA gets reduced it has been shown to be unstable in an aerobic environment. Any amounts of molecular oxygen will react with any reduced state of NrfA and

oxidize it back to its resting state. This major issue of having molecular oxygen around makes it difficult to do further studies with NrfA even with rapid stopped-flow methodologies. To investigation this issue, extensive precautions are taken during preparation, including introduction of anaerobic buffer within the stopped-flow instrument (since it is set up aerobically) and samples are preparation was done all anaerobically. Unfortunately, even after these precautions are taken NrfA is still being oxidized once it loaded into the stopped-flow system (see **Figure 5.6**). In future work we are planning to use a stopped-flow system stored in an anaerobic environment, in collaboration with the Ragsdale group, hence preventing molecular oxygen from oxidizing NrfA.

(A)

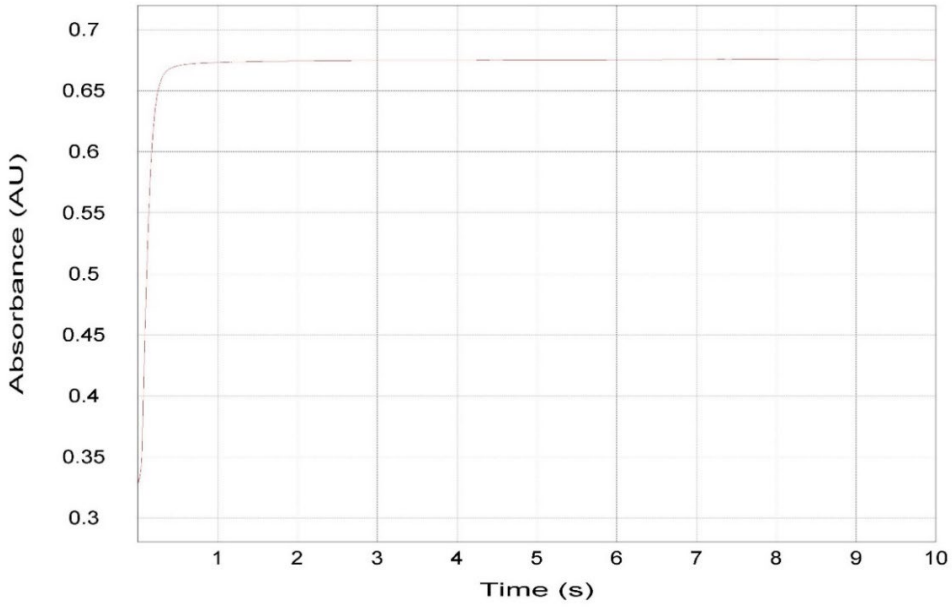

(B)

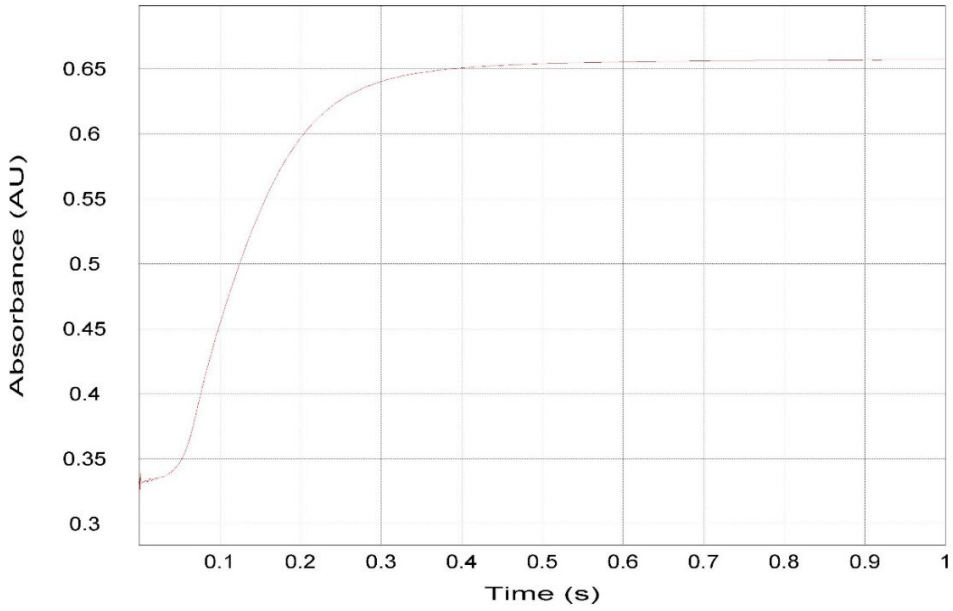

(C)

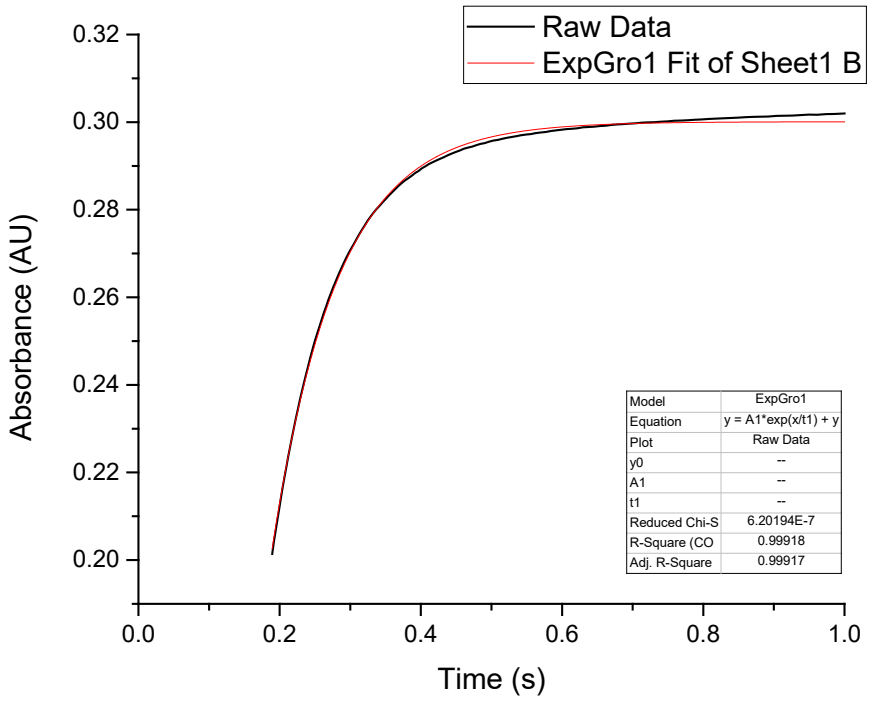

Figure 5.5 Stopped-flow UV-Vis spectra following NrfA [10μM] reduction with excess dithionite [50mM] (A) after 10 seconds and (B) after 1 second. (C) The rate of reduction was calculated utilizing Origin software exponential fit.

(A)

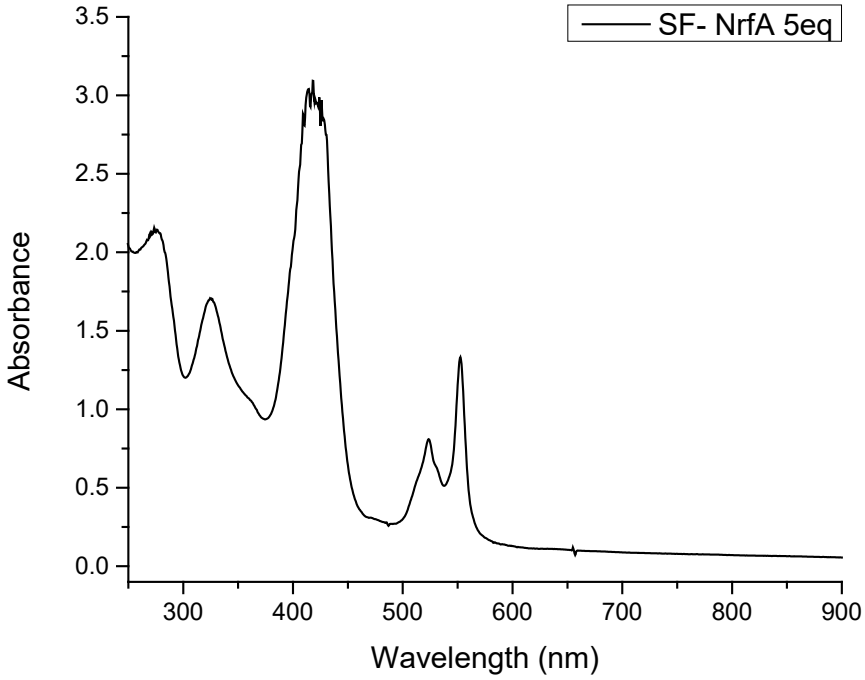

(B)

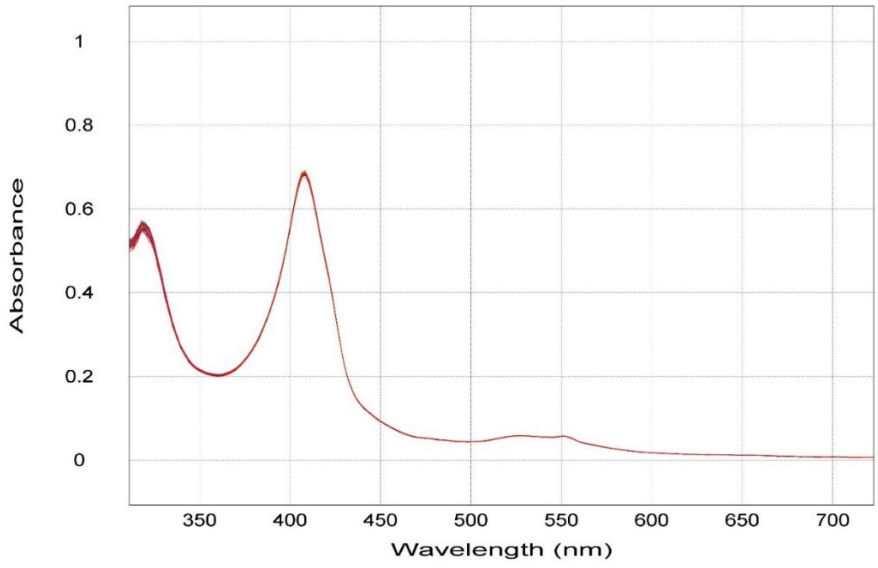

Figure 5.6 (A) UV-visible spectra of NrfA [10μM] fully reduced with 5 equivalents of Ti(III) citrate under anaerobic condition before injection into the stopped-flow instrument. (B) The same

reduced NrfA [10μM] sample after injection into the stopped-flow apparatus, showing the unwanted oxidation process during injection.

Once these issues are resolved, NrfA intermediates can be studied by Stopped-flow UV-Vis spectroscopy. If intermediates with sufficient stability are obtained, they can further be prepared in bulk and then studied using EPR and resonance Raman spectroscopy. Several of the proposed intermediates are paramagnetic (Fe(II)-$NO^{\bullet}$, Fe(III)-NH_2OH and Fe(III)-NH_2) and can be studied with EPR. Resonance Raman spectroscopy, a well-established tool to study the electronic structures of heme proteins,[188-192] can be applied on NrfA. Similar methodologies with resonance Raman spectroscopy have been previously conducted to obtain vibrational assignments for ferric porphyrins.[193-195] In addition, Fe-NO stretching vibrations (in the range of 400-600 cm^{-1}) have been identified in the spectra of $\{FeNO\}^6$, $\{FeNO\}^7$, and $\{FeNHO\}^8$ complexes of myoglobin, other heme proteins, and model systems.[196] Overall, these proposed experiments will help further understand NrfA's complex mechanism.

Bibliography

1. Whitesides, G. M.; Wong, C. H., Enzymes as catalysts in synthetic organic chemistry [new synthetic methods (53)]. *Angew. Chem. Int. Ed.* **1985,** *24* (8), 617-638.
2. Purich, D. L., *Enzyme kinetics: catalysis and control: a reference of theory and best-practice methods*. Elsevier: 2010.
3. Jourdant, A.; González-Zamora, E.; Zhu, J., Wilkinson's catalyst catalyzed selective hydrogenation of olefin in the presence of an aromatic nitro function: a remarkable solvent effect. *J. org. chem.* **2002,** *67* (9), 3163-3164.
4. Vougioukalakis, G. C.; Grubbs, R. H., Ruthenium-based heterocyclic carbene-coordinated olefin metathesis catalysts. *Chem. Rev.* **2010,** *110* (3), 1746-1787.
5. Horvath, I. T.; Anastas, P. T., Innovations and green chemistry. *Chem. Rev.* **2007,** *107* (6), 2169-2173.
6. Lim, X., The new breed of cutting-edge catalysts. *Nature News* **2016,** *537* (7619), 156.
7. Sinou, D., *Metal catalysis in water*. Springer: 1999; p 41-59.
8. Birch, A.; Williamson, D., Homogeneous hydrogenation catalysts in organic synthesis. *Org. React.* **2004,** *24*, 1-186.
9. Eilbracht, P.; Bärfacker, L.; Buss, C.; Hollmann, C.; Kitsos-Rzychon, B. E.; Kranemann, C. L.; Rische, T.; Roggenbuck, R.; Schmidt, A., Tandem reaction sequences under hydroformylation conditions: new synthetic applications of transition metal catalysis. *Chem. Rev.* **1999,** *99* (11), 3329-3366.
10. Sun, H.; Zhang, H.; Ang, E. L.; Zhao, H., Biocatalysis for the synthesis of pharmaceuticals and pharmaceutical intermediates. *Bioorg. med. chem.* **2018,** *26* (7), 1275-1284.
11. Bell, E. L.; Finnigan, W.; France, S. P.; Green, A. P.; Hayes, M. A.; Hepworth, L. J.; Lovelock, S. L.; Niikura, H.; Osuna, S.; Romero, E., Biocatalysis. *Nat. Rev. Methods Primers* **2021,** *1* (1), 1-21.
12. Hammer, S. C.; Knight, A. M.; Arnold, F. H., Design and evolution of enzymes for non-natural chemistry. *Curr. Opin. Green Sustain. Chem.* **2017,** *7*, 23-30.
13. Lu, Y., Biosynthetic inorganic chemistry. *Angew. Chem. Int. Ed.* **2006,** *45* (34), 5588-5601.
14. Matsuo, T.; Hirota, S., Artificial enzymes with protein scaffolds: Structural design and modification. *Bioorg. Med. Chem.* **2014,** *22* (20), 5638-5656.
15. Hauer, B., Embracing nature's catalysts: a viewpoint on the future of biocatalysis. *ACS Catal.* **2020,** *10* (15), 8418-8427.
16. Chakrabarty, S.; Wang, Y.; Perkins, J. C.; Narayan, A. R., Scalable biocatalytic C–H oxyfunctionalization reactions. *Chem. Soc. Rev.* **2020,** *49* (22), 8137-8155.
17. Sheldon, R. A.; Brady, D., The limits to biocatalysis: pushing the envelope. *Chem. Commun.* **2018,** *54* (48), 6088-6104.
18. Ortiz de Montellano, P. R., *Cytochrome P450: Structure, Mechanism, and Biochemistry*. 3rd ed.; Kluver Academic/Plenum Publishers: New York, 2005.

19. McEvoy, J. P.; Brudvig, G. W., Water-splitting chemistry of photosystem II. *Chem. rev.* **2006,** *106* (11), 4455-4483.
20. Krüger, M.; Meyerdierks, A.; Glöckner, F. O.; Amann, R.; Widdel, F.; Kube, M.; Reinhardt, R.; Kahnt, J.; Böcher, R.; Thauer, R. K., A conspicuous nickel protein in microbial mats that oxidize methane anaerobically. *Nature* **2003,** *426* (6968), 878-881.
21. Kazlauskas, R. J., Enhancing catalytic promiscuity for biocatalysis. *Curr. opin. chem. biol.* **2005,** *9* (2), 195-201.
22. Chen, K.; Arnold, F. H., Engineering new catalytic activities in enzymes. *Nat. Catal.* **2020,** *3* (3), 203-213.
23. Wittmann, B. J.; Knight, A. M.; Hofstra, J. L.; Reisman, S. E.; Jennifer Kan, S.; Arnold, F. H., Diversity-Oriented Enzymatic Synthesis of Cyclopropane Building Blocks. *ACS Catal.* **2020,** *10* (13), 7112-7116.
24. Bajaj, P.; Sreenilayam, G.; Tyagi, V.; Fasan, R., Gram-scale synthesis of chiral cyclopropane-containing drugs and drug precursors with engineered myoglobin catalysts featuring complementary stereoselectivity. *Angew. Chem.* **2016,** *128* (52), 16344-16348.
25. Weissenborn, M. J.; Koenigs, R. M., Iron-porphyrin Catalyzed Carbene Transfer Reactions–an Evolution from Biomimetic Catalysis towards Chemistry-inspired Non-natural Reactivities of Enzymes. *Chem. Cat. Chem.* **2020,** *12* (8), 2171-2179.
26. Liu, Z.; Arnold, F. H., New-to-nature chemistry from old protein machinery: carbene and nitrene transferases. *Curr. Opin. Biotechnol.* **2021,** *69*, 43-51.
27. Sheldon, R. A.; Brady, D., Broadening the scope of biocatalysis in sustainable organic synthesis. *ChemSusChem* **2019,** *12* (13), 2859-2881.
28. Hernáiz, M. J.; Alcántara, A. R.; García, J. I.; Sinisterra, J. V., Applied biotransformations in green solvents. *Chem. Eur. J.* **2010,** *16* (31), 9422-9437.
29. Coelho, P. S.; Wang, Z. J.; Ener, M. E.; Baril, S. A.; Kannan, A.; Arnold, F. H.; Brustad, E. M., A serine-substituted P450 catalyzes highly efficient carbene transfer to olefins in vivo. *Nat. Chem. Biol.* **2013,** *9* (8), 485-487.
30. Tegoni, M.; Yu, F.; Bersellini, M.; Penner-Hahn, J. E.; Pecoraro, V. L., Designing a functional type 2 copper center that has nitrite reductase activity within α-helical coiled coils. *Proc. Natl. Acad. Sci. U.S.A.* **2012,** *109* (52), 21234-21239.
31. Lin, Y.-W.; Yeung, N.; Gao, Y.-G.; Miner, K. D.; Tian, S.; Robinson, H.; Lu, Y., Roles of glutamates and metal ions in a rationally designed nitric oxide reductase based on myoglobin. *Proc. Natl. Acad. Sci.* **2010,** *107* (19), 8581-8586.
32. Sono, M.; Roach, M. P.; Coulter, E. D.; Dawson, J. H., Heme-Containing Oxygenases. *Chem. Rev.* **1996,** *96*, 2841-2887.
33. Wang, Z. J.; Peck, N. E.; Renata, H.; Arnold, F. H., Cytochrome P450-catalyzed insertion of carbenoids into N–H bonds. *Chem. Sci.* **2014,** *5* (2), 598-601.
34. Renata, H. W., Z. J.; Kitto, R. Z.; Arnold, F. H., P450-catalyzed asymmetric cyclopropanation of electron-deficient olefins under aerobic conditions. *Catal. Sci. Technol.* **2014,** *4* (10), 3640-3643.
35. McIntosh, J. A.; Coelho, P. S.; Farwell, C. C.; Wang, Z. J.; Lewis, J. C.; Brown, T. R.; Arnold, F. H., Enantioselective Intramolecular C-H Amination Catalyzed by Engineered Cytochrome P450 Enzymes In Vitro and In Vivo. *Angew. Chem. Int. Ed.* **2013,** *52* (35), 9309-9312.

36. Coelho, P. S.; Brustad, E. M.; Kannan, A.; Arnold, F. H., Olefin cyclopropanation via carbene transfer catalyzed by engineered cytochrome P450 enzymes. *Science* **2013,** *339* (6117), 307-310.
37. Arnold, F. H., Directed evolution: bringing new chemistry to life. *Angew. Chem. Int. Ed.* **2018,** *57* (16), 4143-4148.
38. Kan, S. J.; Lewis, R. D.; Chen, K.; Arnold, F. H., Directed evolution of cytochrome c for carbon–silicon bond formation: Bringing silicon to life. *Science* **2016,** *354* (6315), 1048-1051.
39. Garcia-Borràs, M.; Kan, S. J.; Lewis, R. D.; Tang, A.; Jimenez-Osés, G.; Arnold, F. H.; Houk, K. N., Origin and Control of Chemoselectivity in Cytochrome c Catalyzed Carbene Transfer into Si–H and N–H bonds. *J. Am. Chem. Soc.* **2021,** *143* (18), 7114-7123.
40. Huang, X.; Garcia-Borràs, M.; Miao, K.; Kan, S. J.; Zutshi, A.; Houk, K.; Arnold, F. H., A biocatalytic platform for synthesis of chiral α-trifluoromethylated organoborons. *ACS cent. sci.* **2019,** *5* (2), 270-276.
41. Koebke, K. J.; Pinter, T. B.; Pitts, W. C.; Pecoraro, V. L., Catalysis and Electron Transfer in De Novo Designed Metalloproteins. *Chem. Rev.* **2022,** *122* (14), 12046-12109.
42. Zastrow, M. L.; Peacock, A. F.; Stuckey, J. A.; Pecoraro, V. L., Hydrolytic catalysis and structural stabilization in a designed metalloprotein. *Nat. chem.* **2012,** *4* (2), 118-123.
43. Faiella, M.; Maglio, O.; Nastri, F.; Lombardi, A.; Lista, L.; Hagen, W. R.; Pavone, V., De Novo Design, Synthesis and Characterisation of MP3, A New Catalytic Four-Helix Bundle Hemeprotein. *Chem. Eur. J.* **2012,** *18* (50), 15960-15971.
44. Stenner, R.; Steventon, J. W.; Seddon, A.; Anderson, J. R., A de novo peroxidase is also a promiscuous yet stereoselective carbene transferase. *Proc. Natl. Acad. Sci.* **2020,** *117* (3), 1419-1428.
45. Sigman, J. A.; Kwok, B. C.; Lu, Y., From myoglobin to heme-copper oxidase: design and engineering of a CuB center into sperm whale myoglobin. *J. Am. Chem. Soc.* **2000,** *122* (34), 8192-8196.
46. Yeung, N.; Lin, Y. W.; Gao, Y. G.; Zhao, X.; Russell, B. S.; Lei, L.; Miner, K. D.; Robinson, H.; Lu, Y., Rational design of a structural and functional nitric oxide reductase. *Nature* **2009,** *462*, 1079-1082.
47. Mukherjee, S.; Bhagi, A.; Mukherjee, A.; Mukherjee, M.; Lu, Y.; Dey, A., A biosynthetic model of cytochrome *c* oxidase as an electrocatalyst for oxygen reduction. *Nat. Commun.* **2015,** *6*, 8467.
48. Zastrow, M. L.; Pecoraro, V. L., Designing functional metalloproteins: From structural to catalytic metal sites. *Coord. chem. rev.* **2013,** *257* (17-18), 2565-2588.
49. Woolfson, D. N.; Bartlett, G. J.; Burton, A. J.; Heal, J. W.; Niitsu, A.; Thomson, A. R.; Wood, C. W., De novo protein design: how do we expand into the universe of possible protein structures? *Curr. opin. struct. biol.* **2015,** *33*, 16-26.
50. Teale, F. W., Cleavage of the haem-protein link by acid methylethylketone. *Biochim biophys acta* **1959,** *35*, 543.
51. Sreenilayam, G.; Moore, E. J.; Steck, V.; Fasan, R., Metal substitution modulates the reactivity and extends the reaction scope of myoglobin carbene transfer catalysts. *Adv. Synth. Catal.* **2017,** *359* (12), 2076-2089.
52. Heinisch, T.; Ward, T. R., Artificial metalloenzymes based on the biotin–streptavidin technology: challenges and opportunities. *Acc. chem. res.* **2016,** *49* (9), 1711-1721.
53. Wolf, M. W.; Vargas, D. A.; Lehnert, N., Engineering of RuMb: Toward a Green Catalyst for Carbene Insertion Reactions. *Inorg. Chem.* **2017,** *56* (10), 5623-5635.

54. Key, H. M.; Dydio, P.; Clark, D. S.; Hartwig, J. F., Abiological catalysis by artificial haem proteins containing noble metals in place of iron. *Nature* **2016,** *534* (7608), 534-537.
55. Bordeaux, M.; Tyagi, V.; Fasan, R., Highly diastereoselective and enantioselective olefin cyclopropanation using engineered myoglobin-based catalysts. *Angew. Chem.* **2015,** *127* (6), 1764-1768.
56. Shanab, K.; Neudorfer, C.; Schirmer, E.; Spreitzer, H., Green solvents in organic synthesis: an overview. *Curr. Org. Chem.* **2013,** *17* (11), 1179-1187.
57. Nicolas, I.; Roisnel, T.; Le Maux, P.; Simonneaux, G., Asymmetric intermolecular cyclopropanation of alkenes by diazoketones catalyzed by Halterman iron porphyrins. *Tetrahedron Lett.* **2009,** *50* (36), 5149-5151.
58. Wei, Y.; Tinoco, A.; Steck, V.; Fasan, R.; Zhang, Y., Cyclopropanations via heme carbenes: Basic mechanism and effects of carbene substituent, protein axial ligand, and porphyrin substitution. *J. Am. Chem. Soc.* **2017,** *140* (5), 1649-1662.
59. Brandenberg, O. F.; Fasan, R.; Arnold, F. H., Exploiting and engineering hemoproteins for abiological carbene and nitrene transfer reactions. *Curr. Opin. Biotechnol.* **2017,** *47*, 102-111.
60. Dydio, P.; Key, H.; Nazarenko, A.; Rha, J.-E.; Seyedkazemi, V.; Clark, D.; Hartwig, J., An artificial metalloenzyme with the kinetics of native enzymes. *Science* **2016,** *354* (6308), 102-106.
61. Hayashi, T.; Tinzl, M.; Mori, T.; Krengel, U.; Proppe, J.; Soetbeer, J.; Klose, D.; Jeschke, G.; Reiher, M.; Hilvert, D., Capture and characterization of a reactive haem–carbenoid complex in an artificial metalloenzyme. *Nat. Catal.* **2018,** *1* (8), 578-584.
62. Oohora, K.; Meichin, H.; Zhao, L.; Wolf, M. W.; Nakayama, A.; Hasegawa, J.-y.; Lehnert, N.; Hayashi, T., Catalytic cyclopropanation by myoglobin reconstituted with iron porphycene: Acceleration of catalysis due to rapid formation of the carbene species. *J. Am. Chem. Soc.* **2017,** *139* (48), 17265-17268.
63. Tinoco, A.; Steck, V.; Tyagi, V.; Fasan, R., Highly diastereo-and enantioselective synthesis of trifluoromethyl-substituted cyclopropanes via myoglobin-catalyzed transfer of trifluoromethylcarbene. *J. Am. Chem. Soc.* **2017,** *139* (15), 5293-5296.
64. Sreenilayam, G.; Moore, E. J.; Steck, V.; Fasan, R., Stereoselective olefin cyclopropanation under aerobic conditions with an artificial enzyme incorporating an iron-chlorin e6 cofactor. *ACS Catal.* **2017,** *7* (11), 7629-7633.
65. Chandgude, A. L.; Ren, X.; Fasan, R., Stereodivergent intramolecular cyclopropanation enabled by engineered carbene transferases. *J. Am. Chem. Soc.* **2019,** *141* (23), 9145-9150.
66. Vargas, D. A.; Tinoco, A.; Tyagi, V.; Fasan, R., Myoglobin-Catalyzed C− H Functionalization of Unprotected Indoles. *Angew. Chem. Int. Ed.* **2018,** *57* (31), 9911-9915.
67. Carminati, D. M.; Decaens, J.; Couve-Bonnaire, S.; Jubault, P.; Fasan, R., Biocatalytic Strategy for the Highly Stereoselective Synthesis of CHF_2-Containing Trisubstituted Cyclopropanes. *Angew. Chem. Int. Ed.* **2021,** *60* (13), 7072-7076.
68. Che, C.-M.; Lo, V. K.-Y.; Zhou, C.-Y.; Huang, J.-S., Selective functionalisation of saturated C–H bonds with metalloporphyrin catalysts. *Chem. Soc. Rev.* **2011,** *40* (4), 1950-1975.
69. Lu, H.; Zhang, X. P., Catalytic C–H functionalization by metalloporphyrins: recent developments and future directions. *Chem. Soc. Rev.* **2011,** *40* (4), 1899-1909.
70. McQuarters, A. B.; Wolf, M. W.; Hunt, A. P.; Lehnert, N., 1958-2014: After 56 Years of Research, Cytochrome P450 Reactivity Finally Explained. *Angew. Chem. Int. Ed.* **2014,** *53*, 4750-4752.

71. Rittle, J.; Green, M. T., Cytochrome P450 compound I: capture, characterization, and CH bond activation kinetics. *Science* **2010,** *330* (6006), 933-937.
72. Simões, M. M.; Gonzaga, D. T.; Cardoso, M. F.; Forezi, L. d. S.; Gomes, A. T.; Da Silva, F. D. C.; Ferreira, V. F.; Neves, M. G.; Cavaleiro, J. A., Carbene transfer reactions catalysed by dyes of the metalloporphyrin group. *Molecules* **2018,** *23* (4), 792.
73. Dailey, H. A.; Septer, A. N.; Daugherty, L.; Thames, D.; Gerdes, S.; Stabb, E. V.; Dunn, A. K.; Dailey, T. A.; Phillips, J. D., The Escherichia coli protein YfeX functions as a porphyrinogen oxidase, not a heme dechelatase. *MBio* **2011,** *2* (6), e00248-11.
74. Liu, X.; Yuan, Z.; Wang, J.; Cui, Y.; Liu, S.; Ma, Y.; Gu, L.; Xu, S., Crystal structure and biochemical features of dye-decolorizing peroxidase YfeX from Escherichia coli O157 Asp143 and Arg232 play divergent roles toward different substrates. *Biochem. Biophys. Res. Commun.* **2017,** *484* (1), 40-44.
75. Kim, S. J.; Shoda, M., Decolorization of molasses and a dye by a newly isolated strain of the fungus Geotrichum candidum Dec 1. *Biotechnol. Bioeng.* **1999,** *62* (1), 114-119.
76. Singh, R.; Eltis, L. D., The multihued palette of dye-decolorizing peroxidases. *Arch. biochem. biophys.* **2015,** *574*, 56-65.
77. Sugano, Y., DyP-type peroxidases comprise a novel heme peroxidase family. *Cell. Mol. Life Sci.* **2009,** *66* (8), 1387-1403.
78. Weissenborn, M. J.; Löw, S. A.; Borlinghaus, N.; Kuhn, M.; Kummer, S.; Rami, F.; Plietker, B.; Hauer, B., Enzyme-Catalyzed Carbonyl Olefination by the E. coli Protein YfeX in the Absence of Phosphines. *Chem. Cat. Chem.* **2016,** *8* (9), 1636-1640.
79. YfeX-A New Platform for Carbene Transferase Development with High Intrinsic Reactivity. *Chemistry (Weinheim an der Bergstrasse, Germany)* **2022**.
80. Campeciño, J.; Lagishetty, S.; Wawrzak, Z.; Sosa Alfaro, V.; Lehnert, N.; Reguera, G.; Hu, J.; Hegg, E., Cytochrome *c* nitrite reductase from *Geobacter lovleyi* represents a new NrfA subclass. *J. Biol. Chem.* **2020,** *295*, 11455-11465.
81. Tiedje, J. M., Ecology of denitrification and dissimilatory nitrate reduction to ammonium. *Biology of anaerobic microorganisms* **1988,** *717*, 179-244.
82. Lam, P.; Kuypers, M. M. M., Microbial nitrogen cycling processes in oxygen minimum zones. *Annu. Rev. Mar. Sci.* **2011,** *3*, 317-345.
83. Kraft, B.; Strous, M.; Tegetmeyer, H. E., Microbial nitrate respiration–genes, enzymes and environmental distribution. *J. Biotechnol.* **2011,** *155*, 104-117.
84. Einsle, O.; Messerschmidt, A.; Huber, R.; Kroneck, P. M.; Neese, F., Mechanism of the six-electron reduction of nitrite to ammonia by cytochrome c nitrite reductase. *J. A. C. S.* **2002,** *124* (39), 11737-11745.
85. Bykov, D.; Neese, F., Substrate binding and activation in the active site of cytochrome *c* nitrite reductase: a density functional study. *J. Biol. Inorg. Chem.* **2011,** *16*, 417-430.
86. Bykov, D.; Neese, F., Six-Electron Reduction of Nitrite to Ammonia by Cytochrome *c* Nitrite Reductase: Insights from Density Functional Theory Studies. *Inorg. Chem.* **2015,** *54*, 9303–9316.
87. Clarke, T. A.; Hemmings, A. M.; Burlat, B.; Butt, J. N.; Cole, J. A.; Richardson, D. J., Comparison of the structural and kinetic properties of the cytochrome *c* nitrite reductases from *Escherichia coli*, *Wolinella succinogenes*, *Sulfurospirillum deleyianum* and *Desulfovibrio desulfuricans*. *Biochem. Soc. Trans.* **2006,** *34*, 143-145.

88. Sosa Alfaro, V.; Campeciño, J.; Tracy, M.; Elliott, S. J.; Hegg, E. L.; Lehnert, N., Elucidating Electron Storage and Distribution within the Pentaheme Scaffold of Cytochrome *c* Nitrite Reductase (NrfA). *Biochemistry* **2021,** *60* (23), 1853-1867.
89. Sreenilayam, G.; Fasan, R., Myoglobin-catalyzed intermolecular carbene N–H insertion with arylamine substrates. *Chem. Commun.* **2015,** *51* (8), 1532-1534.
90. Steck, V.; Sreenilayam, G.; Fasan, R., Selective Functionalization of Aliphatic Amines via Myoglobin-catalyzed Carbene NH Insertion. *Synlett* **2020,** *31* (03), 224-229.
91. Lewis, R. D.; Garcia-Borràs, M.; Chalkley, M. J.; Buller, A. R.; Houk, K.; Kan, S. J.; Arnold, F. H., Catalytic iron-carbene intermediate revealed in a cytochrome c carbene transferase. *Proc. Natl. Acad. Sci. U.S.A.* **2018,** *115* (28), 7308-7313.
92. Moore, E. J.; Steck, V.; Bajaj, P.; Fasan, R., Chemoselective cyclopropanation over carbene Y–H insertion catalyzed by an engineered carbene transferase. *J. Org. Chem.* **2018,** *83* (14), 7480-7490.
93. Balhara, R.; Chatterjee, R.; Jindal, G., A computational approach to understand the role of metals and axial ligands in artificial heme enzyme catalyzed C–H insertion. *Phys. Chem. Chem. Phys.* **2021,** *23* (15), 9500-9511.
94. Tinoco, A.; Wei, Y.; Bacik, J.-P.; Carminati, D. M.; Moore, E. J.; Ando, N.; Zhang, Y.; Fasan, R., Origin of high stereocontrol in olefin cyclopropanation catalyzed by an engineered carbene transferase. *ACS Catal.* **2018,** *9* (2), 1514-1524.
95. Khade, R. L.; Chandgude, A. L.; Fasan, R.; Zhang, Y., Mechanistic Investigation of Biocatalytic Heme Carbenoid Si-H Insertions. *ChemCatChem* **2019,** *11* (13), 3101.
96. Kruschel, D.; Zagrovic, B., Conformational averaging in structural biology: issues, challenges and computational solutions. *Mol. Biosyst.* **2009,** *5* (12), 1606-1616.
97. Cui, Q.; Karplus, M., Allostery and cooperativity revisited. *Protein Sci.* **2008,** *17* (8), 1295-1307.
98. Dodson, G. G.; Lane, D. P.; Verma, C. S., Molecular simulations of protein dynamics: new windows on mechanisms in biology. *EMBO Rep.* **2008,** *9* (2), 144-150.
99. Su, H.; Ma, G.; Liu, Y., Theoretical insights into the mechanism and stereoselectivity of olefin cyclopropanation catalyzed by two engineered cytochrome P450 enzymes. *Inorg. Chem.* **2018,** *57* (18), 11738-11745.
100. Ahlrichs, R.; Bär, M.; Häser, M.; Horn, H.; Kölmel, C., Electronic structure calculations on workstation computers: The program system turbomole. *Chem. Phys. Lett.* **1989,** *162* (3), 165-169.
101. Smith, W.; Forester, T., DL_POLY_2. 0: A general-purpose parallel molecular dynamics simulation package. *J. Mol. Graph.* **1996,** *14* (3), 136-141.
102. Sherwood, P.; de Vries, A. H.; Guest, M. F.; Schreckenbach, G.; Catlow, C. R. A.; French, S. A.; Sokol, A. A.; Bromley, S. T.; Thiel, W.; Turner, A. J., QUASI: A general purpose implementation of the QM/MM approach and its application to problems in catalysis. *J. Mol. Struct.: THEOCHEM* **2003,** *632* (1-3), 1-28.
103. Sharon, D. A.; Mallick, D.; Wang, B.; Shaik, S., Computation sheds insight into iron porphyrin carbenes' electronic structure, formation, and N–H insertion reactivity. *J. Am. Chem. Soc.* **2016,** *138* (30), 9597-9610.
104. Li, X.; Dong, L.; Liu, Y., Theoretical Study of Iron Porphyrin Nitrene: Formation Mechanism, Electronic Nature, and Intermolecular C–H Amination. *Inorg. chem.* **2020,** *59* (3), 1622-1632.

105. Ren, X.; Fasan, R., Engineered and Artificial Metalloenzymes for Selective C–H Functionalization. *Curr. Opin. Green Sustain. Chem.* **2021**, 100494.
106. Oohora, K.; Onoda, A.; Hayashi, T., Hemoproteins reconstituted with artificial metal complexes as biohybrid catalysts. *Acc. chem. Res.* **2019,** *52* (4), 945-954.
107. Khade, R. L.; Zhang, Y., Catalytic and biocatalytic iron porphyrin carbene formation: Effects of binding mode, carbene substituent, porphyrin substituent, and protein axial ligand. *J. Am. Chem. Soc.* **2015,** *137* (24), 7560-7563.
108. Dennington, R.; Keith, T. A.; Millam, J. M., GaussView 6.0. 16. *Semichem Inc.: Shawnee Mission, KS, USA* **2016**.
109. Olsson, M. H.; Søndergaard, C. R.; Rostkowski, M.; Jensen, J. H., PROPKA3: consistent treatment of internal and surface residues in empirical p K a predictions. *J. Chem. Theory Comput.* **2011,** *7* (2), 525-537.
110. Li, P.; Merz Jr, K. M., MCPB. py: a python based metal center parameter builder. ACS Publications: 2016.
111. Seminario, J. M., Calculation of intramolecular force fields from second-derivative tensors. *Int. J. Quantum Chem.* **1996,** *60* (7), 1271-1277.
112. Wang, J.; Wang, W.; Kollman, P. A.; Case, D. A., Automatic atom type and bond type perception in molecular mechanical calculations. *J. Mol. Graph. Model.* **2006,** *25* (2), 247-260.
113. Jorgensen, W. L.; Chandrasekhar, J.; Madura, J. D.; Impey, R. W.; Klein, M. L., Comparison of simple potential functions for simulating liquid water. *J. Chem. Phys.* **1983,** *79* (2), 926-935.
114. Waheed, S. O.; Chaturvedi, S. S.; Karabencheva-Christova, T. G.; Christov, C. Z., Catalytic mechanism of human ten-eleven translocation-2 (tet2) enzyme: Effects of conformational changes, electric field, and mutations. *ACS Catal.* **2021,** *11* (7), 3877-3890.
115. Christov, C.; Ramanan, R.; Waheed, S. O.; Schofield, C. J., What is The Catalytic Mechanism of Enzymatic Histone N-Methyl Arginine Demethylation and Can it be Influenced by an External Electric Field? *Chem. Eur. J.* **2021,** *27* (46), 11827-11836.
116. Davidchack, R. L.; Ouldridge, T.; Tretyakov, M., New Langevin and gradient thermostats for rigid body dynamics. *J. Chem. Phys.* **2015,** *142* (14), 144114.
117. Chakravorty, D. K.; Wang, B.; Lee, C. W.; Guerra, A. J.; Giedroc, D. P.; Merz, K. M., Solution NMR refinement of a metal ion bound protein using metal ion inclusive restrained molecular dynamics methods. *J. Biomol. NMR* **2013,** *56* (2), 125-137.
118. Bresme, F., Equilibrium and nonequilibrium molecular-dynamics simulations of the central force model of water. *J. Chem. Phys.* **2001,** *115* (16), 7564-7574.
119. Ryckaert, J.-P.; Ciccotti, G.; Berendsen, H. J., Numerical integration of the cartesian equations of motion of a system with constraints: molecular dynamics of n-alkanes. *J. Comput. Phys.* **1977,** *23* (3), 327-341.
120. Gotz, A. W.; Williamson, M. J.; Xu, D.; Poole, D.; Le Grand, S.; Walker, R. C., Routine microsecond molecular dynamics simulations with AMBER on GPUs. 1. Generalized born. *J. Chem. Theory Comput.* **2012,** *8* (5), 1542-1555.
121. Maier, J. A.; Martinez, C.; Kasavajhala, K.; Wickstrom, L.; Hauser, K. E.; Simmerling, C., ff14SB: improving the accuracy of protein side chain and backbone parameters from ff99SB. *J. Chem. Theory Comput.* **2015,** *11* (8), 3696-3713.
122. Roe, D. R.; Cheatham III, T. E., PTRAJ and CPPTRAJ: software for processing and analysis of molecular dynamics trajectory data. *J. Chem. Theory Comput.* **2013,** *9* (7), 3084-3095.

123. Casali, E.; Gallo, E.; Toma, L., An In-Depth Computational Study of Alkene Cyclopropanation Catalyzed by Fe (porphyrin)(OCH3) Complexes. The Environmental Effects on the Energy Barriers. *Inorg. Chem.* **2020,** *59* (16), 11329-11336.
124. Kästner, J.; Carr, J. M.; Keal, T. W.; Thiel, W.; Wander, A.; Sherwood, P., DL-FIND: an open-source geometry optimizer for atomistic simulations. *J. Phys. Chem. A* **2009,** *113* (43), 11856-11865.
125. Billeter, S. R.; Turner, A. J.; Thiel, W., Linear scaling geometry optimisation and transition state search in hybrid delocalised internal coordinates. *Phys. Chem. Chem. Phys.* **2000,** *2* (10), 2177-2186.
126. Pfanzagl, V.; Nys, K.; Bellei, M.; Michlits, H.; Mlynek, G.; Battistuzzi, G.; Djinovic-Carugo, K.; Van Doorslaer, S.; Furtmüller, P. G.; Hofbauer, S., Roles of distal aspartate and arginine of B-class dye-decolorizing peroxidase in heterolytic hydrogen peroxide cleavage. *J. Biol. Chem.* **2018,** *293* (38), 14823-14838.
127. Lehnert, N.; Dong, H. T.; Harland, J. B.; Hunt, A. P.; White, C. J., Reversing Nitrogen Fixation. *Nat. Rev. Chem.* **2018,** *2*, 278-289.
128. Burgess, B. K.; Lowe, D. J., Mechanism of Molybdenum Nitrogenase. *Chem. Rev.* **1996,** *96*, 2983-3012.
129. Hoffman, B. M.; Lukoyanov, D.; Yang, Y.-Z.; Dean, D. R.; Seefeldt, L., Mechanism of Nitrogen Fixation by Nitrogenase: the Next Stage. *Chem. Rev.* **2014,** *114*, 4041-4062.
130. Burford, R. J.; Fryzuk, M. D., Examining the relationship between coordination mode and reactivity of dinitrogen. *Nat. Rev. Chem.* **2017,** *1*, 1-13.
131. Lehnert, N.; Coruzzi, G.; Hegg, E.; Seefeldt, L.; Stein, L. *NSF Workshop Report: Feeding the World in the 21st Century: Grand Challenges in the Nitrogen Cycle*; National Science Foundation: Arlington, VA: Arlington, VA, 2016.
132. Smil, V., Nitrogen cycle and world food production. *World Agriculture* **2011,** *2*, 9-13.
133. Fernandes, S. O.; Bonin, P. C.; Michotey, V. D.; Garcia, N.; LokaBharathi, P., Nitrogen-limited mangrove ecosystems conserve N through dissimilatory nitrate reduction to ammonium. *Sci. Reports* **2012,** *2*, 419.
134. Huygens, D.; Rütting, T.; Boeckx, P.; Van Cleemput, O.; Godoy, R.; Müller, C., Soil nitrogen conservation mechanisms in a pristine south Chilean Nothofagus forest ecosystem. *Soil Biol. and Biochem.* **2007,** *39* (10), 2448-2458.
135. Putz, M.; Schleusner, P.; Rütting, T.; Hallin, S., Relative abundance of denitrifying and DNRA bacteria and their activity determine nitrogen retention or loss in agricultural soil. *Soil Biol. and Biochem.* **2018,** *123*, 97-104.
136. Reguera, G.; Kashefi, K., The electrifying physiology of *Geobacter* bacteria, 30 years on. *Adv. Microb. Physiol.* **2019,** *74*, 1-96.
137. Simon, J.; Gross, R.; Einsle, O.; Kroneck, P. M. H.; Kröger, A.; Klimmek, O., A NapC/NirT-type cytochrome *c* (NrfH) is the mediator between the quinone pool and the cytochrome *c* nitrite reductase of *Wolinella succinogenes*. *Mol. Microbiol.* **2000,** *35*, 686-696.
138. Simon, J.; Pisa, R.; Stein, T.; Eichler, R.; Klimmek, O.; Gross, R., The tetraheme cytochrome *c* NrfH is required to anchor the cytochrome *c* nitrite reductase (NrfA) in the membrane of *Wolinella succinogenes*. *Eur. J. Biochem.* **2001,** *268*, 5776-5782.
139. Simon, J., Enzymology and bioenergetics of respiratory nitrite ammonification. *FEMS Microbiol. Rev.* **2002,** *26*, 285-309.
140. Einsle, O.; Stach, P.; Messerschmidt, A.; Simon, J.; Kröger, A.; Huber, R.; Kroneck, P. M. H., Cytochrome *c* Nitrite Reductase from *Wolinella succinogenes.* Structure at 1.6 Å

Resolution, Inhibitor Binding, and Heme-Packing Motifs. *J. Biol. Chem* **2000,** *275*, 39608-39616.
141. Bamford, V. A.; Angove, H. C.; Seward, H. E.; Thomson, A. J.; Cole, J. A.; Butt, J. N.; Hemmings, A. M.; Richardson, D. J., Structure and spectroscopy of the periplasmic cytochrome c nitrite reductase from Escherichia coli. *Biochemistry* **2002,** *41* (9), 2921-2931.
142. Youngblut, M.; Judd, E. T.; Srajer, V.; Sayyed, B.; Goelzer, T.; Elliott, S. J.; Schmidt, M.; Pacheco, A. A., Laue crystal structure of *Shewanella oneidensis* cytochrome *c* nitrite reductase from a high-yield expression system. *J. Biol. Inorg. Chem.* **2012,** *17*, 647-662.
143. Cunha, C. A.; Macieira, S.; Dias, J. M.; Almeida, G.; Gonçalves, L. L.; Costa, C.; Lampreia, J.; Huber, R.; Moura, J. J.; Moura, I., Cytochrome c nitrite reductase from Desulfovibrio desulfuricans ATCC 27774 the relevance of the two calcium sites in the structure of the catalytic subunit (nrfA). *J. Biol. Chem.* **2003,** *278* (19), 17455-17465.
144. Rodrigues, M. L.; Oliveira, T. F.; Pereira, I. A.; Archer, M., X-ray structure of the membrane-bound cytochrome c quinol dehydrogenase NrfH reveals novel haem coordination. *EMBO J.* **2006,** *25* (24), 5951-5960.
145. Einsle, O.; Messerschmidt, A.; Stach, P.; Bourenkov, G. P.; Bartunik, H. D.; Huber, R.; Kroneck, P. M., Structure of cytochrome c nitrite reductase. *Nature* **1999,** *400* (6743), 476-480.
146. Polyakov, K. M.; Boyko, K. M.; Tikhonova, T. V.; Slutsky, A.; Antipov, A. N.; Zvyagilskaya, R. A.; Popov, A. N.; Bourenkov, G. P.; Lamzin, V. S.; Popov, V. O., High-resolution structural analysis of a novel octaheme cytochrome *c* nitrite reductase from the haloalkaliphilic bacterium *Thioalkalivibrio nitratireducens*. *J. Mol. Biol.* **2009,** *389*, 846-862.
147. Bamford, V. A.; Angove, H. C.; Seward, H. E.; Thomson, A. J.; Cole, J. A.; Butt, J. N.; Hemmings, A. M.; Richardson, D. J., Structure and spectroscopy of the periplasmic cytochrome *c* nitrite reductase from *Escherichia coli*. *Biochemistry* **2002,** *41*, 2921-2931.
148. Schumacher, W.; Hole, U.; Kroneck, M. H., Ammonia-forming cytochrome *c* nitrite reductase from *Sulfurospirillum deleyianum* is a tetraheme protein: new aspects of the molecular composition and spectroscopic properties. *Biochem. Biophys. Res. Commun.* **1994,** *205*, 911-916.
149. Moreno, C.; Costa, C.; Moura, I.; Le Gall, J.; Liu, M. Y.; Payne, W. J.; van Dijk, C.; Moura, J. J. G., Electrochemical studies of the hexaheme nitrite reductase from *Desulfovibrio desulfuricans* ATCC 27774. *Eur. J. Biochem.* **1993,** *212*, 79-86.
150. Einsle, O.; Messerschmidt, A.; Huber, R.; Kroneck, P. M. H.; Neese, F., Mechanism of the Six-Electron Reduction of Nitrite to Ammonia by Cytochrome *c* Nitrite Reductase. *J. Am. Chem. Soc.* **2002,** *124*, 11737-11745.
151. Rudolf, M.; Einsle, O.; Neese, F.; Kroneck, P. M. H., Pentahaem cytochrome *c* nitrite reductase: reaction with hydroxylamine, a potential reaction intermediate and substrate. *Biochem. Soc. Trans.* **2002,** *30*, 649-652.
152. Cunha, C. A.; Macieira, S.; Dias, J. M.; Almeida, G.; Gonçalves, L. L.; Costa, C.; Lampreia, J.; Huber, R.; Moura, J. J. G.; Moura, I., Cytochrome *c* nitrite reductase from *Desulfovibrio desulfuricans* ATCC 27774: The relevance of the two calcium sites in the structure of the catalytic subunit (NrfA). *J. Biol. Chem.* **2003,** *278*, 17455-17465.
153. Bewley, K. D.; Ellis, K. E.; Firer-Sherwood, M. A.; Elliott, S. J., Multi-heme proteins: Nature's electronic multi-purpose tool. *Biochim. Biophys. Acta Bioenerg.* **2013,** *1827*, 938-948.
154. Einsle, O.; Messerschmidt, A.; Stach, P.; Bourenkov, G. P.; Bartunik, H. D.; Huber, R.; Kroneck, P. M. H., Structure of cytochrome *c* nitrite reductase. *Nature* **1999,** *400*, 476-480.
155. Stein, N.; Love, D.; Judd, E. T.; Elliott, S. J.; Bennett, B.; Pacheco, A. A., Correlations between the Electronic Properties of *Shewanella oneidensis* Cytochrome *c* Nitrite Reductase

(*cc*NiR) and Its Structure: Effects of Heme Oxidation State and Active Site Ligation. *Biochemistry* **2015,** *54*, 3749-3758.
156. Walker, F. A., Magnetic spectroscopic (EPR, ESEEM, Mössbauer, MCD and NMR) studies of low-spin ferriheme centers and their corresponding heme proteins. *Coord. Chem. Rev.* **1999,** *185*, 471-534.
157. Zoppellaro, G.; Bren, K. L.; Ensign, A. A.; Harbitz, E.; Kaur, R.; Hersleth, H. P.; Ryde, U.; Hederstedt, L.; Andersson, K. K., Studies of ferric heme proteins with highly anisotropic/highly axial low spin (S= 1/2) electron paramagnetic resonance signals with bis-Histidine and histidine-methionine axial iron coordination. *Biopolymers: Original Research on Biomolecules* **2009,** *91* (12), 1064-1082.
158. Youngblut, M.; Pauly, D. J.; Stein, N.; Walters, D.; Conrad, J. A.; Moran, G. R.; Bennett, B.; Pacheco, A. A., Shewanella oneidensis cytochrome c nitrite reductase (ccNiR) does not disproportionate hydroxylamine to ammonia and nitrite, despite a strongly favorable driving force. *Biochemistry* **2014,** *53* (13), 2136-2144.
159. Ponomarenko, N.; Niklas, J.; Pokkuluri, P. R.; Poluektov, O.; Tiede, D. M., Electron paramagnetic resonance characterization of the triheme cytochrome from Geobacter sulfurreducens. *Biochemistry* **2018,** *57* (11), 1722-1732.
160. Que Jr, L., Physical methods in bioinorganic chemistry. *University Science, Sausilito* **2000**.
161. Brautigan, D. L.; Feinberg, B. A.; Hoffman, B. M.; Margoliash, E.; Preisach, J.; Blumberg, W., Multiple low spin forms of the cytochrome c ferrihemochrome. EPR spectra of various eukaryotic and prokaryotic cytochromes c. *Journal of Biological Chemistry* **1977,** *252* (2), 574-582.
162. Fourmond, V.; Hoke, K.; Heering, H. A.; Baffert, C.; Leroux, F.; Bertrand, P.; Léger, C., SOAS: A free program to analyze electrochemical data and other one-dimensional signals. *Bioelectrochemistry* **2009,** *76*, 141-147.
163. Costa, C.; Moura, J. J.; Moura, I.; Liu, M. Y.; Peck, H. D., Jr.; LeGall, J.; Wang, Y. N.; Huynh, B. H., Hexaheme nitrite reductase from *Desulfovibrio desulfuricans*. Mössbauer and EPR characterization of the heme groups. *J. Biol. Chem.* **1990,** *265*, 14382-14388.
164. Walker, F. A., Models of the bis-histidine-ligated electron-transferring cytochromes. Comparative geometric and electronic structure of low-spin ferro-and ferrihemes. *Chem. Rev.* **2004,** *104*, 589-616.
165. Laviron, E., General expression of the linear potential sweep voltammogram in the case of diffusionless electrochemical systems. *J. Electroanal. Chem. Interf. Electrochem.* **1979,** *101*, 19-28.
166. Armstrong, F. A.; Camba, R.; Heering, H. A.; Hirst, J.; Jeuken, L. J. C.; Jones, A. K.; Léger, C.; McEvoy, J. P., Fast voltammetric studies of the kinetics and energetics of coupled electron-transfer reactions in proteins. *Faraday Discuss.* **2000,** *116*, 191-203.
167. Marritt, S. J.; Kemp, G. L.; Xiaoe, L.; Durran, J. R.; Cheesman, M. R.; Butt, J. N., Spectroelectrochemical characterization of a pentaheme cytochrome in solution and as electrocatalytically active films on nanocrystalline metal-oxide electrodes. *J. Am. Chem. Soc.* **2008,** *130*, 8588-8589.
168. Clarke, T. A.; Edwards, M. J.; Gates, A. J.; Hall, A.; White, G. F.; Bradley, J.; Reardon, C. L.; Shi, L.; Beliaev, A. S.; Marshall, M. J., Structure of a bacterial cell surface decaheme electron conduit. *Proc. Natl. Acad. Sci. U.S.A.* **2011,** *108*, 9384-9389.

169. Pulcu, G. S.; Elmore, B. L.; Arciero, D. M.; Hooper, A. B.; Elliott, S. J., Direct electrochemistry of tetraheme cytochrome c554 from *Nitrosomonas europaea*: redox cooperativity and gating. *J. Am. Chem. Soc.* **2007,** *129*, 1838-1839.
170. Ye, T.; Kaur, R.; Senguen, F. T.; Michel, L. V.; Bren, K. L.; Elliott, S. J., Methionine ligand lability of type I cytochromes c: detection of ligand loss using protein film voltammetry. *J. Am. Chem. Soc.* **2008,** *130*, 6682-6683.
171. Ye, T.; Kaur, R.; Wen, X.; Bren, K. L.; Elliott, S. J., Redox properties of wild-type and heme-binding loop mutants of bacterial cytochromes c measured by direct electrochemistry. *Inorg. Chem.* **2005,** *44*, 8999-9006.
172. Bowman, S. E. J.; Bren, K. L., The chemistry and biochemistry of heme c: functional bases for covalent attachment. *Nat. Prod. Rep.* **2008,** *25*, 1118-1130.
173. Jones, G.; Pickard, M., Effect of titanium (III) citrate as reducing agent on growth of rumen bacteria. *Appl. Environ. Microbiol.* **1980,** *39* (6), 1144-1147.
174. Slater, J. W.; Shafaat, H. S., Nickel-substituted rubredoxin as a minimal enzyme model for hydrogenase. *J. Phys. Chem. Lett.* **2015,** *6* (18), 3731-3736.
175. Petasis, D. T.; Hendrich, M. P., Quantitative Interpretation of Multifrequency Multimode EPR Spectra of Metal Containing Proteins, Enzymes, and Biomimetic Complexes. *Methods Enzymol.* **2015,** *563*, 171-208.
176. Stoll, S.; Schweiger, A., EasySpin, a comprehensive software package for spectral simulation and analysis in EPR. *Journal of magnetic resonance* **2006,** *178* (1), 42-55.
177. Laviron, E.; Bard, A. J., *Electroanalytical Chemistry*. Marcel Dekker: New York, 1982; Vol. 12, p 53-151.
178. Huang, S.; Deng, W.-H.; Liao, R.-Z.; He, C., Repurposing a Nitric Oxide Transport Hemoprotein Nitrophorin 2 for Olefin Cyclopropanation. *ACS Cat.* **2022,** *12*, 13725-13731.
179. Nechay, M. R.; Valdez, C. E.; Alexandrova, A. N., Computational treatment of metalloproteins. *J. Phys. Chem. B* **2015,** *119* (19), 5945-5956.
180. Sheng, X.; Kazemi, M.; Planas, F.; Himo, F., Modeling enzymatic enantioselectivity using quantum chemical methodology. *ACS Cat.* **2020,** *10* (11), 6430-6449.
181. Himo, F., Recent trends in quantum chemical modeling of enzymatic reactions. *J. Am. Chem. Soc.* **2017,** *139* (20), 6780-6786.
182. Bím, D.; Navrátil, M.; Gutten, O.; Konvalinka, J.; Kutil, Z.; Culka, M.; Navrátil, V.; Alexandrova, A. N.; Bařinka, C.; Rulíšek, L. r., Predicting Effects of Site-Directed Mutagenesis on Enzyme Kinetics by QM/MM and QM Calculations: A Case of Glutamate Carboxypeptidase II. *J. Phys. Chem. B* **2022,** *126* (1), 132-143.
183. Keri, R. S.; Rajappa, C. K.; Patil, S. A.; Nagaraja, B. M., Benzimidazole-core as an antimycobacterial agent. *Pharmacol. Res.* **2016,** *68* (6), 1254-1265.
184. Gaba, M.; Singh, S.; Mohan, C., Benzimidazole: an emerging scaffold for analgesic and anti-inflammatory agents. *Eur. J. Med. Chem.* **2014,** *76*, 494-505.
185. Bykov, D.; Neese, F., Six-Electron Reduction of Nitrite to Ammonia by Cytochrome *c* Nitrite Reductase: Insights from Density Functional Theory Studies. *Inorg. Chem.* **2015,** *54* (19), 9303-9316.
186. Bykov, D.; Neese, F., Substrate Binding and Activation in the Active Site of Cytochrome *c* Nitrite Reductase: A Density Functional Study. *J. Biol. Inorg. Chem.* **2011,** *16* (3), 417-430.
187. Bykov, D.; Neese, F., Reductive Activation of the Heme Iron–Nitrosyl Intermediate in the Reaction Mechanism of Cytochrome *c* Nitrite Reductase: A Theoretical Study. *J. Biol. Inorg. Chem.* **2012,** *17* (5), 741-760.

188. Abe, M.; Kitagawa, T.; Kyogoku, Y., Resonance Raman Spectra of Octaethylporphyrinato-Ni(II) and *Meso*-Deuterated and ^{15}N Substituted Derivatives. II. A normal Coordinate Analysis. *J. Chem. Phys.* **1978,** *69* (10), 4526-4534.
189. Choi, S.; Spiro, T. G.; Langry, K. C.; Smith, K. M., Vinyl influences on Protoheme Resonance Raman Spectra: Nickel(II) Protoporphyrin IX with Deuterated Vinyl Groups. *J. Am. Chem. Soc,* **1982,** *104* (16), 4337-4344.
190. Choi, S.; Spiro, T. G.; Langry, K. C.; Smith, K. M.; Budd, D. L.; La Mar, G. N., Structural Correlations and Vinyl Influences in Resonance Raman Spectra of Protoheme Complexes and Proteins. *J. Am. Chem. Soc,* **1982,** *104* (16), 4345-4351.
191. Kitagawa, T.; Abe, M.; Ogoshi, H., Resonance Raman Spectra of Octaethylporphyrinato-Ni(II) and *Meso*-Deuterated and ^{15}N Substituted Derivatives. I. Observation and Assignments of Nonfundamental Raman Lines. *J. of Chem. Phys.* **1978,** *69* (10), 4516-4525.
192. Lee, H.; Kitagawa, T.; Abe, M.; Pandey, R. K.; Leung, H. K.; Smith, K. M., Characterization of Low Frequency Resonance Raman Bands of Metallo-Protoporphyrin ix. Observation of Isotope Shifts and Normal Coordinate Treatments. *J. Mol. Struct.* **1986,** *146*, 329-347.
193. Bostelaar, T.; Vitvitsky, V.; Kumutima, J.; Lewis, B. E.; Yadav, P. K.; Brunold, T. C.; Filipovic, M.; Lehnert, N.; Stemmler, T. L.; Banerjee, R., Hydrogen Sulfide Oxidation by Myoglobin. *J. Am. Chem. Soc,* **2016,** *138* (27), 8476-8488.
194. Das, P. K.; Samanta, S.; McQuarters, A. B.; Lehnert, N.; Dey, A., Valence Tautomerism in Synthetic Models of Cytochrome P450. *Proc. Natl. Acad. Sci. U.S.A.* **2016,** *113* (24), 6611-6616.
195. Paulat, F.; Praneeth, V. K. K.; Näther, C.; Lehnert, N., Quantum Chemistry-Based Analysis of the Vibrational Spectra of Five-Coordinate Metalloporphyrins [M(TPP)Cl]. *Inorg. Chem.* **2006,** *45* (7), 2835-2856.
196. Lehnert, N.; Berto, T. C.; Galinato, M. G. I.; Goodrich, L. E., The Role of Heme-Nitrosyls in the Biosynthesis, Transport, Sensing, and Detoxification of Nitric Oxide in Biological Systems: Enzyme and Model Complexes. In *Handbook Of Porphyrin Science: With Applications To Chemistry, Physics, Materials Science, Engineering, Biology And Medicine* Guilard, R.; Smith, K. M.; Kadish, K. M., Eds. World Scientific: Singapore, 2011; Vol. 14, pp 1-247.